Computational Method for Aerodynamic and Aeromechanical Analysis of Offshore Wind Turbines

Shine Win Naung

PhD

2021

Computational Method for Aerodynamic and Aeromechanical Analysis of Offshore Wind Turbines

Shine Win Naung

A thesis submitted in partial fulfilment of the requirements of the University of Northumbria at Newcastle for the degree of Doctor of Philosophy

Research undertaken in the Faculty of Engineering and Environment

October 2021

Declaration

I declare that the work contained in this thesis has not been submitted for any other award and that it is all my own work. I also confirm that this work fully acknowledges opinions, ideas and contributions from the work of others.

Ethical clearance for the research presented in this thesis has been approved. Approval has been sought and granted by the University Ethics Committee on 11th June 2018.

I declare that the Word Count of this Thesis is 37,950 words.

Name: Shine Win Naung

Signature:

Date: 11 October 2021

Acknowledgement

I would like to express my greatest gratitude to Prof. Mohammad Rahmati, my principal supervisor, for his patient guidance, enthusiastic encouragement and useful critiques for the success of this project and thesis. This project would not have been possible without the funding. I would like to acknowledge the PhD Research Studentship funded by the Faculty of Engineering and Environment at the Northumbria University under the Researcher Development Framework (RDF). In this regard, I acknowledge the financial support received from the Engineering Physics and Science Research Council of the UK. My sincere thanks to Prof. Mohammad Rahmati for selecting and trusting me to undertake this project. I would not have been in this position today without his acceptance and continuous support. I have learned many things from him, both technically and non-technically, which helped me prepared for the project as well as for the establishment of my academic career. Furthermore, I would like to thank the members of the supervision team which include Dr Hamed Farokhi, the second supervisor, and Prof. Dingxi Wang, the external supervisor, for their time, support, and useful suggestions for the project.

I would like to take this opportunity to thank Dr Philip Hackney and Dr Ken Leung for their presence in the Project Approval and Annual Progression meetings as the panel chair and the subject expert, as well as for their constructive comments on the work, which improved the overall quality of the project. In addition, I would like to acknowledge the technical support received from both IT and lab technicians in the Faculty of Engineering and Environment at the Northumbria University. I would also like to appreciate my colleagues and fellow researchers for the fruitful discussions we have had over the past years through our weekly seminars or casual meetings. These discussions have resulted in broadening knowledge in different aspects of the research.

I am very pleased to say that this thesis is dedicated to my parents who have always supported me in every way possible. Without their love, encouragement and support, I would not be here today writing this thesis. Words are never enough to describe either their love or my gratitude for their love and support. I am proud to be their son, and also, I am happy to be their proud son. My thanks also go to my only sister who always stands by me. Finally, I would like to thank my wife, Nay Chi, for her unconditional support and love, and for always being with me.

Abstract

Innovative wind power technologies have led to wind turbines with significantly longer and more flexible blade designs in order to meet the rise in green energy demands. A trend towards larger wind turbine sizes could potentially result in the blades experiencing aeroelastic instability problems. Furthermore, a typical wind farm is composed of multiple large-scale wind turbines, and therefore, the aerodynamics and aeroelasticity of a wind turbine can be influenced by various sources of flow unsteadiness generated by neighbouring wind turbines. The overall aim of this project is, therefore, to analyse the aerodynamics and aeroelasticity of wind turbines by taking various sources of flow unsteadiness into account using a high-fidelity computational method at an affordable computational cost. The computational resources and costs required for the aerodynamic and aeromechanical simulations of wind turbines using high-fidelity numerical methods are very high, which is the main challenge for the wind energy research community. Frequency domain methods, which are widely used in turbomachinery analysis but relatively new for wind turbines, are not only accurate but also computationally efficient for predictions of aerodynamic and aeroelasticity parameters. In this study, a nonlinear frequency domain solution method is proposed for the in-depth aerodynamic and aeromechanical analysis of wind turbines including multiple wind turbine models, taking numerous sources of flow unsteadiness into account.

Various sources of flow unsteadiness, such as the harmonic inflow wakes, the oscillation of a blade structure, and the wake and turbulence from a neighbouring wind turbine are considered, and their effects on the aerodynamics and aeroelasticity of wind turbines are investigated. Different levels of modelling complexity are discussed in this thesis, including modelling and simulation of wind turbine blade aerofoils, rotor blades, complete wind turbine model including a tower, and multiple wind turbines in arrays. The frequency domain solution method makes it possible to model and simulate realistic flow conditions in consideration of the blade vibration as well as the effects of multiple wind turbines models without requiring significant computational resources. The present study reveals that the proposed nonlinear frequency domain solution method not only provides accurate predictions of aerodynamics and aeroelasticity of wind turbines but also reduces the computation time by one to two orders of magnitude compared to the conventional time domain methods.

Publications

1. Win Naung S, Nakchi ME, Rahmati MT (2021) High-fidelity CFD Simulations of Two Wind Turbines in Arrays using Nonlinear Frequency Domain Solution Method; Renewable Energy; 174: 984-1005.
2. Nakchi ME, Win Naung S, Rahmati MT (2021) High-Resolution Direct Numerical Simulations of Flow Structure and Aerodynamic Performance of Wind Turbine Airfoil at Wide Range of Reynolds Numbers; Energy; 225: 120261.
3. Win Naung S, Rahmati MT, Farokhi H (2021) Aeromechanical Analysis of a Complete Wind Turbine Using Nonlinear Frequency Domain Solution Method; ASME. J. Eng. Gas Turbines Power; 143(1): 011018.
4. Win Naung S, Rahmati MT, Farokhi H (2021) Nonlinear frequency domain solution method for aerodynamic and aeromechanical analysis of wind turbines; Renewable Energy; 167: 66-81.
5. Win Naung S, Nakchi ME, Rahmati MT (2021) An Experimental and Numerical Study on the Aerodynamic Performance of Vibrating Wind Turbine Blade with Frequency-Domain Method; J. Appl. Comput. Mech.; 7(3): 1737-1750.
6. Win Naung S, Nakchi ME, Rahmati MT (2021) Prediction of Flutter Effects on Transient Flow Structure and Aeroelasticity of Low-Pressure Turbine Cascade with Direct Numerical Simulations; Aerospace Science and Technology; https://doi.org/10.1016/j.ast.2021.107151.
7. Win Naung S, Rahmati MT, Farokhi H (2021) Direct Numerical Simulation of Interaction between Transient Flow and Blade Structure in a Modern Low-Pressure Turbine; International Journal of Mechanical Sciences; 19: 106104.
8. Nakchi ME, Win Naung S, Rahmati MT (2020) DNS of secondary flows over oscillating low-pressure turbine using spectral/hp element method; International Journal of Heat and Fluid Flow; 86: 108684.
9. Win Naung S, Rahmati MT, Farokhi H (2020) Aeromechanical Analysis of a Complete Wind Turbine Using Nonlinear Frequency Domain Solution Method; Proceedings of the ASME Turbo Expo 2020: Turbomachinery Technical Conference and Exposition. Volume 12: Wind Energy; September 21–25, Virtual, Online.
10. Win Naung S, Rahmati MT, Farokhi H (2020) Numerical Investigation of the Effect of Flutter Instability of the Blade on the Unsteady Flow in a Modern Low-Pressure Turbine; Proceedings of the ASME Turbo Expo 2020: Turbomachinery Technical

Conference and Exposition. Volume 10A: Structures and Dynamics; September 21–25, Virtual, Online.

11. Win Naung S, Rahmati MT, Farokhi H (2019) Aerodynamic Analysis of a Wind Turbine with Elevated Inflow Turbulence and Wake using Harmonic Method; Proceedings of the ASME 2019 38th International Conference on Ocean, Offshore and Arctic Engineering (OMAE2019); June 9-14, Glasgow, Scotland.
12. Win Naung S, Rahmati MT, Farokhi H (2019) Aeromechanical Analysis of Wind Turbines using Non-linear Harmonic Method; Proceedings of the ASME 2019 38th International Conference on Ocean, Offshore and Arctic Engineering (OMAE2019); June 9-14, Glasgow, Scotland.

Table of Contents

Nomenclature

F_L	-	Lift force
F_D	-	Drag force
ρ	-	Air density (1.185 kg/m^3)
${V_r}^2$	-	Relative wind velocity
c	-	Chord length
C_L	-	Lift coefficient
C_D	-	Drag coefficient
Re	-	Reynolds number
C_{ax}	-	Axial chord length
μ	-	Viscosity (1.831×10^{-5} Pa.s)
P_{max}	-	Maximum available power
A	-	Surface area
Ω	-	Control volume
S	-	Surface
U	-	Vectors of conservative flow variables
R	-	Lumped residual and source term
$\vec{F}_I$	-	Inviscid flux vectors
$\vec{F}_V$	-	Viscous flux vectors
Q	-	Quantity of flow variables
d_{face}	-	Numerical dissipation term
t	-	Time
Δt	-	Time-step
ψ	-	Runge-Kutta scheme coefficient
$\overline{U}$	-	Fourier coefficient
A_U	-	Fourier coefficient
B_U	-	Fourier coefficient
m	-	Number of harmonics
ω	-	Fundamental frequency
$[M]$	-	Mass matrix
$[C]$	-	Damping matrix
$[K]$	-	Stiffness matrix
$\vec{d}$	-	Displacement

$\vec{f}$	-	External force
q_i	-	Generalised displacement
$\bar{q}$	-	Mean value of the displacement
q_A	-	Amplitude of the displacement
$\vec{\phi}_i$	-	Mode shape of the structure normalised by the mass
ω_i	-	Natural frequency
ξ_i	-	Damping coefficient
f	-	Interpolation function
$\vec{x}$	-	Coordinates of the boundary nodes
$\vec{x}_{n_k}$	-	Position of the boundary node *n*
N_B	-	Number of boundary nodes
φ	-	Radial basis function
p	-	Polynomial
α	-	Coefficient of interpolation function
β	-	Coefficient of polynomial function
F_R	-	Radial basis function matrix
P_B	-	Polynomial matrix
d_B	-	Value of displacement at the boundary
l	-	Interior arc-length
L	-	Arc-length of a segment
x_{ref}	-	Coordinates of the reference node
x_{new}	-	Coordinates of the new edge of interior points
V_∞	-	Freestream velocity
d	-	Total displacement of wall deformation
$\bar{d}$	-	Mean value of wall displacement
d_A	-	Amplitude of wall displacement
C_p	-	Pressure coefficient
C_{p1}	-	Unsteady pressure amplitude coefficient
AoA	-	Angle of attack
V	-	Velocity magnitude
V_{ref}	-	Reference velocity
D	-	Rotor diameter
σ	-	Inter blade phase angle
w	-	Wind speed

$\bar{w}$	-	Average wind speed
w_A	-	Amplitude of wind speed fluctuations
P	-	Pressure
$\bar{P}$	-	Time-averaged pressure
P_A	-	Fourier coefficient
P_B	-	Fourier coefficient
$\tilde{P}$	-	Unsteady pressure amplitude
F	-	Force applied on the blade
F_{max}	-	Maximum force applied on the blade
τ	-	Torque applied on the blade
τ_{max}	-	Maximum torque applied on the blade
W	-	Aerodynamic work per vibration cycle
t_0	-	Initial time
T	-	Vibration period
p	-	Fluid pressure
v	-	Velocity of the blade due to imposed displacement
$\hat{n}$	-	Surface normal unit vector
m_m	-	Modal mass
ω_v	-	Vibration frequency
d_{max}	-	Maximum vibration amplitude
C_f	-	Skin friction coefficient

Chapter 1. Introduction

1.1. Introduction to the Project

The power generation from renewable energy resources has been significantly increased in recent years. Among renewable energy resources, wind power is one of the fastest-growing and most widely used technologies and green sources of electricity, as the wind is reliable and freely available [1]. Wind energy has become overwhelmingly popular in recent years due to its promising advantages. Approximately 10 GW of electricity is currently produced from offshore wind, and the combined offshore and onshore wind farms can provide power for more than 18 million homes every year in the UK. It is expected that over 10% of UK electricity will be generated from offshore wind in the next few years [2]. The UK government recently published a ten-point plan for a green industrial revolution, targeting net-zero greenhouse gas emissions by 2050 [3]. This significantly raises the demand for energy produced from clean resources, especially from offshore wind as the UK is the world's leader in offshore wind.

To meet the increasing energy demand, the sizes of wind turbines are being increased to capture the wind more effectively and efficiently. Significant technical advances and efforts made over the last decade have made it possible to capture wind energy more efficiently, which could reduce the price of electricity generation [4]. These advances have led to larger, offshore wind turbines with lighter, more flexible blades with considerably larger blade lengths. Figure 1.1 shows the evolution of wind turbine sizes over the past decades. It is seen that the size of a wind turbine has almost doubled every two decades. The largest wind turbine to date is 260 m high with a 220 m rotor diameter, which is higher than the London Eye [5]. A wind turbine is subject to dynamic loadings continuously throughout its life. This, however, has introduced significant aeroelastic instabilities, such as blade flutter and vortex-induced vibrations, which have resulted in several catastrophic failures of wind turbine blades [6, 7]. The main objective of this project is to investigate the aerodynamic and aeroelastic performances of wind turbines using a high-fidelity computational method. Applications of highly efficient numerical methods become particularly important and necessary for wind turbines because they can facilitate the physical understandings of the flow behaviour related to the interactions between the transient flow and the wind turbine structure, especially the blades. This

understanding can be used for multidisciplinary and concurrent optimisation of wind turbines.

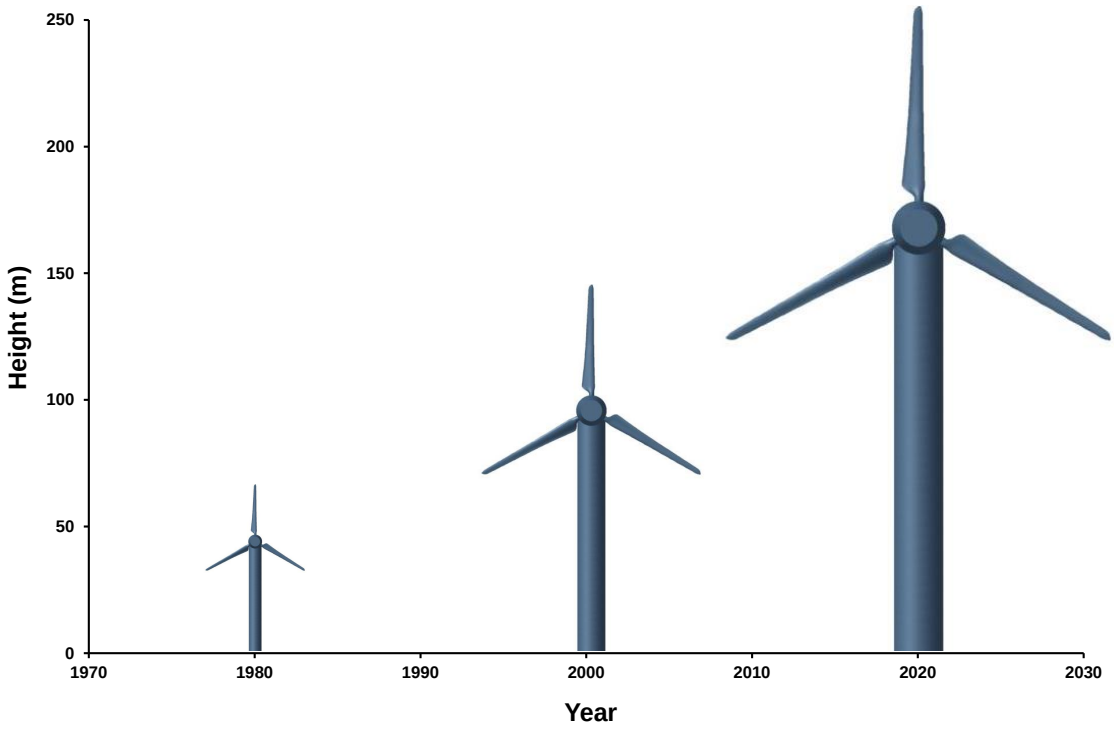

Figure 1.1. Evolution of wind turbine sizes and rotor diameters over the past decades.

Although innovative technologies and advances in wind turbines play vital roles in the success of the wind energy industry, the design and optimisation of wind turbines and wind farms to maximize the energy captured as well as the power generation are still challenging for the industry [8, 9]. The majority of the previous studies, both experimentally and numerically, considered a steady inflow condition, while in reality, the nature of the wind is not steady and changes in time. In addition, a wind farm consists of a number of large-capacity wind turbines and therefore, the flow around a turbine is influenced by the wakes from neighbouring turbines [10]. The flow unsteadiness and turbulence due to the presence of nearby wind turbines can impose a significant impact on wind turbine aerodynamics and aeroelasticity. Among several factors to design and optimise a wind farm layout, the determination of separation distances between adjacent turbines is crucial in minimizing the influence of the wake deficits and turbulence from the upstream wind turbine in addition to maximizing the power output of the downstream turbine [11]. Therefore, another objective of this project is the inclusion of different sources of flow unsteadiness in the numerical investigations and analysis of their impact on wind turbine performances. The calculations and predictions of the flow behaviour

and wake associated with these sources of flow unsteadiness are of utmost importance for the wind turbine aerodynamics and aeroelasticity, which can be utilised for the optimisation of the wind farm layout.

1.2. Aims and Objectives

The primary aims of this project are to develop a highly efficient Computational Fluid Dynamics (CFD) model to analyse aerodynamics and aeroelastic instabilities in offshore wind turbines taking various sources of flow unsteadiness into account while reducing the computation time to the lowest and acceptable level.

The main objectives of the project include:

a) Development of a highly efficient nonlinear frequency domain solution model for aerodynamic and aeromechanical analysis of wind turbines
b) Validation and identification of the adequate working ranges of the frequency domain solution method for the aeromechanical analysis of wind turbines
c) Numerical investigation on the aeroelastic instabilities of wind turbine blades using a highly efficient frequency domain solution technique to understand fluid-structure interactions and to predict aerodynamic and aeromechanical performances of wind turbines taking various sources of flow unsteadiness into account
d) Aerodynamic and aeromechanical analysis of wind turbine rotors considering the inflow wake and turbulence
e) Aerodynamic and aeromechanical analysis of a complete wind turbine including a tower, and investigation on the effects associated with the tower
f) Determination of the capability of the proposed frequency domain solution method with respect to the amplitude of blade vibration of a wind turbine
g) Flow simulations by placing two wind turbines in arrays to analyse the effects and the flow unsteadiness associated with the neighbouring wind turbine, and to determine the minimum distance between the turbines

1.3. Statement of the Distinctiveness and Contribution to the Area of the Study

The distinctive features and the main contributions of this project to date are stated below:

a) The application and extensive validations of the nonlinear frequency domain solution method for the aerodynamic and aeromechanical analysis of wind turbines

b) Numerical Investigations of the aeroelastic instability problems in wind turbines using a highly efficient CFD method which provides a comprehensive understanding of the physics related to fluid-structure interactions at an affordable computational cost
c) Investigation and identification of the adequate working ranges of the frequency domain method on analysing aeroelasticity and the highly unsteady flow due to fluid-structure interactions
d) Inclusion of various sources of flow unsteadiness such as inflow wakes or effects of neighbouring wind turbines and in-depth analysis of their impact on aerodynamics and aeroelasticity of wind turbines
e) Aeromechanical analysis of wind turbines for various inter blade phase angles using a single passage domain

1.4. Overview of the Thesis

This thesis consists of eight chapters. Chapter 2 provides a detailed literature review of the project. The literature review starts with a brief history and evolution of wind energy technology, followed by the fundamentals of wind turbine aerodynamics. Afterwards, this chapter presents aeroelastic instabilities in turbomachines and wind turbines. This section is followed by a discussion of existing experimental and numerical studies for wind turbine applications. The numerical studies involve the review of both aerodynamic and structural modelling methods. The review of frequency domain methods, which are widely used in the turbomachinery community, is also presented in this chapter. This chapter is then concluded with a discussion of the overview of the literature review and the knowledge gap.

The methodology applied in this project is presented in Chapter 3. This chapter begins with an expression of the flow governing equations. This project proposes a nonlinear frequency domain solution method for the aerodynamic and aeromechanical analysis of wind turbines using a modal coupling fluid-structure interaction method. The formulation of the proposed frequency domain method is provided in the following section. Modelling of fluid-structure interaction is presented in Section 3.5, which is followed by the details of the rotor-stator interaction method to account for the interaction and relative motion between the rotating domain and the stationary domain of wind turbine models.

In Chapter 4, the simulations of aerodynamics and aeroelasticity of an oscillating wind turbine blade aerofoil at various angles of attack and Reynolds numbers are presented.

The proposed frequency domain solution method is first applied to the analysis of a linear turbine cascade, and the method is validated against the experiment. Afterwards, the NACA0012 type aerofoil is selected for the wind turbine blade aerofoil. An experiment is also designed and conducted to measure pressure distributions over the aerofoil at various angles of attack. The CFD simulations of this aerofoil are performed using the same conditions as the experiment, and the numerical results are compared to the experimental results for validation. Afterwards, the aeromechanical simulations of the selected aerofoil are conducted for various angles of attack and Reynolds number, and the effects of the angle of attack and Reynolds number on the aerodynamics and aeroelasticity of the blade aerofoil are thoroughly investigated. The proposed frequency domain solution method is extensively validated against the typical time domain solution method for all simulations to ensure the method is accurate in predicting aerodynamic and aeroelasticity parameters.

After the application of the frequency domain method for the analysis of a wind turbine blade aerofoil, the aerodynamic and aeromechanical analyses of a wind turbine rotor using the proposed nonlinear frequency domain solution method are provided in Chapter 5. The aerodynamic analysis of a wind turbine, either experimentally or numerically, is usually conducted using a steady inflow condition. However, the flow unsteadiness of the inflow can affect the aerodynamic and aeroelastic performances of a wind turbine. Therefore, in this chapter, the inflow wakes are generated at various frequencies, and the effects of the wake and turbulence on the aerodynamic flow field around the rotor are investigated. Afterwards, the aeromechanical simulations of the rotor blades using different materials are performed. The unsteady pressure distributions and aeroelasticity parameters such as aerodynamic damping due to the blade vibration are calculated and analysed. Finally, the chapter concludes with the advantages of the proposed frequency domain solution method for the effective and efficient prediction of the aerodynamics and aeroelasticity of wind turbine rotors compared to the typical time domain solution methods.

Chapter 6 demonstrates the high-fidelity CFD simulations of a complete wind turbine model including a tower. Significant computation time is usually required for modelling and simulation of the fluid-structure interaction between the blade and the unsteady flow. Thus, the computational benefits of the proposed frequency domain method provide a solution for these challenges. In this chapter, an aeroelasticity analysis of a complete wind

turbine is investigated. The unsteady flow parameters and the aeroelastic performances of the wind turbine are evaluated. Furthermore, the flow field around the wind turbine due to the presence of a tower is also analysed in this chapter. This chapter then concludes with the comparison between the frequency domain method and the time domain method in terms of computational efficiency and highlights the benefits of the frequency domain solution method for the aeromechanical analysis of complete wind turbine models.

Chapter 7 presents high-fidelity CFD simulations of two wind turbines in arrays using the proposed nonlinear frequency domain solution method. As the aerodynamics of a wind turbine within a windfarm can be influenced by the wake generated from neighbouring wind turbines, this chapter thoroughly investigates the impact of the flow unsteadiness caused by the upstream wind turbine on the downstream one by placing two turbines in arrays. Determination of the distance between wind turbines is crucial for the optimisation of a wind farm layout and the energy output. Therefore, a detailed investigation of the effect of the upstream turbine on the downstream one with respect to the separation distance enables understanding the related impact on both aerodynamic performances and flow behaviour of wind turbines within a wind farm. Traditional time domain solution methods are very time-consuming or impractical in order to perform this type of analysis, which is due to the demand for high computational resources. In this chapter, a novel modelling and computational method employing the nonlinear frequency domain solution method is used to model and simulate two wind turbines in arrays and flow nonlinearities due to their interactions with the flow. Various separation distances are used, and the numerous effects of the upstream wind turbine on the downstream one are thoroughly investigated. This chapter then concludes with the effects of the upstream wind turbine on the downstream one, including the aerodynamic performances and flow behaviour with respect to the separation distance. Extensive validations of the nonlinear frequency domain solution method against the conventional time domain solution method reveal that the proposed frequency domain solution method provides accurate results while reducing the computational cost by one to two orders of magnitude.

Chapter 8 summarises the overall conclusions of the project. Furthermore, this chapter highlights the main contributions and outcomes of this project and provides future work for further contributions to be made.

Chapter 2. Literature Review

2.1. A Brief History of Wind Turbines

A wind turbine is a turbine that uses the kinetic energy in the wind to generate electrical energy using mechanical components. Utilising wind energy was dated back to the very ancient years when the energy from the wind was used for sailing boats [12]. Then, it was gradually discovered that wind could be harvested for greater uses. A windmill, which basically converts wind power to mechanical power, was first introduced in the 7th century for milling grains [13]. Windmills then evolved over time, later being used for several other purposes, such as pumping water and draining rice fields [14]. Towards the end of the 19th century, electricity came into use and the first attempts of producing electricity from wind power, called wind turbines, were being made by Poul La Cour [15]. He transformed the traditional windmill technology into power-generating wind turbines based on scientific principles. His first models of wind turbines followed that of the windmills with four sails. His wind power technology was then expanded to build turbines in various sizes and to yield a higher efficiency in power output. The La Cour models of wind turbines were later replaced by that of Smidth, which incorporated the aerodynamic shape in the rotor designs [15]. The initial wind turbine models of Smidth had two-bladed rotors but the three-bladed rotor design was later developed and used due to some issues related to the dynamic characteristics of the two-blade model. Since then, wind turbine technology has evolved over periods of time aiming to achieve a higher power coefficient. However, in 1920, the scientist Albert Betz proved that a disk-shaped rotor can physically capture only 59.3% of the power available in the air and therefore, the maximum power coefficient that a wind turbine can achieve is 0.593 [16]. His theory, later completed by Glauert [17], is still valid in the present and used for many validations and design processes [18]. A major turnaround in wind power generation was seen after the energy crisis of 1973, which forced countries and governments to search for alternative energy resources, particularly renewable resources, to reduce the dependency on oil for power generation. Since then, the wind power technology thrived in all aspects. In 1980s, several megawatt-scale wind turbines were developed, and the capacity and the size of turbines were constantly increased over the years [19]. Figure 1.1 compares the evolution of wind turbine sizes over the past decades.

2.2. Fundamentals of Wind Turbine Aerodynamics

There are two types of wind turbines such as horizontal-axis wind turbines and vertical-axis wind turbines. As this project aims to analyse offshore wind turbines, only horizontal-axis wind turbines will be presented in this thesis. A horizontal-axis wind turbine consists of three major components: the rotor, nacelle and tower.

The rotor of a modern wind turbine is comprised of three blades. The blades are composed of different aerofoil profiles at different sections of the blade [20]. The main task of a rotor blade is to extract the energy from the wind [21]. Figure 2.1 shows the schematic diagram of the wind interacting with the wind turbine and the detailed description of forces acting on the blade aerofoil. Due to the rotation of the rotor, the relative wind velocity V_r interacts with the blade. The angle between the chord line and the relative velocity is the angle of attack α. When the relative velocity interacts with the wind turbine blade aerofoil, the reaction force F_R occurs on the blade structure. The reaction force is decomposed into the lift force F_L and drag force F_D. The lift force and drag force can be defined as:

$$F_L = 0.5 \,.\, \rho \,.\, V_r^{\,2} . c \,.\, C_L \tag{2.1}$$

$$F_D = 0.5 \,.\, \rho \,.\, V_r^{\,2} . c \,.\, C_D \tag{2.2}$$

where ρ is fluid density and c is the length of the aerofoil chord. C_L and C_D are the lift coefficient and drag coefficient, respectively.

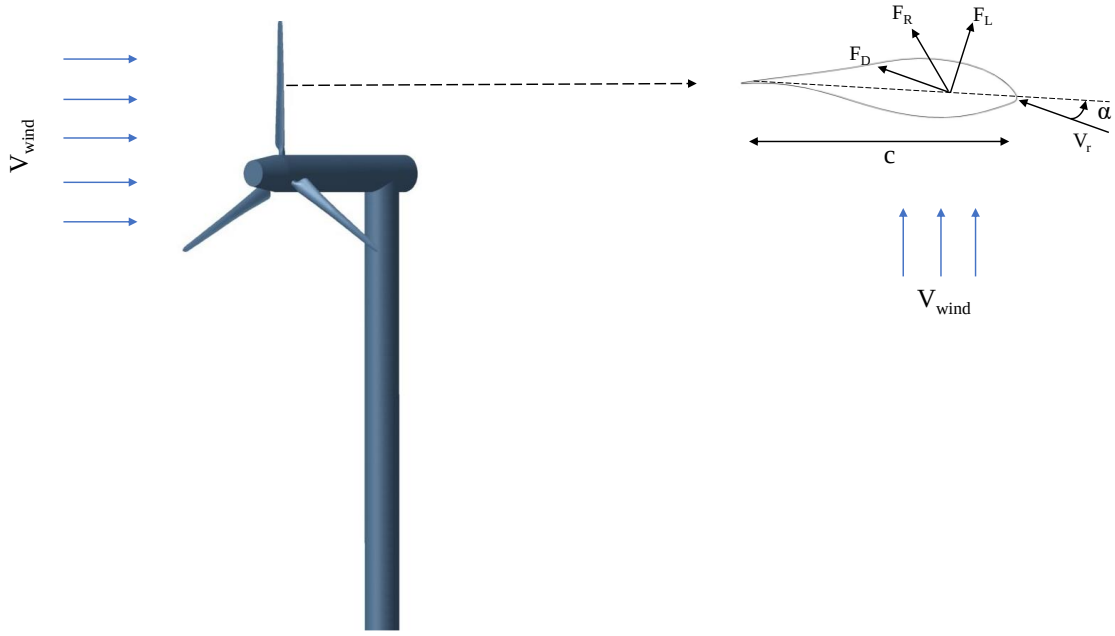

Figure 2.1. Schematic diagram of the wind interaction with the wind turbine and detailed description of forces acting on the blade aerofoil.

Reynolds number *Re* for a flow past an aerofoil can be expressed as:

$$Re = \frac{\rho V_r c_{ax}}{\mu} \tag{2.3}$$

where C_{ax} is the axial chord length and μ is the dynamic viscosity. The lift and drag coefficients can be determined based on the Reynolds number and angle of attack [22]. Similar to aeroplanes, a high ratio of lift to drag coefficient is preferred for wind turbine applications to yield a high lift force for the blade rotation [23]. The drag should be kept as low as possible. When the wind pasts the blade aerofoil, the pressure is distributed over the aerofoil surfaces (See Figure 2.2). Depending on the shape of the aerofoil and angle of attack, the pressure on one side of the aerofoil is greater than that of the other side. This pressure difference between the two surfaces of the aerofoil produces a lift force. Typically, raising the angle of attack causes a bigger pressure difference between the aerofoil surfaces, and thereby, increases the lift. However, it can also cause the flow separation on the suction surface of the aerofoil which introduces the drag [24]. It is found that the flow separation is larger at higher angles of attack [25]. At and beyond the stall angle, the flow starts to separate on the suction surface near the leading edge, and the separation bubbles and flow recirculation can be seen in the separation zone [25]. Figure 2.3 presents an image of flow separation from an aerofoil obtained from a high-resolution

flow simulation. It shows that the flow separation, recirculation and separation bubbles make the flow more unsteady, and vortex shedding happens in the wake region. Due to this highly unsteady flow behaviour, the blade experiences unsteady pressure fluctuations and aerodynamic loads on the pressure and suction surfaces of the blade that can lead to a dynamic stall and aeroelastic instabilities. Figure 2.4 demonstrates a typical lift-drag coefficient curve with respect to the angle of attack. As shown, the lift is linearly increased when the angle of attack is raised until it reaches the maximum point. The angle at which the maximum lift occurs can be understood as the stall angle. On the other hand, the drag curve stays relatively flat with increasing angles of attack. As it comes closer to the stall angle, the drag gradually increases, and it rises suddenly after the stall angle. The regions before and after the stall angle are known as the pre-stall region and the post-stall region, respectively. In the post-stall region, the lift is reduced and the draft is increased, which is not desirable for both aeroplanes and wind turbines [26].

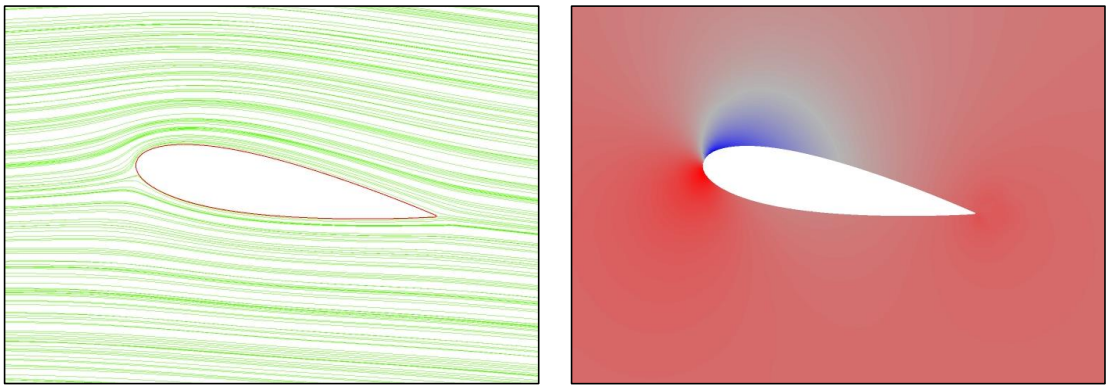

a) Flow streamlines b) Pressure contour

Figure 2.2. Flow streamlines and pressure distribution around an aerofoil.

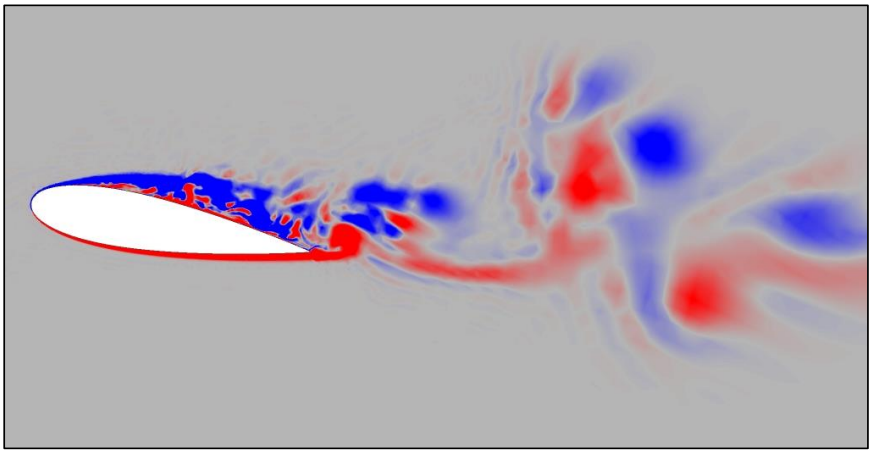

Figure 2.3. Flow separation and vortex generation over an aerofoil.

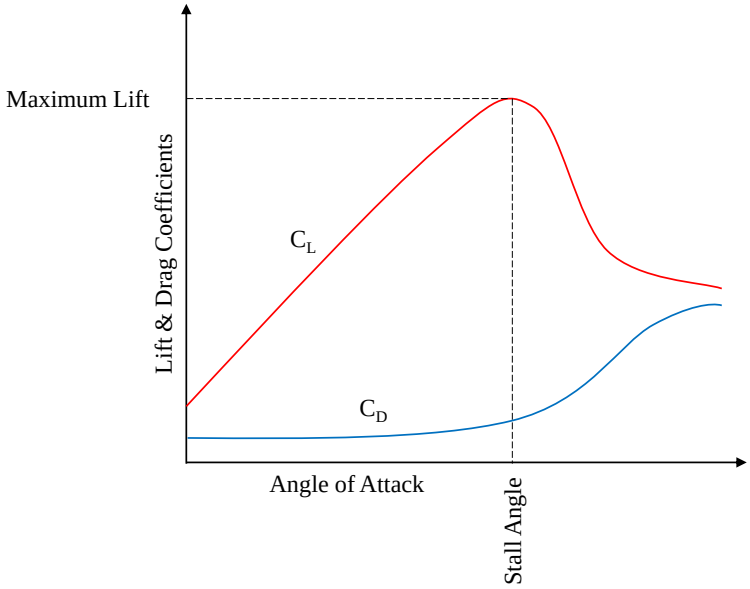

Figure 2.4. Lift-Drag coefficient with respect to the angle of attack.

In Betz's elementary momentum theory [23], an energy converter similar to a wind turbine rotor, which converts the kinetic energy into mechanical energy, is considered as a disk-shaped rotor (see Figure 2.5). In this figure, V_1 and V_2 represent the free-stream inflow velocity and the velocity in the wake region, respectively, and V^* stands for the velocity just behind the rotor after the flow passes through. A is the surface area of the rotor.

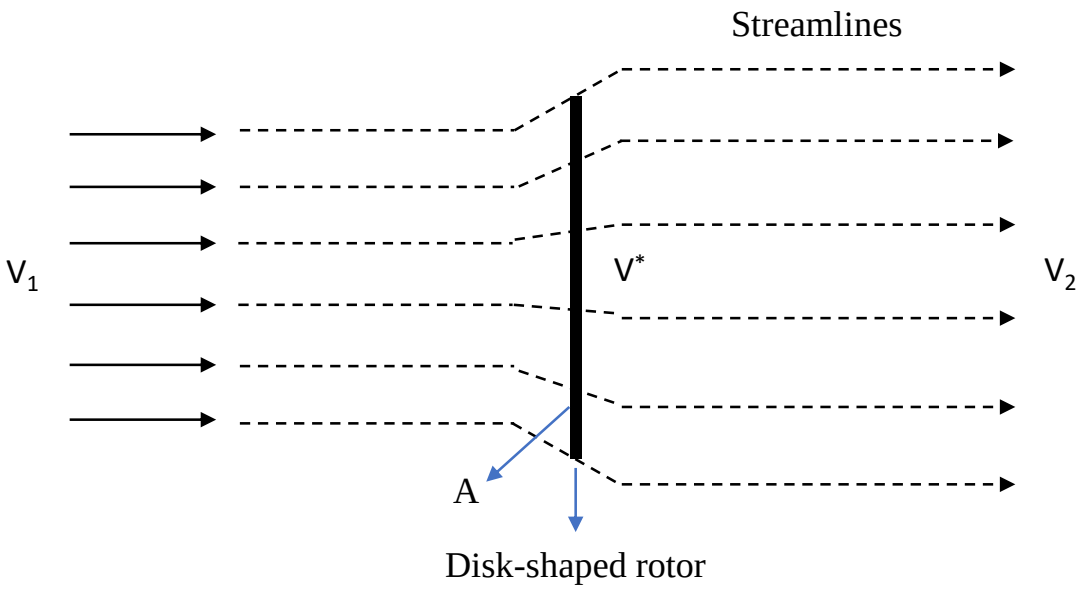

Figure 2.5. Schematic diagram of the flow around a disk-shaped rotor according to Betz's elementary momentum theory.

The maximum power available in the wind can be expressed as:

$$P_{max} = \frac{1}{2}\rho {V_1}^3 A \tag{2.4}$$

Bertz proposed an equation for the power that the rotor can produce as follow:

$$P_{rotor} = \frac{1}{4}\rho A({V_1}^2 - {V_2}^2)(V_1 + V_2) \tag{2.5}$$

The ratio of the power produced by the rotor to the maximum available power in the wind is the power coefficient C_p, and it can be plotted with respect to the velocity ratio as shown in Fig. 2.6. As seen, the maximum power coefficient that a rotor, including a wind turbine rotor, can achieve is 0.593, which is known as the Betz limit [23].

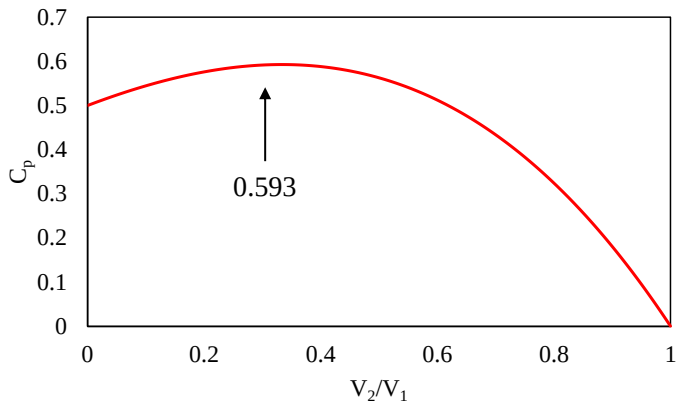

Figure 2.6. Betz's limit.

Apart from the rotor blades, the other main component of a wind turbine is a nacelle, which consists of a drivetrain that is used to convert the kinetic energy captured from the wind by the rotor blades into electrical energy through mechanical components [27]. A drivetrain fundamentally consists of several mechanical components including shafts, gearbox and generator. These components are rested on a bedplate [28]. The aerodynamic loads from the rotor are transferred to the generator through shafts, and a gearbox is used to speed up the low speed introduced by the wind to the high speed that the generator demands [29, 30]. Among all six components of the aerodynamic loads introduced, torque is the main component for the rotation of the generator to generate electricity [31, 32]. Therefore, the aerodynamics of the wind turbine blades are not only important for power production but also related to the performances of mechanical components of a wind

turbine. The vibration of the drivetrain and gearbox, which is also the main source of vibration in a wind turbine, is the focus of the optimisation studies [33]. However, this is out of the scope of this thesis.

2.3. Aeroelastic Instabilities

2.3.1. Aeroelasticity in Turbomachines

Unsteady flows through various blade rows often influence the aerodynamic performance of turbomachines [34]. The interaction between the unsteady flow and the dynamic behaviour of a structure can influence the flow unsteadiness around the structure [35], potentially leading to either an instantaneous or a high cycle fatigue (HCF) failure of a structure. Low-pressure turbines, typically found in modern aero engines, are prone to flow separation and aeroelastic instabilities [36] as the flow passes over the blade aerofoil. These problems can also be found in wind turbines as wind turbine blades consist of a set of different aerofoils and the blade may experience flow separation depending on the blade pitch angle and the angle of attack. The knowledge of aeroelasticity modelling obtained from the studies of low-pressure turbines are relevant to wind turbines and can be used for the optimisation of modern wind turbine blades. Most research is focused on improving the efficiency of turbomachines including low-pressure turbines [37, 38] as well as reducing the weight and the associated manufacturing costs [39].

A significant effort was devoted to producing a high-lift blade design that achieves the required aerodynamic loads on the blade using less weight [40]. However, these designs not only decrease the highly correlated flutter parameter known as a reduced frequency but also introduce the higher per-stage loading [41-43]. The unsteady pressure perturbations due to vibrating aerofoils of a blade operating in the low reduced frequency regime affect the stability of the blade. Moreover, a high aspect ratio of the blade design influences the aeroelasticity parameter such as aerodynamic damping of the blade [44]. Flutter, known as self-excited aeroelastic instability problem, can be a major issue for the blade. The flutter stability can be assessed by means of an aerodynamic damping value that determines whether or not the blade can experience flutter behaviour. The blade vibration is considered unstable when the aerodynamic damping is negative [45, 46]. Furthermore, the interaction between the unsteady flow and the blade is also an important aspect of the turbomachinery analysis as it can influence the aeroelasticity parameters of the blade. It is found through an experiment that the flow in a modern low-pressure turbine is highly unsteady [47]. The high-resolution numerical simulations confirmed this

observation [48, 49]. Laminar flow separation and separation bubbles are identified on the suction surface of the aerofoil of a modern low-pressure [50]. As a wind turbine blade is equipped with various aerofoils, this flow behaviour is also expected in wind turbines [25]. Depending on the curvature of the aerofoil and the angle of attack, the separation of the boundary layer can happen [51, 52]. The rolling up of the separated shear layers and flow recirculation in the separation zone on the suction surface of an aerofoil amplifies the flow unsteadiness and turbulence [53]. The transition of the boundary layer separation to turbulence is enhanced via Kelvin-Helmholtz (KH) instability [54], and the KH mechanism is also identified in wind turbine blade aerofoils [24]. Furthermore, oscillatory incoming wakes and turbulence are the common sources of flow unsteadiness in most turbomachinery applications, which particularly influences the transitional flow structures around the blade aerofoil [55, 56]. It is found that these various sources of flow unsteadiness are affecting the blade structure imposing aerodynamic forces on the blade [57]. This leads to aeroelastic instabilities including vortex-induced vibrations and blade flutter in turbomachines [58]. The aeroelastic instability problems, especially blade flutter, are potential problems that are also linked with the fatigue and fracture of the blade structure including High-Cycle Fatigue (HCF) [59]. This triggers further studies to be carried out to develop numerical methods and tools to investigate the physics of onset of flutter for the wind turbines in order to examine the vibration stress levels and to ensure the blade mechanical integrity.

2.3.2. Aeroelasticity in Wind Turbines

Although the flutter and forced responses have been a problem traditionally associated with the compressors and fans of gas turbines and aero-engines, modern wind turbines may also be prone to similar aeroelastic instability problems due to an increased blade aspect ratio with reduced blade thickness [60]. The interaction between the aerodynamic load and the elastic blade structure is also the main cause of aeroelastic instability problems in wind turbine blades [61]. As discussed, the lengths of wind turbine blades are being increased to capture wind energy more efficiently. Due to the design of extremely long and flexible blades with less weight, wind turbine blades possess lower structural damping values, which leads to instabilities in the structure when excited by the external aerodynamic loads [62]. Hence, the structural stability of the blade has been the focus of many research studies aiming to enhance structural damping [63]. Apart from the structural damping, aerodynamic damping is also required for the design of the wind turbine blades. Aerodynamic damping determines whether the blade vibration, excited by

aerodynamic forces, is damped [64]. The aerodynamic damping value is obtained from the aerodynamic work done per vibration cycle. The aerodynamic work can be computed based on the fluid pressure applied on the blade surface area and the velocity of the blade due to imposed vibrational displacements. Therefore, the aeroelasticity model coupling the structural and aerodynamic calculations is required to ensure the mechanical integrity of wind turbines[64]. Linear aeroelasticity models, which simplifies aeroelastic coupling equations based on the assumption of small deflections, are computationally efficient. As the amplitude of blade deflection is related to the aerodynamic damping, this assumption can cause underestimations of aerodynamic damping. Moreover, studies have shown that wind turbine blade deflections can be large [65]. Fully coupling models are typically used for nonlinear aeroelasticity modelling [66, 67]. However, the equations are complex, and this type of model requires a significant amount of computational cost.

Potential aeroelastic instability problems that can occur in modern wind turbines are stall-inducted vibrations and blade flutter.

Stall-induced vibration: Blades can undergo stall-induced vibrations when the wind turbine operates in the separated flow [68]. Details of stall-induced vibrations related issues can be found in [60, 68]. It is found that the blade vibrations are associated with a combination of natural frequencies and mode shapes of the blade structure [61]. The risks of stall-induced vibrations are mainly associated with the behaviour of the blade structure motion and the characteristics of the blade aerofoils and structure. If the aerodynamic damping is negative, the aerodynamic loads of the blade aerofoils induce energy to the blade vibration, and the blade structure becomes unstable when the structural damping is not sufficient to dissipate the energy. If the aerodynamic damping is positive, the blade vibration is eventually damped. Examples of stall-induced vibrations in wind turbines are discussed in [69-72].

Blade flutter: Blade flutter, on the other hand, can cause more severe aeroelastic instability problems. Blade flutter is known as the self-excited vibration of the blade caused by the interaction between the transient flow and the blade structure [7, 60]. Due to the high flexibility and slenderness of the blade, wind turbine blades are also prone to similar flutter problems as found in aircraft wings and turbine blades of aero-engines [73, 74]. Blade flutter is initiated by the unsteady flow passing over the blade aerofoil surfaces and imposing aerodynamic forces on the blade structure [60]. These aerodynamic forces

gain energy over vibration cycles, which cannot be damped by structural damping [60]. When it happens, the aerodynamic damping coefficient becomes negative, and the blade vibration becomes more severe as the vibration goes on. The blade flutter typically occurs at a frequency close to the natural frequencies of the blade structure [75]. For the analysis of the blade flutter, it is important to consider the aerodynamic effects associated with neighbouring blades. The phase difference between blades is an important aspect of blade flutter. Blades vibrate at a phase angle known as an inter-blade phase angle [75]. For example, if the inter-blade phase angle is zero, all blades vibrate together in the same phase. As a modern wind turbine has three blades, a potential phase angle of vibration between blades is 120^o which means that all three blades vibrate out of phase to each other by 120^o. Although the blades of a wind turbine are far from each other, compared to other turbomachines, the flow from one blade has an impact on the others as the blades rotate, and it is important to take the phase shift between the blades into consideration. The limit of blade flutter in large-scale wind turbines was studied in [76], which showed that the unsteady aerodynamics of the flow has an impact on a flutter limit in wind turbine blades. It was also discussed that the physical properties of the blade such as the centre of mass and the stiffness influenced the limit of blade flutter [77]. Hansen [78] analysed the risk of blade flutter associated with the effect of the blade stiffness based on both isolated rotor-alone mode and full turbine model. In this analysis, a combination of the structural vibration modes of the blade was identified in the flutter process. It was also found that the reduced stiffness of the blade affected the natural frequencies of the blade and thereby influencing the aerodynamic damping of the blade. Furthermore, aeroelastic instabilities, including flutter, of 5 MW onshore and offshore wind turbines are broadly investigated over a range of operating conditions in [79].

2.4. Existing Experimental and Numerical Methods

2.4.1. Experiments and Reference Wind Turbines

As an accurate prediction of aeroelastic instabilities such as flutter and forced response in turbomachines, especially in wind turbines, is one of the greatest challenges faced by the industry due to the high demand of computational resources and time, a lot of efforts have been made over the last decades to seek efficient numerical methods. When it comes to the prediction of aerodynamic and aeroelastic performances of wind turbines, ideally, the analysis should be carried out or validated through full-scale experiments to achieve accurate results. While full-scale wind turbine experiments are not practically feasible, various small-scale experiments were conducted and reported in the literature. The Model

Rotor Experiments In Controlled Conditions, also known as the MEXICO experiment, is popular among the wind energy research community as it includes advanced flow field measurements in addition to the measurement of rotor loads [80, 81]. The measurements database produced from this experiment is widely used by the researchers for the validation of different types of numerical codes and simulations [82, 83]. Another well-known experiment is the "Blind test" experiment, developed and tested at the Norwegian University of Science and Technology [84]. In this experiment, the performance and wake generated of a wind turbine model are measured and predicted in the wind tunnel. Numerous computational models are also developed and compared to the experimental data. Later, this experiment is extended by adding another identical wind turbine model in the wake region of the first turbine. Different configurations such as two in-line models [85], where the second wind turbine is placed right behind the first one, or offset model [86], in which two wind turbines are arranged with an offset so that the second wind turbine is partially in the wake region of the first one, are considered. The effect of the wake generated from the upstream wind turbine on the downstream one is investigated, and the performances of both wind turbines are extensively measured and calculated. Similar to the first "Blind test", various computational models are developed and validated against the measurements.

Moreover, the NREL Phase VI wind turbine was developed by the National Renewable Energy Laboratory (NREL) for a wind tunnel experiment, which can provide unsteady aerodynamics and the behaviour of the three-dimensional flow around the wind turbine [87]. The purpose of this experiment was to provide a complete set of three-dimensional aerodynamic measurements which can be used for the validation of different numerical models and methods. During this experiment, a series of tests were conducted under different operating conditions. In addition, the atmospheric conditions were also measured in this experiment and documented. Various aerodynamic parameters and structural responses were measured in detail. A blind comparison of numerical predictions to the experimental data was also carried out and it can be found in [88]. These data have been served as references for the validation of research studies and numerical simulations. Apart from the NREL Phase VI wind turbine, a large-scale reference wind turbine was also developed by NREL, and it is known as the NREL 5 MW baseline wind turbine [89]. The purpose of developing this wind turbine was to create a wind turbine model which could represent a large-scale offshore wind turbine and wind power technology. Likewise, this mode has been widely used in the wind energy industry for

research and validation purposes [90, 91]. Wind tunnel experiments for wind turbines are typically carried out in a controlled environment subject to a certain inflow and boundary condition. However, these experiments can impose uncertainties while reproducing the environmental conditions in which wind turbines are operated [92] because the majority of experiments do not consider unsteady parameters such as wind shear and dynamic inflow. The sources of flow unsteadiness associated with these physical key factors are ignored in most experiments, which produces uncertainties. Besides, the experiments for aeroelasticity or aeroelastic instabilities of wind turbines integrating the blade vibration are very difficult or sometimes impractical to be performed, and therefore, the majority of wind tunnel experiments including the experiments discussed in this section focus on aerodynamics of wind turbines. Hence, the understanding of aeroelasticity of wind turbine relies upon the development of highly efficient numerical models. Furthermore, the scaling effect encountered with small-scale experiments should also not be neglected, and this can be considered in the numerical models.

2.4.2. Blade Element Momentum Model

With all the advances in computing and technology, several numerical modelling and computational methods are now available for analysing the aerodynamics of wind turbines. Modern wind turbines are designed based on wind turbine specialist codes such as the Blade Element Momentum (BEM) theory [93]. Wang et al. [94] studied the nonlinear aeroelasticity of wind turbine blades using BEM theory and mixed-form formulation of geometrically exact beam theory. Fernandez et al. [95] proposed a methodology for the aeroelasticity analysis of a wind turbine blade based on BEM and Finite Element (FE) models. Likewise, Rafiee et al. [96] conducted an aeroelastic analysis of a wind turbine blade coupling the BEM and FE methods. In these studies, the aerodynamic loads are obtained from the BEM models.

Although the classic BEM method is computationally fast and efficient, it has numerous limitations as the method is based on quasi-steady assumptions. The first limitation is that this method neglects the effects associated with the tip vortex shedding which is one of the main sources of flow unsteadiness in wind turbine aerodynamics. Therefore, the prediction of velocity distribution on the blade surfaces, especially in the blade tip region, becomes inadequate and inaccurate. To solve this problem, tip loss correction models have been developed and used in simulations [97-99]. Another main limitation is related to the turbulent wake in the downstream region. The BEM model becomes problematic

when a wind turbine operates at high tip speed ratios. When it happens, the prediction of velocity behind the rotor in the wake region becomes invalid. As a result, the computed aerodynamic loads become unreasonable. Hence, several correction models have been proposed to take the turbulent wake into consideration [100, 101]. Moreover, the inflow for wind turbines is not always steady. In fact, it changes in time. The inflow wakes and turbulence are present in the real environment. Depending on the nature of the inflow, the aerodynamic loads of a wind turbine are unsteady. However, the classic BEM model has limitations when the inflow wake and turbulence are incorporated. Therefore, corrections for dynamic inflow models are required, and they have been used in numerical simulations [102, 103]. It is shown that a good agreement is obtained between the measurements and the simulations using these models. In addition, the effects related to the dynamic stall is another limitation of the BEM method. Dynamic stall could occur due to a sudden change in the angle of attack of aerofoils and it could lead to the boundary layer separation. In the case of the stall, the flow separation starts from the leading edge which affects unsteady aerodynamic parameters, and the BEM model is incapable of calculating pressure coefficients and aerodynamic loads accurately. Various corrections have been applied to include the dynamic stall in the numerical models [104-106]. Furthermore, other corrections were also proposed and applied in the simulations to improve the accuracy of the BEM method [107-109]. The BEM models, however, are incapable of capturing flow structures and flow details despite applications of corrections, which leads to a lack of understanding on the aerodynamics of wind turbines. Therefore, a high-fidelity computational model is required to capture the necessary flow details.

2.4.3. Vortex Model

Various vortex methods have been developed and applied to the analysis of aerodynamics and the aeroelasticity of wind turbines. Murua et al. [110] proposed an Unsteady Vortex-Lattice Method (UVLM), as an alternative to high-fidelity methods, for the aeroelasticity modelling considering the effects associated with geometric nonlinearities. Lee et al. [111] applied a UVLM method to study and predict the aerodynamic performances and wake structures of a wind turbine. In a numerical study of Chattot [112], a vortex method was used for an aeroelasticity analysis of a wind turbine rotor considering the blade flexibility. Moreover, Breton et al. [113], used a prescribed vortex method to study and understand the behaviour of stall delay in wind turbines. Similarly, Mac Gaunaa et al. [114], also employed a prescribed vortex model to predict the aerodynamic performances of wind turbine rotors. Besides, Riziotis et al. [115] used a free wake vortex method for

the aeroelasticity analysis of wind turbines and the prediction of aerodynamic loads on the rotor blades. Likewise, Jeong et al. [116, 117] applied a free-wake vortex model to study the aerodynamics and aeroelasticity of wind turbine blades under different operating conditions. Rodriguez et al. [118, 119] employed a vortex model for the aerodynamic analysis of offshore wind turbines. The viscous effects, however, are neglected by most vortex models.

2.4.4. Actuator Type Model

The actuator type model, originally developed by Rankine [120] and Froude [121], has been used for the analysis of rotor and propeller performance. The classic actuator models are similar to BEM models. However, they were later combined with flow governing equations such as Navier-Stoles or Euler equations. This method was previously applied to the aerodynamic analysis of the helicopter rotors [122, 123]. In the wind turbine analysis, the wind turbine rotor or blades are represented by a disk or a line model with variable load distributions, known as the actuator disk model or actuator line model, and they have been used for the aerodynamic analysis of wind turbines. Sorensen et al. [124] performed the unsteady flow simulations of wind turbine rotors. In this analysis, rotors are modelled as actuator disk models, and the flow governing equations are solved by a finite difference method. In another numerical study of Madsen [125], the unsteady flow past an actuator disk model was conducted by solving the Navier-Stokes equations. Also, Mikkelsen et al. [126] investigated the effect of coning on the performances of a wind turbine rotor by modelling the rotor as an actuator disk model and solving the Navier-Stokes equations. Furthermore, Sorensen et al. [127] used an actuator disk model to analyse the turbulent wake and vortex states of a wind turbine rotor. In addition to the actuator disk models, the actuator line models are also used for the aerodynamic analysis of wind turbines. Troldborg et al. [128] applied an actuator line model to the simulation of a wind turbine operating in the turbulent wake. Moreover, Sorensen et al. [129] used an actuator line model to analyse the aerodynamic flow field around a wind turbine rotor. Likewise, Shen et al. [130] modelled a wind turbine rotor blade as an actuator line model and performed the aerodynamic simulations to predict the aerodynamic loadings and flow field around a wind turbine rotor. Both actuator disk and line models are usually combined with Navier-Stokes equations replacing the rotor or the blade with an actuator disc or line with distributed loads. However, the loads on the rotor or the blade are calculated based on the BEM theory and the accuracy of the simulation depends on the calculation of the

aerodynamic loads. In addition, the computational costs required by these methods are higher than BEM models [131].

2.4.5. Computational Fluid Dynamics

Computational Fluid Dynamics (CFD) methods, either based on Reynolds Averaged Navier-Stokes (RANS) equations for steady simulations or Unsteady Reynolds Averaged Navier-Stokes (URANS) equations for unsteady simulations, are widely used in the wind energy industry to optimise the performances of wind turbines due to their capabilities of modelling steady and unsteady flows and accurately predicting flow behaviours [132-134]. CFD methods are also coupled with a structural model to study fluid-structure interactions and the aeroelasticity of wind turbines. Wang et al. [135] proposed an FSI modelling method for the wind turbine blade using CFD and FE models and calculated its structural responses such as stress distribution and blade tip deflections. Likewise, Dai et al. [136] analysed the aeroelasticity of wind turbine blades under different yaw conditions using CFD and FE models. Yu et al. [137] developed a coupled CFD and Computational Structural Dynamics (CSD) method based on the URANS model to predict unsteady aerodynamic loads on the wind turbine blade and its time-varying aeroelastic responses. Similarly, Dose et al. [138, 139] employed a coupled CFD-CSD model to perform FSI simulations of wind turbines. Furthermore, CFD methods are also applied to simulations of multiple wind turbines. Allah et al. [140] and Ciri et al. [141] conducted aerodynamic simulations of two in-line wind turbines and analysed the wake behaviour. Choi et al. [142] performed CFD simulations of two wind turbines by varying the separation distance between turbines. Moreover, Korobenko et al. [143] proposed a multi-domain method to perform simulations of two back-to-back wind turbines. The main disadvantage of the CFD methods is their large computational resource requirement. Significant computational cost and resources are required for unsteady computations, especially when multiple wind turbines are involved.

2.4.6. Structural Modelling

Modelling of aeroelasticity requires the coupling of fluid and structural models to investigate the effects and responses associated with the interaction between fluid and structure. There are different types of structural models such as Finite Element Analysis (FEA) models, Multi-Body Dynamics (MBD) models and beam models. FEA models are one of the most used structural models because they can provide details of structural responses depending on the quality of the mesh, and they are often coupled with fluid

models as discussed in detail above. FEA models are used for the static and dynamic analysis of wind turbines. Chazly [144] used an FEA model for the analysis of stress and forced responses of wind turbine blades. Similarly, Tarfaoui [145] analysed the mechanical behaviour and structural responses of wind turbine blades using an FEA model. Moreover, FEA models are also employed for the design and optimisation of wind turbines. Bechly et al. [146] discussed the optimisation of materials for the design of wind turbine blades based on an FEA model. Likewise, Song et al. [147] performed the dynamic analysis of wind turbine blades using FEA models for the optimisation of wind turbine blades. In addition, MBD simulations are also carried out to study the dynamics of wind turbines as it considers the flexibility of wind turbine structures. He et al. [148] proposed a 5-DOF numerical model using an MBD method to analyse vibration responses of wind turbines. Wang et al. [149] studied nonlinear motions of offshore wind turbines with large amplitude based on MBD models. Jin et al. [150] developed flexible models of large-scale wind turbines using MBD techniques to investigate the dynamic behaviour of wind turbine components. Besides, wind turbine blades are long and slender structures, fixed at the hub and free at the tip, and they behave like a cantilever beam. Therefore, wind turbine blades are often modelled as beam models. Among different types of beam models, there are two widely used beam models such as Euler-Bernoulli beam model [151] and Timoshenko beam model [152]. Both models are used in the industry to predict the structural behaviour of wind turbines [153]. Compared to FEA and MBD models, beam models are computationally fast and easy to be implemented. However, the assumptions of small deflection are typically found in beam models. FEA and MBD models can provide a higher level of modelling flexibility, which makes the structural behaviour more realistic. Among these methods, FEA models can be used for the most complex geometries with different levels of complexity. Hence, they are often coupled with fluid models to investigate the aeroelasticity of wind turbines.

For the modelling and simulation of the fluid-structure interaction or aeroelasticity, fluid models and structural models need to be coupled. There are three main coupling methods such as one-way coupling, two-way coupling and modal coupling methods. In one-way and two-way coupling methods, there is an interface between the fluid solver and the structural solver to transfer the solution variables such as pressure and displacement. With a one-way coupling method, the flow simulation is first conducted, and the pressure loads obtained from the flow simulation are transferred to the structural simulation in which the structural responses are calculated based on the imported loads [135, 154]. The

deformation of the structure is not passed back to the flow solver in one-way coupling methods. In reality, the structure is deformed by the fluid loads, and at the same time, the deformation of the structure influences the flow around the structure. A two-way coupling method provides more realistic behaviour, as the displacement of the structure is also transferred to the fluid solver to consider the deformation of the structure in the flow simulation [137, 155]. Therefore, two-way coupling methods are more accurate than one-way coupling methods; however, they are computationally much more expensive [156]. Apart from one-way and two-way coupling methods, the deformation of the structure is also taken into account in the modal coupling method. To apply this method, the mode shape of the structure is needed to be calculated in a structural solver prior to the flow simulation. The mode shape is then imported into the fluid solver where the structural deformation is defined. The vibration of a structure can also be included in a flow simulation using the imported mode shape and a specified vibration frequency. Using this method, the deformation of the structure is simultaneously updated and simulated in the flow simulation, which saves computation time [75, 157]. Figure 2.7 presents the schematic diagram of different coupling methods.

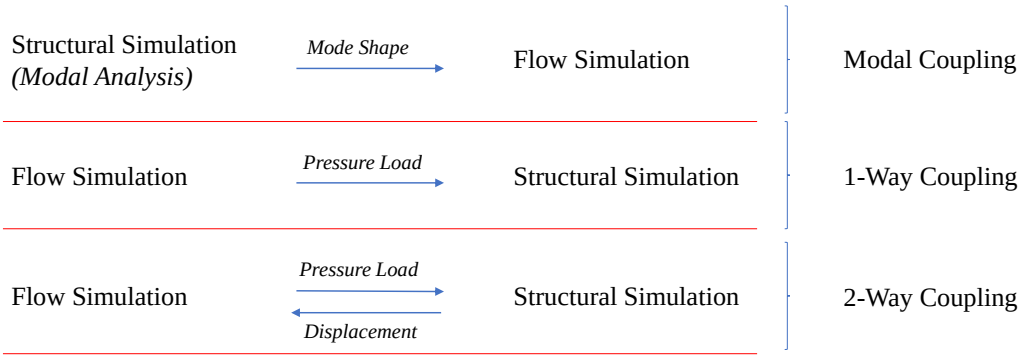

Figure 2.7. Schematic diagram of fluid-structure coupling methods.

2.5. Frequency Domain Methods

As the computational cost of high-fidelity aerodynamic and aeroelasticity simulations remains the main challenge for the industry, not only for wind turbines but also for other turbomachines, numerous studies were conducted over the last decade with the purpose of developing efficient numerical methods which can reduce the computational cost. A time-linearized harmonic frequency-domain method was developed for the efficient calculation and analysis of unsteady flows in turbomachinery, and it was widely used in the turbomachinery industry [158, 159]. This method was later replaced by the harmonic balance method of Hall et al. [160], the harmonic solution method of He [161], and Rahmati et al. [162, 163] for modelling harmonic disturbances and flow nonlinearities.

Rahmati et al. [164] developed a nonlinear frequency domain solution method for the aeroelasticity analysis of multiple blade row configurations. It is found that a fully coupled multiple blade row model yields better accuracy in predicting flutter behaviour of the turbomachines than the simplified isolated one [165]. Liu et al. [166, 167] applied a harmonic balance method to study the aeroelastic motion of an aerofoil. Patil et al. [75] used a frequency domain method for the prediction of aerodynamic damping values of turbomachines. They compared their results to the standard time-marching method and found that the frequency domain method is highly efficient and accurate in predicting aerodynamic damping. In addition, Vilmin et al. [168] also applied a nonlinear harmonic method for modelling unsteady flows for the turbomachinery analysis, particularly focusing on the interface treatment for the rotor-stator interaction. Similarly, Amato et al. [169] used a nonlinear harmonic method to analyse the unsteady flow behaviour in an aeronautical gas turbine. Although frequency domain methods are typically used for the analysis of turbomachinery applications, only a few studies recently applied these methods to wind turbine applications. Horcas et al. [170] performed an aerodynamic simulation on the DTU 10 MW reference wind turbine using the non-linear harmonic method and analysed the flow interaction with the rotor and the tower. They later extended their study to perform an aeroelasticity analysis by coupling a non-linear harmonic method with a structural model [171]. Howison et al. [172] presented an aeroelastic model for wind turbine blades based on the URANS model to carry out the aeroelasticity analysis using the harmonic balance method. The harmonic balance method is also applied by Drofelnik et al. [173] for the aerodynamic analysis of wind turbines under yaw conditions. These studies are based on simple computational models or steady inflow conditions. Therefore, despite recent applications of frequency domain methods for wind turbines, further improvements are still required for an accurate prediction of the aerodynamic and aeromechanical performances of wind turbines taking various sources of flow unsteadiness into account.

2.6. Summary of Literature Review

Based on the literature review, it is clear that high-fidelity computational methods and models are required for an accurate prediction of aerodynamic and aeromechanical performances of wind turbines. However, the existing computational models are either unable to predict the unsteady flow behaviour correctly or demand high computational resources. Therefore, the required confidence and accuracy cannot be obtained with the low-fidelity methods such as the BEM model because of the inadequacy in modelling

flow unsteadiness and turbulence. The high-fidelity numerical methods, such as traditional time domain CFD methods, are, however, not feasible to perform unsteady simulations of wind turbines, especially multiple wind turbines models. The existing aeroelasticity models and solvers used by the manufacturers in the industry mainly rely on BEM methods for the design process of wind turbine blades, which disregards the complex physics of unsteady flow occurring during the fluid-structure interaction process which gives rise to a black-box effect. As a result, the detailed understanding of the interaction between the various sources of unsteadiness and the wind turbine structure, relating to aeroelastic instabilities such as vortex-induced vibration, is still limited, and it requires further investigations. Therefore, a highly efficient numerical method and model should be developed to provide an understanding of the physics behind fluid-structure interactions.

Frequency domain methods are highly efficient, and they can model the physics of flow turbulence and can provide an accurate prediction of aerodynamics and the aeroelasticity of turbomachines. These methods are widely used in the turbomachinery community. However, they are relatively new in the wind energy industry. Due to recent technical and computational advances, frequency domain methods have become more feasible, and they have been recently applied in the analysis of wind turbine applications. Although frequency domain methods have been applied in the wind turbine analysis, it is found that wider applications of the method and further improvements are needed. This project proposes a nonlinear frequency domain solution method for modelling flow nonlinearities and harmonic disturbances to account for different sources of flow unsteadiness for the aerodynamic and aeromechanical analysis of wind turbines. With this method, a single blade is only required for the same accuracy in capturing the unsteady flow compared to the conventional time domain methods applied in most wind turbine simulations, which require modelling of complete rotor blades. The advances and benefits of the frequency domain solution method could lead to a significant reduction in computation time.

Furthermore, CFD simulations of multiple wind turbines in arrays are very rare in the literature and no CFD studies employing frequency domain methods for the simulation of multiple wind turbines have been reported to date. The majority of CFD studies of wind turbines available in the literature have focused only on the rotor-alone models neglecting the effect associated with the tower structure. It is also found that the computational cost of a CFD simulation of a complete wind turbine model including a

tower is very high, and this is challenging for the wind energy industry. This project will provide fundamental understandings of the mechanism behind the interaction between various sources of flow unsteadiness and wind turbines utilising the advances of the nonlinear frequency domain solution method. Moreover, a complete wind turbine model including a tower will also be studied using the proposed method and the effect of flow unsteadiness associated with the tower will be investigated. The outcomes will be significant for the wind turbine industry and results can be served as references for validations of future studies and numerical codes. The proposed project will bridge a key gap in the knowledge of modelling and prediction of aerodynamics and the aeroelasticity of offshore wind turbines.

Chapter 3. Methodology

In this project, the CFD method is used for aerodynamic computation. For the modelling and simulation of the fluid-structure interaction, one-way coupling or two-way coupling methods, as described in the literature review, are typically used. As previously discussed, the structural deformation is not considered in the flow simulation in a one-way coupling method whereas a two-way coupling method is computationally very expensive as both aerodynamic forces and structural displacements are computed and exchanged between the two solvers at every time step. The modal coupling method provides an alternative to these modelling methods as the structural deformation and vibration can be integrated into the flow simulation using the structural model shapes. In the aeroelasticity analysis of a wind turbine, the blade deformation and vibration subject to aerodynamic loads are periodic, and therefore, the modal coupling method is considered suitable for the modelling of fluid-structure interaction and the prediction of the aerodynamic damping. Hence, the modal coupling method is employed in this project. With this method, the modal analysis needs to be conducted prior to the flow simulation to calculate the natural frequencies and the mode shapes of the blade structure. The aforementioned information is then imported into the flow simulation to define the blade vibration in the CFD analysis. The modelling and computation of the unsteady flow due to fluid-structure interactions are all performed in the CFD environment. The details of the employed numerical method are described below.

3.1. Governing Equations

The flow computation is carried out by a commercially available 3D density-based finite volume CFD code, NUMECA FINE/Turbo. The simulations are conducted using an Unsteady Reynolds Averaged Navier-Stokes (URANS) model and the general Navier-Stokes equations written in a Cartesian frame can be expressed as:

$$\frac{\partial}{\partial t}\int_{\Omega} U d\Omega + \int_{S} \vec{F}_I \,.\, d\vec{S} + \int_{S} \vec{F}_V \,.\, d\vec{S} = \int_{\Omega} S_T d\Omega \tag{3.1}$$

where Ω is the volume, S is the surface, U is the vector of the conservative variables, S_T is the source term, and $\vec{F}_I$ and $\vec{F}_V$ are the inviscid and viscous flux vectors, respectively. For the turbulence modelling, three different turbulence models such as Spalart-Allmaras, k-omega SST and k-epsilon models, are tested to compute the pressure distribution on a

wind turbine blade, and the results are compared to the experimental data (see Fig. 3.1). As seen, all three turbulence models predicted similar pressure distributions, and they are in good agreement with the experiment. For the simulations presented in this thesis, the standard one-equation Spalart–Allmaras model is employed to calculate the turbulent eddy viscosity. The Spalart-Allmaras turbulence model becomes popular in the field of turbomachinery, due to its robustness and ability to investigate complex flow behaviours.

The governing equation can be simply expressed as:

$$\frac{\partial}{\partial t}(U) = R(U) \tag{3.2}$$

where R is the lumped residual and the source term. Traditionally, the Navier-Stokes equations are solved in a CFD solver at every time step in the time domain. This type of method is referred to as the time domain method in this thesis.

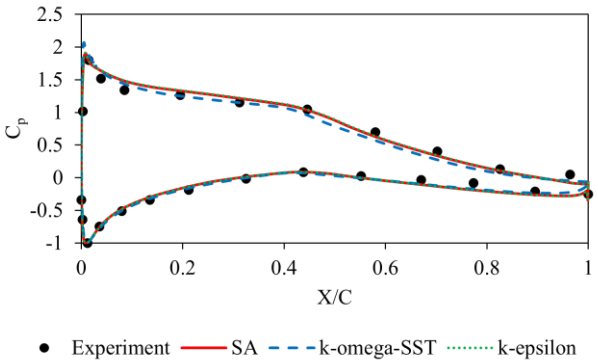

Figure 3.1. Comparison of pressure coefficient distribution on a wind turbine blade between the experiment and the simulations using Spalart-Allmaras, k-omega SST and k-epsilon turbulence models.

3.2. Spatial Discretization

In this project, the spatial discretization is based on a cell centred volume approach, and a 2nd order central scheme is employed. The flow governing equations are discretized as:

$$\int_\Omega \frac{\partial U}{\partial t} d\Omega + \sum_{faces} \vec{F}_I . \Delta\vec{S} + \sum_{faces} \vec{F}_V . \Delta\vec{S} = \int_\Omega S_T d\Omega \tag{3.3}$$

where $\vec{F}_I . \Delta\vec{S}$ and $\vec{F}_V . \Delta\vec{S}$ are the inviscid and viscous fluxes, respectively.

The computation of viscous fluxes is performed in a central way, and the gradients are evaluated on the cell faces. Gauss's theorem is applied to the computation of these face gradients, and the gradient of a quantity *Q* is expressed as:

$$\vec{\nabla}Q = \frac{1}{\Omega}\int \vec{\nabla}\, Q d\Omega = \frac{1}{\Omega} Q d\vec{s} \tag{3.4}$$

The expression of the inviscid fluxes over a *face* surrounded by two neighbouring cells *left* and *right* is given by:

$$\left(\vec{F}.\vec{n}\right)_{face} = \frac{1}{2}\left(\left(\vec{F}.\vec{n}\right)_{left} + \left(\vec{F}.\vec{n}\right)_{right}\right) - \frac{1}{2} d_{face} \tag{3.5}$$

where d_{face} is a numerical dissipation term and is formulated by Jameson type dissipation [174] with a central scheme.

3.3. Temporal Discretization

An explicit 4-stage Rune-Kutta scheme is employed for the temporal discretization.

$\frac{\partial}{\partial t}(U) = R(U)$ can be written as:

$$\begin{aligned} U^1 &= U^n + \psi_1 \Delta t R(U^n) \\ U^2 &= U^n + \psi_2 \Delta t R(U^1) \\ U^3 &= U^n + \psi_3 \Delta t R(U^2) \\ U^4 &= U^n + \psi_4 \Delta t R(U^3) \\ U^{n+1} &= U^4 \end{aligned} \tag{3.6}$$

In these expressions, U^n is the value of *U* at a time-step *t* and U^{n+1} is the value of *U* at a time-step $t + \Delta t$, and ψ determines the stability and the order of accuracy of the Runge-Kutta scheme. A local time-stepping is used for the steady solution and a dual time-stepping method is used for the typical unsteady time domain solution. A multigrid method is also employed to accelerate the convergence. It has been found that a multigrid strategy is efficient and can provide fast convergence. With the multigrid method, the number of iterations required to reach convergence is dramatically reduced using the coarse grid initialisation process. Based on the specified number of grid levels, the flow solution is performed on all grid levels including the finest grid level and the coarsest grid level. Initially, the solution iteration starts on the coarsest grid

level, leading to fast convergence, until it meets the internal convergence criteria or reaches the maximum number of inner iterations. Afterwards, the solver advances to the next grid level by interpolating the flow solution. The same process is repeated until the finest grid level is reached. For N_I numbers of intermediate grid levels between the finest and coarsest grids, the formulation of multigrid can be expressed as:

$$\delta U_a = \Delta t_a \frac{R_a}{\Delta \Omega_a} + \sum_{b=1}^{N_I} \Delta t_b \frac{R_b}{\Delta \Omega_b} + \Delta t_c \frac{R_c}{\Delta \Omega_c} \tag{3.7}$$

where the subscripts *a*, *b* and *c* are corresponding to the finest grid, intermediate grid and coarsest grid levels, respectively, *R* is the net flux, $\Delta\Omega$ is the cell volume, and Δt_a, Δt_b and Δt_c are the time-step on each grid level. To achieve a global time-step size Δt, the following condition needs to be met.

$$\Delta t_c = \Delta t - \Delta t_a - \sum_{b=1}^{N_I} \Delta t_b \tag{3.8}$$

3.4. Nonlinear Frequency Domain Solution Method

In wind turbine aerodynamics and aeroelasticity, the unsteadiness of the flow can be associated with the inflow wake or the blade deflection, which are periodic in time. With the frequency domain solution method, the conservative flow variables from the Navier-Stokes equations are decomposed into the time-averaged and the unsteady fluctuations. Therefore, the unsteady conservative flow variables subject to the source of flow unsteadiness can be represented by the Fourier series for a prescribed fundamental frequency, ω, which can be related to the inflow wake frequency or the blade vibration frequency, and the specified number of harmonics, *m*, as expressed in Eq. (3.9).

$$U = \overline{U} + \sum_{m=1}^{M} [A_U \sin(m\omega t) + B_U \cos(m\omega t)] \tag{3.9}$$

where $\overline{U}$, A_U and B_U are the Fourier coefficients of the conservation variables. The number of harmonics or the order of the Fourier series is an input of the applied numerical method, and the accuracy and resolution of the unsteady flow solution can be controlled through the order of the Fourier series. Substituting this Fourier decomposition (i.e. Eq. (3.9)) into the Navier-Stokes equation (i.e. Eq. (3.2)) yields a new set of unsteady Navier-Stokes equations in the frequency domain as follows:

$$\omega \sum_{m=1}^{M} [mA_U \cos(m\omega t) - mB_U \sin(m\omega t)] = R \quad (3.10)$$

With the frequency domain solution method, this new set of Navier-Stokes equations are solved in the frequency domain. The unsteady period is equally divided into *N = (2m+1)* time levels and the system of nonlinear equations coupling all *N* time levels are solved iteratively.

As the sources of flow unsteadiness discussed in this study are based on a periodic inflow or periodic blade displacement, the fundamental mode (one harmonic) is considered enough and therefore, Eq. (3.9) and Eq. (3.10) are re-written using one harmonic as:

$$U = \bar{U} + [A_U \sin(\omega t) + B_U \cos(\omega t)] \quad (3.11)$$

$$\omega [A_U \cos(\omega t) - B_U \sin(\omega t)] = R \quad (3.12)$$

At three distinctive temporal phases, Eq. (3.11) can be written as follows:

$$U_0 = \bar{U} + B_U \qquad \omega t = 0 \quad (3.13.a)$$

$$U_{\pi/2} = \bar{U} + A_U \qquad \omega t = \pi/2 \quad (3.13.b)$$

$$U_{-\pi/2} = \bar{U} - A_U \qquad \omega t = -\pi/2 \quad (3.13.c)$$

The three Fourier coefficients, $\bar{U}$, A_U and B_U can be calculated based on the above three equations. Substituting these coefficients into Eq. (3.12) at the three phases yields the following equations:

$$\omega \left(\frac{U_{\pi/2} - U_{-\pi/2}}{2} \right) - R_0 = 0 \quad (3.14.a)$$

$$\omega \left(U_0 - \frac{U_{\pi/2} + U_{-\pi/2}}{2} \right) + R_{\pi/2} = 0 \quad (3.14.b)$$

$$\omega \left(U_0 - \frac{U_{\pi/2} + U_{-\pi/2}}{2} \right) - R_{-\pi/2} = 0 \quad (3.14.c)$$

These new sets of Navier-Stokes equations are simultaneously solved by a CFD solver in a similar way to that of the steady-state equations, with the extra term being treated as a source term [164, 165], thereby saving the computation time significantly compared to the conventional time domain method. A central scheme is used for the spatial discretization which is based on a cell centred control volume approach and a four-stage Runge–Kutta scheme is used for the temporal discretization. The flow solution obtained from the frequency domain solution method can be reconstructed in time to have the unsteady periodic flow in time history.

This method belongs to a family of frequency domain methods such as the harmonic balance method of Hall et al. [160] and the phase solution method of He [161]. Moreover, the proposed nonlinear frequency domain solution method is initially developed by Rahmati et al. [164, 165] for the aeromechanical analysis of multi-stage turbomachines. This method is now extended to be applied to wind turbines.

3.5. Fluid-Structure Interaction

The modal coupling method is employed in this study in order to integrate the blade vibration in the flow simulation to perform the aeromechanical simulation of the wind turbine. The modal analysis using a structure solver is required before conducting the flow simulation to calculate the natural frequencies and the mode shapes of the structure.

The solid mechanics of a structure is governed by the following equation:

$$[M]\frac{\partial^2 \vec{d}}{\partial t^2} + [C]\frac{\partial \vec{d}}{\partial t} + [K]\vec{d} = \vec{f} \tag{3.15}$$

where [M] is the mass matrix, [C] is the damping matrix, [K] is the stiffness matrix, $\vec{d}$ is the displacement of the structure, and $\vec{f}$ is the external load.

The global displacement of the structure can be written as:

$$\vec{d} = \sum_{i=1}^{n_{modes}} q_i \vec{\phi}_i \tag{3.16}$$

where q_i is the generalised displacement and $\vec{\phi}_i$ is the mode shapes of the structure normalised by the mass.

Eq. (3.16) can be written in matrix form as:

$$\vec{d} = [\phi]\vec{q} \tag{3.17}$$

Substituting Eq. (3.17) into Eq. (3.15) and multiplying with $[\phi]^T$ yields the following equation.

$$[\phi]^T[M][\phi]\frac{\partial^2\vec{q}}{\partial t^2} + [\phi]^T[C][\phi]\frac{\partial\vec{q}}{\partial t} + [\phi]^T[K][\phi]\vec{q} = [\phi]^T\vec{f} \tag{3.18}$$

Using mass-normalised mode shapes should satisfy that the generalised mass matrix is the unit matrix (i.e. $[\phi]^T[M][\phi] = [I]$) and the generalised stiffness matrix is a diagonal matrix in which the elements are the square of the mode frequency (i.e. $[\phi]^T[K][\phi] = diag[{\omega_i}^2]$). Furthermore, assuming a Rayleigh damping, the generalised damping matrix can be expressed as: $[\phi]^T[C][\phi] = diag[2\xi_i\omega_i]$, where ω_i is the natural frequencies of the structure and ξ_i is the damping coefficient [175, 176].

Substituting them into Eq. (3.18) and expressing the system for every mode *i* yields the following equation:

$$\frac{d^2q_i}{dt^2} + 2\xi_i\omega_i\frac{dq_i}{dt} + \omega_i^2 q_i = \vec{\phi_i}^T\vec{f} \tag{3.19}$$

Prior to the flow simulation, the modal analysis needs to be performed first. A commercial software ANSYS Mechanical is used for the modal analysis to compute the natural frequencies and the mode shapes of the structure employing the Finite Element Analysis (FEA) method. Then, this information is imported into the flow simulation for the blade vibration.

The generalised displacement q_i must be specified for the considered amplitude of deformation and it can be written as:

$$q_i(t) = \bar{q} + q_A\cos(\omega_i t) \tag{3.20}$$

where $\bar{q}$ and q_A are the mean value and amplitude of the displacement, respectively. Having this information, the flow solver computes the deformation of the structure by solving Eq. (3.16) and solves the Navier-Stokes equations using the deformed blade.

The flow chart of the employed FSI computation process is presented in Fig. 3.2. Steady simulation is first performed, and the steady solution is defined to be the initial condition in the unsteady simulation. Before conducting the unsteady simulation, the natural frequencies and the mode shapes of the blade structure, obtained from the modal analysis in an FEA environment, need to be imported into the flow solver. Afterwards, together with the specified time-averaged and amplitudes of the generalised displacement, the flow solver computes the generalised displacement q using Eq. (3.20). Based on the generalised displacement, the flow solver then computes the total deformation of the blade structure and deforms the mesh. Using the deformed blade, the CFD analysis is performed by solving the Navier-Stokes equations. In the case of the time domain solution, these steps are performed at every time step until the flow solution reaches a steady and periodic condition. On the other hand, with the frequency domain solution, the unsteady period is equally divided into $N = (2m+1)$ time levels and the system of nonlinear equations coupling all N time levels are solved iteratively in a similar way to that of the steady-state equations with the extra term being treated as a source term. The frequency domain solution can also be reconstructed in time to have the flow solution in time history. Unsteady flow characteristics are calculated and produced from the analysis. In particular, pressure distributions on the blade surfaces are calculated, which is used to calculate the forces and aerodynamic power acting on the blade structure.

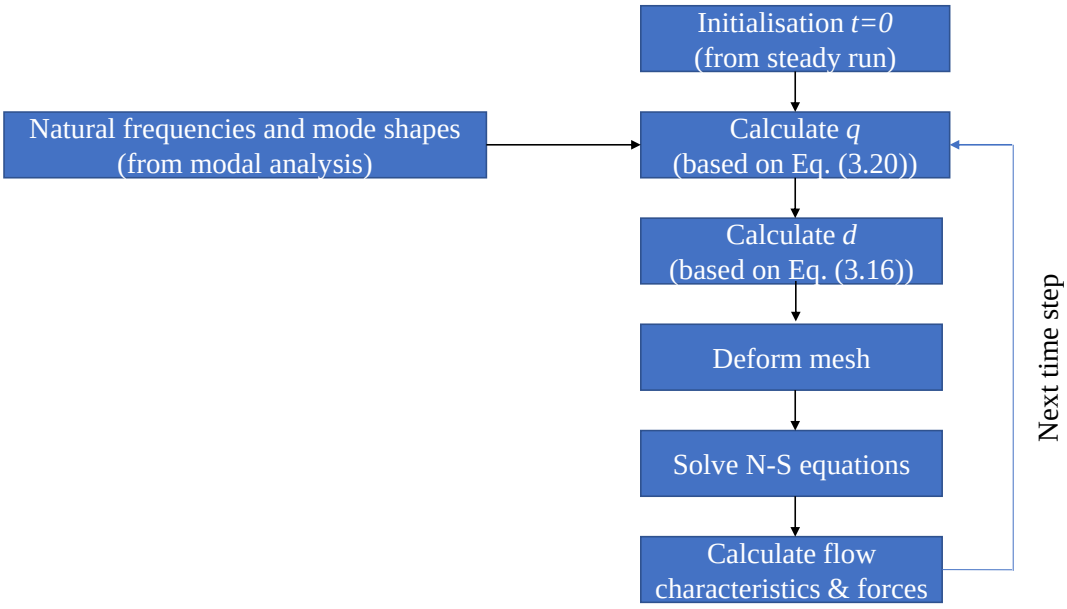

a) Flow chart of the modal coupling FSI method

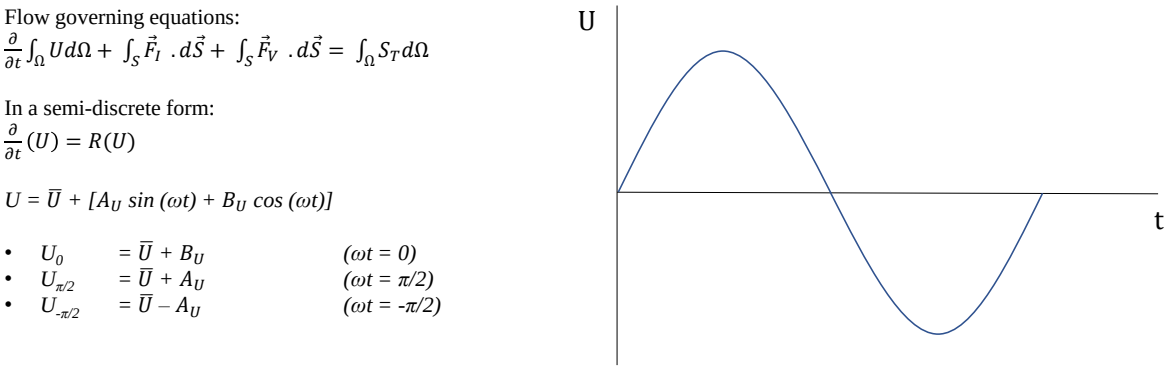

b) Flow solution using one harmonic

Figure 3.2. The flow chart of the modal coupling FSI method and the flow solution of the frequency domain solution method using one harmonic.

3.6. Mesh Deformation

The mesh deformation is a two-step process and is performed based on Radial Basis Function (RBF) and Transfinite Interpolation (TFI) methods. RBF method is used for the deformation of mesh and the TFI method is applied to update the interior grid points, edges and faces. The combination of RBF and TFI methods provides fast computation for the mesh deformation process.

3.6.1. Radial Basis Function (RBF)

RBF method is an effective and efficient tool for mesh deformation [177], and it has been applied to a number of applications. It is found that a high-quality deformed mesh is

achieved using the RBF method. Using this method, the position of the deformed mesh is constructed based on an interpolation function *f*, which is obtained by a sum of radial basis functions as follow:

$$f(\vec{x}) = \sum_{k=1}^{N_B} \alpha_k \varphi\left(\left|\vec{x} - \vec{x}_{n_k}\right|\right) + p(\vec{x}) \tag{3.21}$$

In this equation, $\vec{x}$ is the mesh node position, $\vec{x}_{n_k}$ is the position of the boundary node *n*, N_B is the number of boundary nodes, α is coefficient of the interpolation, φ is the radial basis function, and $p(\vec{x})$ is a polynomial and is given by:

$$p(\vec{x}) = \beta_0 + \beta_1 x + \beta_2 y + \beta_3 z \tag{3.22}$$

The coefficients, α and β, are obtained using the below linear equation.

$$\begin{pmatrix} F_R & P_B \\ P_B{}^T & 0 \end{pmatrix} \begin{bmatrix} \alpha \\ \beta \end{bmatrix} = \begin{bmatrix} d_B \\ 0 \end{bmatrix} \tag{3.23}$$

In this equation, F_R and P_B are the RBF matrix and the polynomial matrix generated at the boundary nodes, respectively. d_B is the value of displacement at the boundary.

3.6.2. Transfinite Interpolation (TF)

TFI is an efficient method, and it is used to update the interior points, edges and faces of the deformed mesh. For a mesh segment from point A to B, the arc-length of an interior point *i* is expressed as:

$$l_i = \sum_{i=A+1}^{j} |x_{ref,i} - x_{ref,i-1}| \tag{3.24}$$

where x_{ref} is the coordinates of the reference node. The arc-length of the segment from point A to B can also be expressed in a similar way as follow:

$$L_{AB} = \sum_{i=A+1}^{B} |x_{ref,i} - x_{ref,i-1}| \tag{3.25}$$

The coordinates of the new edge of interior points x_{new} can be obtained by performing a linear interpolation, and it can be expressed as:

$$x_{new,i} - x_{ref,i} = \left[1 - \frac{l_i}{L_{AB}}\right](x_{new,A} - x_{ref,A}) + \left[\frac{l_i}{L_{AB}}\right](x_{new,B} - x_{ref,B}) \quad (3.26)$$

This methodology is performed in all directions for the computation of 3D blocks.

3.7. Rotor-Stator Interaction

The relative motion between successive rows of rotating and stationary domains, such as rotor and tower, are the main sources of flow unsteadiness that affects the flow around the wind turbines in arrays. In this study, a rotor-stator interface is employed to exchange the flow solution between the rotating domain which includes a rotor and the stationary domain which includes a tower. The task of the rotor-stator interface is to match the flow solution between the upstream and downstream sides and to ensure the continuity of the unsteady flow across the interface.

The rotor-stator interface must be defined in the mesh generator after the mesh for each domain has been generated. The boundaries from the upstream domain and the downstream domain are connected using a full non-matching interface type, which allows connecting the grids with several blocks with non-matching boundaries. It means that the grid boundaries with different pitch lengths (i.e., rotational periodicity) can be connected. After connecting all grids together and defining the rotor-stator interface, a single grid file is imported into the flow solver where the rotor-stator interaction is set up, which indicates the flow direction, typically from the upstream to downstream direction. But the flow interaction between the rotor and stator is taken into account by transferring and exchanging the flow data between the two domains.

The standard sliding-plane method which is a time-accurate solution is applied for the time domain solution. In this method, by using a direct local interpolation method, the instantaneous flow information is exchanged across the interface at each time step. This method requires the same rotational periodicity on both sides, which means a full wheel of the rotor and the stator (both 360-degree grids) are required.

With a frequency domain solution method, on the other hand, the conservative flow variables can be decomposed into a time-averaged value and unsteady perturbations for a specified number of harmonics (m), based on Fourier decomposition of the unsteady

flow as expressed in Eq. (3.11). The equality of rotational periodicity is obtained through the phase-shift periodicity as the harmonic components are phase-shifted between periodic boundaries. Hence, the interaction between the rotor and the stator (i.e., the tower in this study) can be modelled by computing the time-averaged flow and the unsteady perturbations from the two adjacent rows and transferring the flow characteristics between the upstream row and the downstream row to ensure the continuity of the unsteady flow across the rotor-stator interface. The resolution and the continuity of the flow can be controlled through the order of the Fourier series or the number of harmonics. In this project, one harmonic is found to be enough to resolve the unsteady flow solution due to the rotor-tower interaction. The schematic view of the rotor-stator interaction is shown in Fig. 3.3.

The main emphasis of the rotor-stator interface using the frequency domain method is to pass the time-averaged and unsteady perturbations across the interface. A non-reflecting flux-averaged method [178] is employed to pass the time-averaged flow variables across the rotor-stator interface. Using this method, the conservation of mass, momentum and energy fluxes is obtained. Incoming and outgoing flow characteristics are calculated from the time-mean values, and the local characteristics are injected in a local non-reflective boundary treatment. To pass the unsteady disturbances across the rotor-stator interface, there are two main tasks to be completed, which include time reconstruction and Fourier processing to pass unsteady components of different sources.

3.7.1. Time Reconstruction

After completion of the simulation, the flow solution obtained from the frequency domain method needs to be reconstructed in time to obtain the unsteady flow in time history, which can be used to produce instantaneous flow data that can be compared to the time domain method. The proposed method has the ability to reconstruct the harmonic solution in time history. During the time reconstruction process, the total number of time steps should be defined. This determines the total physical time length in a period of harmonic oscillation that corresponds to the fundamental frequency of the frequency domain solution. The instantaneous positions of flow data points on the interface of the upstream domain, relative to the downstream turbine, are determined by their initial positions, rotational speed and the time taken relative to the reference point. The time trace reconstruction of the flow variables at any point on the interface of the upstream domain can be performed based on Eq. (3.11). Although a single blade is used for the simulation,

the flow solution for a full wheel of rotor or stator blades can be reconstructed. This is, in fact, the advantage of the frequency domain solution method. Based on the maximum number of blades available in a rotor or stator and the specified inter blade phase angle, the reconstruction for a full wheel of blades can be done using the phase shift periodicity. The conservative flow variables *U* on the interface of the downstream domain in time is obtained based on that of the upstream domain as follow:

$$U\,(t_i) = \; U_i{}'\;(i = 0,1,2,\dots,n) \tag{3.27}$$

where, $U_i{}'$ is the flow variables at a time t_i on the interface of the upstream domain and *n* is the number of time steps required to complete one complete cycle of the unsteady flow.

3.7.2. Fourier Processing

After the time reconstruction is complete for each side of the interface, the temporal Fourier transformation is employed to generate Fourier components of the flow variables for the downstream domain as follow:

$$A_U = \frac{\omega}{\pi}\sum_{i=1}^{n}(U_i)\sin\,(\omega t_i)\Delta t_i \tag{3.28.a}$$

$$B_U = \frac{\omega}{\pi}\sum_{i=1}^{n}(U_i)\cos\,(\omega t_i)\Delta t_i \tag{3.28.b}$$

$$\bar{U} = \frac{\omega}{2\pi}\sum_{i=1}^{n}(U_i)\Delta t_i \tag{3.28.c}$$

where ω is the fundamental frequency, *n* is the number of time steps taken for the time reconstruction of $U(t_i)$ series, and $\bar{U}$ is the time-averaged value of the flow variables. For a specified number of harmonic *m*, *N = (2m+1)* time instances are required for the time reconstruction of the flow variables.

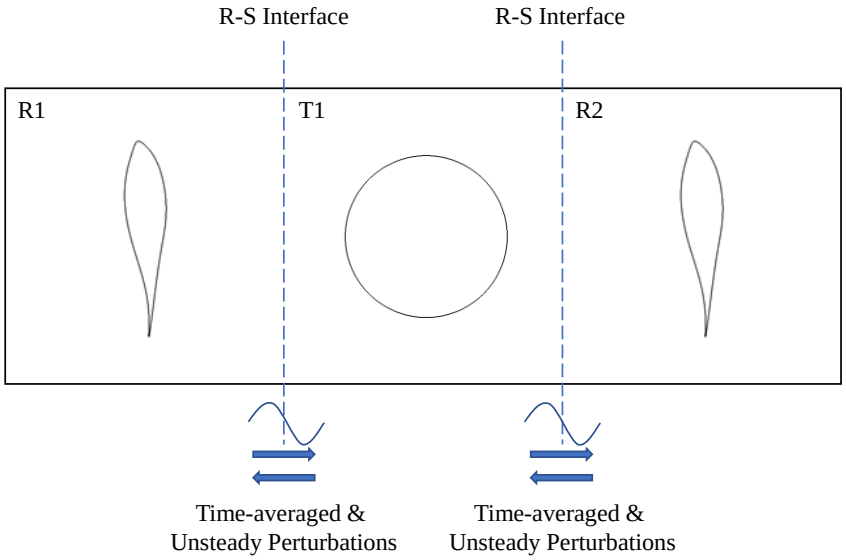

Figure 3.3. Schematic diagram of the rotor-stator interaction between the wind turbines in arrays. (R1: Rotor of the upstream wind turbine; T1: Tower of the upstream wind turbine; R2: Rotor of the downstream wind turbine).

3.8. Summary of Methodology

In this chapter, the computational methodology is presented for the aerodynamic and aeromechanical analysis of wind turbines including the multiple wind turbines model. A nonlinear frequency domain solution method is proposed for these analyses. With this method, the flow governing equations can be re-written in the frequency domain, and a new set of unsteady Navier-Stokes equations are iteratively solved in the frequency domain. A 2^{nd} order accurate central scheme is applied for the spatial discretization and an explicit 4-stage Rune-Kutta scheme is used for the temporal discretization. The main advantage of the frequency domain solution method is a precise prediction of the periodic unsteady flow at an affordable computational cost. Only a single blade is required for the modelling. The modal coupling FSI method is employed for the modelling and simulation of fluid-structure interactions. The deformation of the blade structure is included and simultaneously updated in the flow simulation. This method provides an alternative to the traditional one-way and two-way coupling methods as the motion of the blade structure is integrated into the flow simulation using the structural mode shapes and the specified vibration frequency and amplitude. Using this method, modal analysis is required before the flow simulation to compute the natural frequencies and mode shapes of the blade structure that is used to define the blade oscillation in the flow simulation. Radial Basis Function (RBF) and Transfinite Interpolation (TFI) methods are employed for the mesh

deformation. Rotor-stator interfaces are used for the connection between rotor and stator (i.e., tower in this study) models and the transfer of the flow data between the upstream and downstream domains. A standard sliding-plane method is used for the time domain solution and a frequency domain solution method is used for the frequency domain solution. The flow solution obtained from the frequency domain solution method is then reconstructed in time to have the unsteady flow solution in time history.

Chapter 4. Aerodynamic and Aeromechanical Analysis of a Wind Turbine Blade Aerofoil

The objective of this chapter is to employ a high-fidelity numerical method that can investigate the aerodynamic and aeromechanical performances of a wind turbine blade aerofoil at an affordable computational cost. A nonlinear frequency domain solution method is proposed and employed in this study. Before applying this method for wind turbines, the frequency domain method is used for the aeromechanical analysis of a linear turbine cascade, and the results are compared to the experiment for validation. Afterwards, the proposed frequency domain solution method is applied to the aerodynamic and aeromechanical analysis of a wind turbine blade aerofoil to investigate the details of the flow field at a wide range of parameters including angles of attack and Reynolds numbers. The NACA0012 aerofoil is selected for these analyses. The pressure distributions on the surfaces of this aerofoil at various angles of attack are experimentally measured in this study. The numerical model is validated against the experiment. Furthermore, using a highly efficient frequency domain solution method, the unsteady pressure distributions and aeroelasticity parameters are computed at various angles of attack and Reynolds numbers. The results obtained from the frequency domain solution are compared to those of the traditional time domain solution for extensive validations to ensure that this method captures the unsteady flow and computes the unsteady flow parameters precisely. Results indicate that the difference of unsteady pressure distributions between the two surfaces of the aerofoil becomes larger as the angle of attack is increased. It is found that the flow separation on the suction surface is reduced by raising the Reynolds number as the flow is more resistant to separation at higher wind speeds. The turbulent flow develops in the downstream region due to the laminar vortex shedding at low Reynolds numbers. It is also revealed that the Reynolds number has an impact on the aeroelasticity, and the aerodynamic damping is greater at higher Reynolds numbers. The comparisons between the frequency domain method and the time domain method show that the frequency domain solution method is not only accurate but also computationally very efficient as the computation time is reduced by 90%.

4.1. Physical Description

A wind turbine blade is typically composed of different types of aerofoils at different sections, and each section of the blade has a different pitch angle in order to optimise the

lift coefficient. In this study, the NACA0012 is selected and assumed to be the mid-section of a wind turbine blade. Figure 4.1 shows the schematic diagram of the physical model of the mid-section of the wind turbine blade using the NACA0012 aerofoil. The chord length and the span of the physical model used in the experiment are 0.063 m and 0.049 m, respectively. The aerofoil has an effective surface area of 0.0031 m^2. The angle of attack of the aerofoil is varied between 0^o to 25^o during the experiment. The uniform freestream velocity (V_∞) is applied in the stream-wise direction, and the Reynolds number is calculated based on the inflow speed and the chord length.

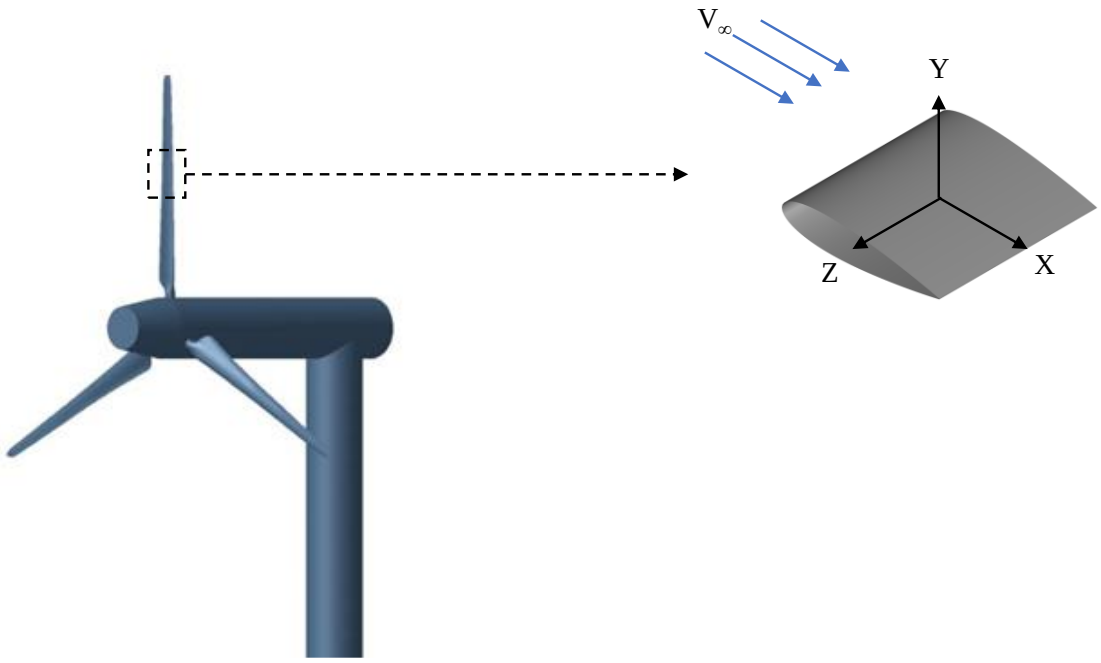

Figure 4.1. Schematic diagram of the physical model of the NACA0012 aerofoil.

4.2. Experimental Description

The selected NACA0012 aerofoil, presented in the physical description section, is placed inside a simple miniature wind tunnel of the AF10 airflow bench experiment, available at the Northumbria University. The AF10 airflow bench consists of a fan that collects the air from the environment and delivers it into the wind tunnel which sits above the wind tunnel. The air speed flowing into the wind tunnel can be adjusted using a valve.

The aerofoil is carefully fixed in the wind tunnel to ensure the air flows over the surfaces of the aerofoil and the flow is two-dimensional representing the flow at the mid-section of a blade and avoiding tip vortices. The aerofoil and the wind tunnel are set up vertically. The aerofoil is rotatable to have the desired angle of attack (AoA). Pressure sensors are

integrated on both pressure and suction surfaces of the aerofoil. These pressure sensors are connected to the manometer, where the measurements are collected, through small pipe connectors. There are twelve pressure sensors over the aerofoil with six on each surface. In addition, three other pressure sensors are used to measure the pressure inside the airbox, the pressure at the inlet of the wind tunnel, and the atmospheric pressure.

The pressure measurements are indicated by the liquid inside the manometer. The liquid is water, but it is stained with a blue dye for clear visualisation. Although it is a small-scale wind tunnel experiment, the results and measurements can be scaled up for the analysis of larger aerofoils. In this experiment, the angles of attack are varied from 0^o up to 25^o with an increment of 5^o, and the pressure distributions on the aerofoil surfaces are measured. The experiment is conducted at the Reynolds number of 4×10^6. The Reynolds number is calculated based on the inflow speed and the chord length. The details of the experimental set-up are shown in Fig. 4.2.

a) AF10 airflow bench and overall set-up

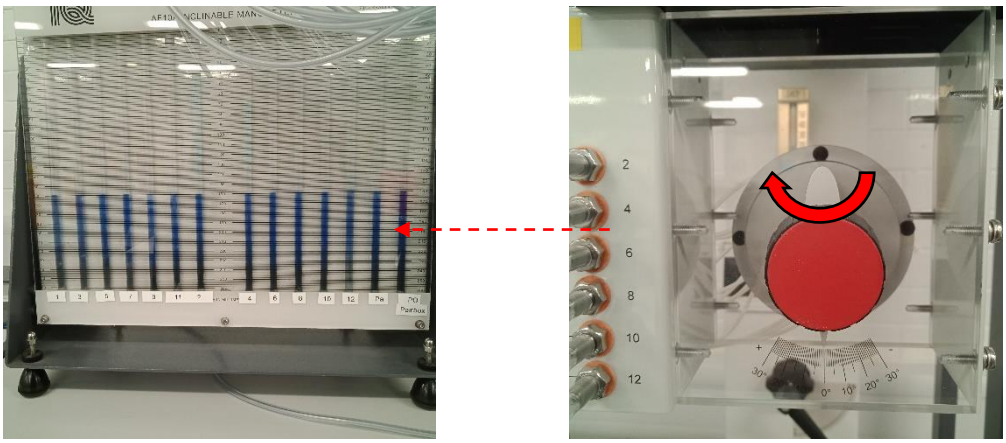

b) Manometer c) Aerofoil inside a wind tunnel

Figure 4.2. Overall experimental set-up of the AF10 airflow bench experiment.

4.3. Computational Description

The details of the computational domain and mesh generated for the simulations are presented in Fig. 4.3. The domain is based on a two-dimensional model with a span-wise extension, known as a quasi-3D model, to analyse the two-dimensional flow at the blade mid-span. It is important to make sure that the computational domain is adequate in all directions. The inflow and outflow boundaries are located 3*C* upstream of the leading edge and 4*C* downstream of the trailing edge, respectively, where *C* is chord length. The far-field boundaries are placed 2*C* from the origin of coordinates. All of these boundaries are considered to be far enough from the blade. As a quasi-3D model is employed, a span-wise extension needs to be specified. A span-wise extension used in this model is 1*C* which is considered big enough to capture the two-dimensional flow at the blade mid-span. Great care is given to the generation of the mesh. Hexahedral elements are used throughout the domain as it is understood that hexahedral mesh can provide better quality and accuracy compared to other unstructured mesh types such as tetrahedral mesh. A boundary layer inflation is also generated in the mesh to resolve the boundary layer flow sufficiently. For this purpose, the first layer thickness, the width of the first cell close to the blade, is 10^{-5} m to make sure that the dimensionless near-wall resolution normal to the blade, y^+, is less than one all over the blade. 20 grid points are distributed with a growth rate of 1.2 in the boundary layer inflation to capture the flow phenomena inside the boundary layer. The generated mesh contains 120, 62 and 50 grid points in the stream-wise, pitch-wise and span-wise directions, respectively.

A velocity inflow is applied at the inlet and a pressure outlet boundary is used at the outlet. The inlet velocity is varied to acquire the desired Reynolds number for different analyses.

A far-field boundary is specified in the pitch-wise direction and a mirror boundary is defined on each side of the domain in the span-wise direction. A solid wall boundary condition is applied to the surfaces of the aerofoil. A stationary wall boundary is used in the steady aerodynamic simulations which are compared to the experiment for validation. A deforming wall boundary with a periodic displacement is defined in the aeromechanical simulations. The displacement of the wall deformation is defined as follow:

$$d(t) = \bar{d} + d_A \cos(\omega_i t) \tag{4.1}$$

where $\bar{d}$ and d_A are the mean value and amplitude of the blade displacement, and the blade wall boundary is deformed with respect to the blade displacement.

In this chapter, the steady flow simulations are first performed for various angles of attack, and the results are compared to the experimental results for validation of the CFD model. Afterwards, the blade vibration is integrated into the flow simulation by prescribing the vibration frequency and amplitude to the aerofoil. The aeromechanical simulations using the vibrating blade are performed for the angles of attack of 0^o, 5^o and 10^o to analyse the effect of the angle of attack on the unsteady and aeroelasticity parameters. Then, the effects of Reynolds number on the unsteady flow behaviour and aeroelasticity parameters are also investigated using the aerofoil with 10^o angle of attack. The flow simulations are carried out in a three-dimensional CFD environment. The flow governing equations are provided in Chapter 3 (refer to Sections 3.1). A nonlinear frequency domain solution method, proposed in Section 3.4, is used to carry out the aeromechanical simulations. As only a section of the blade is simulated in this case, the first natural frequency from the MEXICO wind turbine model, which will be discussed in the next chapter, is adopted to be the vibration frequency, and the frequency is 15 Hz. The vibration amplitude is set to be 1% of the chord length. The modal coupling method, presented in Section 3.5, is applied to the aeromechanical simulations.

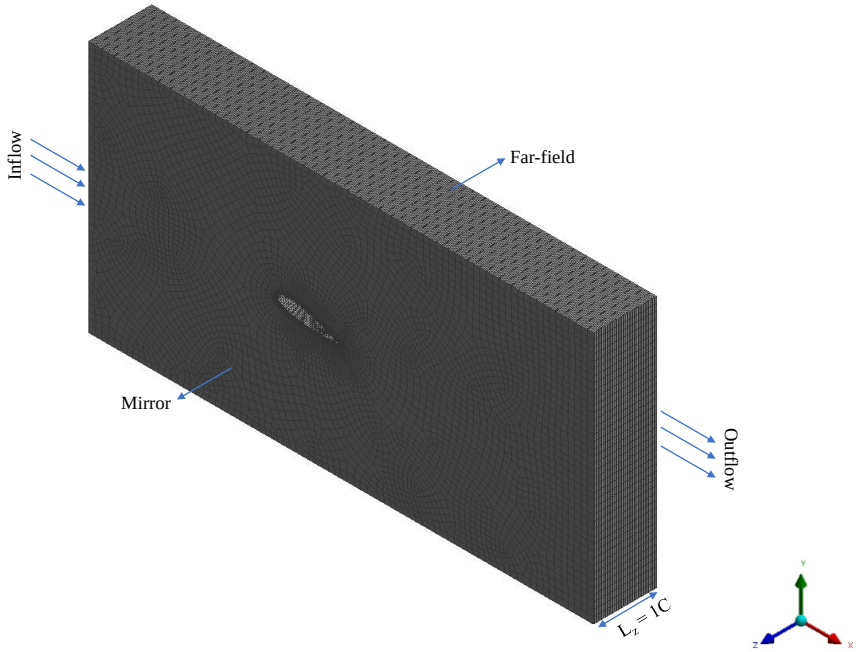

a) Computational domain with boundary conditions

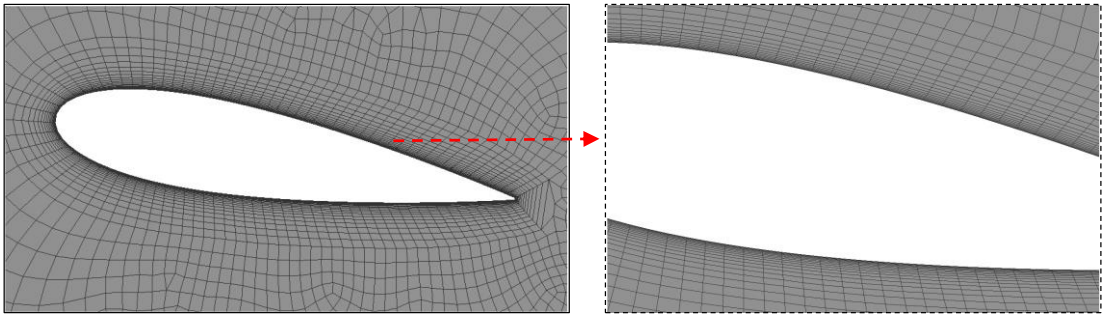

b) Blade-to-blade view of the mesh c) Boundary layer mesh

Figure 4.3. Details of computational domain and mesh with boundary conditions.

4.4. Validation

Before applying the proposed frequency domain solution method for the analysis of the presented wind turbine blade aerofoil, it is necessary to validate the method to ensure accuracy. However, it is understood that the experiments for the aeromechanical analysis are too difficult or impractical to be performed, and there are no such experiments for wind turbines presented in this thesis. As a wind turbine blade is made of aerofoils and the aeroelasticity problems potentially encountered by wind turbine blades can be similar to those of other turbine blades such as low-pressure turbines, the experiment for the aeroelasticity analysis of the linear turbine cascade, designed by Huang et al. [58], is employed to validate and verify the proposed frequency domain solution method in predicting unsteady pressure and aeroelasticity parameter such as aerodynamic damping. In this experiment, there are seven blades in the cascade, and one of these seven blades, the middle blade, is only excited by a motor at a vibration frequency of 23 Hz to impose

the bending mode of vibration to the blade structure. In the aeromechanical analysis of turbomachines, 1-3% of chord length are typically set as the vibration amplitude. In fact, 3% chord was set to be the vibration amplitude in the experiment. For the purpose of the direct comparison to the experiment, 3% chord is also set as the vibration amplitude in the CFD simulations. During the experiment, the unsteady parameters are measured for different IBPA values. The details of the geometry and physical parameters of the linear turbine cascade can be found in [58].

In this thesis, the IBPA of 180^{o} case is reproduced using the numerical simulations employing the frequency domain method. The physical parameter including the vibration frequency and amplitudes are kept the same as the experiment. The Reynolds number of 2×10^{5} is used in both the experiment and simulations. The computational domain and grid generated for the simulations are presented in Fig. 4.4. The mesh is generated using O4H topology in a structured grid generator. The generated mesh consists of $177 \times 59 \times 57$ grid point distributions in the stream-wise, pitch-wise and span-wise directions. The blade, hub and shroud are treated as solid wall boundaries. A velocity inflow is applied at the inlet and a pressure outlet is defined at the outlet. The translational periodic boundary interfaces are applied in the pitch-wise directions in order to represent a row of blades in a cascade.

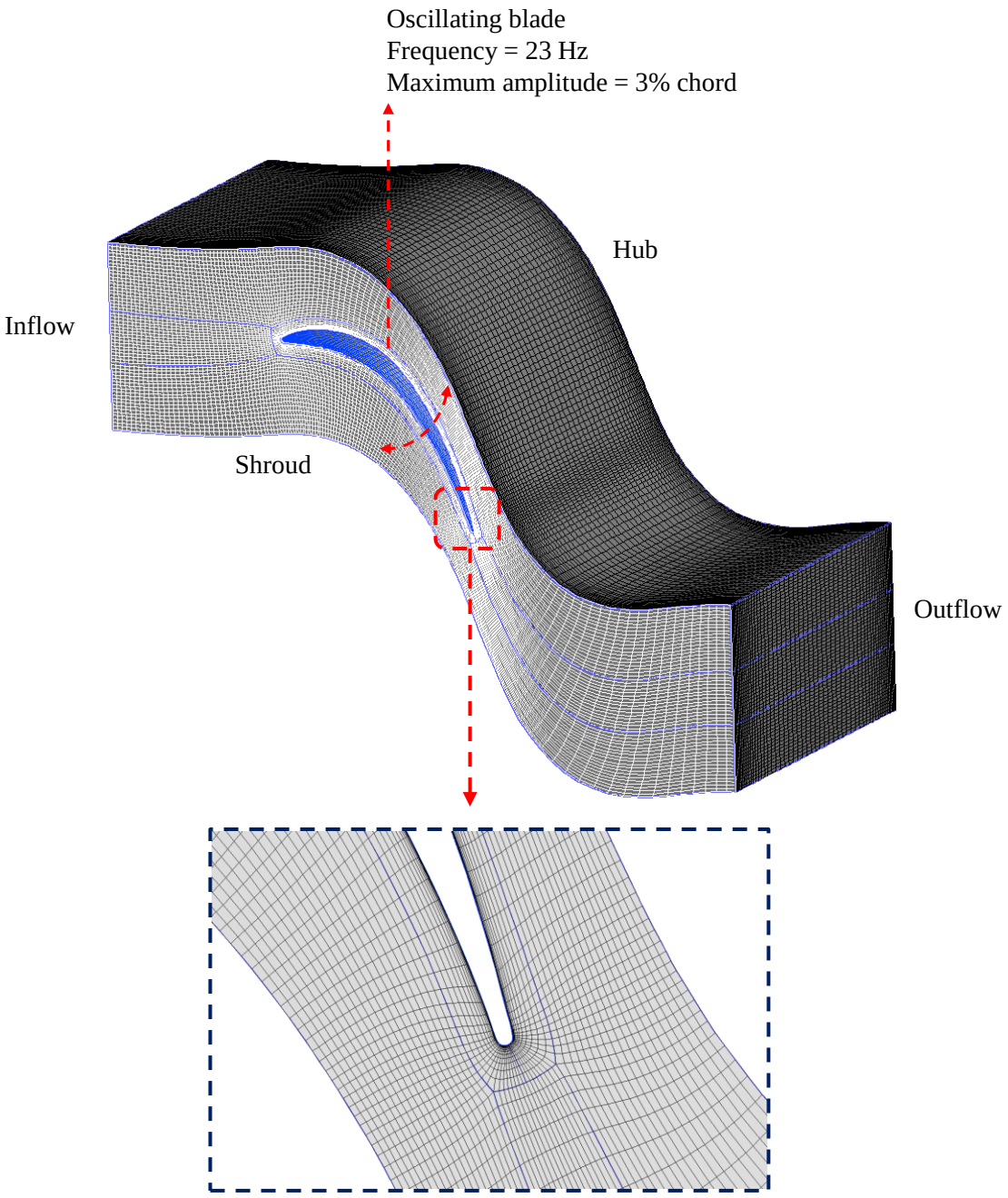

Figure 4.4. Detailed computational domain and grid of the linear turbine cascade.

The unsteady flow parameters due to the blade vibration can be divided into the time-averaged value and the unsteady perturbations. Unsteady pressure distributions on the surfaces of the blade are mainly analysed in this chapter. The comparisons of the time-averaged pressure coefficient (C_p) and the unsteady pressure amplitude coefficient (C_{p1}) distributions on the surfaces of the aerofoil between the experiment and the present simulation using the proposed frequency domain solution method for an IBPA of 180^o are presented in Fig. 4.5. The results are extracted at different sections of the blade including 30%, 50% and 80% span sections. As seen, the results are in good agreement, which indicates that the frequency domain solution method predicted unsteady pressure

distributions on the blade surfaces correctly. It is found that the unsteady perturbations are higher in the blade outer region where the vibration amplitude is larger. Apart from the unsteady pressure distribution, one of the most important aeroelasticity parameters in the analysis of turbomachinery is aerodynamic damping. The aerodynamic damping for the blade of this linear turbine cascade for an IBPA of 180^o obtained from the experiment and the present simulation are compared in Table 4.1. It is seen that the results agree well with each other.

Based on the results obtained and validation against the experiment, it is concluded that the frequency domain solution method can provide an accurate prediction of unsteady pressure distributions and aeroelasticity parameters such as aerodynamic damping for the analysis of turbomachines. Therefore, this method will be applied to the aerodynamic and aeromechanical analysis of wind turbines. Throughout the thesis, the proposed frequency domain solution method will be extensively validated against the conventional time domain methods. In addition, the capability of the frequency domain solution method is investigated and validated against the highly accurate time domain solution by means of direct numerical simulations for both aerodynamic and aeromechanical analysis of low-pressure turbine cascade, and the detailed analysis can be seen in Appendix. It is also revealed that the frequency domain solution method can capture the highly unsteady flow structures and predict aeroelasticity parameters accurately.

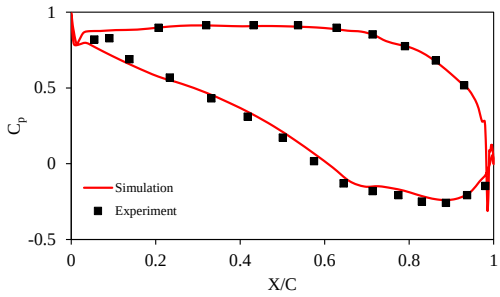

a) C_p at 30% span

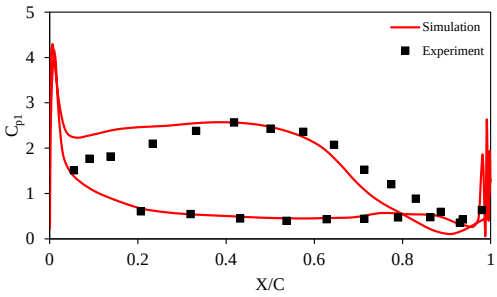

b) C_{p1} at 30% span

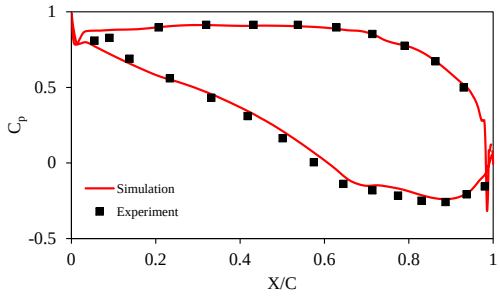

c) C_p at 50% span

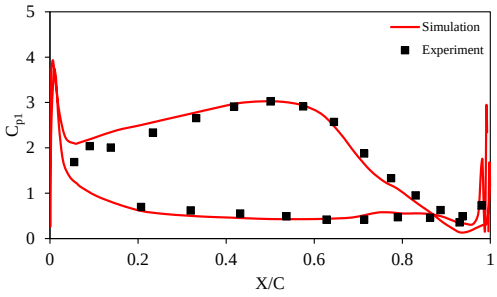

d) C_{p1} at 50% span

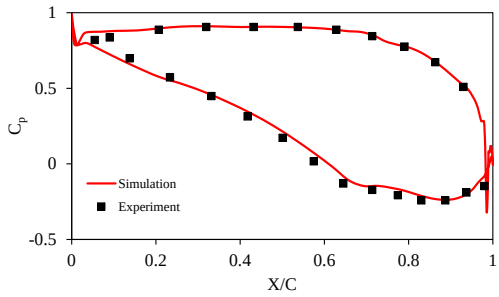

e) C_p at 80% span

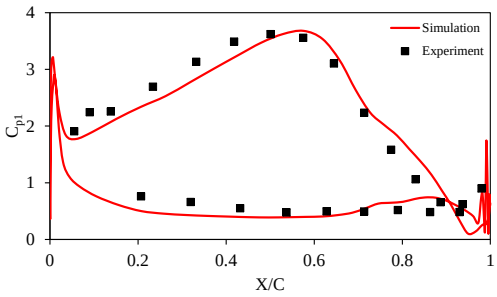

f) C_{p1} at 80% span

Figure 4.5. Time-averaged pressure coefficient (C_p) and unsteady pressure amplitude coefficient (C_{p1}) distributions at different sections of the blade of the linear turbine cascade.

Table 4.1. Aerodynamic damping

Method	**Aerodynamic damping**
Experiment	0.52
Simulation	0.57

4.5. Results and Discussions

4.5.1. Aerodynamic Analysis of Aerofoil at Various Angles of Attack

Figure 4.6 demonstrates the pressure coefficients obtained from the experiment and the CFD simulations. Both the experiment and simulations are conducted for various angles of attack ranging from 0^o to 25^o with an increment of 5^o. At the angle of attack of 0^o, the same amount of flow passes over both pressure and suction surfaces of the aerofoil due to the symmetric profile, which leads to the same pressure distributions on both surfaces of the aerofoil. Therefore, in Fig. 4.6 (a), no pressure difference between the pressure and suction surfaces is observed. Theoretically, there is no lift at this angle of attack. As the angle of attack is raised to 5^o, the pressure difference between the two surfaces of the aerofoil starts to occur generating a lift force. The highest and lowest pressure coefficients are observed around the leading edge. The pressure difference between the two surfaces is greater at the angle of attack of 10^o as the pressure on the pressure surface becomes significantly larger than that of the suction surface leading to an increased lift coefficient. At this angle, the flow starts to separate from the suction surface near the trailing edge. When increasing further the angle of attack to 15^o, a great pressure difference between the two surfaces is seen near the leading edge; however, the pressure difference is reduced at around X/C=0.4 which continues up to the trailing edge. It is mainly due to the flow separation on the suction surface, and the flow separation point moves towards the leading edge as the angle of attack is increased. Due to the flow separation, the flow recirculation and separation bubbles exist in the separation zone which causes turbulence around the aerofoil. It can be noted that the flow behaviour is nearly that of the stall at this angle of attack. At the angles of attack of 20^o and 25^o, it can be clearly seen that the pressure is not increased much near the leading edge compared to that of the 15^o; however, the pressure difference and distribution between the two surfaces is significantly reduced afterwards, approximately from X/C=0.1. This indicates that the flow separation becomes too large, and the flow is separated nearly from the leading edge of the aerofoil, which results in a turbulent flow and flow recirculation on the suction surface and a loss of lift coefficient. Therefore, it can be concluded that the stall angle is past and the angles of attack of 20^o and 25^o fall within the post-stall region. In terms of comparison between the experiment and the simulation for validation, it is seen that excellent agreement is obtained between the two methods. A slight difference between the experiment and the simulation is seen on the pressure surface at A0A = 5^o. The reason for this can be concluded as the angle not being exactly 5^o while manually setting during the experiment.

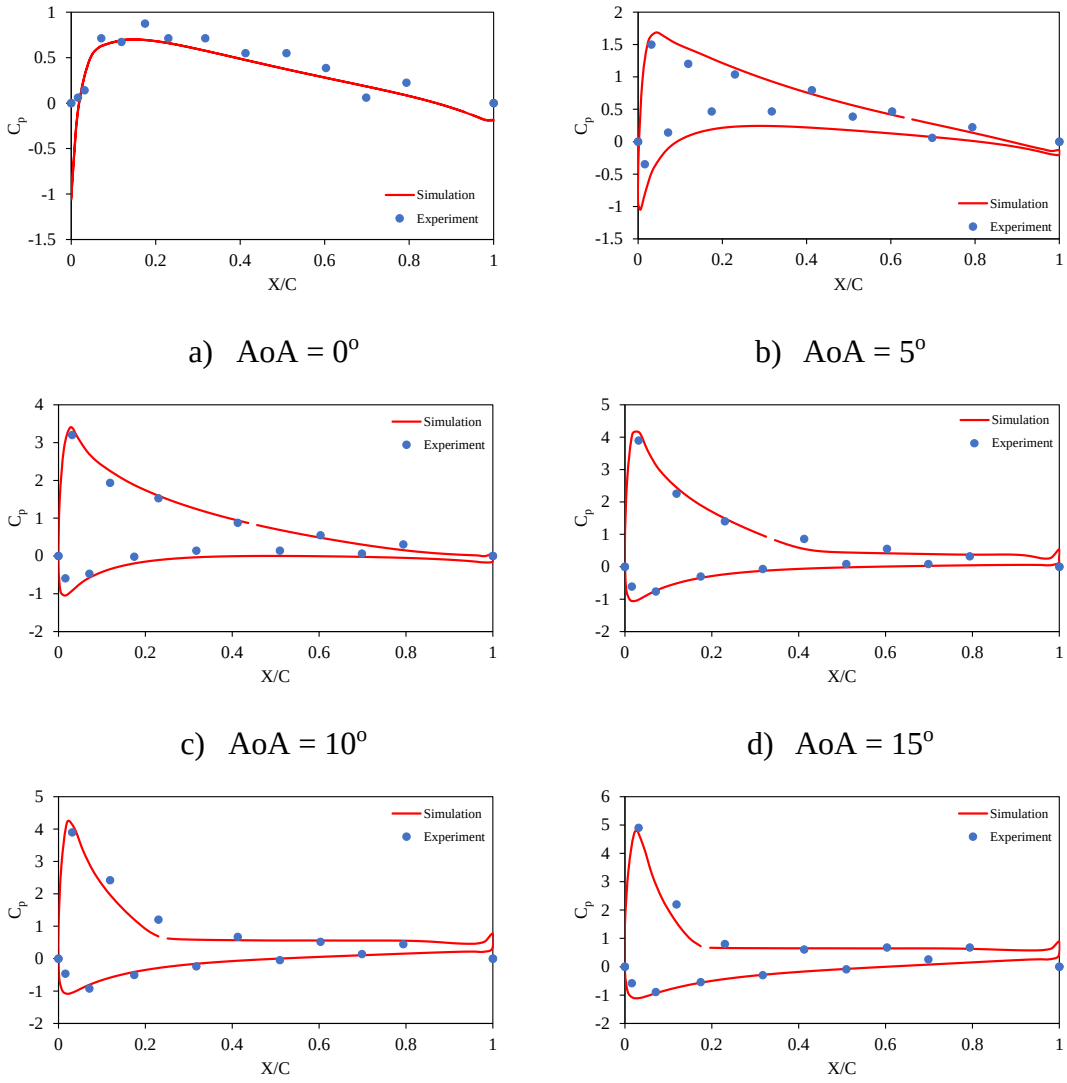

a) AoA = 0° b) AoA = 5°

c) AoA = 10° d) AoA = 15°

e) AoA = 20° f) AoA = 25°

Figure 4.6 Pressure coefficient at various angles of attack.

4.5.2. Aeromechanical Analysis of Aerofoil at Various Angles of Attack

After having validated the numerical model against the experiment, the aeromechanical simulations of this aerofoil are performed by integrating the blade vibration in the flow simulation. The first vibration mode is assumed to be the mode of vibration of the aerofoil. The vibration frequency, adopted from the modal analysis of the MEXICO wind turbine model, is 15 Hz, and the vibration amplitude is set to be 1%C. Due to the blade vibration, the flow is unsteady, and the flow variables change in time. As the blade is periodically oscillating, the flow unsteady parameters are also periodic in time. Among others, the unsteady pressure distributions on the blade aerofoil surfaces are mainly analysed in the aeromechanical analysis with the purpose of obtaining the aeroelasticity parameters such

as aerodynamic damping. For this analysis, the angles of attack of 0°, 5° and 10° are used because these angles are typically found as pitch angles of wind turbines.

Due to the periodic oscillation, unsteady pressure distributions over the aerofoil surfaces can be decomposed into the time-averaged value and the unsteady fluctuations. Figure 4.7 presents the time-averaged pressure coefficient and the unsteady pressure amplitude coefficient distributions at the three angles of attack. These parameters are calculated using the frequency domain solution method. As the experiment is only available for the rigid aerofoil, the results from the frequency domain solution using the blade vibration are validated against the conventional time domain solution method. As seen, the time-averaged pressure coefficients are similar to those of the steady simulations as previously shown. This is expected because the blade oscillation is periodic in time, and the time-averaged values can be similar to those of the steady flow simulations without vibration. The periodic movement of the blade imposes unsteady flow fluctuations on the aerofoil surfaces. The maximum amplitudes of unsteady pressure distributions are seen at the leading edge in all cases. However, at the angle of attack of 0°, the unsteady pressure distributions are almost the same on the pressure and suction surfaces in terms of both time-averaged and amplitude of the unsteady pressure. As the angle of attack is increased, the pressure fluctuations on the pressure and suction surfaces are different which impose aerodynamic loads. It is seen that the difference in unsteady pressure amplitude between the two surfaces is larger at the angle of attack of 10°. The difference in unsteady pressure fluctuations is present up to X/C=0.3 and it becomes very small afterwards at both 5° and 10° angles of attack. It is observed that the results from the frequency domain solution method and the time domain method agree well with each other, which indicates that the frequency domain method computed the unsteady pressure distributions correctly.

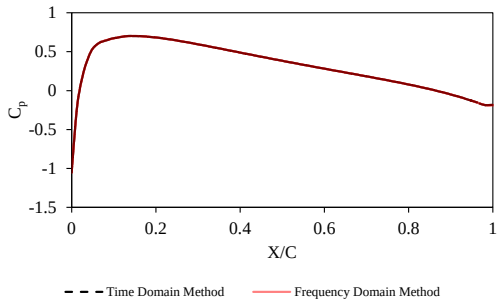

a) C_p at AoA=0°

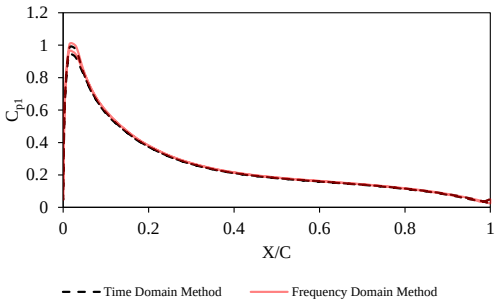

b) C_{p1} at AoA=0°

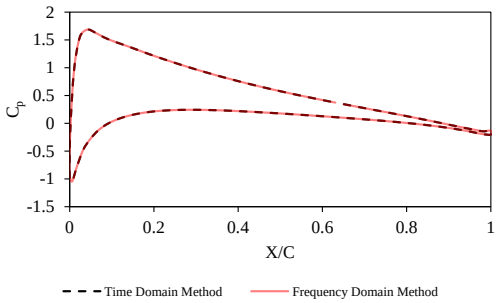

c) C_p at AoA=5°

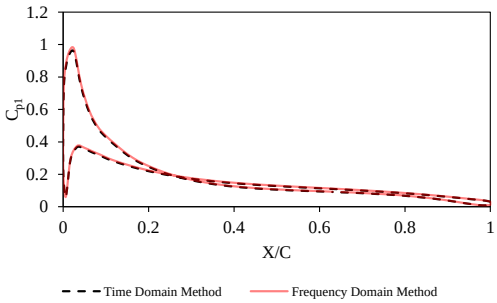

d) C_{p1} at AoA=5°

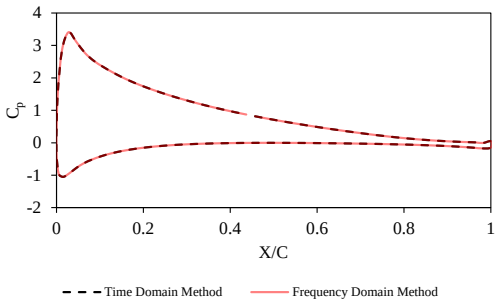

e) C_p at AoA=10°

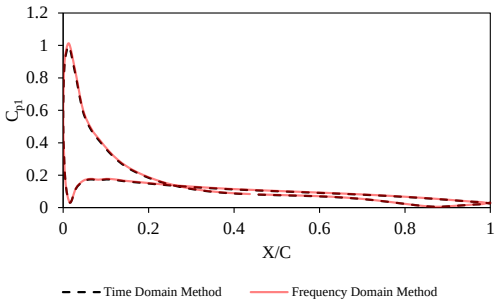

f) C_{p1} at AoA=10°

Figure 4.7. Time-averaged pressure coefficient (C_p) and unsteady pressure amplitude coefficient (C_{p1}) at different angles of attack.

Figure 4.8 shows the instantaneous pressure contours on the surfaces of the aerofoil, after 25 vibration periods, at various angles of attack. At AoA=0°, the maximum pressure is seen near the leading edge from where the same amount of pressure is distributed over the pressure and suction surfaces, which results in zero lift. When AoA is increased to 5°, the pressure difference between the two surfaces of the aerofoil can be observed. The contour indicates that the maximum pressure is found near the leading edge where the inflow interacts with the aerofoil. Then, the pressure is unevenly distributed over the aerofoil surfaces resulting in a higher pressure on the pressure surface whereas a lower pressure is observed on the suction surface. This pressure difference between the two surfaces starts to produce a lift force. At AoA=10°, the pressure difference between the two surfaces becomes larger leading to a stronger lift. It is seen in the contour that the pressure on the suction surface is significantly lower than that of the pressure surface. Compared to the 5° angle of attack, the pressure is also much lower on the suction surface at this angle.

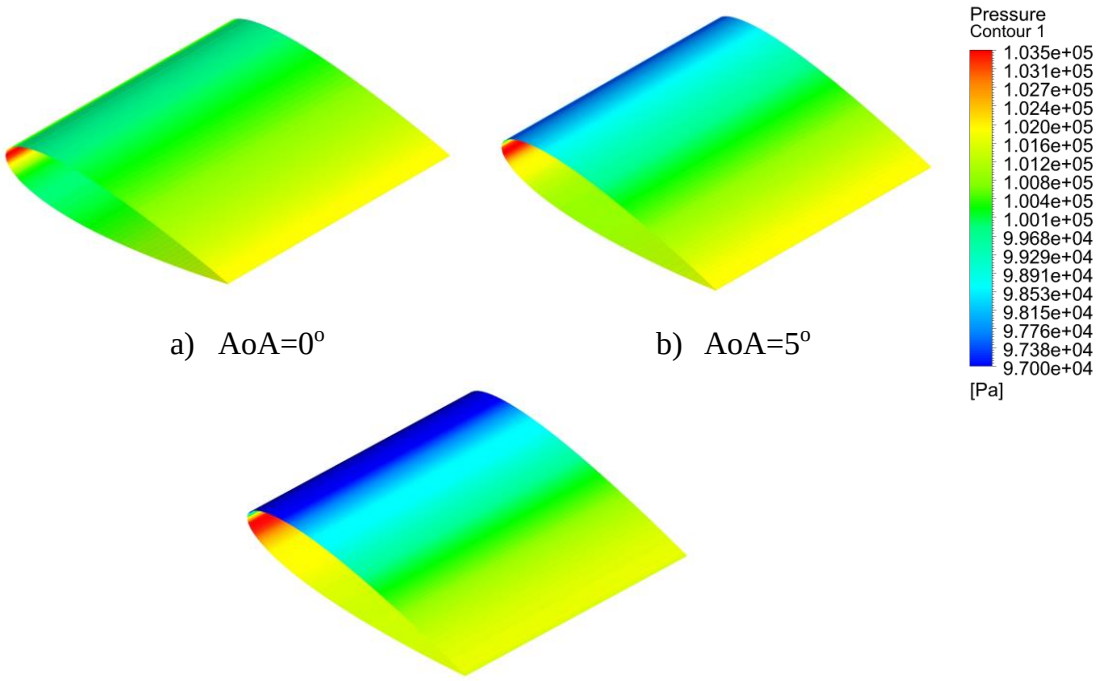

a) AoA=0^o b) AoA=5^o

c) AoA=10^o

Figure 4.8. Instantaneous pressure contours on the aerofoil surfaces at different AoAs.

The pressure distributions on the aerofoil surfaces, presented in Fig. 4.8, can be better visualised with the pressure distributions around the aerofoil. Figure 4.9 demonstrates the instantaneous pressure contour around the aerofoil at various angles of attack. When the angle of attack is 0^o, as discussed, the pressure is maximum at the leading edge, and then, the pressure is distributed equally on the pressure and suction surfaces. Raising the angle of attack changes the stagnation point. At the angle of attack of 5^o, the maximum pressure concentration is shifted slightly towards the pressure surface. As a result, the pressure on the suction surface is lower than that of the pressure surface. Increasing the angle of attack further to 10^o makes the shift of the maximum pressure concentration towards the pressure surface even further and the pressure difference between the two surfaces even higher. It is seen that the pressure near the leading edge is much higher and stronger on the pressure surface compared to the suction surface, which leads to a greater difference in pressure distributions between the two surfaces of the aerofoil.

Theoretically, the pressure distribution around an aerofoil is inversely proportional to the velocity distribution. Figure 4.10 illustrates the instantaneous velocity contours around the aerofoil at various angles of attack. The dimensionless velocity (V/V_{ref}) is provided for these contours. It is seen that the velocity is zero at the stagnation point where the flow interacts with the aerofoil whereas the pressure is maximum at this point. At the angle of

attack of 0^o, higher velocity fields are equally distributed over the aerofoil surfaces; however, lower pressure fields are seen on these surfaces in terms of pressure. At this angle of attack, the flow is attached to the aerofoil surface without a lift. At AoA=5^o, it is obvious that the flow stagnation point shifts slightly towards the pressure surface as previously seen in the pressure contours. The relative velocity is then distributed over the suction surface, which leads to higher velocity distributions on the suction surface. The flow is mostly attached to the aerofoil surface, but a very small flow separation is observed at the trailing edge. Raising the angle of attack to 10^o makes the shift of the stagnation point toward the pressure surface even further. As a result, the flow with a high-velocity field is distributed over the suction surface until the aft region from where the flow is separated. The velocity on the suction surface at this angle of attack is higher than at any other angles. Generally, with an inflow angle, the velocity is higher on the suction surface and lower on the pressure surface whereas the pressure is higher on the pressure surface and lower on the suction surface. Figure 4.11 presents the flow distribution over the blade aerofoil in terms of velocity streamlines. This figure further demonstrates the shift of the flow interaction point with the aerofoil depending on the angle of attack and the flow separation from the trailing edge, especially at the 10^o angle of attack.

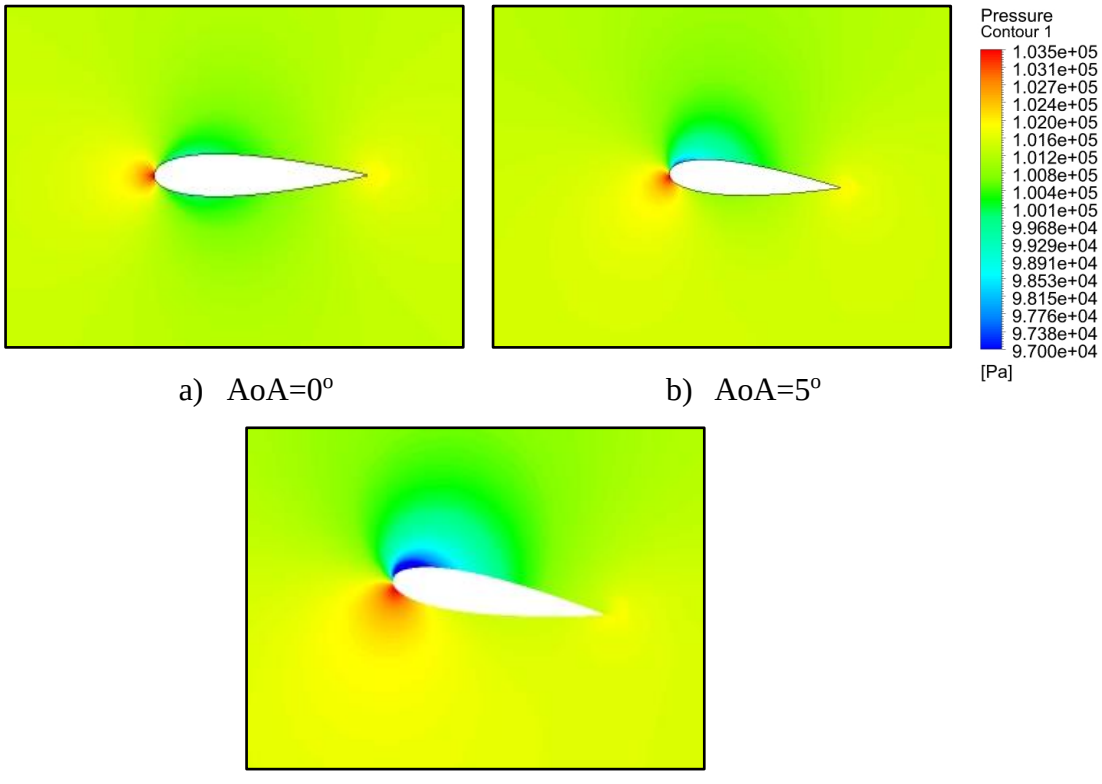

a) AoA=0^o b) AoA=5^o

c) AoA=10^o

Figure 4.9. Instantaneous pressure contour around the aerofoil at different AoAs.

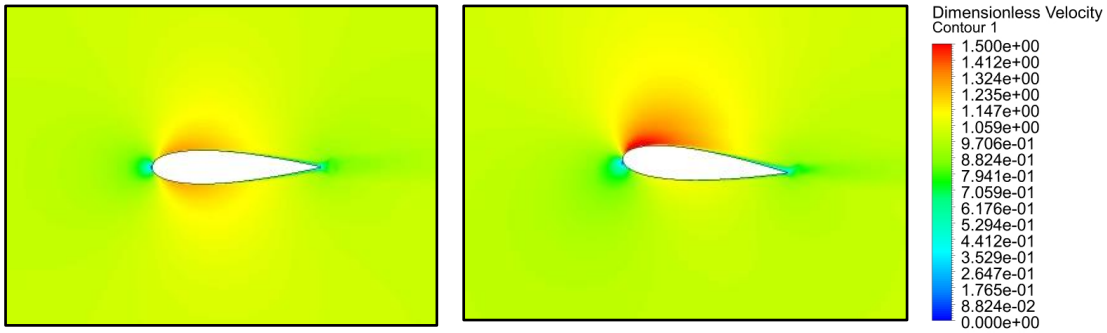

a) AoA=0^o b) AoA=5^o

c) AoA=10^o

Figure 4.10. Instantaneous dimensionless velocity (V/V_{ref}) contours around the aerofoil at different angles of attack.

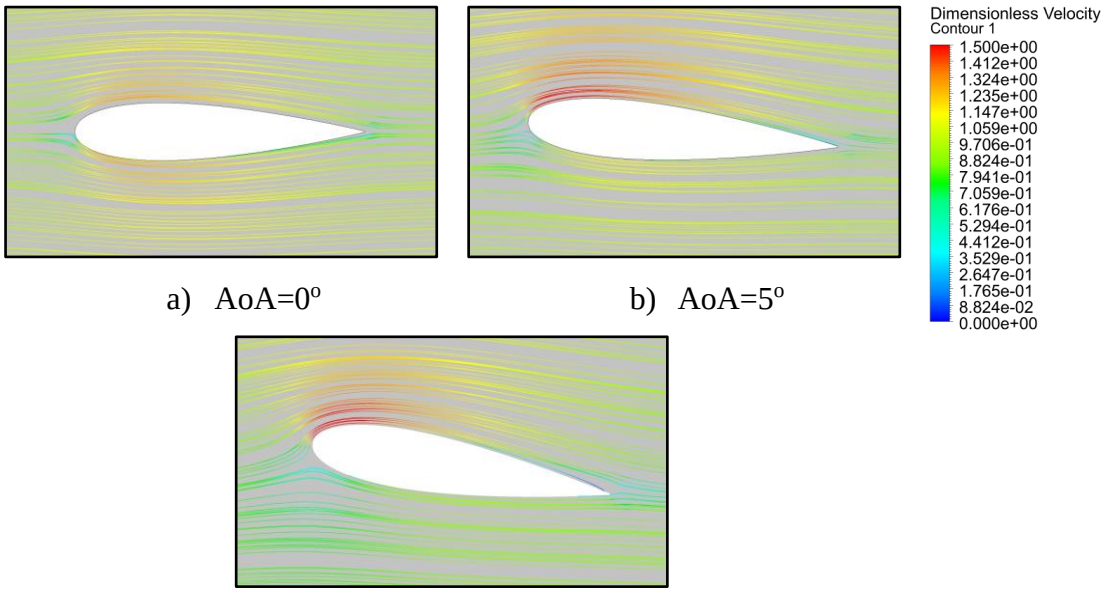

a) AoA=0^o b) AoA=5^o

c) AoA=10^o

Figure 4.11. Instantaneous dimensionless velocity (V/V_{ref}) streamlines around the aerofoil at different angles of attack.

The very important parameter in the aeromechanical analysis is the aerodynamic damping value which determines the stability of the blade. If the aerodynamic damping is negative, it is possible that the blade vibration could undergo flutter behaviour. In this study, the

aerodynamic damping of the blade aerofoil at various angles of attack are calculated using both frequency domain and time domain solution methods to validate the accuracy of the frequency domain solution on predicting the aeroelasticity parameter. The aerodynamic damping values obtained from both methods for various angles of attack are listed in Table 4.2. It is observed that the blade vibration is stable at the considered three angles of attack, and the aerodynamic damping is slightly increased when raising the angle of attack from 0^o to 10^o. A good agreement in predicting the aerodynamic damping is obtained between the frequency domain and time domain methods. Therefore, it can be concluded that the frequency domain solution method can predict accurate aeroelasticity parameters for the aeroelasticity analysis of wind turbine blade aerofoils.

Figure 4.12 shows the total wall work distribution over the surfaces of the aerofoil, which is directly related to the calculation of the aerodynamic damping and the determination of the stability of the blade. The positive values of the total wall work contour represent the stabilising effect and the negative values represent the destabilising effect. It is seen that the aerofoil possesses a dominant stabilising effect at all angles of attack resulting in positive values of aerodynamic damping as previously discussed. The maximum stabilising effect is seen on the surface proximity to the leading edge. In detail, at the angle of attack of 0^o, these stabilising effects are equally present on both pressure and suction surfaces. When raising the angle of attack from 0^o to 5^o and 10^o, it is found that the stabilising effect becomes stronger on the suction surface than the pressure surface.

Table 4.2. Aerodynamic damping at different angles of attack.

Solution Method	**AoA=0º**	**AoA=5º**	**AoA=10º**
Frequency Domain Solution Method	0.39	0.40	0.41
Time Domain Solution Method	0.40	0.42	0.43

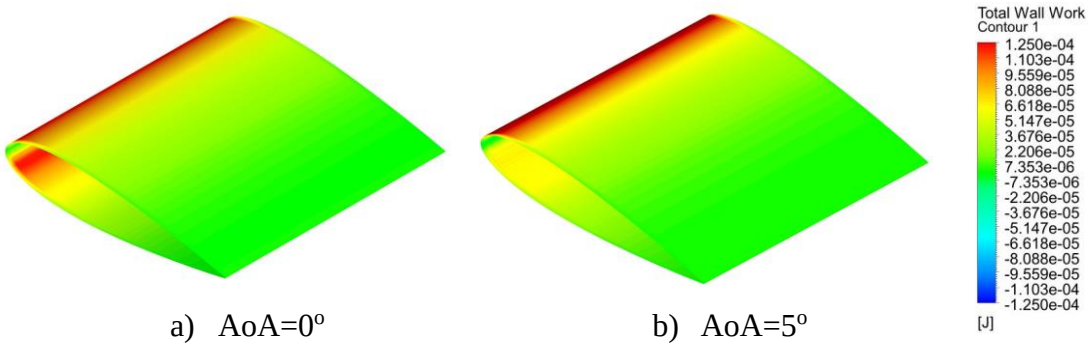

a) AoA=0^o b) AoA=5^o

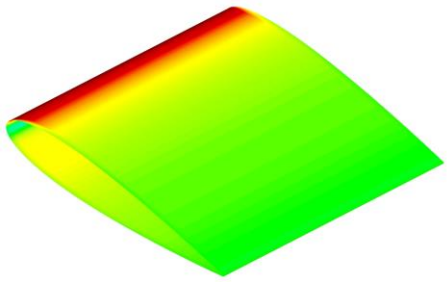

c) AoA=10^{o}

Figure 4.12. Total wall work contour on the aerofoil surfaces at different AoAs.

4.5.3. Aeromechanical Analysis of Aerofoil at Various Re Numbers

The aeromechanical simulations of the NACA0012 aerofoil at various Reynolds numbers are presented in this section. The Reynolds numbers are varied from 4×10^5 to 4×10^6, and their effects on the unsteady pressure distributions and the aerodynamic damping are investigated. The required Reynolds numbers are obtained by varying the inflow speed. The mesh is carefully generated to ensure that the dimensionless wall distance, y^+ value, remains below one at all Reynolds numbers studied in this chapter. These simulations are performed based on an angle of attack of 10^{o} because this represents a relatively large angle of attack typically found in wind turbines. Figure 4.13 plots the time-averaged pressure coefficient and the unsteady pressure amplitude coefficient distributions at different Reynolds numbers. It is seen that the time-averaged pressure coefficient distribution is relatively the same at all Reynolds numbers. In terms of the unsteady pressure coefficient distribution, the maximum value is found at the leading edge where the flow interacts with the oscillating aerofoil. A great difference in unsteady pressure difference, however, is observed over the aerofoil at each Reynolds number. At Re = 4×10^5, The unsteady pressure amplitude coefficient gradually rises approximately from X/C=0.1 and reaches its second peak at around X/C=0.5, which then slowly drops. This indicates that the unsteady pressure fluctuation is high along the chord of the aerofoil at lower Reynolds numbers. This is because the boundary layer is affected by the adverse pressure gradient and therefore, the flow separation and vortex generation due to flow recirculation on the suction surface become larger at lower wind speeds. The separation significantly affects the pressure variation on the aerofoil surfaces. When the Reynolds number is increased to 8×10^5, a similar rising pattern of unsteady pressure and the behaviour of fluctuations are observed; however. the amplitude at X/C=0.5 is much smaller than that of Re = 4×10^5. Raising the Reynolds number further reduces this behaviour of unsteady pressure distribution along the chord. At Re = 2×10^6 and Re = 4

$\times 10^6$, the unsteady pressure distribution along the aerofoil is similar; however, the amplitude is slighter lower at Re = 4×10^6 than that of Re = 2×10^6. Physically, increasing wind speeds, thereby achieving higher Reynold numbers, reduces the size of the boundary layer separation as the flow is more resistant to separation at higher wind speeds. These observations indicate that the unsteady pressure fluctuation is affected by Reynolds numbers as the pressure variation over the aerofoil surfaces is related to the wind speeds.

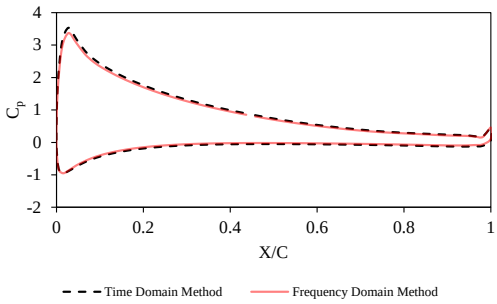

a) C_p at Re = 4×10^5

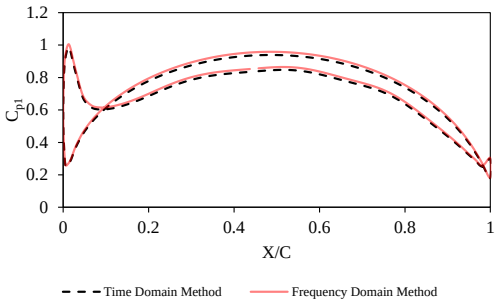

b) C_{p1} at Re = 4×10^5

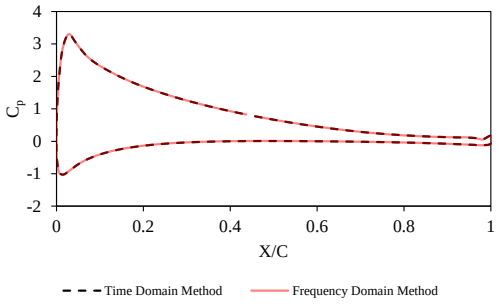

c) C_p at Re = 8×10^5

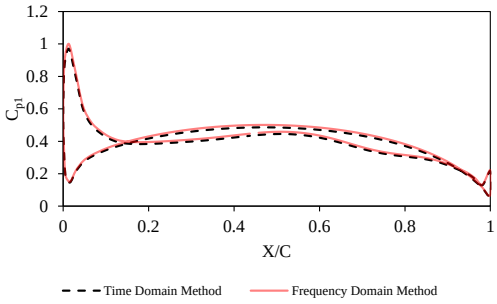

d) C_{p1} at Re = 8×10^5

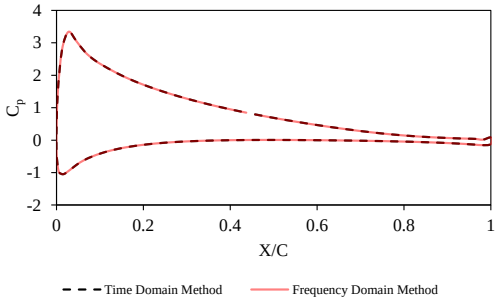

e) C_p at Re = 2×10^6

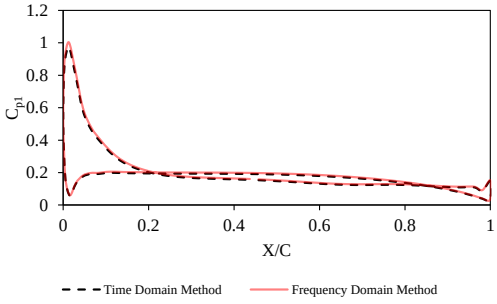

f) C_{p1} at Re = 2×10^6

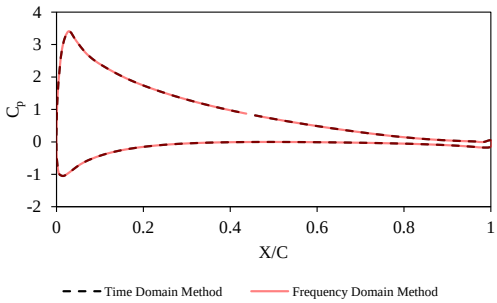

g) C_p at Re = 4×10^6

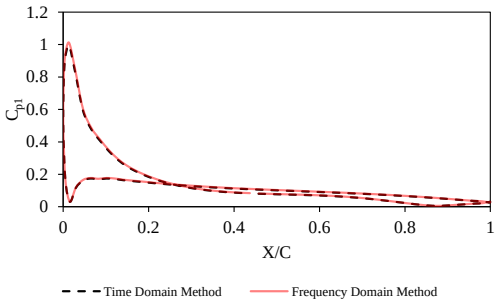

h) C_{p1} at Re = 4×10^6

Figure 4.13. Time-averaged pressure coefficient (C_p) and unsteady pressure amplitude coefficient (C_{p1}) at different Reynolds numbers.

Figure 4.14 presents the instantaneous pressure contours for different Reynolds numbers. The contours are plotted using dimensionless pressure. It is observed that the pressure difference between the pressure and suction surfaces is larger at Re = 4×10^5 than that of any other cases. The pressure is stronger on the pressure face and is lower on the suction surface. Compared to other Reynolds numbers, the pressure on the pressure surface is also much higher at Re 4×10^5. Raising the Reynolds number reduces the pressure difference between the two surfaces of the aerofoil. At Re = 2×10^6 and Re = 4×10^6, the pressure distribution is similar in both cases; the pressure difference is stronger at lower Reynolds numbers.

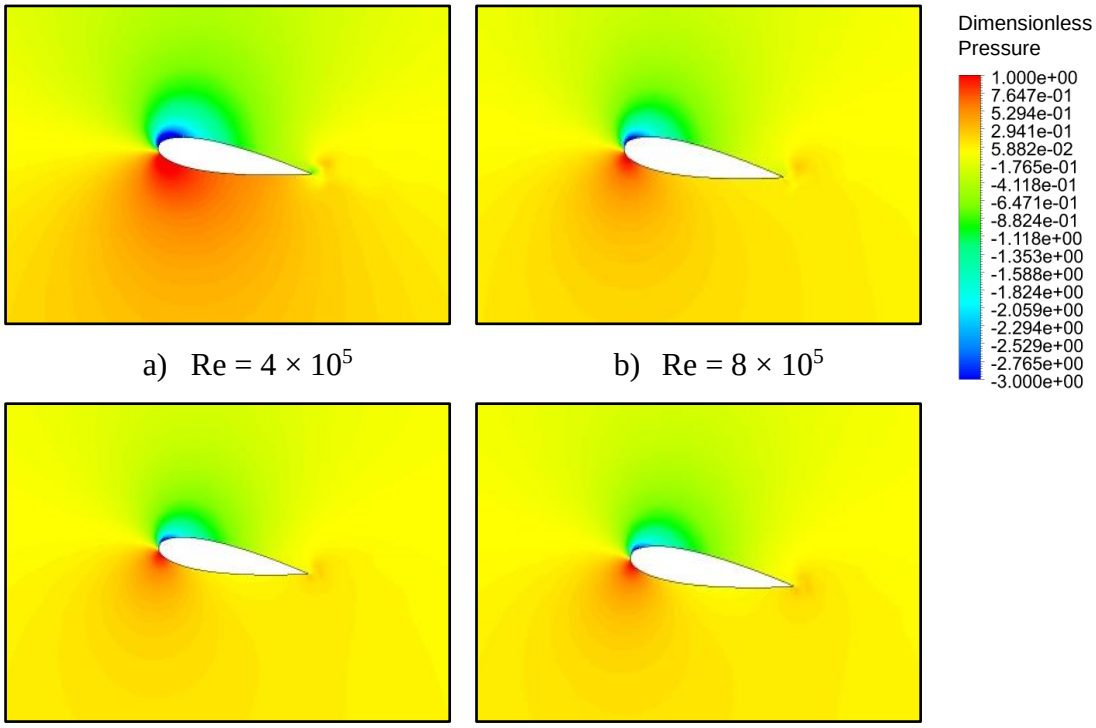

a) Re = 4×10^5 b) Re = 8×10^5

c) Re = 2×10^6 d) Re = 4×10^6

Figure 4.14. Instantaneous dimensionless pressure contours at different Re numbers.

The effect of the Reynolds number on the flow field around the aerofoil can be visualised in terms of velocity distributions. The instantaneous dimensionless velocity contours around the aerofoil at different Reynolds numbers are demonstrated in Fig. 4.15. These velocity distributions are based on an oscillating blade aerofoil which majorly disturbs the flow around the aerofoil. It is observed that the flow unsteadiness is higher at lower Reynolds numbers whereas the flow separation is reduced at higher Reynolds numbers. The flow remains attached to the pressure surface and separates from the suction surface when the Reynolds number is 4×10^5, and the flow separation is developed on the suction surface before shedding from the trailing edge. As the flow separation and vortex generation process continue, the separated shear layers from the suction surface combine with the flow structures from the pressure surface, which leads to vortex shedding from the trailing edge of the aerofoil. As a result, the flow becomes unsteady and turbulent downstream of the trailing edge. The vortex structures left from the trailing edge are similar to the Karman vortex. Raising Reynolds number to Re = 8×10^5 increases the separation resistance of a turbulent boundary layer and reduces the flow turbulence on the aerofoil surfaces. Formation of the laminar vortex shedding and the laminar to turbulence transition near the trailing edge can still be seen at this Reynolds number, however, the vortex shedding frequency is smaller than that of Re = 4×10^5. In contrast

to the Reynolds number of Re = 8 × 10^5, the size of the laminar vortex shedding is much smaller, almost undetectable with the URANS model, at Re = 2 × 10^6. The behaviour of vortex shedding is completely undetected at Re = 4 × 10^6 as the flow becomes much stronger at higher Reynolds numbers, which ultimately reduces the separated shear layers and flow recirculation. The turbulent boundary layer also becomes uniform at higher Reynolds numbers. The conclusions can be drawn from these observations that the size of flow separation can be reduced by increasing Reynolds number and the flow is more unsteady with laminar vortex shedding at lower Reynolds numbers.

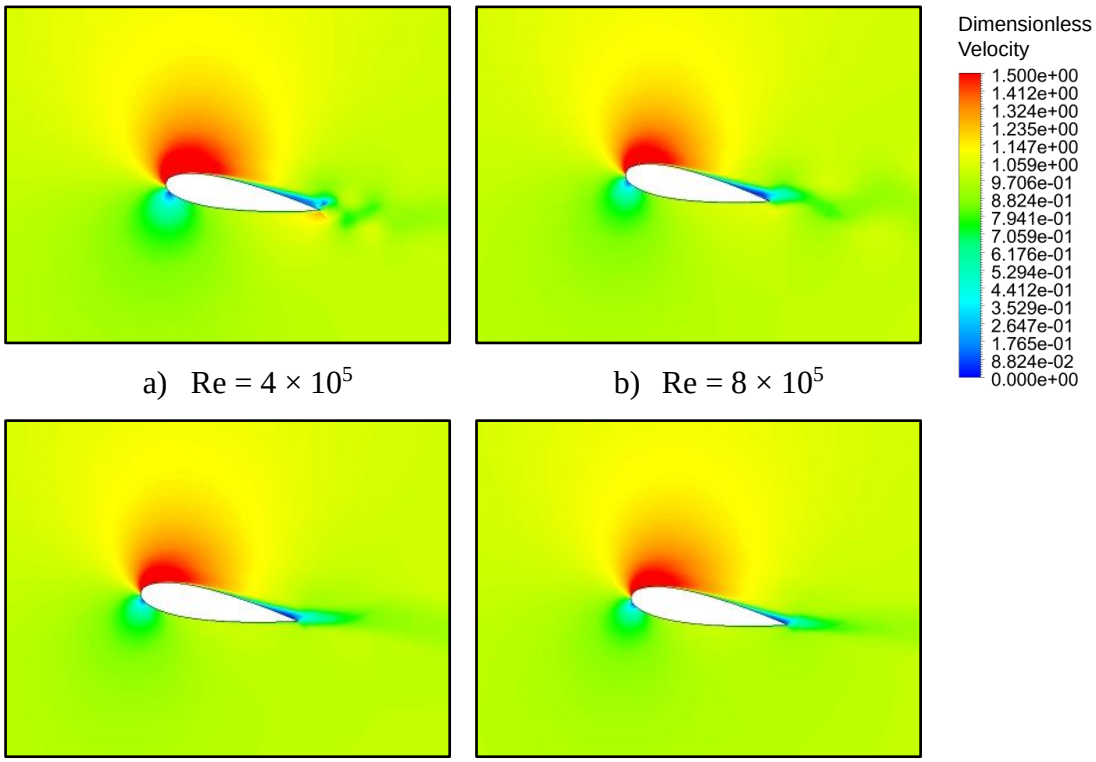

a) Re = 4 × 10^5 b) Re = 8 × 10^5

c) Re = 2 × 10^6 d) Re = 4 × 10^6

Figure 4.15. Instantaneous dimensionless velocity contour at different Reynolds numbers.

Figure 4.16 illustrates the velocity streamlines around the aerofoil at different Reynolds numbers, which provides further information on the flow behaviour when interacting with the aerofoil. The dimensionless velocity is used for a direct comparison between different Reynolds numbers. The behaviour of flow recirculation is noticed in the flow separation zone at Re = 4 × 10^5, 8 × 10^5 and 4 × 10^6. They are stronger at lower Reynolds numbers. Vortex shedding from the trailing edge of the aerofoil is also identified at lower Reynolds numbers. At the Reynolds number of 4 × 10^6, the flow is most attached to the aerofoil surfaces with some separation near the trailing edge. This is another indication that the

flow separation is reduced by increasing the Reynolds number as expected because the flow is more resistant to detachment and the boundary layer is less affected by the adverse pressure gradient at higher wind speeds compared to lower wind speeds.

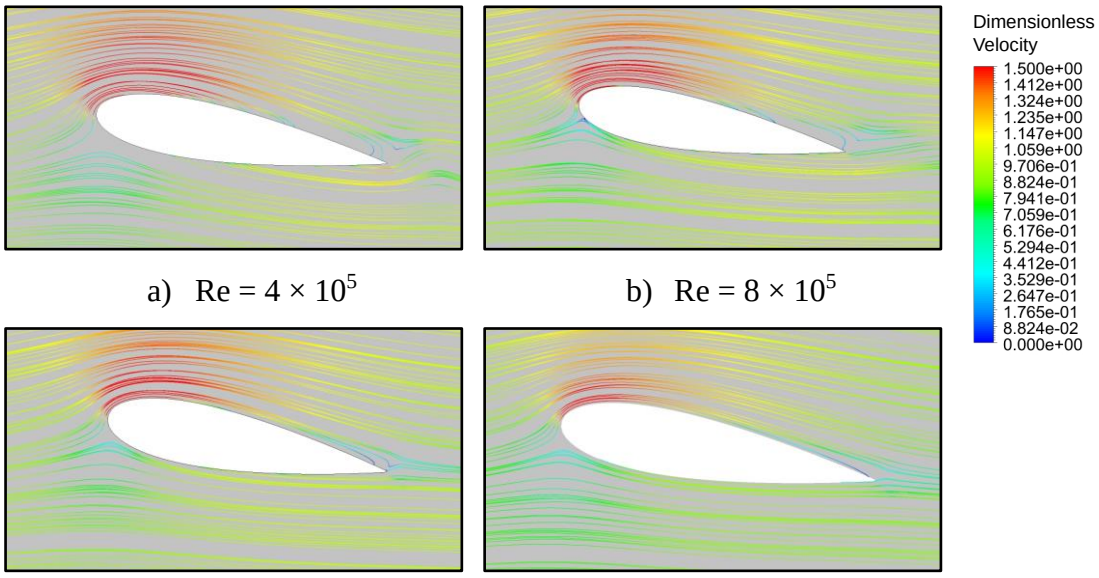

a) Re = 4×10^5 b) Re = 8×10^5

c) Re = 2×10^6 d) Re = 4×10^6

Figure 4.16. Instantaneous dimensionless velocity streamlines at different Reynolds numbers.

Similar to the previous analyses for various angles of attack, the aerodynamic damping values are also calculated to investigate the effect of different Reynolds numbers on the aeroelasticity parameter of the blade aerofoil. Likewise, the aerodynamic damping values are computed using both frequency domain and time domain methods. The results are compared to each other to validate the frequency domain solution method. It is found that the results obtained from the frequency domain solution are in close agreement with the conventional time domain solution (See Table 4.3). In terms of the effect of Reynolds number, it is seen that, although the aerodynamic damping values are positive at all Reynolds numbers, the aerodynamic damping is relatively low at Re = 4×10^5 and 8×10^5, which gradually increases when raising the Reynolds number to 2×10^6. At Re = 4×10^6, the aerodynamic damping is larger than that of Re = 2×10^6 by 56% and that of Re = 2×10^6 by 88%. This is a clear indication that the blade stability is more affected by the flow unsteadiness due to the blade vibration at lower Reynolds numbers. This observation is also consistent with the velocity contours and streamlines. As discussed, the flow unsteadiness is higher due to vortex generation at lower Reynolds numbers. The vortex generation and the pressure fluctuation, as previously seen, impose aerodynamic loads on

the blade structure. As the blade gains energy from the flow, it is possible that the blade vibration could lead to flutter instability when the aerodynamic damping is not sufficient enough to damp the vibration. Therefore, the selection of operating conditions including Reynolds numbers is very important for the design process of the offshore wind turbine blades.

The simulations discussed in the chapter are all performed on the same computer using the same computational resources. In terms of the computational cost, the frequency domain solution method is significantly more efficient than the conventional time domain solution method, and the computation time is reduced by 90% using the frequency domain method.

Table 4.3. Aerodynamic damping at different Reynolds numbers.

Method	**Re=4×10^5**	**Re=8×10^5**	**Re=2×10^6**	**Re=4×10^6**
Frequency Domain Solution Method	0.05	0.08	0.18	0.41
Time Domain Solution Method	0.07	0.10	0.20	0.43

4.6. Summary of the Chapter

The aeromechanical analyses of a wind turbine blade aerofoil, NACA0012, at various angles of attack and Reynolds numbers, are presented in this chapter. The proposed frequency domain solution method is first applied to the aeroelasticity analysis of a linear turbine cascade for validation purposes. It is revelated that the results are in very good agreement with the experiment. Moreover, the CFD model of the wind turbine aerofoil is validated against the experiment for various angles of attack. It is found that the numerical results and the experimental results are in close agreement.

Using the validated CFD model, the aeromechanical simulations of this aerofoil at the angles of attack of 0^o, 5^o, and 10^o are performed by integrating the blade vibration in the flow simulation. At the angle of attack of 10^o, small flow separation is detected on the suction surface of the aerofoil near the trailing edge. In terms of blade stability, the blade vibration is considered stable at all angles of attack as the aerodynamic damping values are positive. Only a slight difference is seen between different angles of attack with the maximum value found at 10^o. A dominant stabilising effect is detected at all angles, especially near the leading edge. Having analysed the effect of different angles of attack on the aeroelasticity parameters, further flow simulations are conducted using various

Reynolds numbers. It is observed that the unsteady pressure fluctuations along the chord length are higher at lower Reynolds numbers. Pressure contours indicate that the pressure on the pressure surface of the aerofoil at $Re = 4 \times 10^5$ is higher than that of any other cases. Flow visualisations using velocity contours and flow streamlines show that the laminar vortex shedding is identified at lower Reynolds numbers, clearly at $Re = 4 \times 10^5$ and 8×10^5. The flow separation and recirculation in the separation zone are also detected on the suction surface at these Reynolds numbers. This behaviour is reduced when raising the Reynolds number, as the flow is mostly attached to the surface with a small separation near the trailing edge. Results indicate that the aerodynamic damping is relatively low at $Re = 4 \times 10^5$ and $Re = 8 \times 10^5$. The aerodynamic damping is increased as the Reynolds number is raised, and it is the highest at $Re = 4 \times 10^6$.

Overall, an excellent agreement is obtained between the proposed frequency domain and time domain solution methods throughout the analysis. However, the frequency domain solution method solves significantly faster than the time domain solution method by 90%. Therefore, it is concluded that the frequency domain solution method is highly efficient, and it can be reliably used for the aeromechanical analysis of wind turbine blades.

Chapter 5. Aerodynamic and Aeromechanical Analysis of a Wind Turbine Rotor

The aerodynamic simulations of wind turbines are typically carried out using a steady inflow condition. However, the aerodynamics and aeroelasticity of wind turbine blades can be significantly affected by inflow wakes due to the environmental conditions or the presence of neighbouring wind turbines. In this chapter, the effects of flow unsteadiness on the aerodynamics and aeroelasticity of the wind turbine rotor are investigated. It is expected that the unsteadiness of the wake can have an impact on the aerodynamic flow field around the wind turbine rotor and it could also influence the aeroelasticity of the wind turbine. The computational cost of high-fidelity aerodynamic and aeroelasticity simulations of wind turbines remains the main challenge for the research industry. One of the distinctive features of the present work is the application of the highly efficient nonlinear frequency domain solution method for modelling harmonic disturbances for the aerodynamic and aeromechanical analysis of wind turbines. A test case wind turbine is selected for the aerodynamic and aeromechanical analysis as well as for the validation of the method used. The effects of different material properties along with a large vibration amplitude on the aeroelasticity parameter known as aerodynamic damping of the wind turbine blade are also investigated in the present work. Compared to the conventional time domain solution methods, which require prohibitively large computational costs for modelling and solving aerodynamics and aeroelasticity of wind turbines, the proposed frequency domain solution method can reduce the computational cost by one to two orders of magnitude. The results obtained in this analysis provides an understanding of the flow around a wind turbine subject to unsteady aerodynamic loads, and the proposed computational method can be applied to the analysis of large offshore wind turbines at an affordable computational cost.

5.1. Physical Description

The MEXICO Experiment is a wind tunnel experiment that was performed in the German-Dutch Wind Tunnel (DNW) [80-83]. The blade is 2.04 m long and the rotor diameter is 4.5 m. The wind turbine has a three-bladed rotor, and the blade design is based on three aerodynamic profiles such as DU91-W2-250, RISO-A1-21, and NACA 64-418. Numerical simulations have also been conducted previously on this wind turbine [179-183]. The wind speed and the rotational speed selected in this study are 15 m/s and 424.5

RPM, respectively, and the blade pitch angle is -2.3 degrees. The CFD model used in this study is first validated against the experimental data. The proposed nonlinear frequency domain solution method is employed for both aerodynamic and aeromechanical analysis of this wind turbine. Due to the lack of experimental data or previous studies for the types of unsteady analysis discussed in this study, the conventional time domain solution method is used for validation purposes. For the aeromechanical analysis, the modal analysis is conducted before the flow simulation and the natural frequencies and the structural mode shapes are extracted from the modal analysis. To investigate the effect of material properties on the aeroelasticity of the blade. two different materials are considered and used in this study. The first one is an Aluminium Alloy with a density of 2770 kg/m^3, Young's modulus of 7.1×10^{10} Pa, and a Poisson ratio of 0.27 to be similar to the one used in the experiment. The other one is a composite material, approximated by the orthotropic material properties as presented in Table. 5.1, as modern wind turbines are designed using composite materials which can reduce weight. It should be noted that the main purpose of this analysis is to investigate the effect of material properties on the aeroelasticity parameter, especially the aerodynamic damping, of the blade. The material properties used in this study are approximations and may not necessarily represent the actual properties used for commercial wind turbine blades.

Table 5.1. Orthotropic material properties of the composite material.

Density (kg/m^3)	1550
Young's Modulus-X (Pa)	1.1375×10^{11}
Young's Modulus-Y (Pa)	7.583×10^{9}
Young's Modulus-Z (Pa)	7.583×10^{9}
Poisson's Ratio-XY	0.32
Poisson's Ratio-YZ	0.37
Poisson's Ratio-XZ	0.35
Shear Modulus-XY (Pa)	5.446×10^{9}
Shear Modulus-YZ (Pa)	2.964×10^{9}
Shear Modulus-XZ (Pa)	2.964×10^{9}

5.2. Computational Description

The three-dimensional computational domain and grid are created using a Rounded Azimuthal O4H topology in a structured grid generator. The grid consists of five blocks. An O-mesh is used in the skin block surrounding the blade whereas an H-mesh is used in

other blocks such as the inlet block, the outlet block, the upper block above the blade section and the lower block under the blade section. The first layer's thickness is 10^{-5} meters to keep the y^+ value less than one. The flow inlet and outlet are located 10R upstream of the rotor and 25R downstream of the rotor, respectively, and the far-field boundary is placed 5R from the origin of coordinates where R is the rotor radius. After a grid independence study, the selected grid involves 4.5 million grid points in a single passage domain which is 1/3 of the full rotor model. The computational domain of a single passage, the mesh around the blade in the blade-to-blade view and the 3D view of the mesh of the blade are shown in Fig. 5.1. A single passage domain (i.e., 120^o grid) is used for the frequency domain method whereas a full passage domain (i.e., 360^o grid including all three blades) is used for the time domain method.

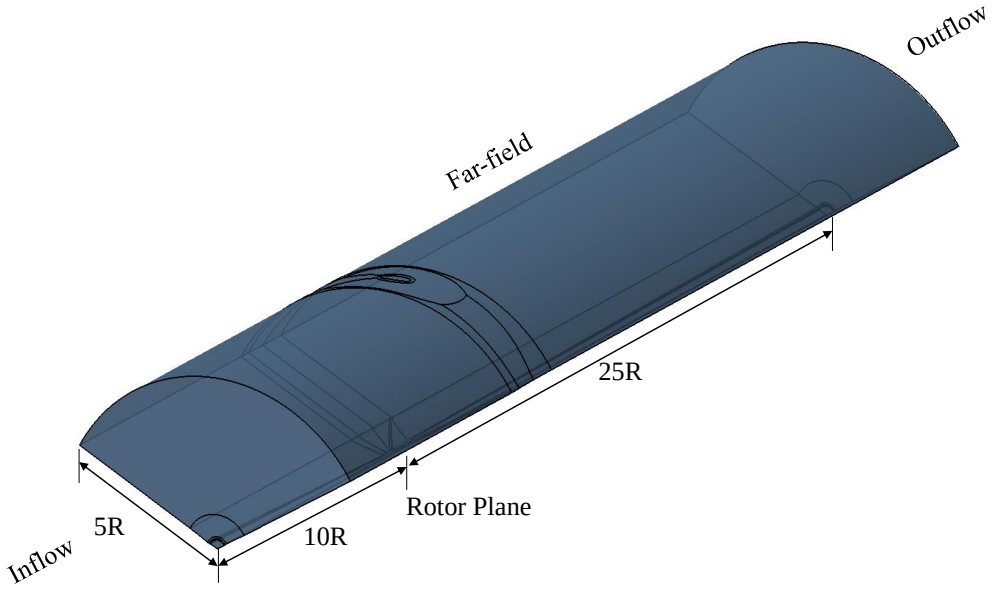

a) Computation domain

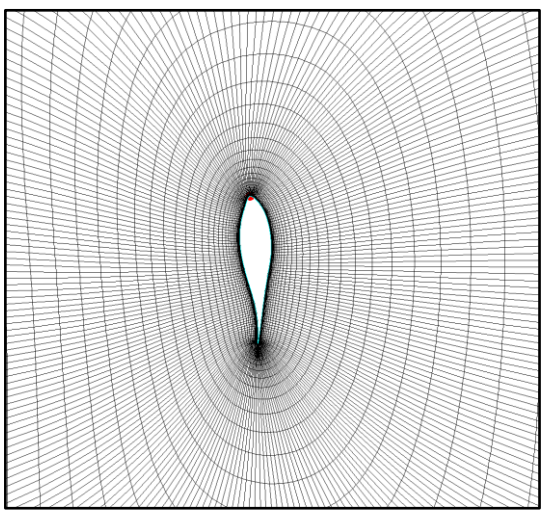

b) Blade-to-blade view

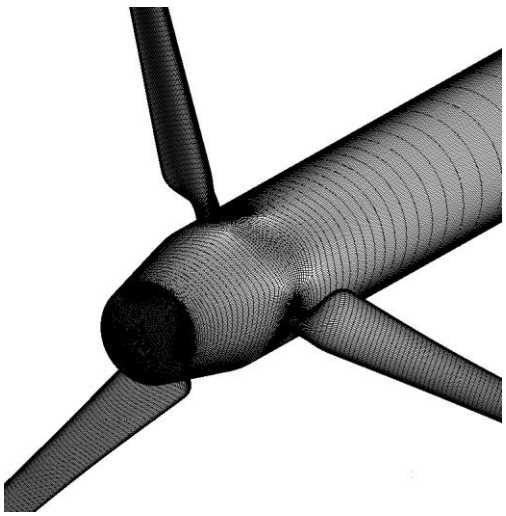

c) 3D view

Figure 5.1. Computational domain, the blade-to-blade view and 3D view of the mesh.

The solid wall boundary condition is applied to the blade and the hub. A stationary wall boundary is defined in the aerodynamic analysis whereas the deforming wall boundary with a periodic displacement is defined in the aeromechanical analysis. In the case of the aeromechanical simulation, the global displacement of the blade structure is obtained based on the specified generalised displacement and the imported natural frequency and the mode shape. Hence, the global displacement of the blade becomes:

$$d(t) = \bar{d} + d_A \cos(\omega_i t) \tag{5.1}$$

where $\bar{d}$ and d_A are the mean value and amplitude of the blade displacement, and the blade wall boundary is deformed with respect to the blade displacement.

The external boundary condition, also known as a far-field boundary, is defined on the far-field boundaries dealing with the external flow computations. A full rotor model with all three blades without using periodic boundaries is used for the time domain method. On the other hand, a single passage domain is used for the frequency domain solution method, and the harmonic components are phase-shifted between the periodic boundaries by a given Inter Blade Phase Angle (IBPA), σ, as expressed in the following equations [164, 165] where the subscript 1 and 2 are corresponding to the referenced passage and its neighbouring one, respectively.

$$A_{U,2} = A_{U,1} \cos(\sigma) - B_{U,1} \sin(\sigma) \tag{5.2.a}$$

$$B_{U,2} = A_{U,1} \sin(\sigma) + B_{U,1} \cos(\sigma) \tag{5.2.b}$$

In this chapter, the flow simulation is carried out using NUMECA FINE/Turbo and the structural simulation is conducted using ANSYS Mechanical. The fluid and structural governing equations are provided in Chapter 3 (refer to Sections 3.1 and 3.5). The nonlinear frequency domain solution method, proposed in Section 3.4, is employed to perform the aerodynamic and aeromechanical simulations. The modal coupling method, presented in Section 3.5, is applied to the modelling and simulation of fluid-structure interaction.

The majority of the previous studies considered a steady wind flow for the simulations, while in reality, the nature of the wind is not steady. The wind speed changes in time or

is affected by the objects present in the surroundings such as nearby wind turbines. The flow unsteadiness can impose a significant impact on wind turbine aerodynamics or aeroelasticity. In order to consider the unsteady nature of inflow, a wake is introduced at the inlet to study its effects on the aerodynamics of the wind turbine rotor. In this study, a harmonic wake is considered to represent the unsteady nature of the wind of which the speed varies in time. The inflow wind speed, *w*, is generated based on the Fourier series as follow.

$$w = \bar{w} + w_A \sin(\omega_w t) \tag{5.3}$$

where $\bar{w}$ is the averaged wind speed, w_A is the amplitude of the unsteady fluctuation, and ω_w is the frequency of the wake. For the purpose of simplicity and validation of the proposed method, only one harmonic is used to implement the harmonic inflow wakes in this study. The number of harmonics can be further increased to better represent the actual wind condition. In this analysis, the averaged wind speed is the same as the steady simulation which is 15 m/s and the amplitude of 5 m/s is selected to cover a wide range of wind speeds as well as to investigate the effect of relatively high fluctuations. Four frequencies, 5 Hz, 10 Hz, 15 Hz and 20 Hz, are considered for the wake frequencies in this work, and the effects of each frequency on the aerodynamics of the wind turbine rotor are investigated. The reason behind the selection of wake frequencies and amplitude is to investigate the effects of a wide range of frequencies at a relatively high amplitude of fluctuation on the aerodynamics of a wind turbine rotor. These frequencies cover a wide range of inflow frequencies, and their effects can be thoroughly analysed. The nonlinear frequency domain method is used for this analysis, and the results are validated against the time domain method. This marks one of the distinctive features of this project as the majority of studies available in the literature are based on a steady inflow, and in addition, this is the first time that the nonlinear frequency domain method is used to analyse the aerodynamics of a wind turbine based on the inflow wake.

The aeromechanical analysis of the selected wind turbine is performed by integrating the blade vibration in the flow simulation. Before performing the CFD simulations, the modal analysis is conducted using an FEA method to compute the natural frequencies and the structural mode shapes of the blade. The first vibration mode is selected for the mode of vibration of the blade and prescribed in the CFD simulation for the aeroelasticity analysis. The shape of the first vibration mode of the blade is presented in Fig. 5.2. The first natural

frequencies of the blade using an Aluminium Alloy and composite material, obtained from the modal analysis, are 15.611 Hz and 6.82 Hz, respectively. The material properties used to model the Aluminium Alloy and composite material blade are provided in Section 5.1. The frequency domain solution method combined with a phase shift solution method is applied for the aeromechanical analysis of the wind turbine for the considered IBPA value. It is understood that the experimental data for this analysis are not available and thus, the frequency domain solution method is validated against the time domain solution method. For the blade vibration, the first vibration mode is prescribed in which the first natural frequency is defined to be the vibration frequency. In the aeromechanical analysis of turbomachines, relatively small amplitudes are typically used. However, previous studies suggest that the deflection of the blade can be up to 9% of the blade span [171]. Therefore, a relatively large amplitude of 9% of the span is used in this study. In order to highlight the capability of phase-shifting between the blades of the proposed numerical method and investigate the blade vibration with a different phase angle between the rotor blades, the IBPA for this simulation is set to 120^{o}.

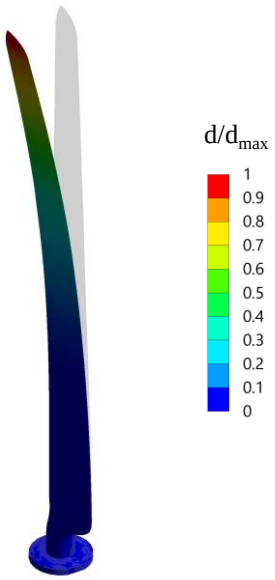

Figure 5.2. First vibration mode of the MEXICO wind turbine blade.

5.3. Results and Discussions

5.3.1. Aerodynamic Analysis of the Wind Turbine Rotor

The steady pressure coefficient distributions using a steady inflow are first compared against the experiment as well as the previous simulation performed by Sorensen et al. [179] to validate the CFD model used. Figure 5.3 presents the comparison of the steady pressure coefficients extracted at 25%, 35%, 60%, 82% and 92% span blade sections. As

seen, slight differences are seen between the CFD simulations and the experiment at the blade inner sections, 25% and 35% blade span, due to the pressure transducers related problem. It was reported in the technical reports of the experiment that there was instability in the pressure transducers, occurred at 25% and 35% span sections, during the experiment and the results at 60%, 82% and 92% span sections are more reliable [80, 81]. In fact, this problem was also discussed in [179, 180]. Overall, the present simulation results are very close to those of Sorensen et al. [179] and they are in good agreement with the experiment.

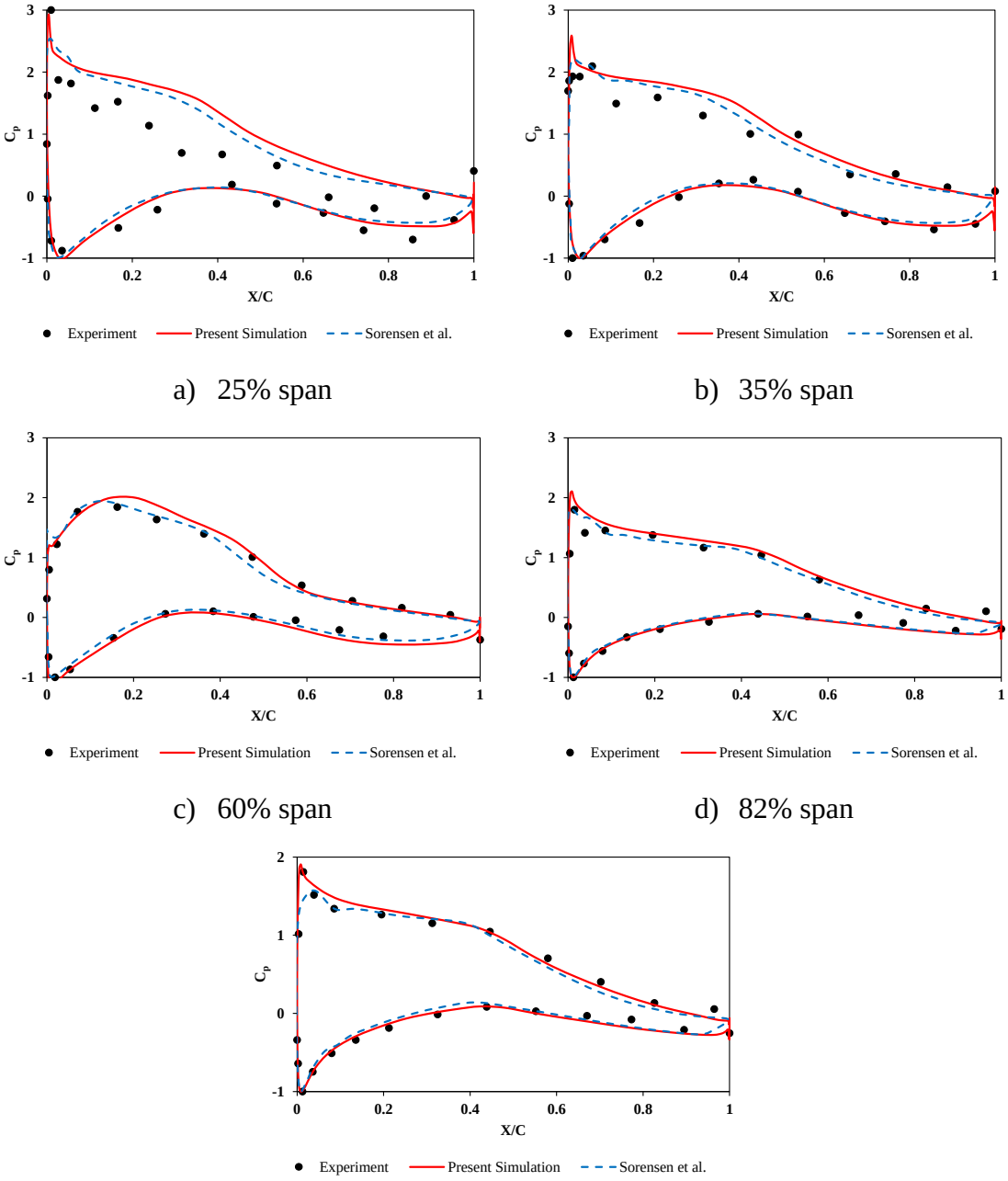

a) 25% span

b) 35% span

c) 60% span

d) 82% span

e) 92% span

Figure 5.3. Steady pressure coefficient distributions at different sections of the blade.

After having validated the CFD model used, a series of further simulations are conducted generating inflow wakes at different frequencies at the inlet. Unsteady pressure distribution can be divided into time-averaged value and amplitude of fluctuation, and it can be written as:

$$P = \bar{P} + P_A \sin(\omega t) + P_B \cos(\omega t) \tag{5.4}$$

where $\bar{P}$ is the time-averaged pressure, and P_A and P_B are Fourier coefficients. The unsteady pressure amplitude can be defined as $\sqrt{{P_A}^2 + {P_B}^2}$.

The unsteady pressure terms are only visible in the harmonic inflow cases, as the harmonic disturbances are present due to the wake. Figure 5.4 presents the comparisons of the time-averaged pressure coefficient C_p and the unsteady pressure amplitude coefficient C_{p1} distributions at the blade mid-span section for each frequency computed from both time domain and frequency domain methods. As seen, they are in very good agreement in both perspectives. It is also noticed that the unsteady pressure distributions vary with different inflow wake frequencies which indicates that the flow unsteadiness due to the wake depends on the frequency. It is observed that the amplitude of unsteady pressure distribution is maximum at the leading edge and is reduced by approximately 80% on both surfaces of the blade at X/C=0.2. Some small deviations in unsteady pressure amplitude are seen on the suction surface at around X/C=0.4. This is due to the building up of vorticity structures on the suction surface of the blade. No difference is seen between different frequencies in terms of the time-averaged pressure coefficients. This is expected as the same average wind speed is used and hence the mean value of pressure distributions could be similar to each other. Good agreements between the two methods are also observed at the other blade sections.

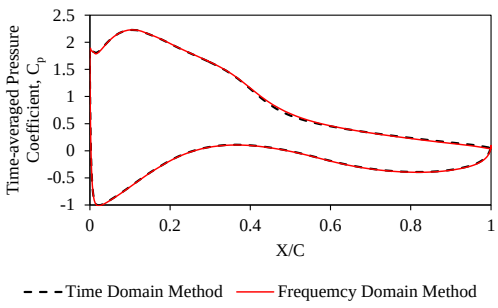

a) C_p at 5 Hz

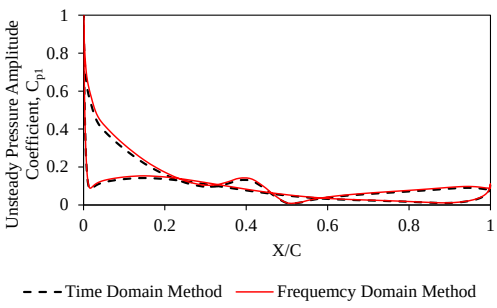

b) C_{p1} at 5 Hz

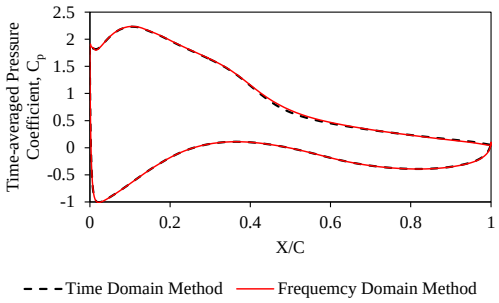

c) C_p at 10 Hz

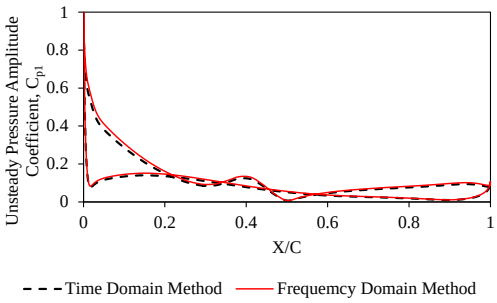

d) C_{p1} at 10 Hz

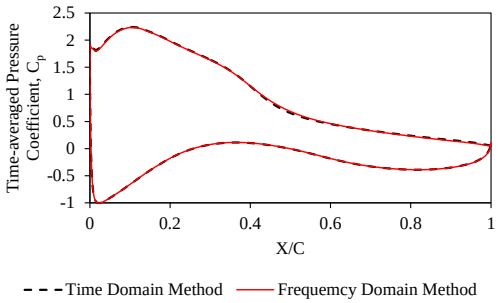

e) C_p at 15 Hz

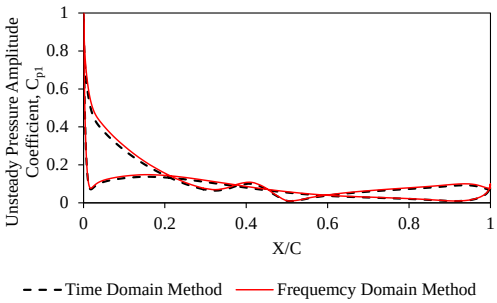

f) C_{p1} at 15 Hz

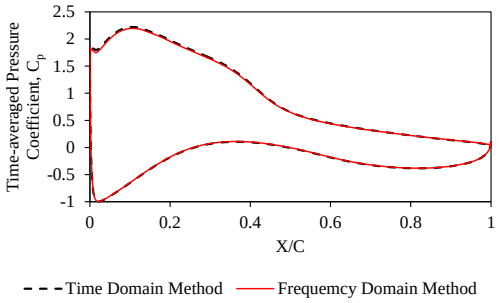

g) C_p at 20 Hz

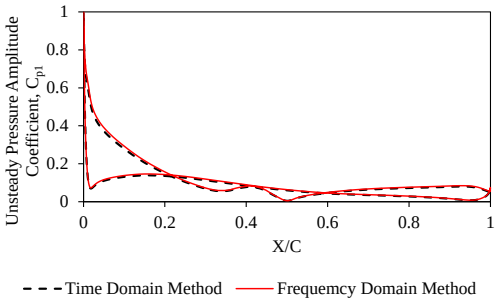

h) C_{p1} at 20 Hz

Figure 5.4. Time-averaged pressure coefficient (C_p) and unsteady pressure amplitude coefficient (C_{p1}) at different wake frequencies.

It is now evident that the frequency domain method can be used for the computation of unsteady pressure distribution on the blade surfaces subject to inflow wakes. However, it is also important to analyse the pressure field around the rotor. The pressure coefficient profiles along the rotation axis from one rotor diameter upstream to one rotor diameter downstream at different frequencies computed from both methods are compared in Fig. 5.5. As shown, the results calculated from both methods agree well with each other. Therefore, it is concluded that the unsteady pressure distribution and the flow field around the wind turbine rotor can be reliably computed using the frequency domain method.

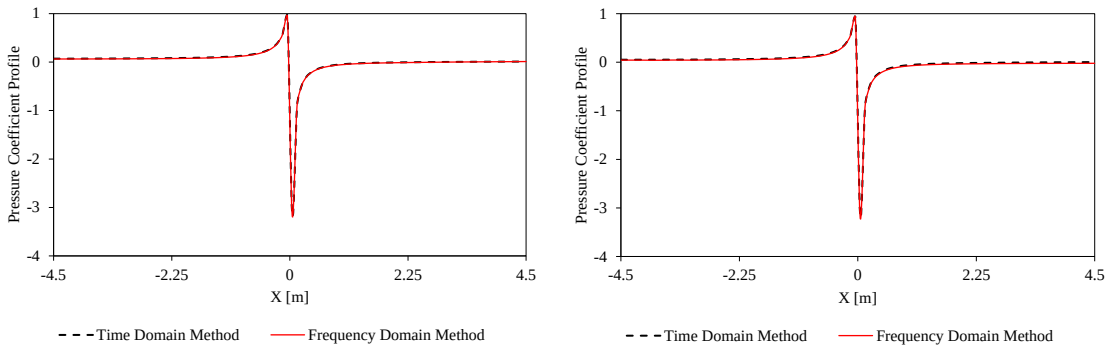

a) 5 Hz

b) 10 Hz

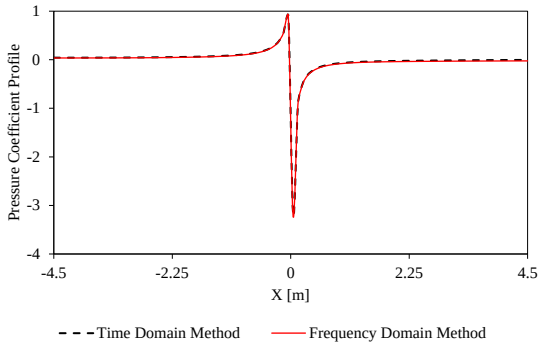

c) 15 Hz

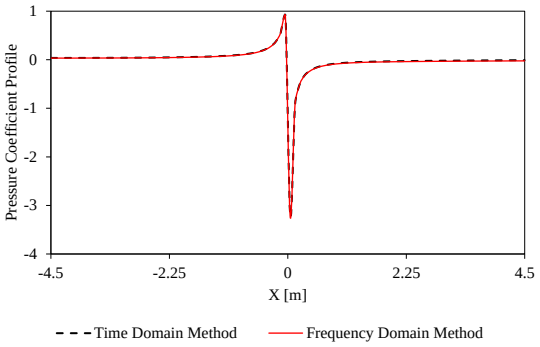

d) 20 Hz

Figure 5.5. Pressure coefficient profiles at different wake frequencies ('0' marks the rotor plane; negative axis and positive axis represent upstream and downstream of the rotor, respectively).

The effect of unsteadiness of the inflow wakes on the flow field around the rotor can be identified using the velocity magnitude contours in the meridional view as well as the blade-to-blade view. Figure 5.6 demonstrates the instantaneous velocity fields around the wind turbine rotor in the meridional view for the steady inflow case as well as the harmonic inflow cases. It is seen that the inflow wakes influence the flow around the rotor blades and affect the vortex shedding process. The vortex structures generated from the blades are disturbed by the wakes and thereby influencing the downstream wake behind the rotor. It is observed that the velocity fields behind the rotor are distorted by the inflow wakes whereas the flow field is steady in the steady inflow case. The flow unsteadiness is higher at lower frequencies which is in agreement with unsteady pressure distributions seen in Figs. 5.4. The vortex generation process is also influenced by the wakes as the velocity bubbles generated from the tip of the blade and the flow left from the blade and the hub differ with inflow wake frequencies. The flow unsteadiness and the effects of the wakes are visible at all frequencies; however, the velocity field behind the rotor is lower at 20 Hz compared to the flow fields at lower wake frequencies.

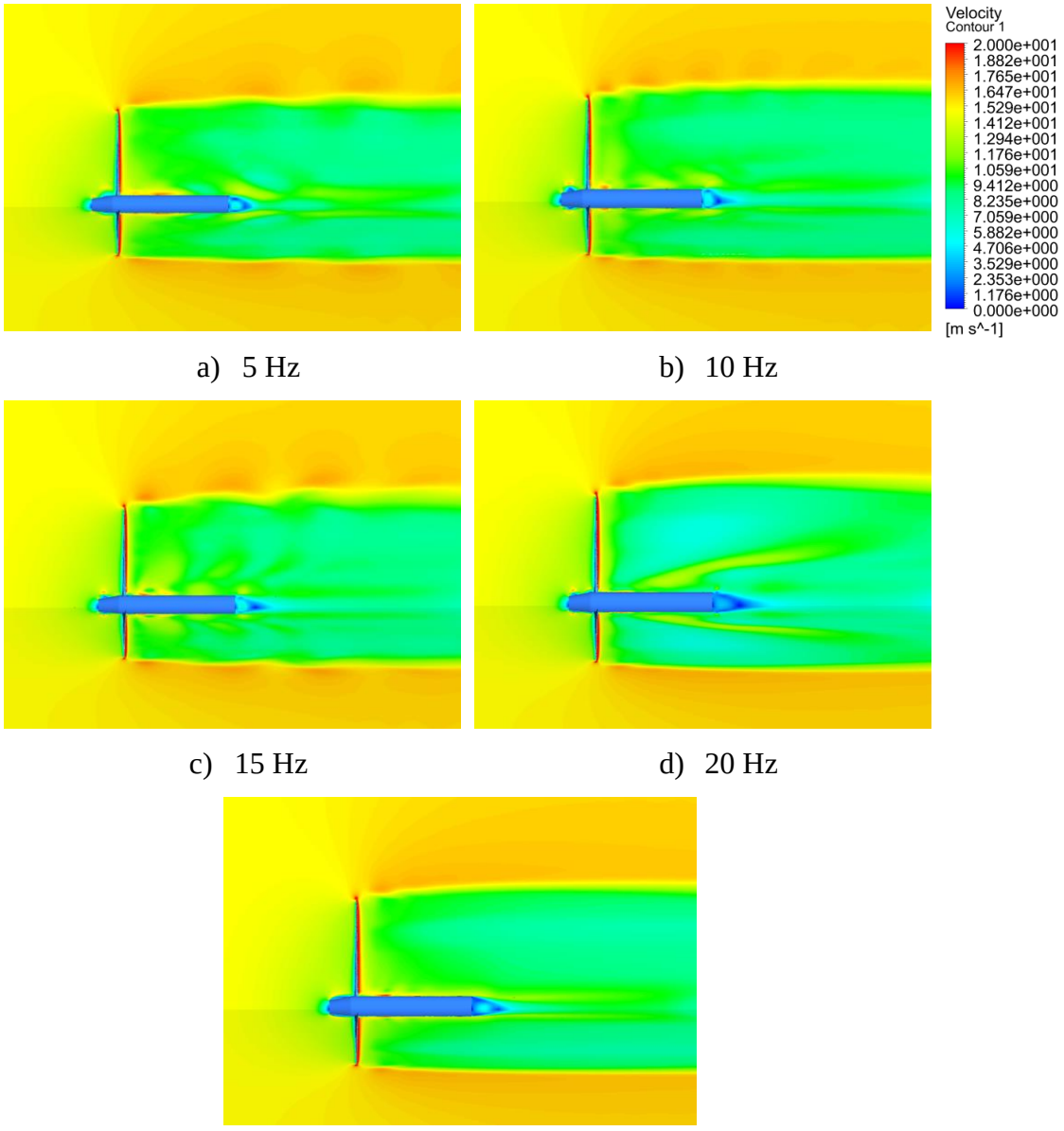

a) 5 Hz b) 10 Hz

c) 15 Hz d) 20 Hz

e) Steady inflow

Figure 5.6. Velocity fields in the meridional view from the harmonic inflow cases at different frequencies and the steady inflow case.

Figures 5.7 shows velocity distributions around the blade aerofoil at different wind speeds at the 25% span and 75% span, respectively, to investigate the effect of wind speed fluctuations on the flow. These two blade sections are chosen to represent the blade inner region, where it has a larger blade section pitch angle and the outer region with a lower blade pitch angle. In the blade inner region, flow separation from the suction surface of the blade is observed at higher wind speeds. However, the flow is mostly attached with a little separation near the blade trailing edge at lower wind speeds. Likewise, the separation is also larger at higher wind speeds in the blade outer region. The high-velocity

concentration is found near the leading and trailing edges. Compared to the blade inner region, the velocity magnitude is higher in the outer region.

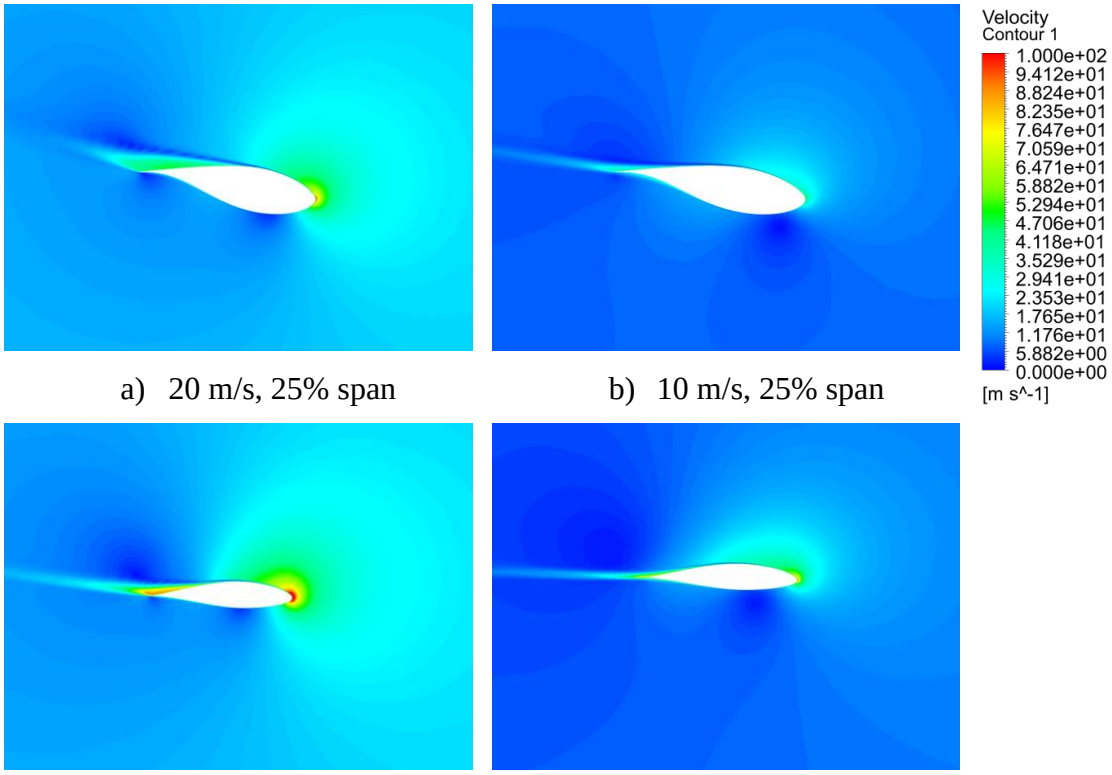

a) 20 m/s, 25% span b) 10 m/s, 25% span

c) 20 m/s, 75% span d) 10 m/s, 75% span

Figure 5.7. Velocity distributions in the blade-to-blade view at 25% span and 75% span sections when the wind speed at 20 m/s and 10 m/s.

Figure 5.8 illustrates the pressure contours in the blade-to-blade view for the selected two sections at relatively high and low wind speeds. The pressure is generally the highest near the leading edge where the relative wind velocity interacts with the blade aerofoil. Depending on the speed of the wind, the pressure distributions over the aerofoil surfaces change. At higher wind speeds, the high-pressure concentration is seen on the pressure surface near the leading edge whereas it is slightly shifted towards the leading edge when interacting with low wind speeds. The difference in pressure distribution between the two surfaces is higher at 20 m/s compared to that of 10 m/s. These differences in both velocity and pressure distributions, which are constantly changing in time, impose aerodynamic loads on the blade. Figure 5.9 presents the dimensionless force, denoted by F/F_{max} and calculated as *(Force Applied on Blade Surface – Average Force Applied on Blade Surface)/(Maximum Force Applied on Blade Surface)*, over the physical time of 0.5 sec obtained from different inflow cases. Due to the nature of the harmonic inflow wakes, loads of the blade are sinusoidal of which the frequencies are similar to that of the inflow

wakes whereas the loads are stable in the steady inflow case. The amplitude of the forces distributed over the blade surfaces also depends on the wake frequencies and it gets larger as the frequency increases. This is because the inflow wakes produce additional flow disturbances and vortex structures on the blade surfaces, and the intensity of the vortex generation is stronger at higher wake frequencies. Not only the aerodynamic loads could result in the blade structure vibration but also the resonance could occur when the wake frequency is close to the natural frequencies of the blade, which is dangerous for the blade and the wind turbine. Thus, it is also very important to analyse the aeroelasticity of the wind turbine rotor which will be discussed in the next section.

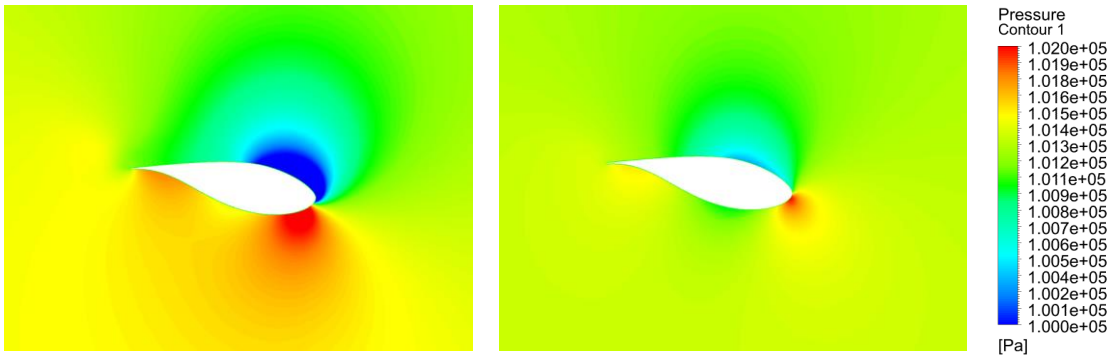

a) 20 m/s, 25% span b) 10 m/s, 25% span

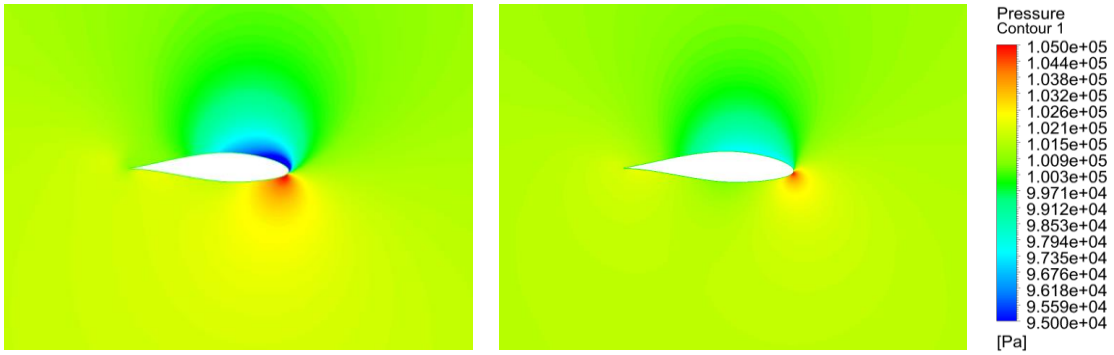

c) 20 m/s, 75% span d) 10 m/s, 75% span

Figure 5.8. Pressure distributions in the blade-to-blade view at 25% span and 75% span sections when the wind speed at 20 m/s and 10 m/s.

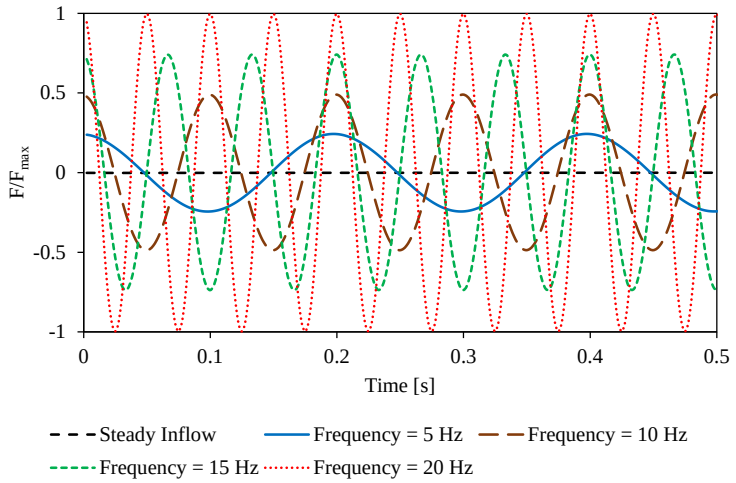

Figure 5.9. Coefficients of forces distributed over the blade surfaces from the steady inflow case and the harmonic inflow cases.

It can be concluded from this analysis that the flow is affected by all wakes considered in this study. The unsteadiness of the inflow wake has a direct impact on the flow field around the rotor imposing aerodynamic loads on the blade structure. Depending on the frequency and the amplitude of the wake, the rate of impact on the aerodynamics of the rotor will vary. Very good agreements between the time domain method and the frequency domain method are obtained in this work which ensures that the frequency domain solution method can be used reliably to analyse the aerodynamics of the wind turbine considering the inflow wakes and unsteadiness. The computation time required by the frequency domain solution method is at least one order of magnitude less than the time domain solution method.

5.3.2. Aeromechanical Analysis of the Wind Turbine Rotor

The aeromechanical analysis of the selected wind turbine is discussed in this section. The unsteady pressure distributions can be described in terms of unsteady pressure amplitude coefficient and unsteady pressure phase angle. The sources of flow unsteadiness, in this case, are associated with blade vibration. The unsteady pressure amplitude coefficient C_{p1} and unsteady pressure phase angle are extracted at two blade sections, 30% and 90% span sections, and they are obtained from the time domain solution method and the frequency domain solution method for the selected two materials. The results are plotted in Fig. 5.10. These blade sections are chosen to represent the blade root region and tip region where the flow is complex. The results obtained from the two methods are in good agreement with each other for all cases which indicates that the frequency domain method

captures the unsteady flow adequately even when using a relatively large amplitude of vibration at the first vibration mode. Good agreements are also obtained at other blade sections, but they are not shown in this section to keep it more concise. The unsteady pressure distributions show that some fluctuations are seen at the blade inner region if the composite material is used. The differences in unsteady pressure profiles between the two cases are related to the different vibration frequencies due to different material properties. The amplitude of pressure fluctuation is found to be the highest at the leading edge where the flow interacts with the blade aerofoil. It is then reduced along the chord length with some fluctuations on the suction surface. This fluctuation is related to the flow separation and vortex generation due to blade vibration. The unsteady pressure phase angle deviates approximately between 100^{o} and -100^{o}, and the deviation is more significant at the 30% span section, especially when using the composite material. Pressure contours on both pressure and suction surfaces of the blade are presented in Fig. 5.11 for visualization of pressure distributions over the blade surfaces.

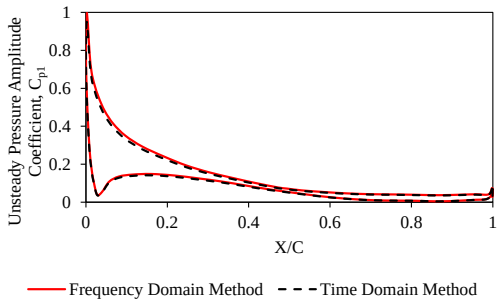

a) C_{p1}, aluminium alloy, 30%

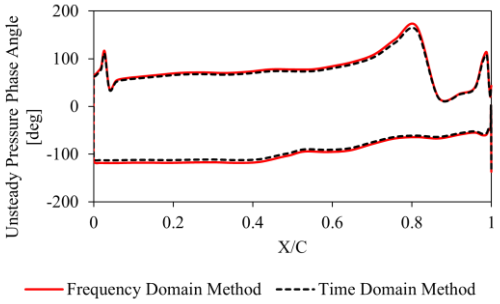

b) Phase, aluminium alloy, 30%

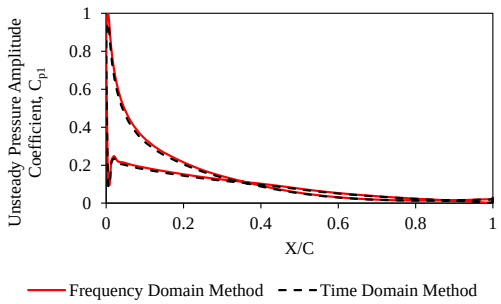

c) C_{p1}, aluminium alloy, 90%

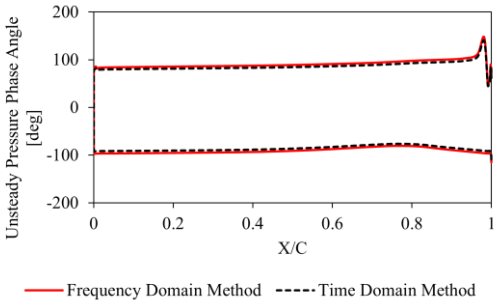

d) Phase, aluminium alloy, 90%

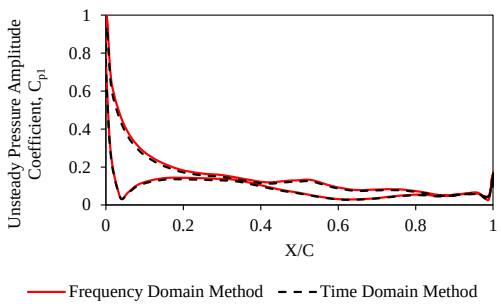

e) C_{p1}, composite material, 30%

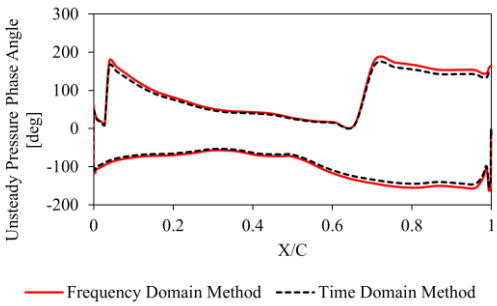

f) Phase, composite material, 30%

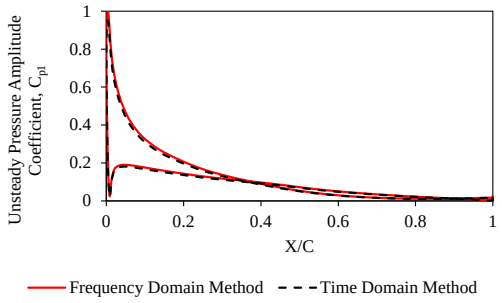

g) C_{p1}, composite material, 90%

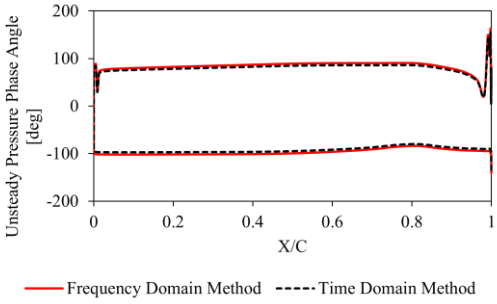

h) Phase, composite material, 90%

Figure 5.10. Unsteady pressure amplitude coefficient (C_{p1}) and unsteady pressure phase angle distributions at 30% span and 90% span sections of the blade with aluminium alloy and composite material.

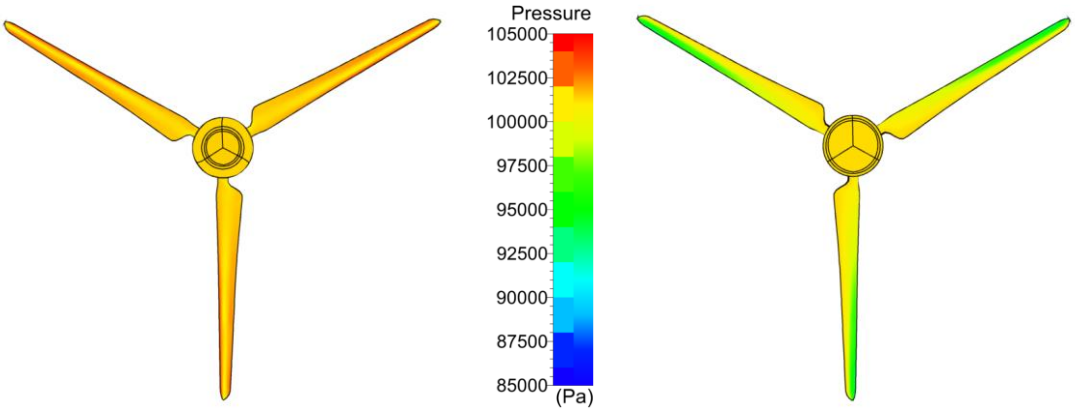

a) Pressure surface

b) Suction surface

Figure 5.11. Pressure contours on pressure and suction surfaces of the blade.

Figure 5.12 presents the dimensionless forces, expressed as F/F_{max}, applied on the blade surfaces over a complete vibration period due to the blade vibration using two materials. The coefficients are calculated as *(Force on Blade – Average Force on Blade)/(Maximum Force on Blade)*. Despite using the same vibration amplitude, the main parameters to define blade vibration such as frequency and mode shape, obtained from the FEA analysis using two different materials, are different for each case. It is noted that the forces applied

on the blade are reduced by 6% with the composite material. As the magnitude of forces applied on the blade is directly associated with the structural responses, the composite material can reduce the risk of aeroelastic instability associated with the blade vibrations. From the structural point of view, the flap-wise bending caused by the wind pressure is resisted by the blade structure with both pressure and suction surfaces of the blade carrying the loads. The composite material possesses the properties which provide more flexibility to resist the bending loads, and therefore, it can reduce the material fatigue to the minimum level. Furthermore, as the IBPA of 120^{o} is used in this study, three blades are vibrating out of phase with each other which could potentially impose the instability to the structure even greater. Figure 5.13 shows the displacement profiles over two vibration periods and the displacement contour for visualization of the blade deflection. Blade 1 represents the one at the 12 o'clock position. Positive and negative values of the displacement represent the blade deflecting backwards and forward, respectively.

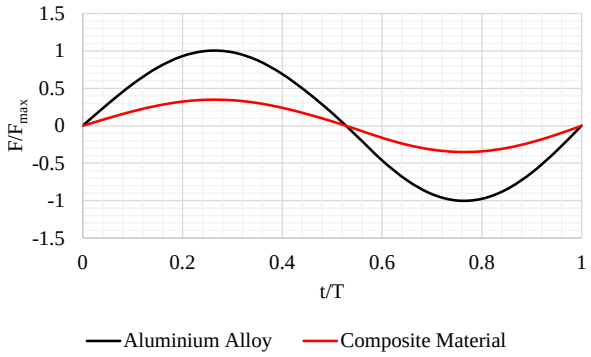

Figure 5.12. Coefficients of force applied on the blade using aluminium alloy and composite material over one vibration period.

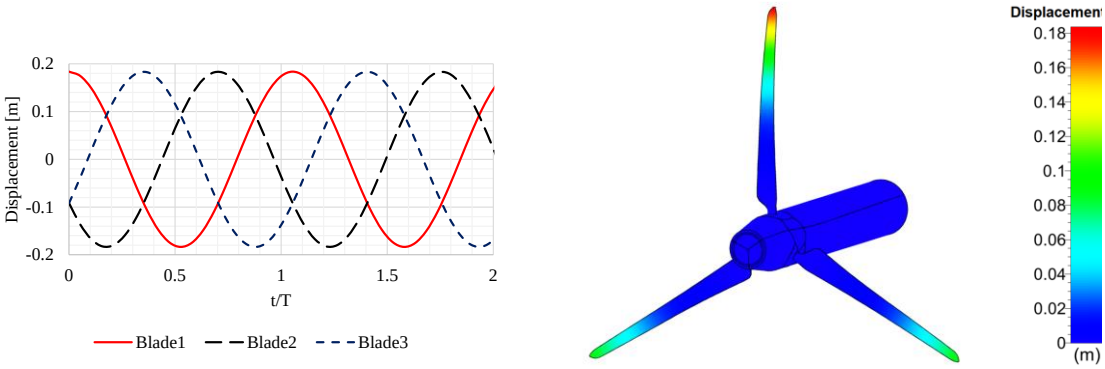

a) Displacement profile b) Displacement contour

Figure 5.13. Displacement profiles over two vibration periods and displacement contour on the blade surfaces.

The aeroelasticity parameter, known as the aerodynamic damping, can be calculated based on the aerodynamic work per vibration cycle and it can be expressed as:

$$W = \int_{t_0}^{t_0+T} \int_A p\vec{v}.\hat{n}dAdt \tag{5.5}$$

where t_0 is the initial time, T is the vibration period, p is the fluid pressure, v is the velocity of the blade due to the imposed displacement, A is the blade surface area, and $\hat{n}$ is the surface normal unit vector. The aerodynamic damping is computed as $W/m_m\omega_v^2 d_{max}^2$ where m_m is the modal mass, ω_v is the vibration frequency, and d_{max} is the maximum vibration amplitude. If the aerodynamic damping is positive, the blade vibration can be considered stable. The aerodynamic damping values, obtained from the time domain solution method and the frequency domain solution method, for the blade with two materials are outlined in Table 5.2. As seen, the results obtained are close to each other. The aerodynamic damping values are positive indicating that the vibration is damped in both cases. However, the composite material can provide better stability as the aerodynamic damping is larger than that of Aluminium Alloy. This is also consistent with Fig. 5.12 in which the forces applied on the blade surfaces are lower with the composite material. Aerodynamic power distributions on both pressure and suction surfaces of the blade can be seen in Fig. 5.14 which denotes that the blade has the stabilizing effect on both surfaces around the tip of the blade. Overall, it can be concluded that the frequency domain solution method can be reliably used for the aeromechanical analysis of wind turbine rotors and blades considering large deflections with different IBPA values. Only a single passage domain with one blade is required for this analysis with the proposed nonlinear frequency domain solution method.

Table 5.2. Aerodynamic damping values of the blade with two selected materials.

Material	**Time Domain Method**	**Frequency Domain Method**
Aluminium Alloy	0.227	0.230
Composite Material	0.698	0.707

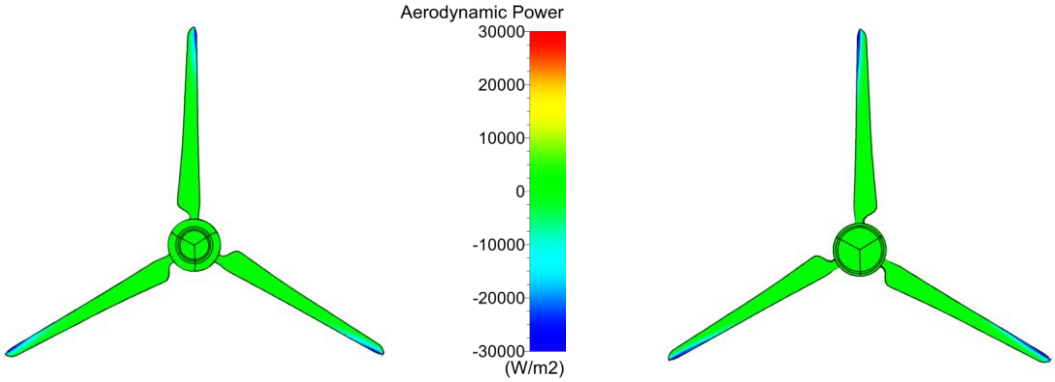

a) Pressure surface b) Suction surface

Figure5.14. Aerodynamic power contours on surfaces of the wind turbine blade.

5.3.3. Computational Costs

All simulations discussed are performed on a single CPU with a 3.40 GHz Intel (R) Core (TM) i5-7500 CPU. The computation takes 3 hours using the frequency domain method, whereas it takes about 150 hours, using 40 steps per revolution and 100 inner iterations, with the time domain solution method.

5.4. Summary of the Chapter

The aerodynamic and aeromechanical analysis of a test case wind turbine, the MEXICO-Experiment wind turbine, are conducted using a highly efficient nonlinear frequency domain solution method in this chapter.

The CFD model used in this work is validated against the experiment as well as the previous simulation, and a good agreement is obtained between them. Using the validated CFD model, the harmonic inflow wakes at different frequencies are generated at the inlet and the effects of the inflow unsteadiness on the aerodynamics of the wind turbine rotor are analysed. Results indicate that the flow fields around the wind turbine rotor are influenced by the inflow wakes and the unsteadiness of the flow imposes aerodynamic loads on the blade structure. The effects of the inflow wake on the flow fields are noticeable at all frequencies. Therefore, it can be concluded from this analysis that the unsteadiness of the inflow wakes has an impact on the aerodynamic flow field around the wind turbine rotor, and it could also influence the aeroelasticity of the wind turbine significantly as the forces applied on the blade are directly associated with the wake frequencies.

The aeromechanical analysis of the selected wind turbine is then conducted using two different materials. A relatively large deflection of 9% of the span is considered in this analysis. The unsteady pressure distributions over the blade surfaces are computed using both frequency domain and time domain methods, and the results obtained are close to each other. The aerodynamic damping values indicate that the blade vibrations are stable in both cases using two materials. However, it is found that the composite material provides a greater aerodynamic damping value than the aluminium alloy even when the blade is vibrating with a large vibration amplitude.

The proposed nonlinear frequency domain method is extensively validated against the time domain method, and an excellent agreement is obtained between the two methods. In terms of computational cost, the proposed nonlinear frequency domain solution method can reduce the computation time by one to two orders of magnitude compared to the conventional time domain solution method. In conclusion, the nonlinear frequency domain solution method can be reliably and efficiently used for the aerodynamic analysis as well as the aeromechanical analysis of wind turbines considering relatively large amplitudes of vibration for any IBPA using a single passage domain that reduces the computation time significantly.

Chapter 6. Aeromechanical Analysis of a Complete Wind Turbine

The high-fidelity computational fluid dynamics (CFD) simulations of a complete wind turbine model usually require significant computational resources. The computation time is challenging when the fluid-structure interactions between the blade and the flow are considered. The aeromechanical analysis of a complete wind turbine model using a high-fidelity CFD method is discussed in this chapter. The most distinctiveness of this study is the application of the nonlinear frequency domain solution method to analyse the forced response and flutter instability of the blade as well as to investigate the unsteady flow field across the wind turbine rotor and the tower. This method also enables the aeromechanical simulations of wind turbines for various inter blade phase angles in a combination with a phase shift solution method. Extensive validations of the nonlinear frequency domain solution method against the conventional time domain solution method reveal that the proposed frequency domain solution method can reduce the computational cost by one to two orders of magnitude.

6.1. Physical Description

The MEXICO-Experiment wind turbine, presented in Chapter 5 (see section 5.2), is used for this study. A tower model is added in order to simulate a complete wind turbine model. Most numerical studies performed on this turbine are based on a rotor-alone model neglecting the tower effect. Furthermore, these studies only considered steady flow conditions which ignore the impact associated with various sources of flow unsteadiness. In this study, the simulation of a complete wind turbine model is performed and the effect of the flow interaction with the tower on the flow field around the wind turbine is analysed. The selected operating parameters of this wind turbine, which are used in the present simulations, are listed in Table 6.1. The blade vibration is also integrated into the flow simulation to investigate the effects related to the flow unsteadiness due to the blade vibration. The natural frequencies and mode shapes of the blade are first computed through the modal analysis before the flow simulation. The first vibration mode of the blade, obtained from the modal analysis, is prescribed to be the blade vibration in the CFD simulation. The shape of the blade vibration can be visualised in Fig. 6.1. The aluminium alloy is used for the material of the blade to be similar to the one used in the experiment. It has a density of 2770 kg/m3, Young's modulus of 7.1×10^{10} Pa, and a

Poisson ratio of 0.27. For the blade vibration, the first vibration mode is used with the first natural frequency, 15.611 Hz, as the vibration frequency. An IBPA value of 120^{o} is selected, which indicates that the three blades are vibrating out of phase to each other by 120^{o}. Figure 6.1 shows the schematic diagram of the physical model.

Table 6.1. Parameters of the MEXICO-Experiment wind turbine.

Number of Blades	3
Blade Length	2.04 m
Rotor Diameter	4.5 m
Design Wind Speed	15 m/s
Rotational Speed	424.5 RPM
Design Pitch Angle	-2.3^{o}

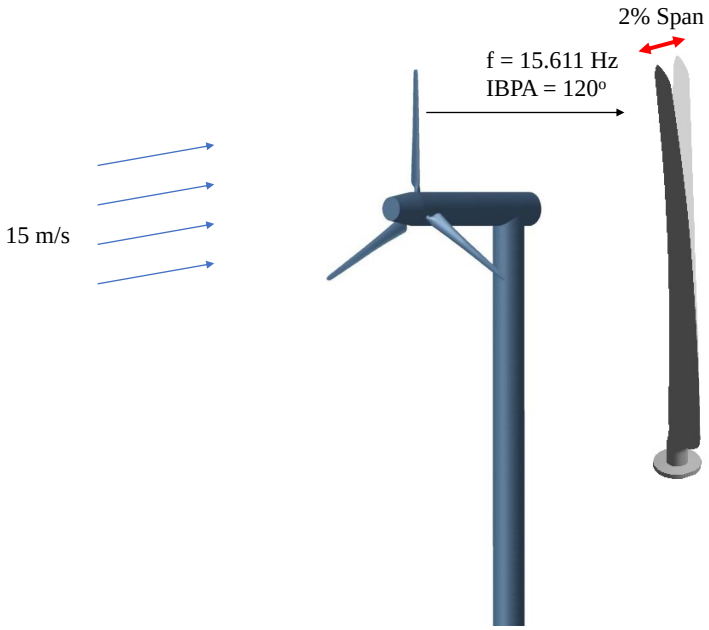

Figure 6.1. Schematic diagram of the physical model.

6.2. Computational Description

A structured grid generator is used to generate a three-dimensional computational domain and grid. In order to simulate the complete wind turbine model, the rotor side and the tower side are meshed separately, and they are connected through a rotor-stator interface. A Rounded Azimuthal O4H topology is used for the generation of both rotor and tower grids. Each grid consists of five blocks such as the skin block surrounding the blade, the inlet block located upstream of the leading edge, the outlet block located downstream of the trailing edge, the upper block located above the blade section, and the lower block

located under the blade section. An O-mesh is used for the skin block whereas an H-mesh is used for the remaining blocks. With the frequency domain solution method, only a single passage of the rotor is required whereas a full passage domain (360^o) including three blades is used for the time domain solution method. A 360^o grid is generated for the tower side. The flow inlet and outlet are located 2R upstream of the rotor and 4R downstream of the rotor, respectively, and the far-field boundary is placed 3R from the origin of coordinates, where R is the rotor radius. There are studies in the literature which used similar domain sizes and showed that they can accurately predict the blade loading and flow behaviour [135, 171, 184]. Therefore, it can be noted that the considered distances for far-field boundaries are sufficiently far away from the turbine. The first cell layer thickness is 10^{-5} meters to ensure that the y^+ value is less than one. A single passage of the rotor side of the grid has 4.5 million grid points and the tower side of the grid has 9 million grid points. A grid sensitivity study is also carried out to ensure that the grid size is suitable for this study. Figure 6.2 presents the differences in computing the blade loads such as torque with respect to the combined rotor and tower grid size. As seen, less than one percent improvement is obtained beyond the selected grid size of 13 million grid points. It can be said that this grid size can provide adequate accuracy to compute the aerodynamic parameters and aerodynamic damping. Therefore, the selected grid size can be considered suitable for the present work. The generated computational domain and grid is shown in Fig. 6.3.

The flow simulation is performed using a CFD method in NUMECA FINE/Turbo and the structural simulation is conducted using an FEA method in ANSYS Mechanical. The modal coupling FSI method, as described in the methodology section in Chapter 3, is employed to conduct the aeromechanical analysis. The first vibration mode is prescribed to be the mode of blade vibration. This type of analysis is conducted for the first time for this wind turbine including the tower. The nonlinear frequency domain solution method is applied to this analysis. With the frequency domain method, the flow variables are decomposed into the time-averaged value and unsteady perturbations for a specified number of harmonic and a fundamental frequency. The source of flow unsteadiness is related to the blade vibration in this study, and therefore, the fundamental mode (one harmonic) is considered enough for the analysis. As the experiment for the aeromechanical analysis is always difficult to be performed and no experimental data for such analysis are available for this wind turbine, the conventional time domain solution method is used for validation purposes. The time-accurate solution is performed over

several blade vibration cycles until a steady-periodic state is reached. The time-step of 0.003 s, corresponding to 20 steps per period, using 100 inner iterations is found to be sufficient for this analysis. The solid wall boundary condition is applied on the blade, the hub and the tower. The external boundary condition, which is a non-periodic one, is defined to treat the far-field boundaries dealing with the external flow computations. For the periodic boundaries of the rotor, the direct periodic (repeating) condition is applied for the time domain method whereas only a single passage domain is required for the frequency domain solution method. With the frequency domain method, the harmonic components are phase-shifted between the periodic boundaries by a given IBPA. A rotor-stator interface connecting the rotor side of the grid and the tower side of the grid is introduced to simulate a complete wind turbine model. The purpose of using a rotor-stator interface is to exchange the flow data between the rotating domain, which involves a rotor, and the stationary domain, which involves a tower. A detailed description of the rotor-stator interaction can be found in Chapter 3 (refer to Section 3.7). The conservative flow variables are transferred between the upstream and downstream domains using the frequency domain method in the frequency domain solution and a sliding plane method in the time domain solution.

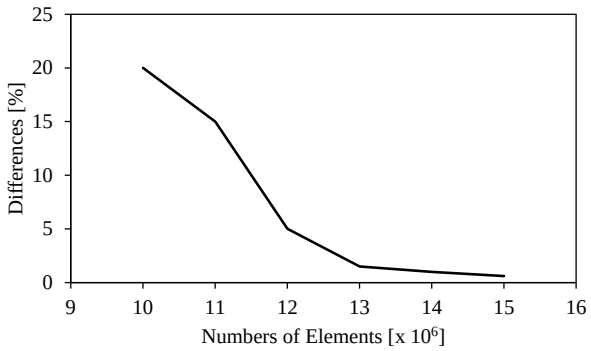

Figure 6.2. Grid sensitivity study

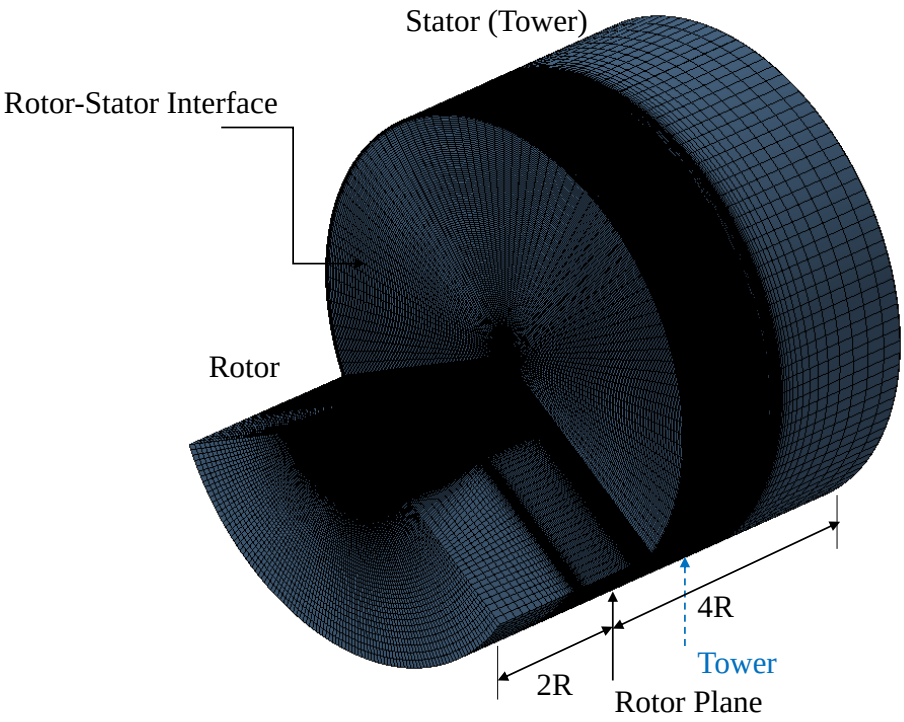

a) Computational domain

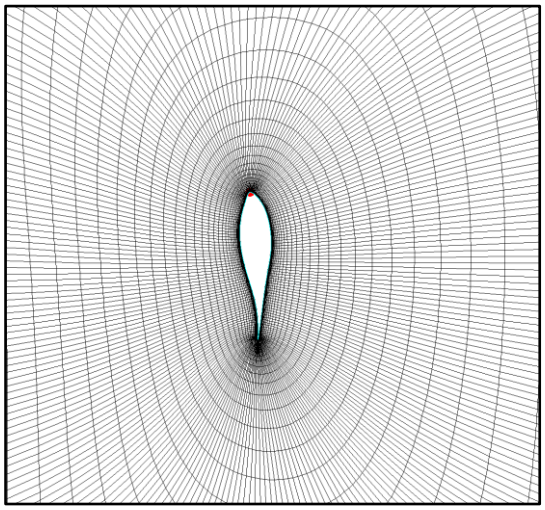

b) Blade-to-blade view

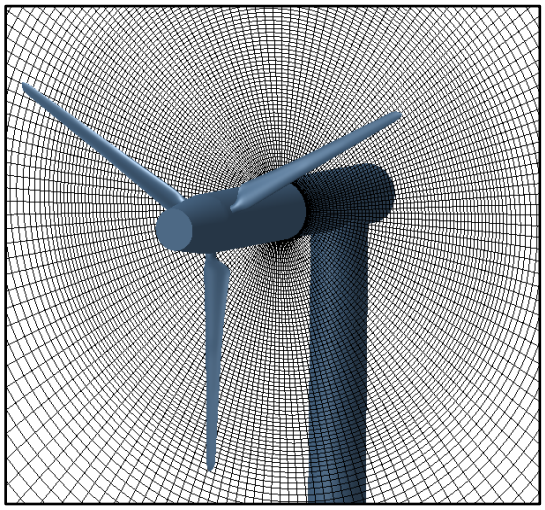

c) Rotor-stator interface

Figure 6.3. Computational domain, blade-to-blade view of the mesh and rotor-stator interface of the computational model.

6.3. Results and Discussions

First of all, the CFD model is validated by comparing the steady pressure coefficient distributions obtained from this work to the experiment as well as the previous simulation. The detailed comparisons at different sections of the blade are presented in Chapter 5 (see Fig. 5.2). Overall, the present simulation results are very close to those of Sorensen et al. [179] and they are in good agreement with the experiment.

Unsteady pressure distributions on the blade surfaces due to the blade deflection can be expressed in terms of the unsteady pressure amplitude coefficient and phase angle. Figure 6.4 presents the comparison of the unsteady pressure amplitude coefficient and unsteady pressure phase angle distributions at three blade sections computed from the time domain solution method and the frequency domain solution method. As seen, they are in good agreement. This ensures that the frequency domain method can be used for the calculation of unsteady pressure distributions associated with the blade deflection. Furthermore, Fig. 6.5 illustrates the pressure coefficient profiles along an axis parallel to the rotation axis, located at the blade mid-span, from one rotor diameter upstream to one rotor diameter downstream of the rotor plane, obtained from both time domain and frequency domain methods. This figure shows the pressure distribution across the wind turbine and the comparison between the two methods in predicting the pressure profile along a horizontal axis through a rotor-stator interface. As shown, both methods predicted a similar pressure distribution across the rotor and the tower including a small disturbance that occurred due to the presence of the tower.

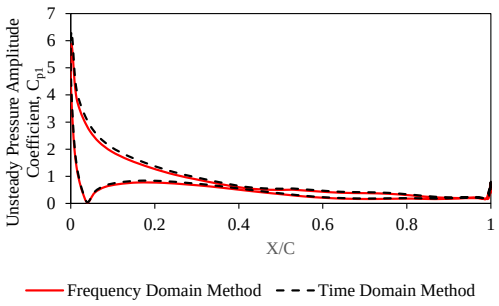

a) C_{p1} at 30% span

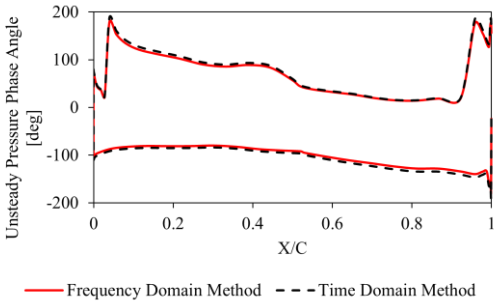

b) Phase angle at 30% span

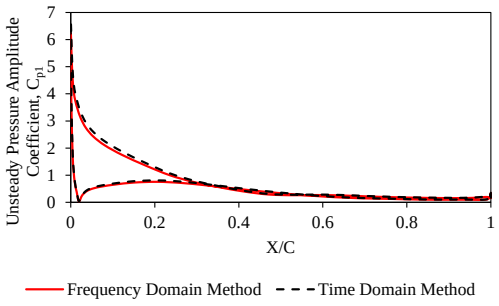

c) C_{p1} at 50% span

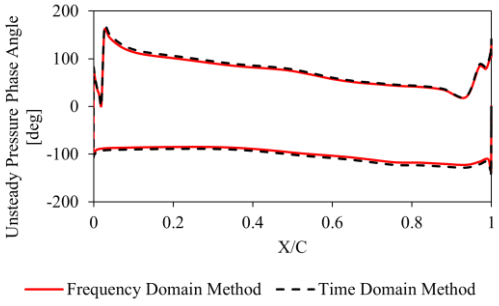

d) Phase angle at 50% span

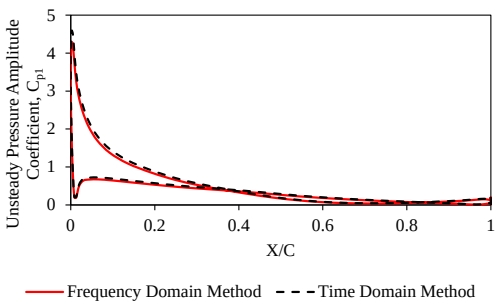

e) C_{p1} at 90% span

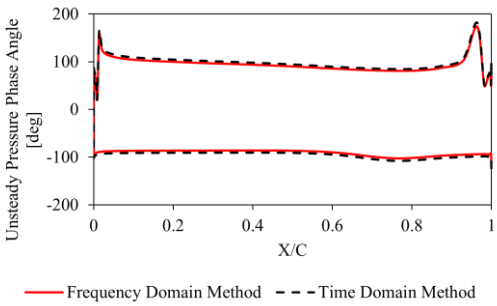

f) Phase angle at 90% span

Figure 6.4. Unsteady pressure amplitude coefficient (C_{p1}) and unsteady pressure phase angle at different blade sections.

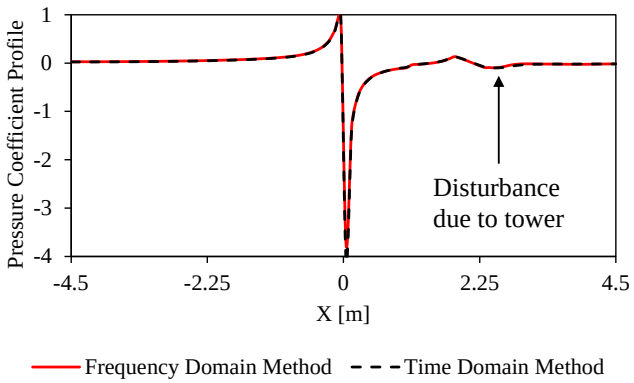

Figure 6.5. Pressure coefficient profile across the wind turbine.

In addition to the pressure coefficients, the time-averaged skin friction coefficients at 30% and 90% of the blade span sections are compared between the time domain method and the frequency domain method, and they are shown in Fig. 6.6. As shown, they agree well with each other. Good agreements between the two methods are also obtained at other sections. Figure 6.7 demonstrates blade loads such as torque and axial thrust profiles as well as the aerodynamic power profile for one rotor revolution computed from both time domain and frequency domain methods. It is seen that the loads applied on the blade surfaces are directly associated with the blade vibration, and they fluctuate at the vibration frequency over a blade revolution. Likewise, the results obtained from the two methods are in good agreement.

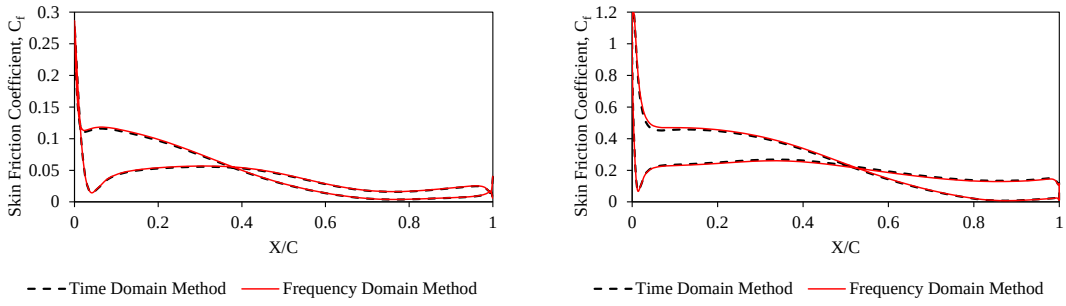

a) 30% span b) 90% span

Figure 6.6. Time-averaged skin friction coefficients at different sections of the blade.

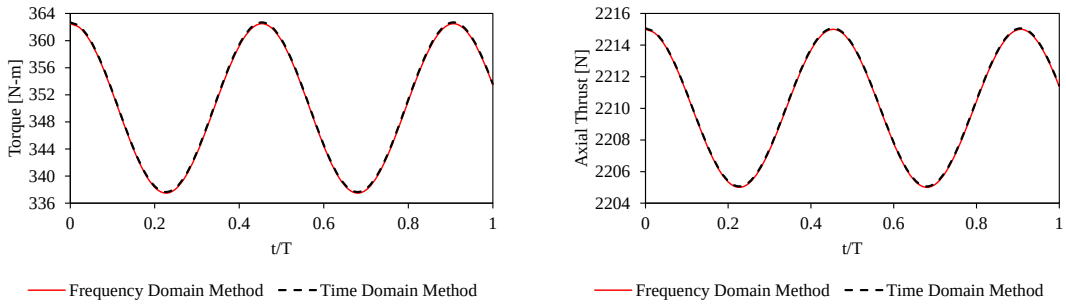

a) Torque profile b) Axial thrust profile

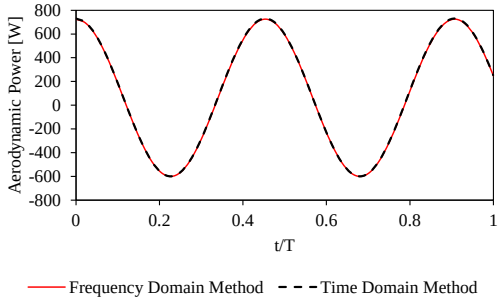

c) Aerodynamic power profile

Figure 6.7. Torque, axial thrust and aerodynamic power profiles for one rotor revolution.

The aerodynamic damping value, calculated from the aerodynamic work per vibration cycle, is typically used in turbomachinery analysis to analyse whether the blade structure vibration can lead to the flutter phenomena. The aerodynamic damping is evaluated using both methods and they are listed in Table 6.2. As shown, they are close to each other. The aerodynamic damping is positive which shows that the fluid damps the blade structure vibration. The blade displacement profiles for one rotor revolution and displacement contour are presented in Fig. 6.8, which demonstrates that each blade vibrates out of phase with respect to the others by a phase angle of 120^o degrees. Only a single passage domain is required for this analysis with the frequency domain method whereas a 360^o rotor

domain including all three blades is required for the time domain method resulting in much more computation time.

Table 6.2. Aerodynamic damping of the blade.

Method	Aerodynamic Damping
Frequency Domain Solution Method	0.25
Time Domain Solution Method	0.26

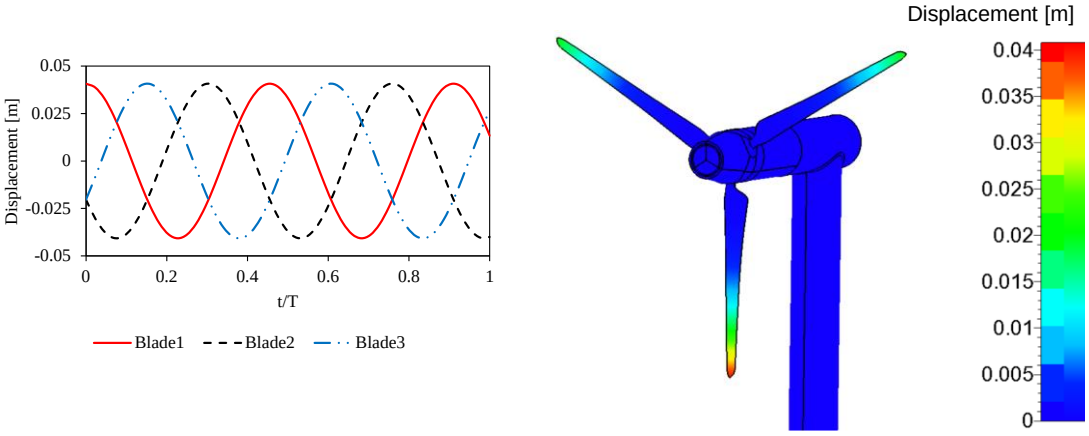

a) Displacement profiles b) Displacement contour

Figure 6.8. Displacement profiles and displacement contour of the rotor blades (Blade 1 represents the one at six o'clock position. Positive and negative values of displacement represent blade deflecting backwards and forward, respectively).

As the tower is present in the present simulation, it is also required to analyse the effects associated with the tower. Figure 6.9 demonstrates the velocity flow fields on a plane normal to the wind direction, extracted just behind the rotor, at the middle between the rotor and the tower, and just before the tower, to visualise the behaviour of the flow interaction with the rotor and the tower. As shown in Fig. 6.9 (a), the high velocity is built up along the leading edge of the blade as the blade rotates generating the blade tip vortex as well as leaving the lower velocity field behind the trailing edge. In Fig. 6.9 (b), the high-velocity field generated by the blade tip, known as the tip vortex, moves a little farther away from the blade. This process can be identified as the wake expansion process. The wake expansion can be further visualised in the meridional view in Fig 6.10. As the flow approaches the tower, the flow is disturbed by the tower structure resulting in the high-velocity field on each side of the tower as well as the flow separation and recirculation behind the tower (see Fig. 6.9 (c)). The interaction between the unsteady

flow field and the tower can also be better visualised in the meridional view, as illustrated in Fig. 6.10. It is seen that the flow is highly distorted by the tower structure, and the flow separation and recirculation are observed behind the tower, leading to further unsteadiness and instability in the downstream wake. It should be noted that the images presented in Figs. 6.9 and 6.10 are obtained from the time reconstruction of the frequency domain solution. The images from the time domain solution are not shown as they are very similar.

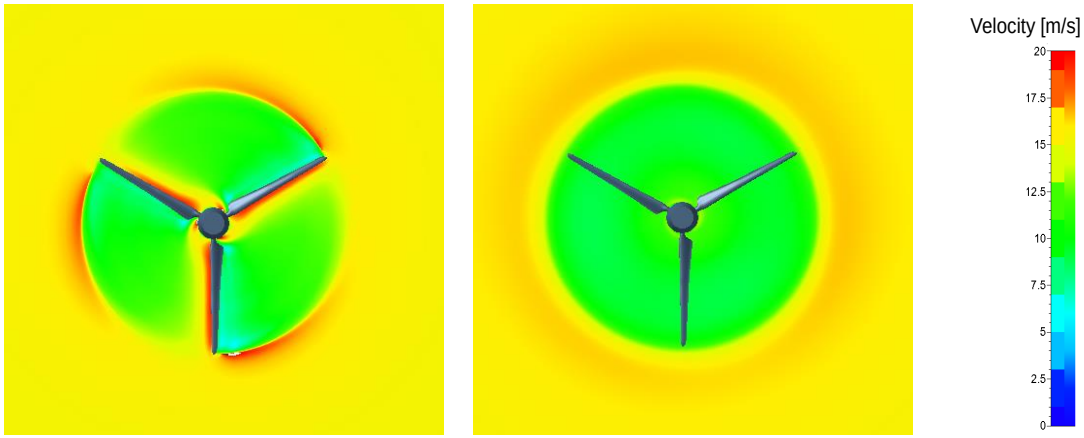

a) Just behind rotor b) Between rotor & tower

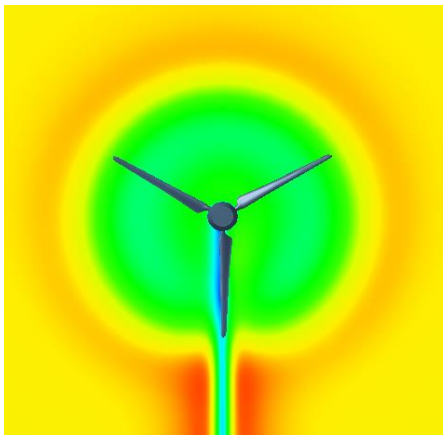

c) Just before tower

Figure 6.9. Velocity fields on the plane extracted just behind the rotor, at the middle between the rotor and the tower, and just before the tower.

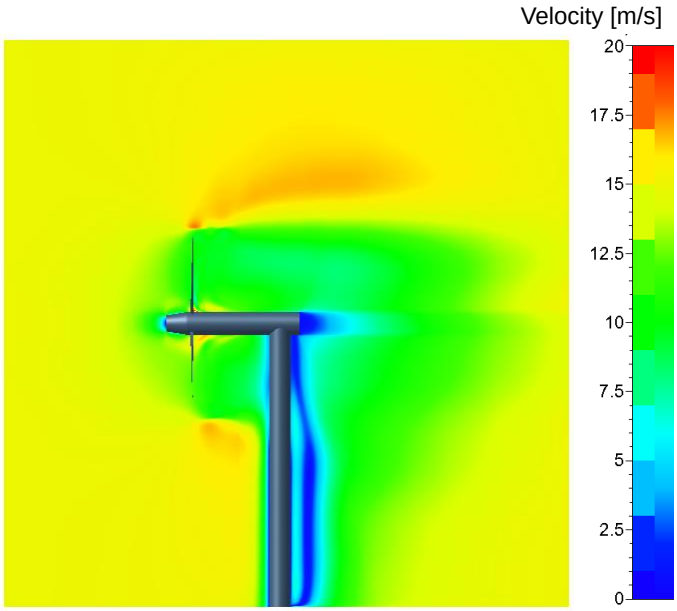

Figure 6.10. Velocity fields in the meridional view.

The flow unsteadiness associated with the flow interaction between the rotating and stationary components of the wind turbine can be indicated by further flow visualisations. Figure 6.11 presents the vorticity field and flow streamlines around the wind turbine. The development of tip vorticity due to the rotation of the wind turbine rotor and the advection and diffusion of vorticity can be clearly observed in the figure. The kinetic energy in the wind is captured by the rotor blade and therefore, the pressure field just behind the rotor is lower compared to the upstream of the rotor. The vorticity generated from the rotor blade is distorted by the tower, which leads to an increase in turbulence and instability in the downstream flow. The formation of vortex structures along the tower height is also observed. As shown in Fig. 6.11 (b), the flow streamlines passing through the rotor is disturbed by the tower structure, and some of the streamlines stick around the tower attributing to the formation of vortex structures along the tower. After interaction with the rotor and the tower, the streamlines in the downstream region become unstable and disorganised resulting in a turbulent wake.

a) Vorticity

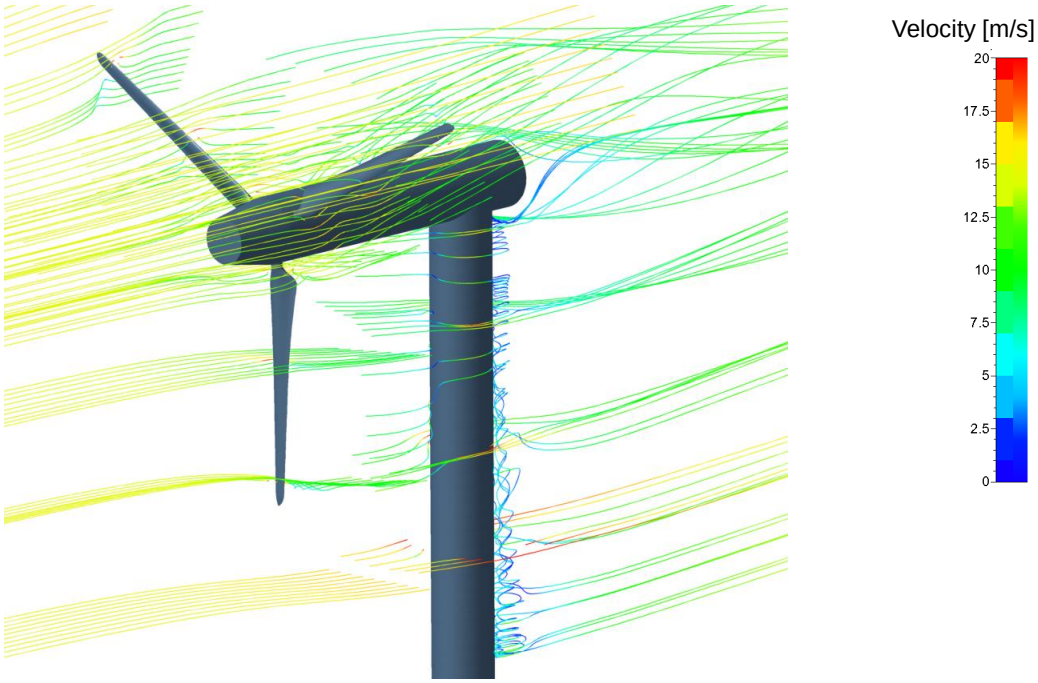

b) Flow streamlines

Figure 6.11. Vorticity field and flow streamlines around the wind turbine.

The simulations discussed in this chapter are performed on a single CPU with a 3.40 GHz Intel (R) Core (TM) i5-7500 CPU. In terms of computation time, it takes 17 hours using the frequency domain method. However, it takes 10 days on the same computer with the fully unsteady time domain solution method with the time-step of 0.003 s.

6.4. Summary of the Chapter

The aeromechanical analysis of a complete wind turbine model including a tower is presented in this chapter. The aeromechanical simulation of this wind turbine is conducted using the proposed frequency domain solution method in a combination with the phase-shift method. The time domain method is adopted to validate the frequency domain method due to the lack of experimental data. The unsteady pressure coefficients at different blade sections are computed and compared between the two methods, and the results agree well with each other. The pressure profile across the rotor and the tower is also calculated and both methods predicted similar pressure distributions. In addition, the skin friction coefficients at different blade sections, blade loads such as torque and axial thrust profiles as well as the aerodynamic power profile for one rotor revolution are computed, and the results are compared between the two methods. Likewise, they are in very good agreement. The stability of the blade vibration is also examined in this study computing the aerodynamic damping value. It is shown that the blade vibration is damped, and the aerodynamic damping values predicted from both methods are close to each other. Flow visualisations in terms of velocity magnitude indicate that the flow is distorted by the tower and the flow interaction with the tower results in further unsteadiness and instability in the downstream wake. These results provide a good indication of the unsteady and aeroelastic behaviour of a complete wind turbine model, and they are directly relevant to offshore wind turbine models as it is expected that the offshore wind turbine blades can have similar aeroelastic instability problems.

It was concluded in Chapter 4 that the proposed frequency domain solution method can be efficiently used for the analysis of wind turbine rotors. Using the proposed modelling strategy in this chapter, the frequency domain method can also be used for the simulation of complete wind turbine models. The comparison of the computational cost shows that the frequency domain solution method is much faster than the time domain solution method, and the computation time can be reduced by one to two orders of magnitude using the frequency domain method. In conclusion, the frequency domain solution method can be reliably used for the aeromechanical analysis of complete wind turbine models, including large offshore wind turbines, for any IBPA values saving computation time significantly.

Chapter 7. Aerodynamic Analysis of Wind Turbines in Arrays

The aerodynamics of a wind turbine within wind farms is strongly influenced by the wake of neighbouring wind turbines. In particular, the performance of a wind turbine can be dramatically reduced depending on its location in the wake region of an upstream turbine. A detailed investigation of the effect of the upstream turbine on the downstream turbine with respect to their distances is essential for the design and optimisation of wind farm layouts. As discussed in previous chapters, the fully unsteady time domain solution CFD method can provide detailed information of this interaction effect; however, they are computationally expensive to model and simulate multiple wind turbines. In this chapter, a novel modelling and computational method is proposed to simulate two wind turbines in arrays by considering them as a multi-stage turbine model. A nonlinear frequency domain solution method is then employed to model flow nonlinearities due to their interactions. The distances between the turbines are varied, and the effects of the upstream wind turbine on the downstream one are thoroughly investigated. Extensive validations of the nonlinear frequency domain solution method against the conventional time domain solution method reveal that the proposed frequency domain solution method provides accurate results while reducing the computational cost by one to two orders of magnitude.

In this study, wind turbines in arrays will be modelled in multi-row configurations and the distance between the upstream turbine and the downstream one will be varied. The considered distances between the two turbines are 2D, 5D and 10D, where D is the rotor diameter, and the effects of the upstream wind turbine on the downstream one will be investigated. It is understood that the standard separation distance between wind turbines in most optimisation studies is 5D [11]. To simulate the scenario in which the downstream turbine is located in the vicinity of the upstream turbine or far away from the upstream turbine, the distances of 2D and 10D are selected in addition to the standard separation distance of 5D. This is the first time that a frequency domain method is applied to the investigation of multiple wind turbines. The main distinctive feature of this work is the modelling of wind turbines in arrays as a multi-stage turbine model and the application of the frequency domain solution method, which reduces the computation time significantly to a reasonable and affordable level.

7.1. Physical Description

Figure 7.1 shows the schematic view of two wind turbines in arrays with different distances used in the present study. In this study, the MEXICO-Experiment wind turbine model is modified to model the wind turbines in arrays by adding another rotor behind the first wind turbine. Each wind turbine has three blades, and the blade is 2.04 m long. The rotor diameter, D, is 4.5 m. The separation distance between the turbines in the axial direction (W) is defined in terms of rotor diameter, D, and the considered distances between the turbines are 2D, 5D and 10D in this study. To evaluate the effects of wind turbines in arrays on the flow behaviour and to analyse the aerodynamic performances of the wind turbines, the design condition from the experiment which corresponds to the wind speed of 15 m/s, the rotational speed of 424.5 RPM and the pitch angle of -2.3^{o} are used in this study. Both upstream and downstream wind turbines are kept at the same rotational speed.

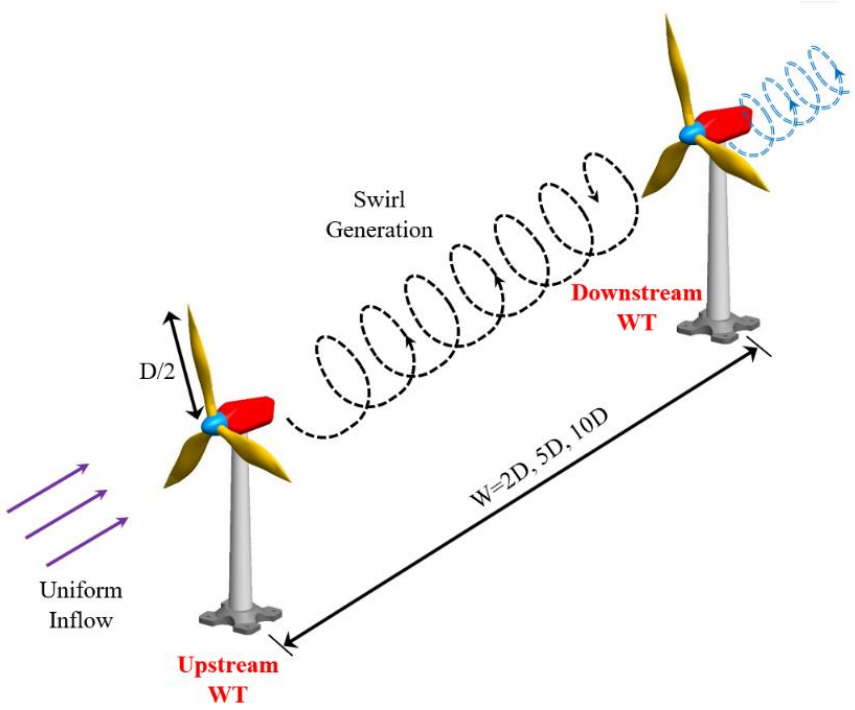

Figure 7.1. Schematic view of the two wind turbines in arrays with different separation distances.

7.2. Computational Description

A new type of modelling method to simulate multiple wind turbines is proposed in this study. Multiple wind turbines in arrays can be modelled in a multiple-row configuration considering it as a multi-stage turbine. In this study, there are two wind turbines in arrays, separated by a separation distance. In terms of modelling, ideally, there should be a rotor model and a tower model from each wind turbine. However, as this study investigates the

effect of the upstream wind turbine on the aerodynamic performances of the blades of the downstream turbine, only the rotor model of the downstream turbine without the tower is included in the wind turbines in arrays model to reduce the computation time. Using the proposed method, a series of turbines can further be modelled by adding more rotors and stators (i.e., towers). The pitch angle of the blade is -2.3^{o}. For a direct comparison, the same blade profiles and pitch angle are used for both upstream and downstream wind turbines, and only the separation distance between the turbines is varied. In order for the rotor-stator interface to work effectively for the flow continuation, all rotor blades and stator blades (i.e., tower in this model) should be modelled on the same hub. Therefore, an infinitely long hub is employed in this study to connect the rotors and the tower. An infinitely long hub model was also employed in the simulation of wind turbines before [180], and it is assumed that the effect of the hub on the flow field around the wind turbine is not significant.

A structured grid generator is used to generate a three-dimensional computational domain and grid. In order to model wind turbines in arrays, the rotors and the tower are meshed separately, and they are connected through a rotor-stator interface. A Rounded Azimuthal O4H topology is used for the generation of both rotor and tower grids. Each grid consists of five blocks such as the skin block surrounding the blade, the inlet block located upstream of the leading edge, the outlet block located downstream of the trailing edge, the upper block located above the blade section, and the lower block located under the blade section. An O-mesh is used for the skin block whereas an H-mesh is used for the remaining blocks. The frequency domain solution method only requires modelling of a single passage or a single blade of a full rotor wheel, which is one of the main advantages of this method for the analysis of turbomachines with multiple blade rows. Using the frequency domain solution method, the harmonic components of the flow variables can be phase-shifted between periodic boundaries by a given IBPA. Therefore, a 120^{o} grid is only required for the rotor model for the frequency domain solution (see Fig. 7.2 (b)). On the other hand, the time domain solution method requires a full wheel of rotor and stator with all blades for the time-accurate solution. Figure 7.2 (a) shows the overall view of the computational domain including all three blades and a tower. This is, in fact, the domain used for the time domain solution. A 360^{o} grid is generated for the tower domain. The flow inlet and outlet are located 2D upstream of the rotor and 4D downstream of the rotor, respectively, and the far-field boundary is placed 1.5D from the origin of coordinates, where D is the rotor diameter. The first cell layer thickness is 10^{-5} meters to ensure that

the y^+ value is less than one. The generated grid consists of 4.5 million grid points in each of the rotor domains with a single blade and 7.5 million grid points in the tower domain. Therefore, a total of 16.5 million grid points are required for the frequency domain solution whereas 34.5 million grid points are required for the time domain solution. The generated computational domain and the grid are shown in Fig. 7.2.

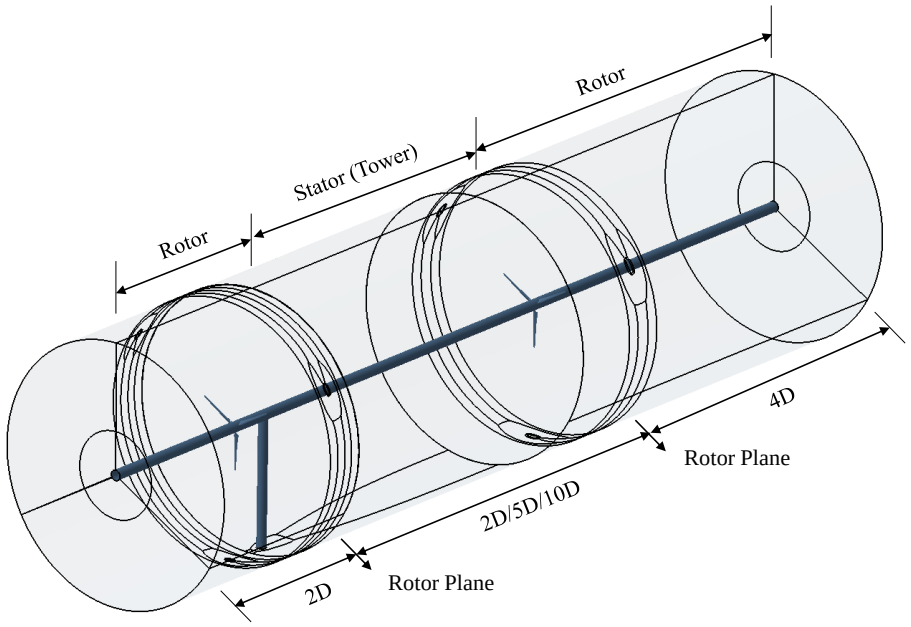

a) Computational domain

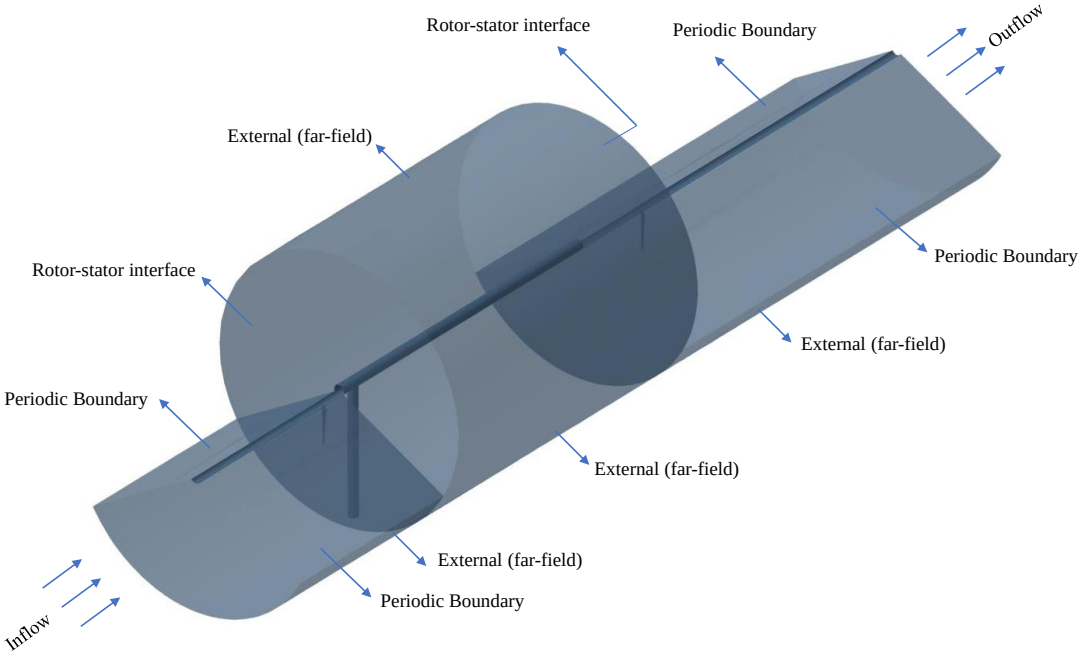

b) Details of boundary conditions

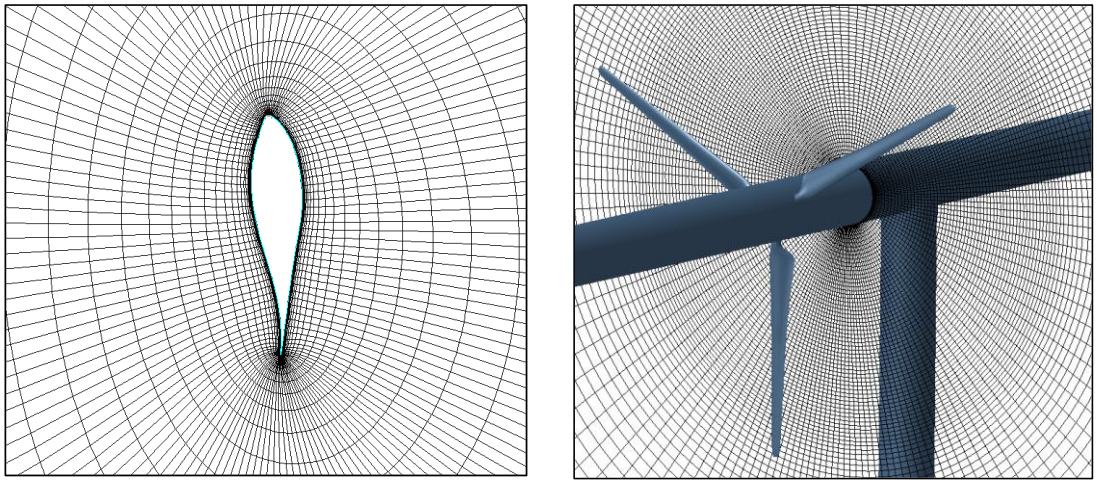

c) Blade-to-blade view

d) Rotor-stator interface

Figure 7.2. The computational domain, details of boundary conditions, mesh in blade-to-blade view and rotor-stator interface generated for the simulations.

In the present work, a three-dimensional density-based finite volume solver NUMECA FINE/Turbo is employed for the flow computation. The simulations are performed based on the URANS model. The flow is governed by the Navier-Stokes equations and the flow government equations are presented in Chapter 3 (refer to Section 3.1). The proposed nonlinear frequency domain solution method is employed for the unsteady flow simulation. This method is validated against the traditional time domain method. In this study, the sources of the flow unsteadiness are associated with the flow interaction in the multiple row configurations (i.e., the interaction between the rotor, tower (stator) and rotor). The unsteady terms corresponding to the flow unsteadiness can be represented by a Fourier series for a prescribed fundamental frequency and a specified number of harmonics *m*. The accuracy of the unsteady solution can be controlled through the order of the Fourier series. In this work, as the source of flow unsteadiness is related to the flow interaction between the rotor and the tower, which is periodic in time, the fundamental mode (one harmonic) is considered enough to resolve the flow. The blade passing frequency is the fundamental frequency of the system. A new set of Navier-Stokes equations are solved in the frequency domain with the frequency domain method. With this method, the unsteady period for one complete rotor rotation is equally divided into $N = (2m+1)$ time levels and the system of nonlinear equations coupling all N time levels are then solved iteratively. The details of the frequency domain method are provided in Chapter 3 (refer to Section 3.4).

The relative motion between successive rows of rotating and stationary domains such as rotor and tower is the main source of flow unsteadiness that affects the flow around the wind turbines in arrays. In this study, a rotor-stator interface is employed to exchange the flow solution between two adjacent rows (i.e., rotor and tower). The standard sliding-plane method which is a time-accurate solution is applied for the time domain solution. Using this method, the instantaneous flow data are transferred between the upstream and downstream domains through the rotor-stator interface at every time step by using a direct interpolation method. To apply this method, the pitch on the upstream and downstream sides of the interface should be equal to avoid any assumption of time periodicity as a boundary condition treatment. On the other hand, the frequency domain method is used for the frequency domain solution. The details of the rotor-stator interaction method can be found in Section 3.7 in Chapter 3.

The solid wall boundary condition is applied on the blade, the hub and the tower. The external boundary condition, which is a non-periodic one, is defined to treat the far-field boundaries dealing with the external flow computations. A rotor-stator interface is used to connect the outflow surface of the rotor domain of the first wind turbine and the inflow surface of the tower domain of the first wind turbine. The same interface type is used to connect the outflow surface of the tower domain of the first wind turbine and the inflow surface of the rotor domain of the second wind turbine. Using the rotor-stator interface, the flow data can be transferred between the upstream row and the downstream row (i.e., rotor and tower). The time domain solution requires a full wheel of the rotor and the stator. Therefore, the direct periodic (repeating) condition is applied for the time domain method whereas only a single passage domain with a periodic boundary condition is required for the frequency domain solution method. With the frequency domain method, the harmonic components are phase-shifted between the periodic boundaries by an IBPA to account for the flow unsteadiness related to the phase-shift.

7.3. Results and Discussions

Before performing simulations of multiple wind turbines, it is essential to ensure the accuracy of the numerical model employed in this study. To this end, the simulation of a single wind turbine is first performed, and the pressure coefficients are compared to the experimental data and the numerical data of Sorensen et al. [179]. Detailed comparisons between the simulation and the experiment can be found in Chapter 5. It can be seen that the present numerical results at different span sections are in good agreement with the

experiment and the reference simulation, indicating that the CFD model used is accurate enough to predict pressure distributions on the blade surfaces.

Figure 7.3 shows the comparison of the time-averaged pressure coefficient on the blade surfaces of the upstream wind turbine between the proposed frequency domain solution method and the time domain solution method based on the case in which the downstream wind turbine is placed at 2D behind the upstream wind turbine. The results are extracted at 25%, 30%, 50% 90% and 95% of the blade span sections. As seen, the results of the frequency domain method are in excellent agreement with the time domain method at different span sections.

Furthermore, Fig. 7.4 presents the variation of the time-averaged pressure coefficient on the blade surfaces of the downstream wind turbine at different span sections obtained from both time domain and frequency domain methods. Likewise, the results are obtained at different sections of the blade. As shown, the results from both methods are close to each other at all sections of the blade including 25% and 95% span sections, representing the blade root section and the tip section, respectively, where the flow is complex, which becomes problematic for the numerical methods. Therefore, it can be concluded that the frequency domain solution method accurately predicted pressure distributions on the surfaces of the blade of both upstream and downstream turbines. Contrary to the upstream wind turbine, significant deviations in the pressure distributions on the blade surfaces are observed at different sections, which is mainly due to the effect of the wake generated from the upstream wind turbine.

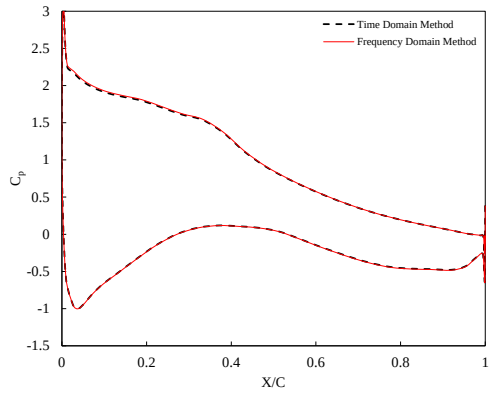

a) 25% span

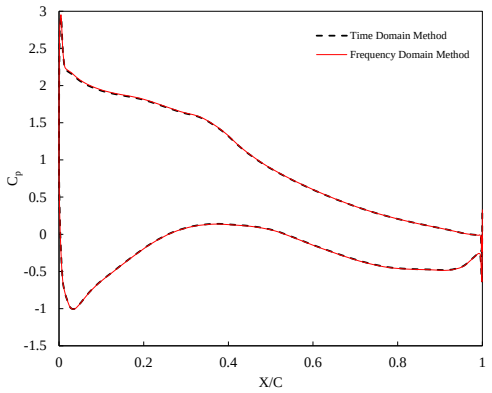

b) 30% span

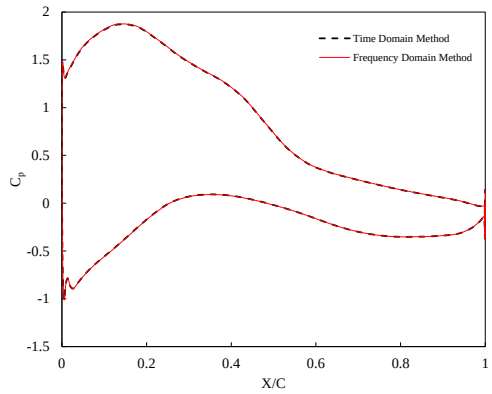

c) 50% span

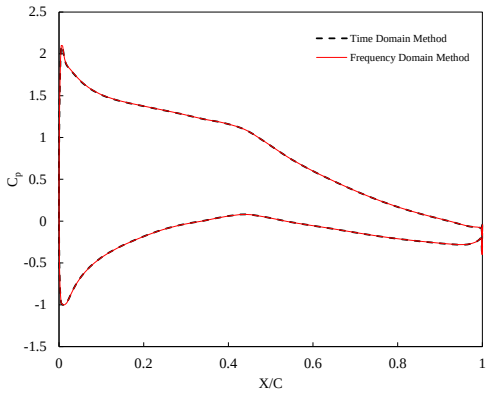

d) 90% span

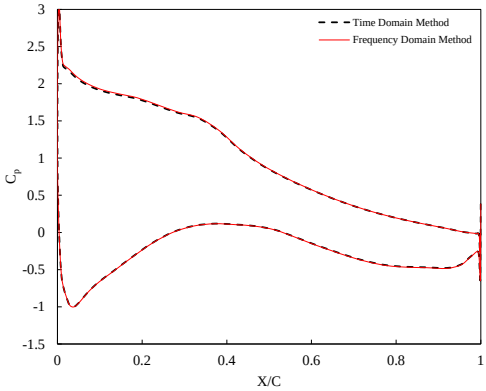

e) 95% span

Figure 7.3. Time-averaged pressure coefficient distributions at different blade sections of the upstream wind turbine obtained from the time domain method and the frequency domain method.

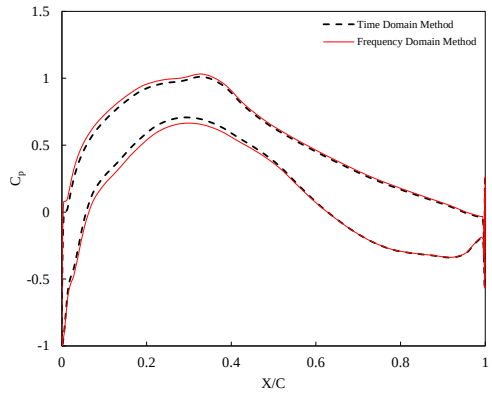

a) 25% span

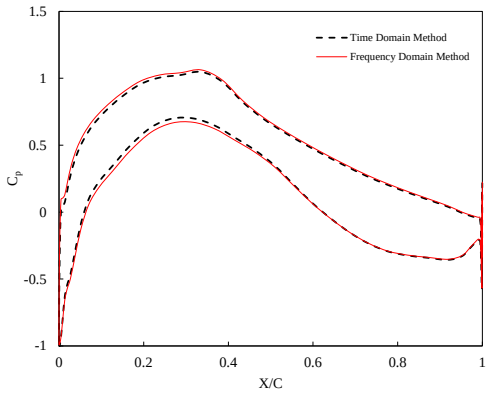

b) 30% span

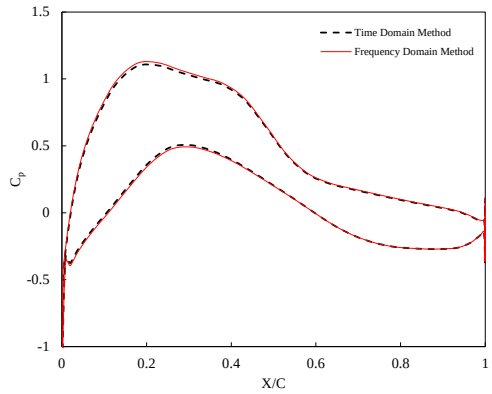

c) 50% span

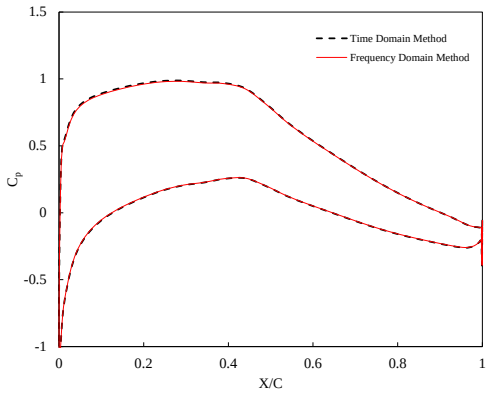

d) 90% span

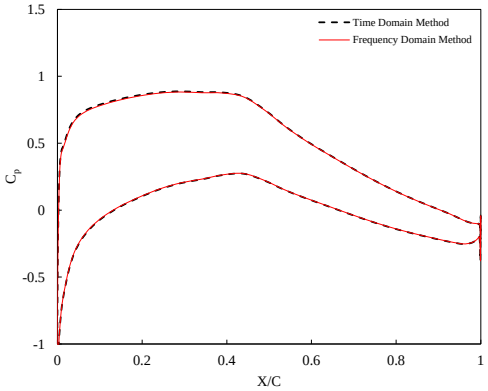

e) 95% span

Figure 7.4. Time-averaged pressure coefficient distributions at different blade sections of the downstream wind turbine obtained from the time domain method and the frequency domain method.

The comparison between the time domain method and the frequency domain method on predicting the skin friction coefficient distributions on the blade surfaces of the upstream wind turbine and downstream wind turbine at the separation distance of 2D are presented in Figs. 7.5 and 7.6, respectively. Similar to pressure coefficients, the results are provided at different blade span sections, including 25%, 30%, 50%, 90% and 95% of the blade span. Likewise, the skin friction coefficients at different sections of the blade of both upstream and downstream wind turbines obtained from the frequency domain method are close to that of the typical time domain method. It is understood that the flow behaviours in the blade root region and the blade tip region are sometimes difficult to be accurately predicted by the numerical models due to the complex flow nature. However, it is seen that the results at all sections, including the 25% and 95% span sections obtained from

both methods are in good agreement, which indicates that the frequency domain method is accurate enough for the prediction of the aerodynamic parameters.

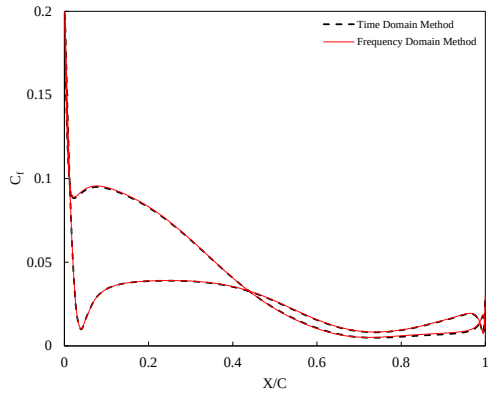

a) 25% span

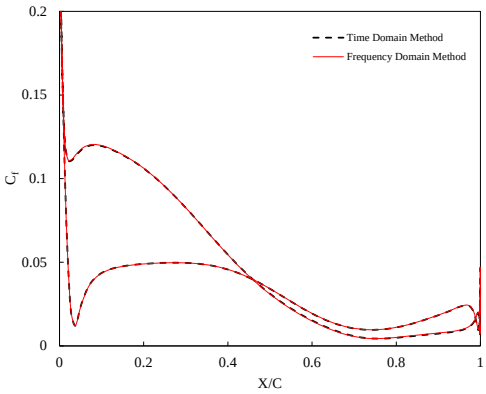

b) 30% span

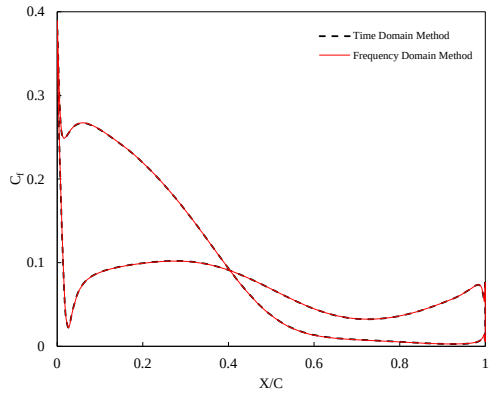

c) 50% span

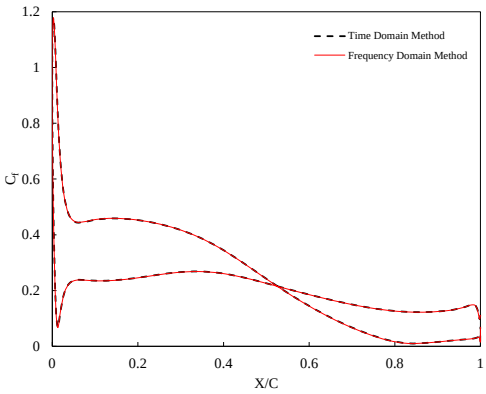

d) 90% span

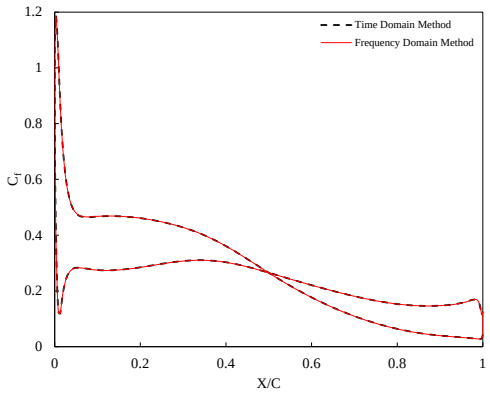

e) 95% span

Figure 7.5. Time-averaged skin friction coefficient distributions at different blade sections of the upstream wind turbine obtained from the time domain method and the frequency domain method.

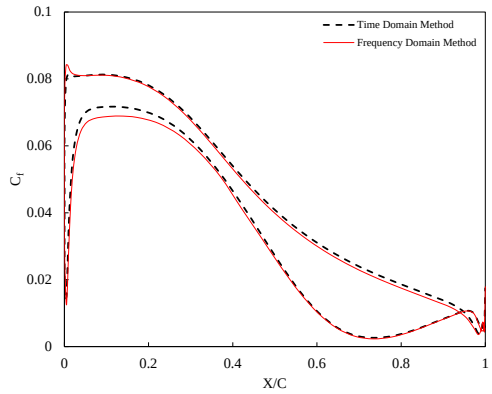

a) 25% span

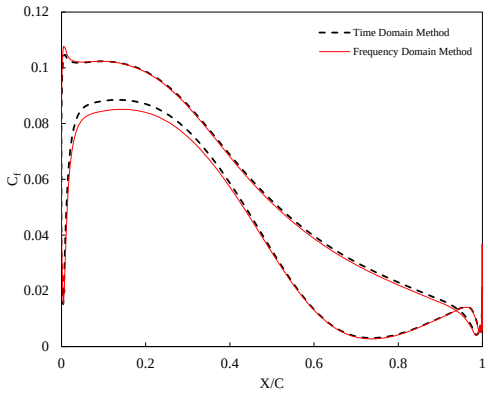

b) 30% span

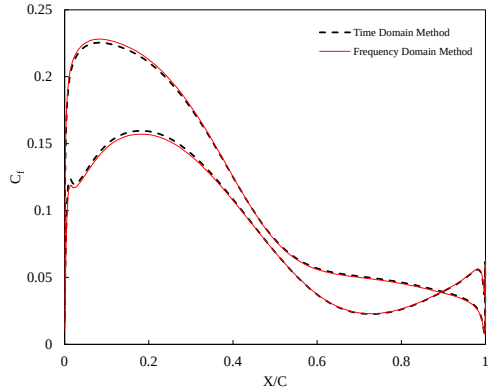

c) 50% span

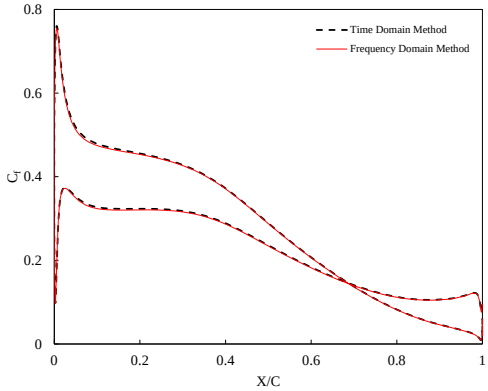

d) 90% span

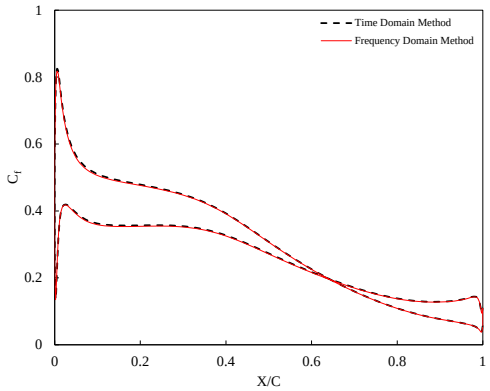

e) 95% span

Figure 7.6. Time-averaged skin friction coefficient distributions at different blade sections of the downstream wind turbine obtained from the time domain method and the frequency domain method.

Figure 7.7 demonstrates the comparison between the frequency domain method and the time domain method for the dimensionless wake profile, on the horizontal plane at the blade mid-span section, extracted at 1D before the downstream wind turbine. The purpose

of this comparison is to validate the frequency domain solution method in predicting the downstream wake profile. These profiles are shown for a distance of 1D to each side from the rotor centre. Slight deviations are observed between the two methods; however, the differences are very small, and the results obtained are in good agreement. The wake profile is calculated based on the variations of the velocity magnitude over the reference inflow velocity (V/V_{ref}). It is seen that the lowest peak of the wake occurs near the X/D=0, which is at the rotor centre, and it has a symmetrical profile on both sides. Consequently, it can be deduced that the numerical model employed in the present study is able to capture the unsteady flow and predict the wake accurately. This also indicates that the flow variables are exchanged correctly at the interface between the rotating and stationary domains.

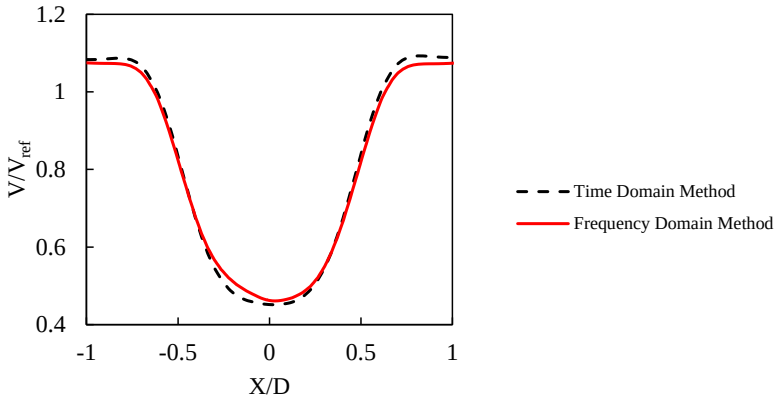

Figure 7.7. Wake profiles extracted at one rotor diameter before the downstream wind turbine obtained from the time domain method and the frequency domain method.

In-depth discussions on the effect of the upstream wind turbine on the downstream one will be presented in the next section. The results show that not only the proposed frequency domain solution method can capture the unsteady flow and calculate flow parameters accurately but also the rotor-stator interface has been applied correctly as the results are in close agreement between the two methods for both wind turbines. In order to highlight the advantage and the capability of the frequency domain method and also for a direct comparison between the two methods, the computational costs are compared for a period of an unsteady solution on a single CPU with a 3.40 GHz Intel (R) Core (TM) i5-7500 CPU. For the time domain solution, both a dual time-stepping method and a time-consistent multigrid method are employed for an effective and efficient computation. From a sensitivity study conducted, a time-step size of 0.003 s, which is a minimum of 40 steps per revolution, is found to be sufficient and used for the time domain solution. It

has been proved that these methods can accelerate the computation. The simulation using the frequency domain method takes 6 hours, whereas that of the time domain method takes 200 hours even with an efficient computation. The required number of periods for an unsteady solution depends on the rotational speed and the distance between the two turbines. However, with a frequency domain solution method, the unsteady perturbations are computed based on a period of the unsteady flow and the solution can be reconstructed in time to have the flow solution in time history. The computational efficiency of the proposed frequency domain solution technique is considerable even when using a single CPU, and simulations of multiple wind turbines can be performed efficiently with this method. Therefore, it is concluded that the frequency domain solution method can be reliably utilised for further simulations of wind turbines in arrays by varying the distance between the two turbines.

Figure 7.8 compares the time-averaged pressure coefficients obtained from the upstream wind turbine and the downstream wind turbine using different separation distances. The black line represents the pressure coefficient from the rotor blades of the upstream wind turbine whereas the rest of them are from that of the downstream wind turbine at different separation distances. The effect of the wake from the upstream wind turbine on the downstream one can be seen at all distances. The impact is much higher and more significant at the separation distances of 2D and 5D. This indicates that the separation distance of 5D is not far enough for the downstream wind turbine to avoid pressure losses if the downstream wind turbine is to be placed in the wake region of the upstream one. The flow recovers beyond the distance of 5D, and the downstream wind turbine is less affected by the upstream one at 10D distance. However, there is still a noticeable impact from the upstream wind turbine at this far distance. This is because the flow turbulence and unsteady perturbations from the upstream wind turbine still exist at 10D distance. Although these effects are lower at 10D, the inflow for the downstream wind turbine is not entirely uniform with a lower velocity magnitude compared to the upstream turbine. This results in deviations in pressure distribution between the upstream and downstream turbines. The results illustrate that the pressure coefficient on the blade surfaces of the downstream turbine at X/C=0.2 is increased by approximately 30% by raising the distance from 2D to 10D at 50% span. Strong deviations in pressure distributions are detected near the leading edge of the blades whereas a similar trend is noticed after X/C=0.5. These pressure deviations are mainly caused by the non-uniform inflow with a lower velocity magnitude which alters pressure distributions near the leading edge. These

observations indicate that the effect of the upstream wind turbine can be reduced by raising the distance from 5D to avoid significant pressure losses for the downstream wind turbine.

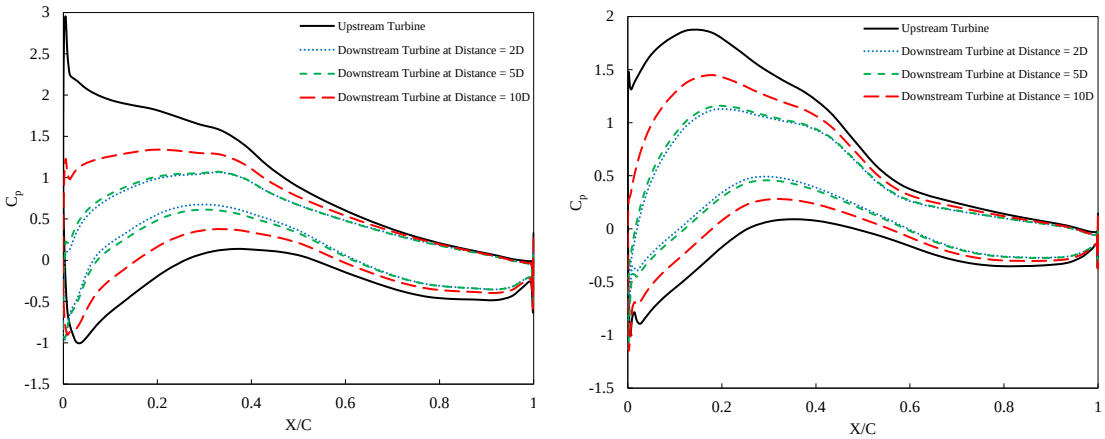

a) 30% span

b) 50% span

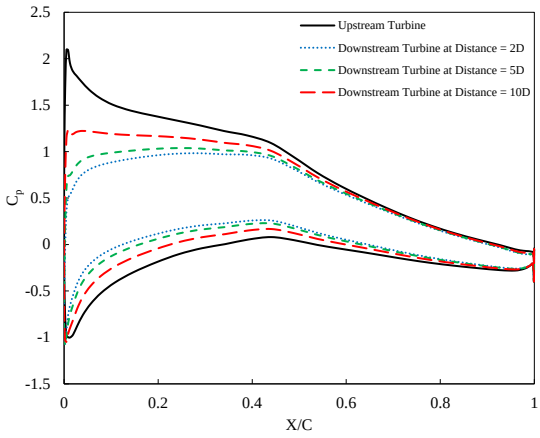

c) 90% span

Figure 7.8. Time-averaged pressure coefficient distributions at different blade sections of the upstream wind turbine and the downstream wind turbines at different separation distances.

Unsteady pressure distributions on the blade surfaces of both upstream and downstream wind turbines can be visualised in Figs. 7.9 and 7.10. Unsteady pressure distribution can be decomposed into the time-averaged value $\bar{P}$ and amplitude of unsteady fluctuations $\tilde{P}$. Figure 7.9 presents the time-averaged pressure contour on the pressure and suction surfaces of both wind turbines. On the blade of the upstream wind turbine, higher pressure distributions are seen on the pressure surface near the leading edge and the trailing edge whereas lower pressure distributions are observed on the suction surface from approximately 40% of the blade span. In the case of downstream wind turbines, pressure

distributions on the blade surfaces are lower due to the wake of the upstream wind turbine. At the separation distances of 2D and 5D, the pressure is higher near the trailing edge than the leading edge. A lower pressure field is developed within 60% - 100% of the blade span sections on the suction surface, which is shorter than that of the upstream wind turbine. In the case of 10D separation distance, the pressure seems to recover as it is far away from the upstream wind turbine. On the pressure surface, the pressure is higher near both leading and trailing edges than that of the 2D and 5D cases whereas the low-pressure field starts to occur at approximately 55% of the blade span section, which is closer to that of the upstream wind turbine. However, the effect of the upstream wind turbine is still present by a noticeable amount, even at this far distance, as pressure distributions on the blade surfaces of the downstream wind turbine are lower.

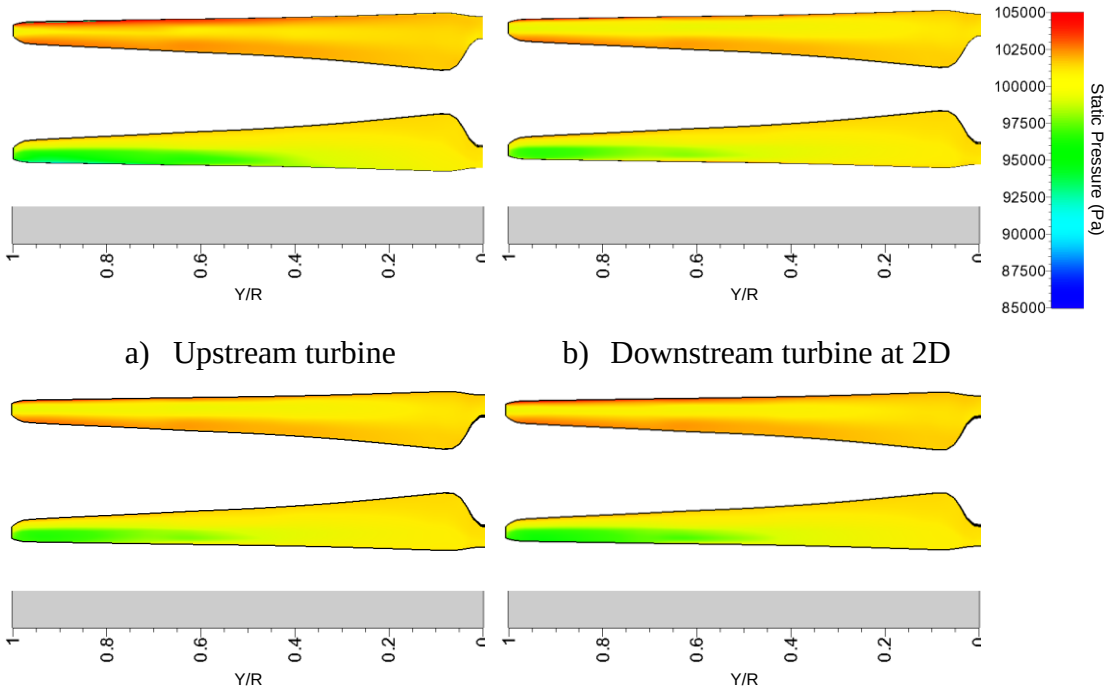

a) Upstream turbine b) Downstream turbine at 2D

c) Downstream turbine at 5D d) Downstream turbine at 10D

Figure 7.9. Time-averaged pressure ($\bar{P}$) distributions on the pressure surface *(upper)* and the suction surface *(lower)* of the blade from the upstream wind turbine and the downstream wind turbine at different separation distances.

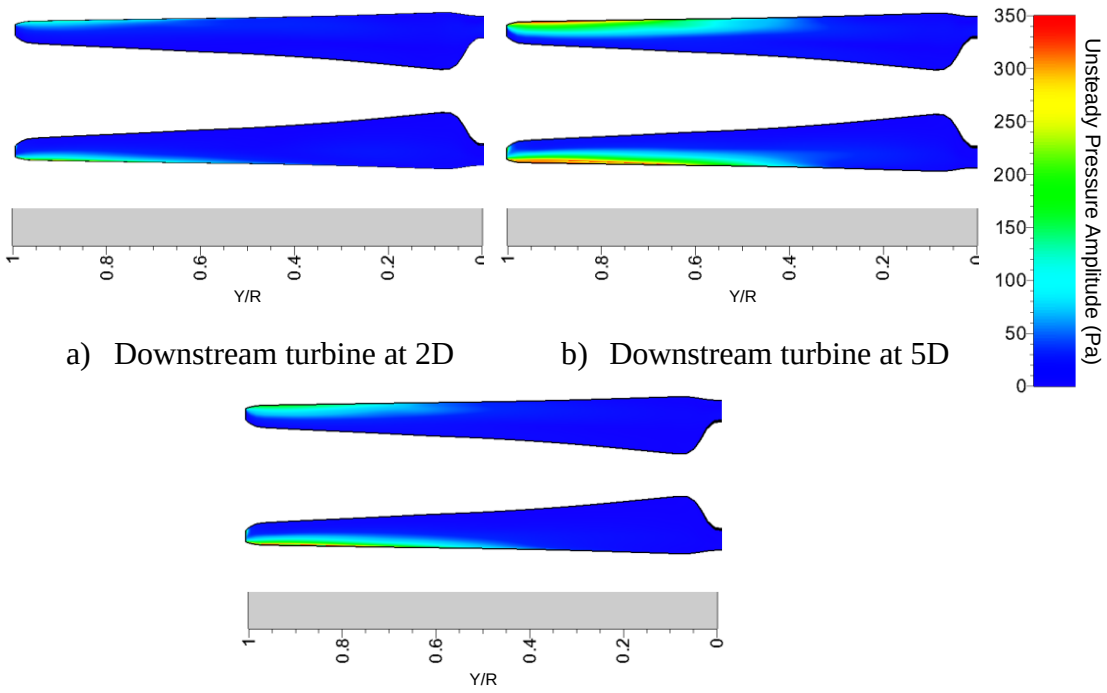

a) Downstream turbine at 2D b) Downstream turbine at 5D

c) Downstream turbine at 10D

Figure 7.10. Unsteady pressure amplitude ($\tilde{P}$) distributions on the pressure surface *(upper)* and the suction surface *(lower)* of the blade from the downstream wind turbine at different separation distances.

Figure 7.10 depicts the unsteady pressure amplitude contours on the pressure and suction surfaces of the downstream wind turbine placed at different separation distances behind the upstream wind turbine. The amplitudes of unsteady fluctuations are only visible in the cases of the downstream turbine. At the separation distance of 2D, unsteady pressure fluctuations are seen near the blade tip on both surfaces. However, compared to the 2D separation distance case, the amplitude of the unsteady pressure is much higher at the 5D separation distance. Unsteady pressure distributions are also seen on both surfaces, around the leading edge, starting from approximately 40% of the blade span section. In the case of 10D separation distance, the unsteady pressure fluctuations tend to decrease, as they are lower than that of the 5D separation distance case. However, the amplitude and fluctuations are still higher than the 2D separation distance case. These results and observations show that the far wake imposes more turbulence and flow disturbances, and it has a more significant impact on the unsteady pressure distributions on the blade surfaces of the downstream wind turbine than the near wake as the amplitude is maximum at 5D separation distance and it tends to reduce beyond this distance.

Pressure distributions on the blade surfaces are directly related to the aerodynamic loads acting on the blade surfaces. The aerodynamic loads applied on the blade surfaces are provided in terms of torque and force profiles. The force profiles are evaluated based on the axial thrust. Figure 7.11 shows the torque and force coefficient profiles acting on the surfaces of the upstream wind turbine and downstream one at different separation distances. The coefficients, denoted by τ/τ_{max} for torque and F/F_{max} for force, are defined as: *(Torque on Blade-Average Torque on Blade)/(Maximum Torque on Blade)* and *(Force on Blade-Average Force on Blade)/(Maximum Force on Blade)*, respectively. Both torque and force profiles are plotted with respect to the transient dimensionless computation time for one complete rotor revolution. The results show that, in the case of the upstream wind turbine, the force profile is nearly uniform with some fluctuations whereas the deviation of the torque profile is noticeably stronger. However, harmonic force profiles are detected for both torque and force profiles on the blade of the downstream wind turbines. The amplitudes of the torque and force coefficients are intensified by 75% and 70%, respectively, when increasing the separation distance from 2D to 5D and then they tend to reduce by 20% and 50%, respectively, when increasing the distance between the wind turbines from 5D to 10D. It is noted that the difference in amplitude between the 5D and 10D cases is smaller for torque profiles than force profiles. In both cases, the aerodynamic loads acting on the blade surfaces are maximum at the 5D separation distance due to the flow turbulence and the far wake effect from the upstream wind turbine. These are consistent with the unsteady pressure distributions discussed in Fig. 7.10.

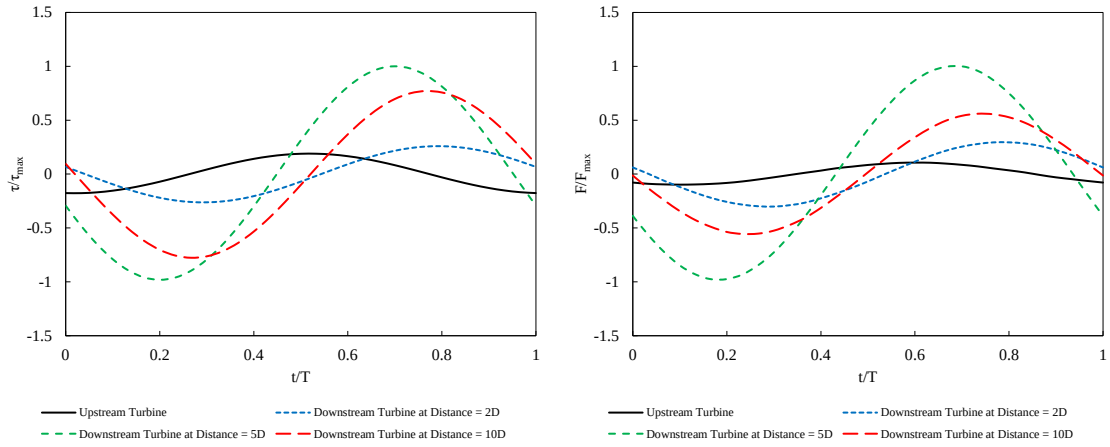

a) Torque profile b) Force profile

Figure 7.11. Torque and force profiles applied on the blade surfaces obtained from the upstream and downstream wind turbines at different separation distances.

Figure 7.12 demonstrates the comparison of the skin friction coefficients on the blade surfaces of the upstream wind turbine and the downstream one placed at different separation distances. Similar to pressure coefficient distributions, the skin friction coefficients on the blade surfaces of the downstream wind turbine are most affected by the upstream wind turbine at the separation distances of 2D and 5D. However, it is less affected at the separation distance of 10D as it is very far from the upstream wind turbine. At this distance, the wake generated from the upstream wind turbine recovers and the flow is nearly uniform again. This leads to a similar trend of skin friction coefficient distribution on the blade surfaces of the downstream wind turbine as that of the upstream turbine, but some noticeable variations and effects from the upstream turbine are still observed. The results show that the skin friction coefficient is the highest near the leading edge of the wind turbine blade due to the boundary-layer flow formation in this region. The fluctuations in the skin friction coefficient with respect to X/C are mainly related to the flow separation and recirculation over the suction surface of the blade.

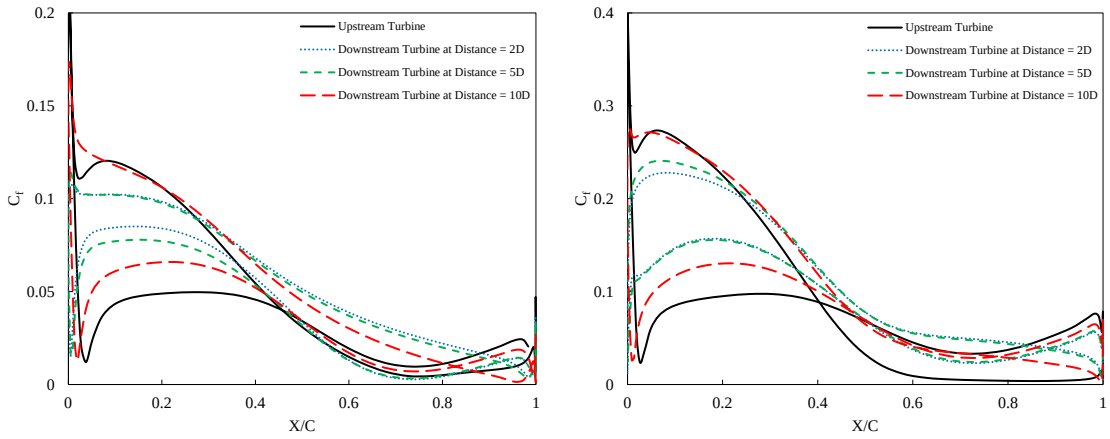

a) 30% span

b) 50% span

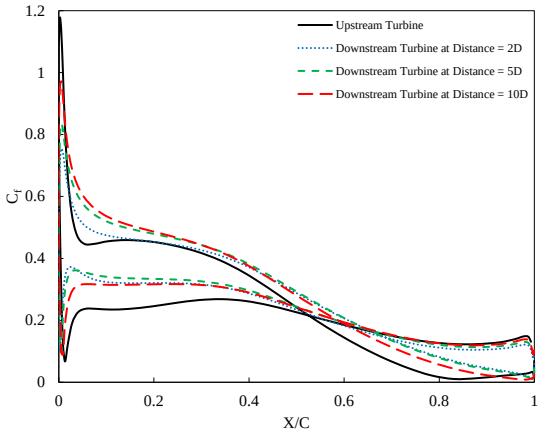

c) 90% span

Figure 7.12. Time-averaged skin friction coefficient distributions at different blade sections of the upstream wind turbine and the downstream wind turbines placed at different distances behind the upstream turbine.

Figure 7.13 illustrates the instantaneous velocity profiles or wake profiles calculated at 1D before the downstream wind turbines at different separation distances. They are obtained from the frequency domain solution and the instantaneous velocity profiles are plotted from the time reconstruction of the frequency domain solution. By plotting the instantaneous velocity profiles, the behaviour of flow in both space and time (i.e., the velocity magnitude at different locations at a certain physical time) can be determined. The profiles are extracted on the horizontal plane at the blade mid-span section for a distance of 1D to each side from the rotor centre. These profiles demonstrate the wake profiles with respect to the distance from the upstream wind turbine as well as the inflow profile for the downstream wind turbine. The -0.5X/D to 0.5X/D region lies within the rotation of the blades and the velocity in this region is reduced as the flow interacts with the blade which then captures the energy from the wind. The results show that the amplitude of the wake profile becomes smaller by increasing the distance from the upstream wind turbine. The minimum peak of the wake occurs around the rotor centre; however, it is shifted towards 0.09X/D at 9D behind the upstream wind turbine which is 1D before the downstream wind turbine at the separation distance of 10D. It was observed that the unsteady perturbations are maximum at the 5D separation distance, which is why a small shift in the profile is seen at the 4D distance. It is also noted that the wake beyond 5D distance gradually recovers; however, the unsteady perturbations are still present with low intensity. Even at the distance of 10D which is far away from the first turbine, where

the flow seems to be more uniform, the perturbations and swirl flow are not completely vanished. Furthermore, as a result of the recovery process from the unsteady fluctuations, the inflow profile for the downstream turbine is not aligned with the rotor. This is the reason why the minimum peak for the velocity profile at 9D distance shifts slightly towards the positive side. The fact that the wake profiles at 4D and 9D distances shift towards the positive side is related to the direction of the rotation of the rotor as both turbines rotate in the same direction with the same rotational speed. These profiles indicate that the wake from the upstream wind turbine is still significant at the distance of 4D behind the upstream turbine. Therefore, a great impact on flow parameters was seen on the blade of the downstream wind turbine placed up to 5D from the upstream turbine. However, at the distance of 9D, the amplitude of the wake profile reduces and the inflow velocity for the downstream wind turbine tends to be closer to the reference velocity.

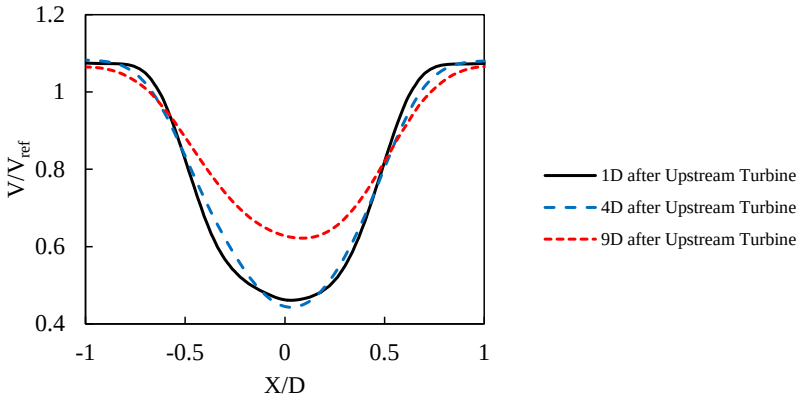

Figure 7.13. Wake profiles calculated at the distances of 1D, 4D and 9D behind the upstream wind turbine.

Figure 7.14 demonstrates the wake profiles 1D after both upstream and downstream wind turbines with different separation distances. The profiles are extracted in a similar way to the previous profiles. This figure compares the near wake profiles after the flow interaction with each turbine. Compared to the upstream wind turbine, the velocity drop in the region of the blade rotation (i.e., -0.5X/D to 0.5X/D) is more sudden and significant in the cases of the downstream wind turbine and some variations are also seen near the rotor centre. The amplitudes of the wake profiles at the distance of 1D behind the downstream turbine reduce by increasing the distance between the two turbines. A large separation distance reduces the impact on the downstream turbine, and the magnitude of the wake generated from the downstream turbine at the separation distance of 10D is

closer to that of the upstream turbine compared to other cases. Furthermore, it is noted that the inflow is completely uniform and steady at a reference velocity for the upstream wind turbine whereas the profile is parabolic with a lower magnitude but stronger velocity distribution in the blade tip region for the downstream wind turbine. The inflow profiles for each downstream turbine case can be understood by looking at the profiles presented in Fig. 7.13. For instance, the profile at 9D distance is the inflow profile for the downstream turbine at 10D distance. By increasing the separation distance to 10D, the intensity of the flow perturbation and recirculation are reduced, but their effects are still present. This is the main reason why the wake profiles at 1D behind the upstream wind turbine and the downstream wind turbine are not similar. The impact of the swirl flow produced by the upstream wind turbine on the downstream one is significant at the separation distance of 2D, and it is reduced by increasing the distance to 10D, but it is not vanished. The main reasons for obtaining different shapes of the wake profile can be explained in a similar way. The recirculation and flow perturbations generated from the upstream wind turbine alongside the lower velocity magnitudes due to the wakes will have a noticeable impact on the amplitude of the wake profiles of the downstream one. The flow structures become more non-uniform by reducing the distance between the wind turbines from 10D to 2D.

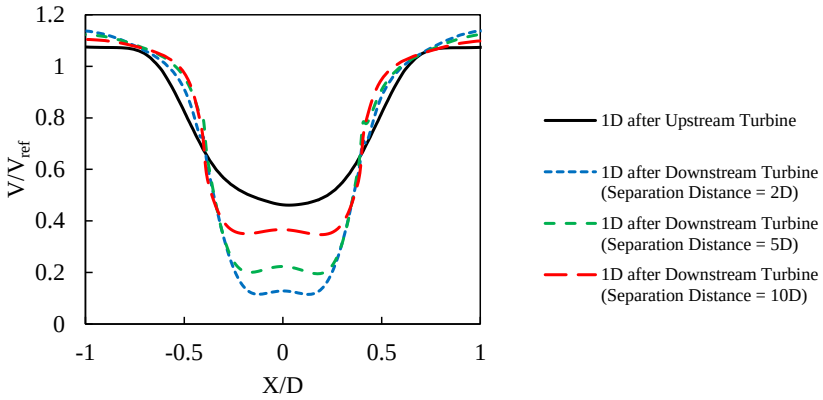

Figure 7.14. Wake profiles calculated at 1D after the upstream wind turbine and 1D after the downstream wind turbines at different separation distances.

The wake profiles, discussed in Fig. 7.14, can be better understood by looking at velocity contours extracted at 1D behind each turbine on the plane normal to the wind direction (See Figure 7.15). This figure particularly provides the flow information for visualisation of the flow condition at the same distance behind each turbine. It is seen that, in the case of the upstream wind turbine, the velocity distribution from the blade tip region to the

blade root region is relatively linear whereas multiple layers of different velocity magnitudes are observed behind the rotors of downstream wind turbines. The velocity field is significantly affected after the flow interacts with the downstream wind turbine. The flow condition at the distance of 1D behind the downstream turbine depends on the separation distance. The velocity magnitude within the blade rotation, especially from approximately 40% to 80% span, is dramatically reduced when the downstream turbine is closer to the upstream turbine and it rises as the separation distance increases. Significant drops in the wake profiles, seen in Fig. 7.14, are associated with this physical phenomenon.

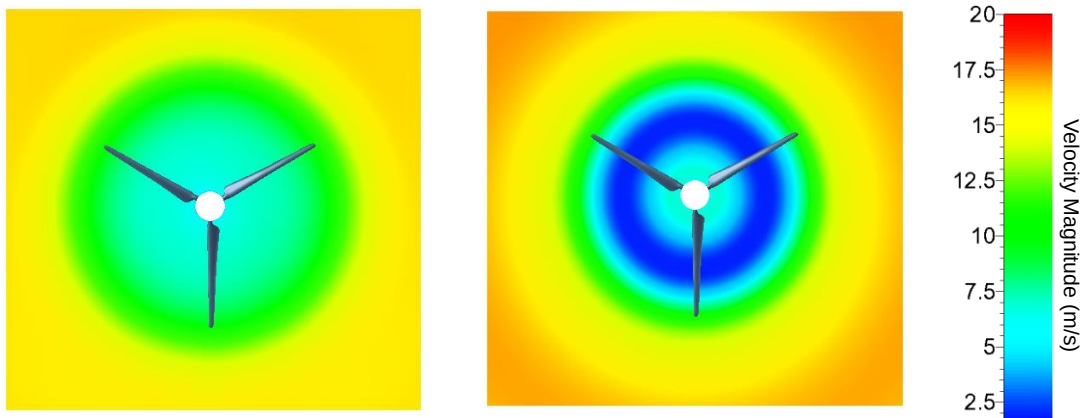

a) Upstream turbine b) Downstream turbine at 2D

c) Downstream turbine at 5D d) Downstream turbine at 10D

Figure 7.15. Velocity fields on the plane extracted at 1D behind the upstream wind turbine and the downstream wind turbines at different separation distances.

The instantaneous velocity contours in the meridional view from different separation distance cases are provided in Fig. 7.16 to visualise the flow field around and between the two wind turbines. The uniform inflow velocity is dramatically reduced after the flow

interaction with the upstream wind turbine. In the case of 2D separation distance, the lower velocity field or the wake and the swirl flow generated from the upstream turbine are still strongly present at the distance of 2D where the downstream turbine is located. As a result, the flow around the downstream turbine is most dominated by the wake of the upstream turbine at this distance and the velocity magnitude is further reduced behind the downstream turbine. In the case of 5D separation distance, the wake from the upstream turbine gradually reduces but its influence on the downstream turbine is still significant. However, at 10D separation distance, the lower velocity field resulted from the flow interaction with the upstream turbine shrinks as the wake recovers and the flow seems to be nearly uniform again. The swirl flow is transferred through the incoming wind and the rotor rotation. It loses its intensity over time as the degree of turbulence is correlated with the freestream velocity, and it diffuses into the atmosphere. However, it should be noted that, as discussed in Fig. 7.14, the swirl flow and unsteady perturbations from the upstream turbine are still present at this distance. Despite the flow becoming more uniform at the 10D distance compared to other cases, it is not entirely uniform yet as the velocity profile is parabolic in shape. It is seen that the magnitude of the inflow velocity is lower than the reference velocity; however, it is larger than any other cases. As a result, the trends of the distributions of flow parameters such as pressure on the blade surfaces on the downstream turbine are similar to that of the upstream turbine with less magnitude due to lower inflow velocity. Furthermore, it is also observed that the separation distance has an impact on the vortex generation and flow circulation from the tips of the blades of the downstream wind turbine. The size of the tip vortex structures around the downstream turbine at the separation distance of 2D is higher than that of any other cases as it combines with those from the upstream turbine due to the small separation distance. As the separation distance increases, the vortex structures generated from the blades of the upstream turbine continue to a certain distance before gradually losing their intensity, but it is too far to reach the downstream turbine if the turbine is placed at the 10D distance. As the inflow for the downstream wind turbine is not uniform and identical as it is for the upstream one, the wake behind the downstream turbine involves more turbulence and unsteadiness. The flow recirculation generated from the upstream wind turbine also has an impact on the flow disturbance and boundary-layer disruption near the blades of the downstream rotor. The flow unsteadiness and the influences of the wakes on the flow field around the wind turbines are considerable at different separation distances.

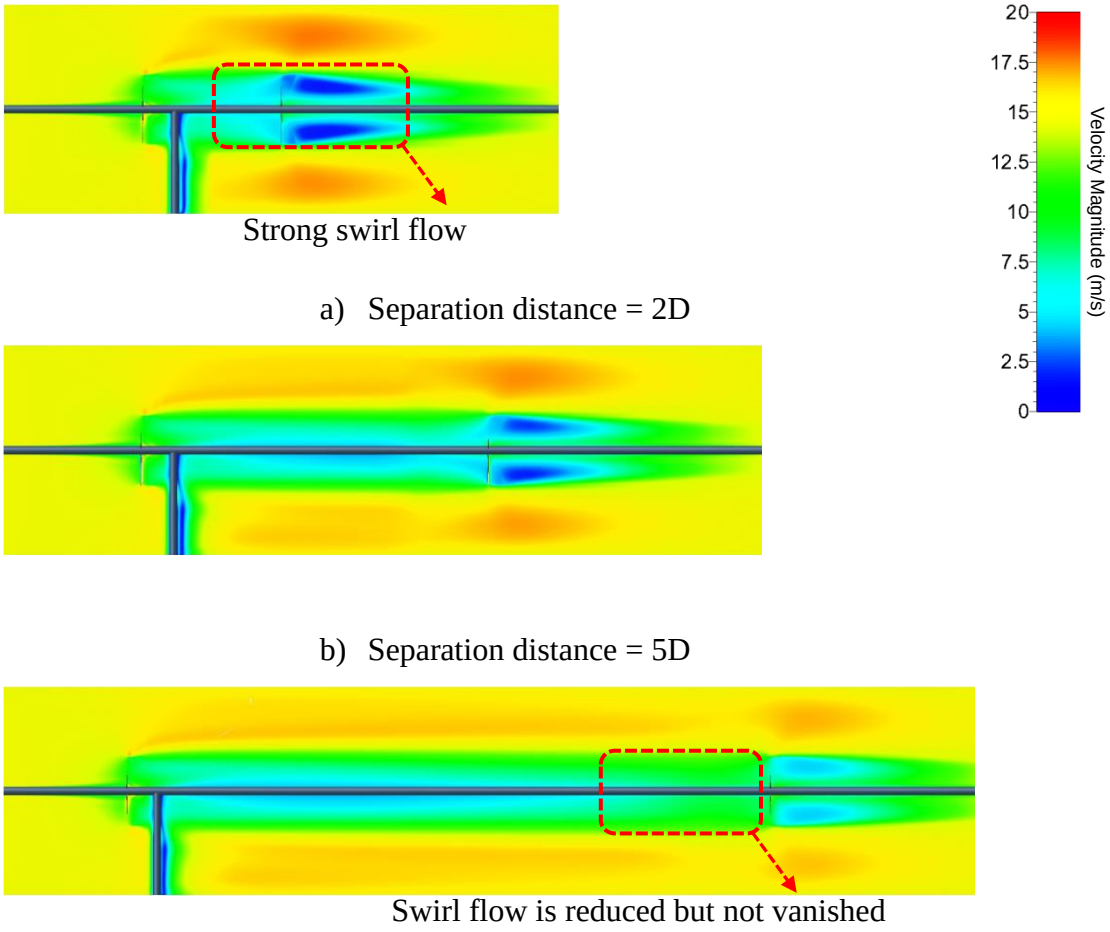

Figure 7.16. Velocity fields around the wind turbines in the meridional view from different separation distance cases.

Figure 7.17 demonstrates the vorticity field generated from the upstream and downstream wind turbines and the velocity streamlines passing through both turbines. In these figures, the mass transport process of the fluid flow with respect to the rotation of the wind turbine rotor can be visualised. It is seen that the fluid particles are carried along the blades as the rotor rotates, and the tip vorticity is generated at the blade tip. The recurring pattern of vortex generation and the wind flow pushes the vorticity field away from the turbine which then gradually diffuses into the atmosphere. The effect of the upstream turbine on the downstream one can be seen in Fig. 7.17 (b) by means of flow streamlines. It is observed that the flow passing through the upstream wind turbine is turbulent and non-uniform. Hence, the downstream wind turbine experiences, depending on its location, the non-uniform unsteady inflow and pressure loss compared to the upstream turbine.

a) Vorticity field

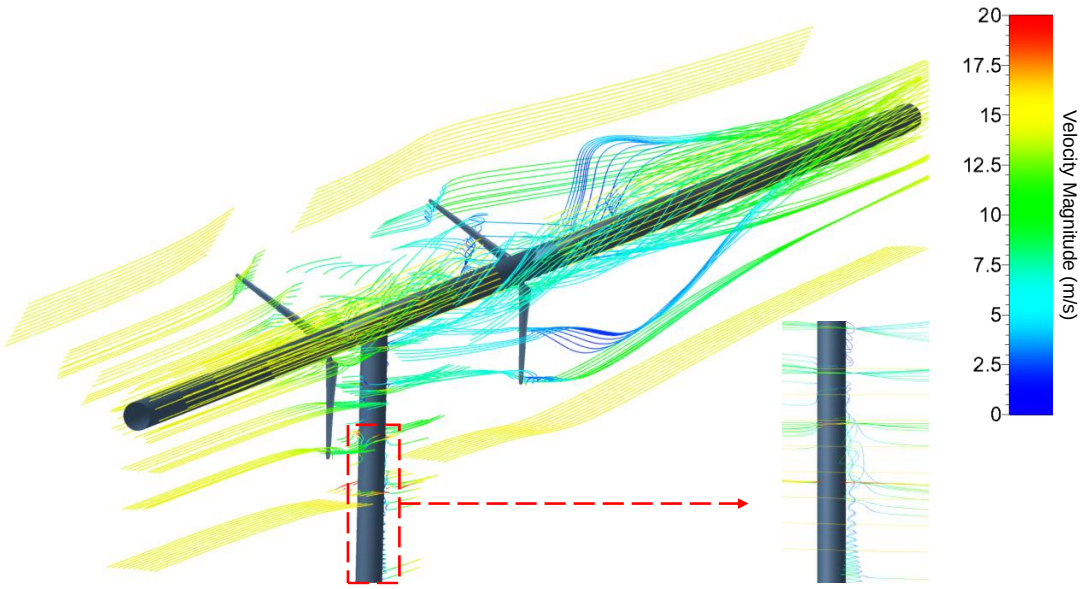

b) Velocity streamlines

Figure 7.17. Vorticity field and velocity streamlines around the upstream and downstream wind turbines at 2D separation distance.

Pressure distributions around the aerofoil at the blade mid-span section from both wind turbines are presented in Fig. 7.18. Generally, the pressure is higher on the pressure side and lower on the suction side of the aerofoil, and the highest-pressure concentration is typically found near the leading edge. In the case of the upstream wind turbine, the highest pressure is observed on the pressure side near the leading edge. The pressure distributions and the location of the highest-pressure concentration around the aerofoil of the downstream wind turbine depend on the separation distance from the upstream turbine.

At the separation distances of 2D and 5D, pressure distribution on both sides of the aerofoil is much lower than that of the upstream turbine, and the highest pressure is seen at the leading edge. In the case of the 10D separation distance, pressure distribution recovers as it is higher than the 2D and 5D cases but still lower than that of the upstream wind turbine. However, the highest-pressure concentration point shifts slightly towards the pressure surface.

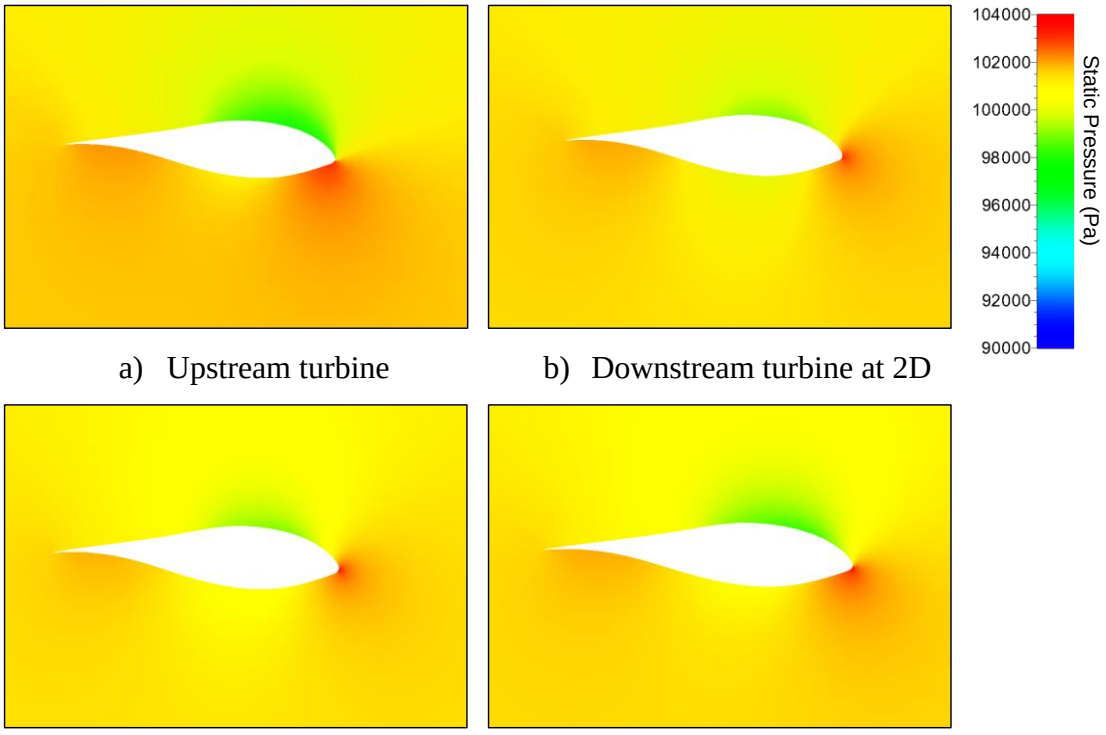

Figure 7.18. Pressure distributions around the aerofoil at the mid-span section of the blade of the upstream wind turbine and the downstream wind turbines at different separation distances.

Velocity distributions around the aerofoil at the blade mid-span section from both wind turbines are shown in Fig. 7.19. In the case of the upstream wind turbine, the high-velocity concentration is seen around the leading edge. After the relative velocity interacts with the blade aerofoil, the velocity is distributed from the pressure surface near the leading edge over to the suction surface up to half of the chord length. A little flow separation from the suction surface is also seen near the trailing edge. However, in the cases of the downstream wind turbine with separation distances of 2D and 5D, the velocity magnitude is lower than that of the upstream turbine and the velocity distribution is slightly different.

The flow interaction point with the blade aerofoil moves towards the leading edge and the velocity is distributed from the leading edge over to the suction surface. The flow separation is very small compared to the upstream turbine. At 10D distance, the velocity magnitude tends to increase again as the wake from the upstream turbine recovers. The flow interaction point shifts a bit towards the pressure surface and the velocity distribution is similar, but with less magnitude, to that of the upstream turbine.

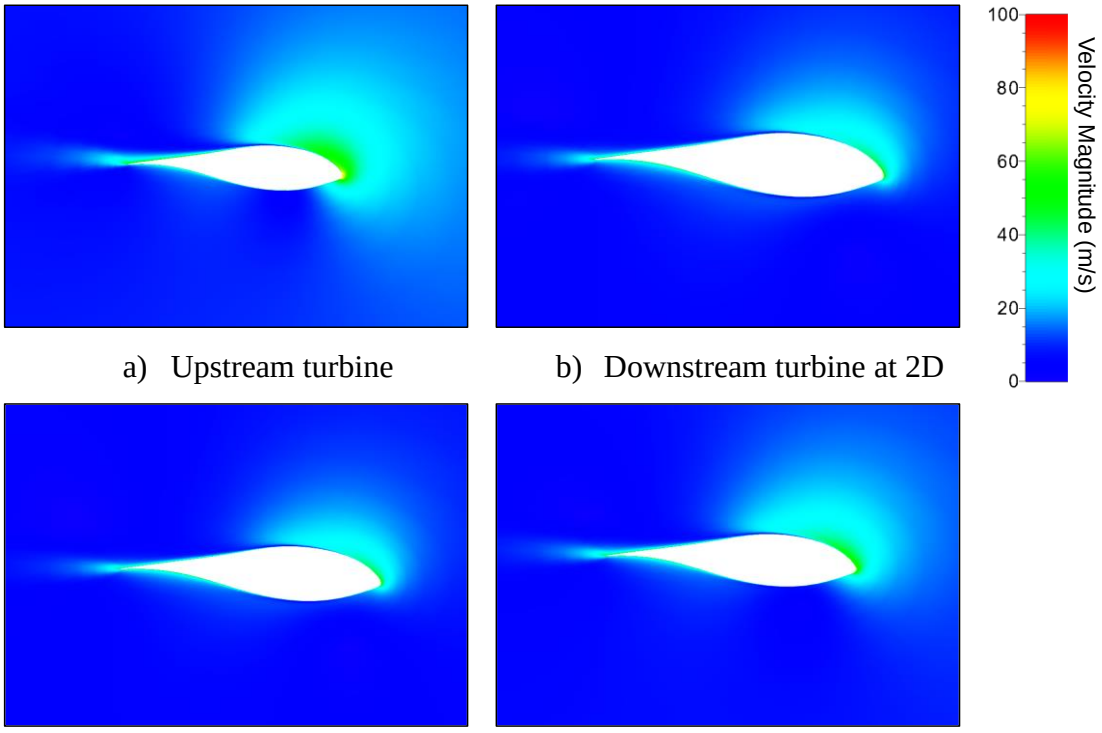

a) Upstream turbine b) Downstream turbine at 2D

c) Downstream turbine at 5D d) Downstream turbine at 10D

Figure 7.19. Velocity distributions around the aerofoil at the mid-span section of the blade of the upstream wind turbine and the downstream wind turbines at different separation distances.

Figure 7.20 shows the relative velocity streamlines around the aerofoil at the blade mid-span section of both wind turbines. This can be visualised together with the velocity distribution, presented in Fig. 7.19. The direction of the relative velocity and the flow interaction with the aerofoil are different between the upstream and downstream wind turbines, and they also depend on the separation distances between the turbines. In the case of the upstream wind turbine, the angle of attack is larger than any other cases due to the uniform inflow. The wakes from the upstream wind turbine trigger flow disturbances, which changes the direction of the inflow for the downstream turbines. As

a result, the angle of attack for the blade of the downstream wind turbine is smaller than that of the upstream turbine. The angle of attack is much smaller in the cases of 2D and 5D separation distance as the wake from the upstream wind turbine is significant at these distances and the flow around the downstream wind turbine is highly influenced by the wake. However, the angle of attack becomes larger and closer to that of the upstream turbine at the 10D distance as the wake from the upstream turbine recovers and the inflow velocity for the downstream turbine is nearly uniform again.

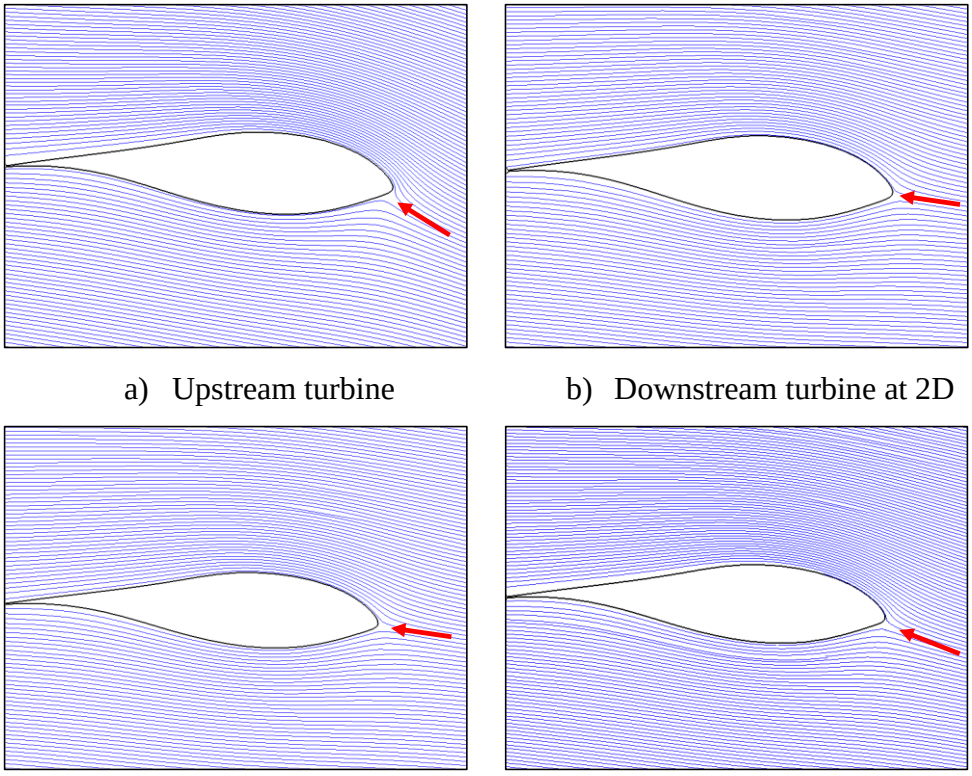

a) Upstream turbine b) Downstream turbine at 2D

c) Downstream turbine at 5D d) Downstream turbine at 10D

Figure 7.20. Flow streamlines around the aerofoil at the mid-span section of the blade of the upstream wind turbine and the downstream wind turbines at different separation distances.

Figure 7.21 illustrates the relative velocity streamlines in the rotating frame of reference for the upstream and downstream wind turbines. In order to highlight the flow streamlines generated from the upstream wind turbine alone, the streamlines from a single turbine case are presented for the upstream turbine. The streamlines are provided up to 4D downstream of all turbines. The three-dimensional view and meridional view are provided for better visualisation and comparison between different cases. This figure clearly shows the effects of the upstream wind turbine on the flow circulation and wake

recovery process behind the downstream wind turbine at different separation distances. Three layers of streamlines from the blade root region, the blade mid-span region and the blade tip region where the tip vortex is generated are presented. In the case of the upstream wind turbine, due to the uniform and steady inflow condition, a recurring pattern of flow streamlines are generated from each layer of the rotor blades. It is also seen that the streamlines are consistent up to the 4D distance, which indicates that the downstream wake is still strong. This is also consistent with the aerodynamic parameters of the blades of the downstream turbine placed at 2D and 5D, where the flow is strongly influenced by the wake of the upstream turbine. For the downstream wind turbines, the flow generated from the tip of the blade slightly expands and then gradually becomes smaller as it moves further away from the turbine whereas the flow from the blade root region is circulated around the hub. The major difference between the cases can be seen in the streamlines generated from the blade mid-span region. This is also consistent with the velocity contours presented in Fig. 7.15 in which it was seen that the velocity fields in the region of 40% - 80% span were significantly affected. In the case of 2D separation distance, the circulation of the flow streamlines from the blade mid-span region suddenly expands by a great extent after leaving the blades which then graduate reduces. Compared to the 2D distance case, the expansion of the flow streamlines is smaller in the 5D distance case whereas no noticeable expansion is observed in the 10D distance case. It is noticed that the streamline behaviours from the 10D distance case tend to be similar, but with some deviations, to those of the upstream turbine because it is placed at a relatively far distance and the inflow condition is more uniform than the other two cases. In terms of the wake recovery process, it is seen that the recovery of the velocity magnitude is shorter in the 5D case than in the 2D case. However, in the case of 10D separation distance, the velocity field behind the rotor of the downstream turbine remains relatively greater compared to the other two cases due to the nearly uniform inflow, which then gradually recovers to reach the reference velocity in the far downstream region. Therefore, it is now evident that the flow unsteadiness and turbulence resulted from the upstream wind turbine have a great influence on the vortex generation and the wake recovery process of the downstream wind turbine.

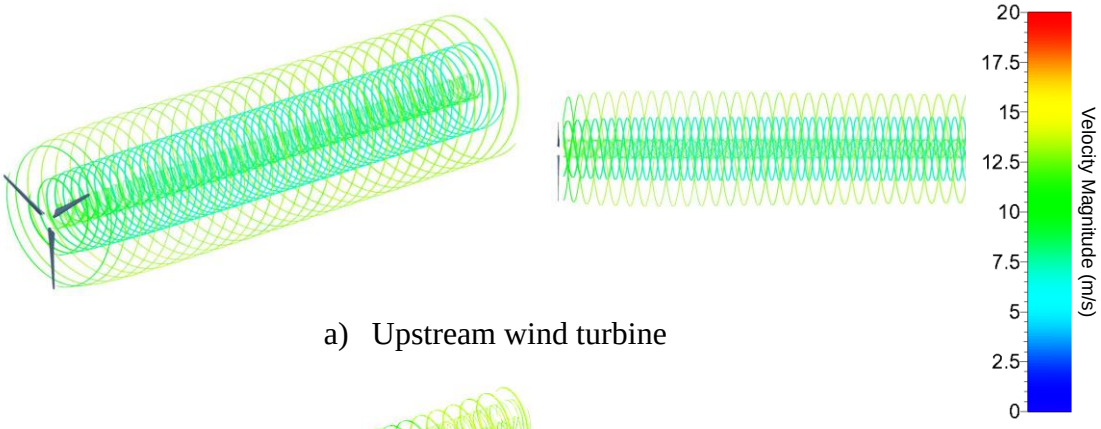

a) Upstream wind turbine

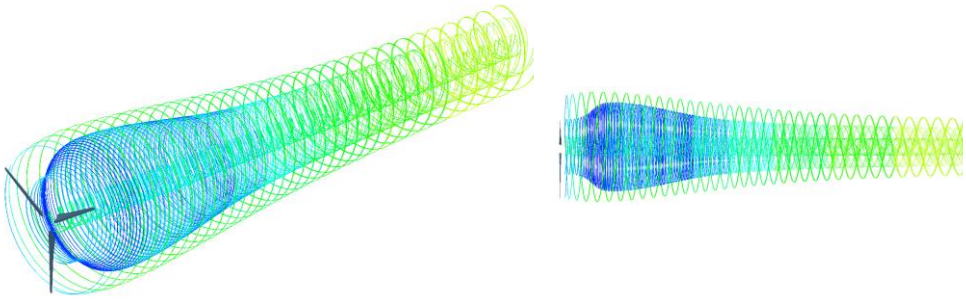

b) Downstream wind turbine at separation distance = 2D

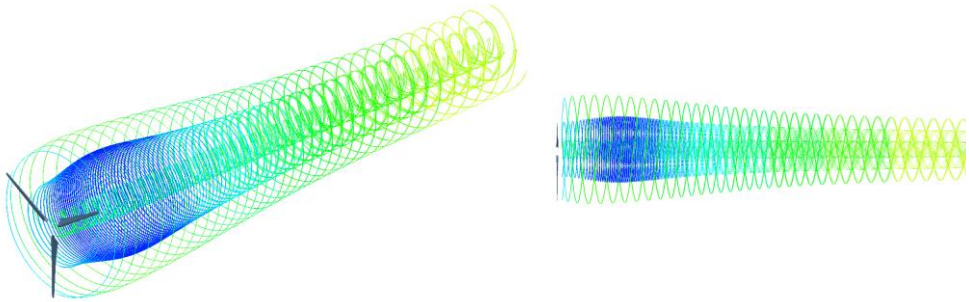

c) Downstream wind turbine at separation distance = 5D

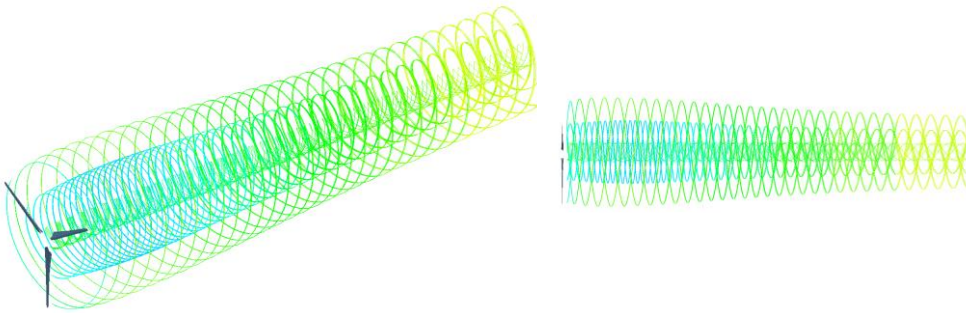

d) Downstream wind turbine at separation distance = 10D

Figure 7.21. Flow streamlines generated from the upstream wind turbine and downstream wind turbines at different separation distances.

7.4. Summary of the Chapter

In the present study, numerical simulations have been performed to investigate the effects of separation distances between upstream and downstream wind turbines in arrays on the aerodynamic performances and flow field around both wind turbines. A novel frequency domain solution method is employed for the first time to model the wind turbines in arrays as a multi-stage turbine in a multi-stage configuration.

It is found that pressure coefficient and skin friction coefficient distributions on the blade surfaces of the downstream wind turbine are significantly influenced by the wake of the upstream wind turbine. The effect of the upstream wake is significant up to the separation distance of 5D and then it gradually reduces. The far wake from the upstream turbine has more effect on the downstream turbine than the near wake. The amplitudes of unsteady fluctuations including pressure and force distribution on the blade surfaces are maximum at the separation distance of 5D. The flow field and wake from the upstream turbine gradually recover beyond the distance of 5D and the aerodynamic performances of the downstream wind turbine tend to increase again. Furthermore, flow visualisations show that the velocity field behind the downstream turbine is most affected in the 40% - 80% span region of the blade rotation, and the impact is more significant at smaller separation distances. Therefore, it is certain that the downstream wind turbine cannot be placed within the separation distance of 5D. According to Sun et al. [11], the minimum spacing restriction of 5D is employed in recent optimisation studies. Furthermore, it is understood that the common practice for the placement of the downstream wind turbine in most practical applications is around 7D. Hence, a conclusion is drawn based on the results obtained, the reference studies and the common practice that the separation distance should be larger than 5D, and it is recommended that the downstream turbine is placed between 5D and 10D away from the upstream turbine to reduce its effects as well as to optimise the performances of the downstream turbine and the wind farm.

In terms of the computational cost, the frequency domain solution method can reduce the computation time by one to two orders of magnitude in contrast to the time domain method. Although only the rotor of the downstream turbine is considered in this study, further turbines can also be added, and more complex simulations can be performed due to the advantages and capabilities of simulating a series of rotor-stator interactions with the proposed frequency domain solution method.

Chapter 8. Overall Conclusions and Future Work

8.1. General Conclusions

The present PhD thesis proposes a highly efficient nonlinear frequency domain solution method for the aerodynamic and aeromechanical analysis of offshore wind turbines, taking various sources of flow unsteadiness into account. Modelling and simulation of fluid-structure interaction are required for the investigation and prediction of aeroelastic instabilities in wind turbines. The relative motion between the stationary and rotating components of a wind turbine should be considered to analyse the impact of the tower on the flow structures and behaviour. Furthermore, the identification and analysis of the effect of flow unsteadiness associated with different sources of flow unsteadiness including those related to neighbouring wind turbines in a wind farm on aerodynamic performances are very important to optimise the wind farm layout and the energy output. These challenging aspects are considered and discussed in this thesis by using highly accurate CFD simulations.

The numerical investigations of the flow behaviour and the aeromechanical performances of a wind turbine blade aerofoil at various angles of attack and Reynolds numbers are carried out in this thesis. From the aeromechanical analysis at different angles of attack, it is found that raising the angle of attack causes a greater difference in unsteady pressure distribution over the pressure and suction surfaces of the aerofoil. Flow visualisations show that the flow around the aerofoil is affected by the blade vibration. The aerodynamic damping values are positive for all angles of attack, and it is slightly larger at 10^{o}. The blade aerofoil possesses a dominant stabilising effect at all angles of attack. In terms of Reynolds number, the unsteady pressure fluctuations are higher at lower Reynolds numbers. Raising the Reynolds number reduces the unsteady pressure amplitude along the chord of the aerofoil. Pressure distributions around the aerofoil show that the pressure difference between the two surfaces of the aerofoil is higher at $Re = 4 \times 10^5$ than other Reynolds numbers. Velocity contours and streamlines around the aerofoil demonstrate that the flow unsteadies is higher with the laminar vortex shedding identified at $Re = 4 \times 10^5$ and $Re = 8 \times 10^5$. The flow separation and recirculation in the separation zone are both detected on the suction surface at a lower Reynolds number, but they are reduced by increasing the Reynolds number. It is found that the aerodynamic damping is relatively low at $Re = 4 \times 10^5$ and $Re = 8 \times 10^5$ and is increased as the Reynolds number is raised.

The aerodynamic and aeromechanical simulations of the MEXICO-Experiment wind turbine rotor are then performed using the proposed nonlinear frequency domain solution method. The harmonic inflow wakes are generated at various frequencies, and the effects of the inflow turbulence and wake on the aerodynamic performances and the flow field around the wind turbine are investigated. Results obtained show that the aerodynamic flow fields around the wind turbine are distorted by the flow unsteadiness due to the inflow wakes. All wake frequencies have an impact on the aerodynamics of the wind turbine rotor. It is, therefore, concluded that the flow unsteadiness related to the inflow turbulence and wake has a dramatic influence on the aerodynamics of the wind turbine rotor, and it could also influence the aeroelasticity of the wind turbine significantly. The aeromechanical simulations are also performed for this wind turbine using two different materials based on a relatively large deflection of 9% of the span at an IBPA of 120^{o}. The aerodynamic damping values are positive which show that the blade vibrations are damped using the two materials. However, it is found that the use of a composite material could reduce the force applied on the blade surfaces and thereby providing a greater aerodynamic damping value subject to a relatively large amplitude of vibration.

The study is then extended to an aeromechanical simulation of a complete wind turbine model including the tower at an IBPA of 120^{o}. A rotor-stator interface is treated to transfer the flow data between the rotating domain, which includes the rotor, and the stationary domain, which includes the tower. The time-averaged pressure and unsteady pressure distributions at different blade sections are predicted using the proposed frequency domain method and the time domain method. The pressure coefficient profile across the wind turbine indicates that the pressure variation is disturbed by the presence of the tower. Furthermore, the skin friction coefficients at different blade sections as well as the blade loads such as torque, axial thrust and aerodynamic power profiles for one rotor revolution are also calculated using both methods. Extensive validations in terms of different unsteady parameters revealed that the results obtained from the frequency domain solution are in close agreement with the time domain solution. Moreover, both methods predicted similar aerodynamic damping values, and it is found that the blade vibration is considered stable as the aerodynamic damping is positive. It is also observed that the flow around the wind turbine is primarily influenced by the presence of the tower. The interaction between the flow and the wind turbine structures including the tower leads to further unsteadiness and instability in the downstream wake.

The aerodynamic simulations of two wind turbines in arrays are also discussed in this thesis to analyse the impact of flow unsteadiness associated with a neighbouring wind turbine on the aerodynamic performances. An advanced computational modelling method is proposed to model and simulate multiple wind turbines in arrays as a multi-stage turbine. The effects of the wake and turbulence generated from the upstream wind turbine on the downstream one with respect to separation distances are investigated in terms of various aerodynamic parameters such as pressure coefficient, skin friction coefficient and aerodynamic load distributions on the surfaces of the blade of both turbines. Results show that pressure coefficient and skin friction coefficient distributions on the blade surfaces of the downstream wind turbine are strongly affected by the wake and turbulence generated from the upstream wind turbine. A great impact on the downstream turbine is noticeable up to the separation distance of 5D which gradually reduces afterwards. It is found that the far wake has more impact on the downstream turbine than the near wake because the amplitudes of unsteady perturbations are maximum at 5D separation distance. The wake profiles and visualisations of flow fields indicate that the impact on the flow behind the downstream turbine is more severe in the 40% - 80% span region of the blade rotation with dramatic fluctuations. A conclusion is drawn based on the results obtained and the reference studies that the downstream wind turbine should be separated between 5D and 10D from the upstream wind turbine to optimise the aerodynamic performances of wind turbines and the power output of the windfarm.

The proposed frequency domain solution method is extensively validated against the time domain solution method throughout this thesis. The extensive validations reveal that the frequency domain method computed both aerodynamic and aeroelasticity parameters of wind turbines accurately. However, it solves significantly faster than the conventional time domain solution method, and the computational cost is reduced by one to two orders of magnitude. Furthermore, it is found that the proposed frequency domain method makes it possible to perform the aeromechanical analysis for various IBPAs using a single blade as well as model complete wind turbines and multiple wind turbines in arrays. Therefore, it is concluded that the proposed nonlinear frequency domain solution method can be reliably and efficiently used for the aerodynamic and aeromechanical analysis of offshore wind turbines at an affordable computational cost, which will be very useful for the design and optimisation of wind turbines and wind farms.

8.2. Future Work

So far, the aerodynamic and aeromechanical analyses of wind turbines including wind turbines in arrays models are carried out using the frequency domain solution method. In the future, it is also necessary to investigate further the capability of this method to analyse large amplitudes of complete wind turbine models in consideration of rotor-tower interactions as the sizes of wind turbines increase, which could potentially lead to large amplitudes of vibration. The future work includes the use of a real geometry of modern offshore wind turbines which possess extremely long blades and large rotor diameter. It could not only determine the capability of the proposed method but also facilitate the resources to broaden understanding of the aerodynamics and aeroelasticity associated with real-size offshore wind turbines. In addition, the wind turbines in arrays models discussed in this thesis are based on an in-line arrangement. In the future, investigating different array configurations will be required including arranging wind turbines in an offset configuration with an angle. Moreover, it is also anticipated to add more rows for the inclusion of more wind turbines to better represent a windfarm model and to analyse the unsteady flow associated with several neighbouring wind turbines. Apart from the steady and harmonic inflows, already discussed in this thesis, it is essential to implement real wind conditions to evaluate more physical and realistic flow behaviours and performances of wind turbines.

As it is highlighted in this thesis, the experiments for the aeromechanical analysis of wind turbines are very difficult to be performed, the research studies and industry mainly focus on numerical modelling and simulations. To strengthen the confidence regarding these numerical models and ensure accuracy, experiments are necessary. In the future, an advanced wind tunnel experiment should be designed to not only investigate the aeroelasticity of wind turbine blades but also validate the numerical models. Furthermore, comparing them with fully coupled fluid-structure interaction models could provide more understanding of each method and this is also necessary in the future. Besides, a fully coupled FSI model will make it possible to study vortex-induced vibrations over the wind turbine blades in addition to the blade flutter behaviour. In addition, as discussed in the Appendix, it is found that the unsteady flow is highly distorted by the blade vibration. In order to obtain details of flow structures associated with fluid-structure interactions, high-fidelity numerical models such as direct numerical simulation (DNS) model or large eddy simulation (LES) model should be considered in the future.

Appendix

Numerical Investigation of Interaction between Transient Flow and Blade Structure in a Modern Low-Pressure Turbine using Direct Numerical Simulations

A feature of a modern aeronautical Low-Pressure Turbine (LPT) is the high blade loadings with complex, transient and separated flow regimes. Most existing research have focused only on analysing the transient flow and flow separation in such turbines. The aerodynamics of a modern LPT, however, can be significantly influenced by the interaction between the unsteady flow field and the blade structure motion in a complex non-linear fashion which could lead to aeroelastic instabilities such as flutter. Therefore, the understanding of the mechanism of the interaction between the flow field unsteadiness and the blade structure in a modern LPT is essential to examine the vibration stress levels to ensure the blade mechanical integrity. The overarching aim of this study is to explore the forced response and flutter instability in a modern LPT using a high-fidelity direct numerical simulation (DNS) method and to verify the capability of the frequency domain method on analysing and predicting the transitional flow structures and the aeroelasticity parameters subject to the various sources of unsteadiness associated with the fluid-structure interaction. Direct numerical simulations are highly efficient, and they can provide a detailed insight into the physics of turbulence. Due to recent technical and computational advances, DNS has become more feasible, and it has been used in various engineering applications [185-189]. The novelty of this work, first and foremost, is using a high-fidelity DNS method to explore the mechanism of flutter and forced response in a modern LPT, T106A turbine, and to study the effects of various sources of unsteadiness on the aeroelastic instabilities of the blade. Secondly, this study investigates and identifies the adequate working ranges of a frequency domain method, which has been widely used for the aeromechanical analysis of turbomachines, on predicting the behaviour of the highly unsteady flow due to the fluid-structure interaction in an LPT. Another emphasis of this study is the determination of the capability of the Unsteady Reynolds Averaged Navier–Stokes (URANS) model for the aeroelasticity analysis of an LPT involving the highly unsteady flow. This physical understanding of the transient flow structures is directly relevant to other turbomachines including wind turbines, and it will bridge a key gap in the knowledge of aeroelasticity modelling and analysis of the unsteady flow relating to turbomachines prone to aeroelastic instabilities such as wind turbines.

Physical Description

In the present study, a modern LPT, T106A linear turbine cascade, which involves highly unsteady and complex transitional flow structures, is chosen for the DNS simulations. Based on the available experiment and its data [47], various numerical studies [48-56] were performed to validate the different numerical models and to predict the flow structures inside this turbine. All the aforementioned studies, which employ high-fidelity numerical methods such as Large-Eddy Simulation (LES) or DNS methods, analysed the two-dimensional transitional flow structures and flow separation at the mid-section of a stationary blade structure. In order to highlight the effect of the blade oscillation on the unsteady flow behaviour compared to the previously studied stationary blade cases and to determine the capability of a frequency domain method in predicting them, similar geometrical and physical parameters as the previous studies were selected. The blade aspect ratio and pitch-chord ratio are selected as 1.760 and 0.799, respectively. The Reynolds number is calculated based on the inflow speed and the axial chord length of the blade. The Reynolds number of 5.1×10^4 is mainly used; however, it is also varied from 2.5×10^4 to 7.5×10^4 with the velocity inlet angle $\alpha=45.5^o$ to analyse the effect of Reynolds number on the flow behaviour. The details of the geometry and physical parameters of the T106A LPT blade are presented in Fig. A.1. In this study, a 2D model representing the mid-section of the blade is first presented. The analysis is then extended to the 3D analysis to investigate the effects associated with the 3D model and the 3D blade vibration on the flow structures. The Inter Blade Phase Angle (IBPA), an import design parameter of an aeroelasticity analysis of turbomachines, which determines the vibration phase angle between consecutive blade rows, is also varied in this work. The IBPA of 0^o and 180^o are selected in a manner to completely analyse the in-phase and out-of-phase circumstances among two adjacent blades. A frequency domain method is applied to both 2D and 3D cases to determine its capability in capturing the unsteady flow structures and predicting aeroelasticity parameters. Titanium Alloy is selected as the blade material with a density of 4620 kg/m^3, Young's modulus of 9.60×10^{10} Pa and Poisson's ratio of 0.36.

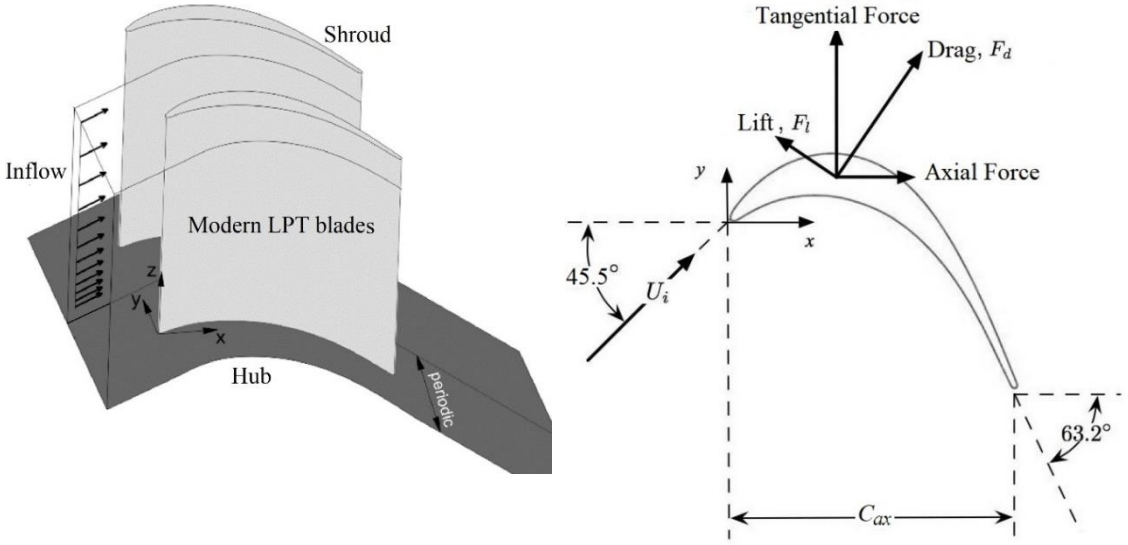

a) Geometry of T106 LPT blade b) Physical parameters

Figure A.1. Geometry and physical parameters of the T106A LPT blade.

Computational Description

Computational domains for a 2D model representing the mid-section of the blade and a 3D model including the hub and the shroud are created for the simulations. A schematic diagram of the computational domain used in this work is presented in Fig. A.2. It is important to ensure that the entire domain is optimal in all stream-wise, pitch-wise and span-wise directions to capture and resolve the necessary flow structures. The span-wise extension used for the 2D model is $0.2C_{ax}$ where C_{ax} is the axial chord length. Previous studies [48-56] suggest that $0.2C_{ax}$ or $0.15C_{ax}$ should be sufficient to capture the separated flow transition. Therefore, the span-wise length of $0.2C_{ax}$ is considered enough in this study. In the case of the 3D model, the span of the blade is $2.5C_{ax}$ to take the 3D vibration mode of the blade into account. Moreover, the wake profiles are investigated at the section of 40% chord downstream of the trailing edge in the experiment as well as the numerical studies, and therefore the outlet of the domain is placed $2C_{ax}$ from the trailing edge of the blade in this study to fully resolve the downstream wake region. Although the length of $1C_{ax}$ is enough, which is mostly used in previous studies, that of $2C_{ax}$ ensures that the downstream wakes and flow structures are captured which is particularly important when the blade vibration is involved. The same length from the leading edge of the blade is used for the inlet. In the pitch-wise direction, the pitch length is $0.9306C_{ax}$, which is consistent with the experiment and other studies. Therefore, the domain used in this study is considered adequate in all directions for the present study. A single domain is used for the 0^o IBPA case. In the case of 180^o IBPA, another identical domain is added on the top

of the reference domain and an internal interface using the general connection type is employed to connect the two domains and to transfer the flow data across the interface.

The grid employed in this study is carefully generated using a structured grid generator, NUMECA AutoGrid5, based on structured multi-block techniques to be suitable for DNS computations. The O4H topology is used to create the grid which consists of five blocks: the skin block which is an O-mesh surrounding the blade, the inlet block which is an H-mesh located upstream of the leading edge, the outlet block which is an H-mesh located downstream of the trailing edge, the upper block which is an H-mesh located above the blade section, and the lower block which is an H-mesh located under the blade section. The mesh in the skin block, the upper block, the lower block and the outlet block are significantly refined to resolve the necessary flow structures. As a steady inflow is only considered in this study, a coarser mesh is generated in the inlet block to reduce the total number of cells and the computation time. The first layer thickness, which is the width of the first cell close to the wall, is selected with care to capture the flow phenomena inside the boundary layers. The non-dimensional wall distance, y^+ value, is less than one in this study. The grid point distributions in the stream-wise direction and the pitch-wise direction in a single domain are 1028 and 140, respectively. 65 layers are used in the span-wise extension in the 2D model whereas 115 layers are distributed along the span of the blade in the span-wise direction in the 3D model.

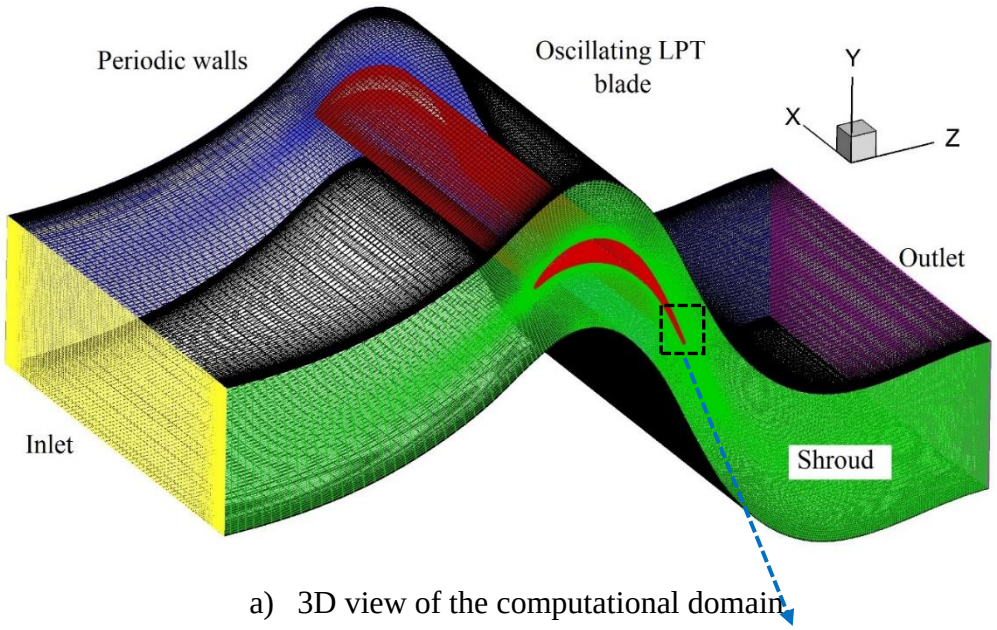

a) 3D view of the computational domain

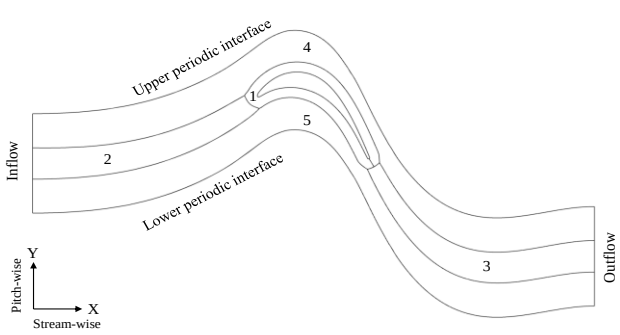

b) Schematic diagram of the domain

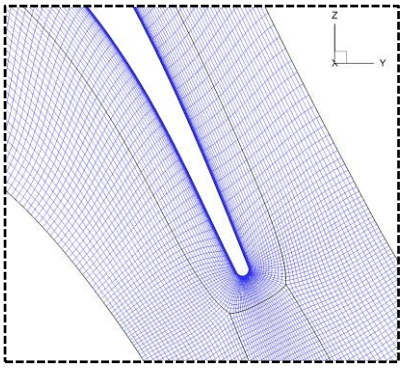

c) Boundary layer mesh

Figure A.2.Detailed view and schematic diagram of the computational domain and grid, and the boundary layer mesh of the T106 LPT.

The analysis of unsteady flow using the stationary blade is initially performed with the purpose of validating the CFD model. After validation, the blade is imposed a vibration with a frequency and amplitude to initiate the flutter instability in the T106A turbine and to analyse the interaction between the transient flow and the blade structure vibration. The first vibration mode is approximated by imposing a periodic displacement in the pitch-wise direction on the blade. Both the time domain method and the frequency domain method are used for the unsteady simulations using the vibrating blade. By using the same numeric for both methods, the capability of the frequency domain method on analysing the forced response and flutter instability in modern LTPs involving highly unsteady flow can be determined. The primary flow simulations are conducted using the DNS method. However, the results from the URANS model will also be added to the comparison in the

case using the vibrating blade to investigate the differences between the DNS model and the URANS model, and to identify their capabilities.

The flow is governed by the Navier-Stokes equations and a set of the unsteady Navier-Stokes equations are solved by a three-dimensional pressure-based finite volume solver. the general Navier-Stokes equations are presented in Chapter 3 (refer to Equations 3.1 and 3.2).

With the DNS method, the Navier-Stokes equations are directly solved without any turbulence model. The pseudo-time marching approach is used for the steady-state solution. For the unsteady solution, the advection terms are discretized using a bounded high-resolution advection scheme and the temporal derivatives are discretized using a 2nd order backwards Euler approximation for the time domain method.

In the cases of the flutter and forced response instability problems of the turbomachinery, the source of unsteadiness of the flow is mainly due to blade vibration. Therefore, in this study, the unsteadiness of the flow is associated with the frequency and amplitude of the blade oscillation. As the blade is periodically vibrating, the unsteady flow variables, *U*, can be represented by a Fourier series, based on the harmonic solution, for a prescribed fundamental frequency, ω, and the specified number of harmonics, *m*, as expressed in Eq. (A.1).

$$U = \bar{U} + \sum_{m=1}^{M}[A_m \sin(m\omega t) + B_m \cos(m\omega t)] \quad \text{(A.1)}$$

where $\bar{U}$, A_m, and B_m are the Fourier coefficients of the conservation variables. Substituting Equation (A.1) into the semi-concrete form of the Navier-Stokes equations yields the following equations.

$$\omega \sum_{m=1}^{M}[mA_m \cos(m\omega t) - mB_m \sin(m\omega t)] = R \quad \text{(A.2)}$$

The frequency domain method, typically used in the turbomachinery analysis, is also implemented in this work with a pressure-based solution approach to identify its capability. Using this method, the unsteady period is equally divided into $N = (2m+1)$ time levels and the system of nonlinear equations coupling all *N* time levels are solved iteratively. In this method, the time derivatives are evaluated via spectral approximation.

To resolve the unsteady flow accurately, the time-step size, Δt, must be small enough such that a fluid particle moves only a fraction of the mesh spacing h with fluid velocity u in each step, and it is given by [190]:

$$\Delta t = C_{FL}\frac{h}{u} \tag{A.3}$$

where C_{FL} is the CFL number and it is kept in the range of 0.5-1 throughout the computation to ensure a very small time-step which leads to Δt of 10^{-5}.

For the boundary conditions imposed in the simulations, the velocity inflows are applied at the inlet and the pressure outlet boundary condition is defined at the outlet. The solid wall boundary conditions are applied on the blade surfaces. The periodic boundary conditions are applied in the pitch-wise direction and the mirror boundary conditions are applied in the span-wise direction. The details of the boundary conditions are described below.

Inlet

A velocity inlet boundary condition is defined where the flow enters the domain. As there is an inflow angle, the velocity components are specified in the Cartesian frame of reference as follow:

$$u_{inlet} = \sqrt{{u_x}^2 + {u_y}^2} \tag{A.4.a}$$

$$u_x = u_{inlet}\cos(45.5) \tag{A.4.b}$$

$$u_y = u_{inlet}\sin(45.5) \tag{A.4.c}$$

u_{inlet} is calculated based on the required Reynolds number of 5.1×10^4 and the axial chord length, and the Z-component of the velocity (i.e., velocity in the span-wise direction), u_z, is zero.

Outlet

A pressure outlet boundary condition is defined where the flow leaves the domain. The atmospheric pressure of 1 atm is specified at the outlet.

Wall

A no-slip wall boundary condition is defined over the blade surfaces. The hub and the shroud of the T106A turbine cascade are also treated as solid walls. The stationary wall boundary is specified in the stationary blade case whereas the deforming wall boundary with a periodic displacement is specified in the vibrating blade case. In the case of the vibrating blade, the global displacement of the blade structure can be defined in Equations 3.11 and 3.14, presented in Chapter 3.

Mirror and Periodicity

The symmetry boundary condition is specified on each side of the domain in the span-wise direction in the 2D model so that the flow on one side of the domain is the mirror image of that of the other side. The translational periodicity is implemented in the pitch-wise direction to represent a straight row of turbine blades of the linear cascade.

Results and Discussion

Analysis of the Interaction between Transient Flow and Stationary Blade

Before analysing the effect of the blade structure vibration on the unsteady flow, the unsteady simulation using the stationary blade is first conducted to validate the CFD model. The numerical results are compared to the experiment as well as the reference DNS simulations for validation. The time-averaged static pressure coefficient, C_p, can be defined as $(p_w - p_{ref})/(p_{t\text{-}in}\text{-}p_{ref})$, where p_w is the blade wall static pressure, p_{ref} is the reference outlet pressure, and $p_{t\text{-}in}$ is the inlet total pressure. The time-averaged C_p distribution computed from the present simulation is compared to the experiment as well as the previous DNS simulation performed by Wissink et al. [54], and they are presented in Fig. A.3. As seen, the pressure computed from the present simulation is in very good agreement with the experiment as well as the reference DNS simulation.

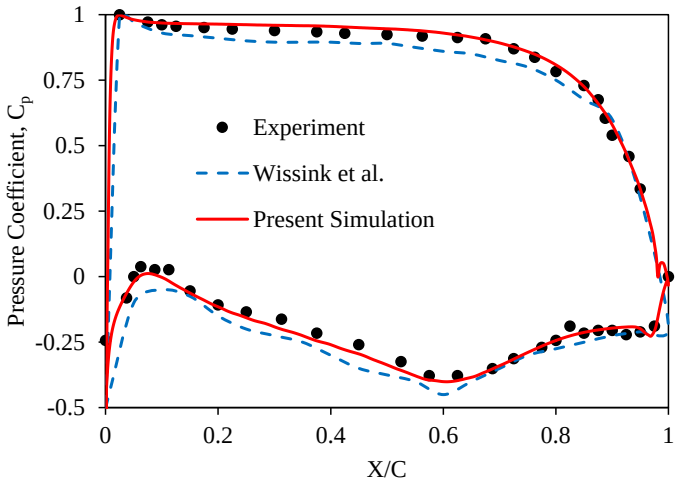

Figure A.3. Time-averaged pressure coefficient distributions at the blade mid-span obtained from the experiment, the reference DNS simulation of Wissink et al. [54] and the present DNS simulation.

The wake loss profile, also called wake deficit, ω_u, can be defined as $(p_{t\text{-}in}\text{-}p_t)/(p_{t\text{-}in}\text{-}p_{ref})$, where p_t is the total pressure, and it is computed at 40% chord downstream of the blade trailing edge. Similar to C_p, the time-averaged wake loss profile calculated from the present simulation is compared to the experiment as well as the DNS simulation of Michelassi et al. [55], and they are shown in Fig. A.4. A slight difference can be seen between the DNS computations and the experiment. This has been discussed in previous studies [48, 56]. Overall, a good agreement is obtained between the present simulation and the experiment, and the results are close to that of Michelassi et al. [55]. Therefore, it can be noted that the present CFD model captured the wake loss reasonably well and this is considered enough for further investigations involving the blade vibration.

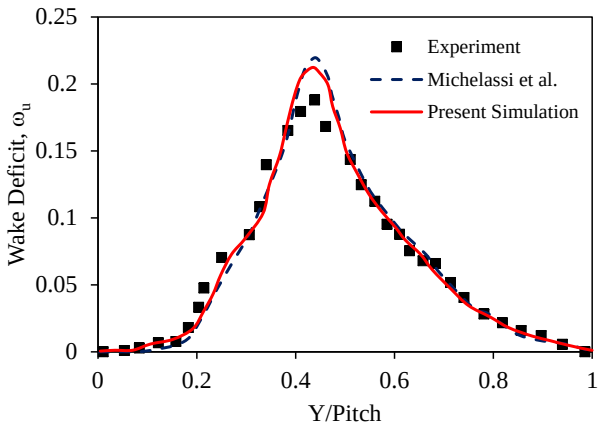

Figure A.4. Wake loss profiles obtained from the experiment, the reference DNS simulation of Michelassi et al. [55] and the present DNS simulation.

In addition to the pressure coefficient distribution and the wake loss profile, the shear stresses on the blade surfaces are also computed, and they are compared to the previous DNS simulation performed by Michelassi et al. [55], and they can be seen in Fig. A.5. As shown, they are in very good agreement. Therefore, it is concluded that the CFD model used in the present study is valid for further investigations after having obtained the results which agree well with the experiment as well as the reference DNS simulations.

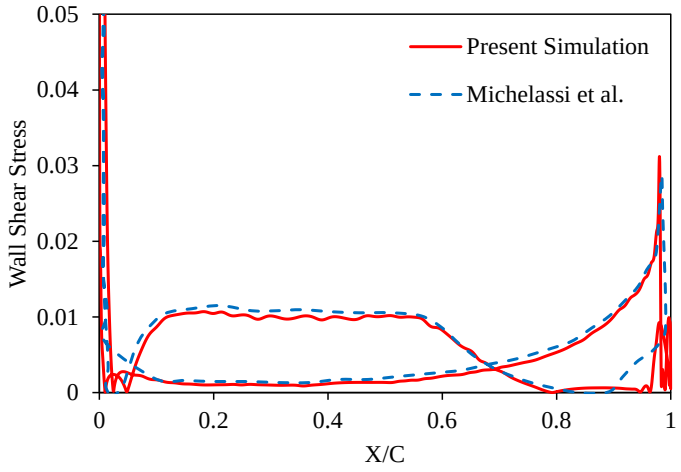

Figure A.5. Wall shear stress on the blade surfaces at the blade mid-span obtained from the present DNS simulation and the reference DNS simulation of Michelassi et al. [55].

After having validated the CFD model in terms of the time-averaged parameters, it is also crucial to visualise and analyse the vorticity to determine whether this model captures the necessary flow structures, which is very important for this study. Figure A.6 illustrates the instantaneous vorticity structures, at four equally spaced time-steps, obtained from the present simulation. Although a single passage domain is simulated in this study, the additional two passages are added and shown for better visualisation of the flow structures. As seen, on the pressure side of the blade, the flow remains laminar and attached whereas the flow separates in the aft region on the suction side which leads to laminar vortex-shedding from the trailing edge of the blade of which the flow structures are similar to that of Karman vortex. As time goes on, the evolution of coherent structures and separation of shear layers can be observed. The rolling up and breaking down of the separated shear layer occur due to Kelvin-Helmholtz instability which results in a transition to turbulence near the trailing edge and forming unsteady and complex vortex structures further downstream. After a certain period, the flow structure is stretched near

the trailing edge and the organised mushroom-like vortex structures are developed to form a fully turbulent wake in the downstream region.

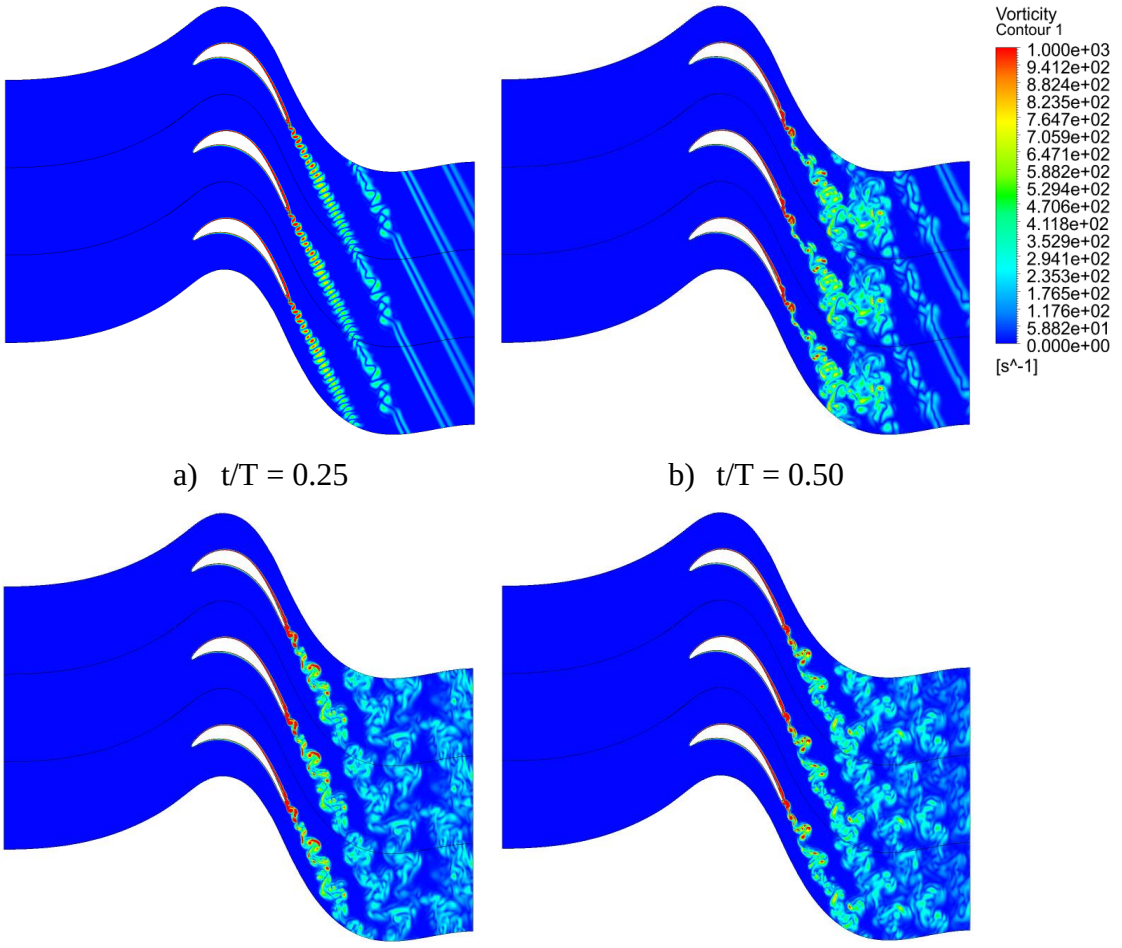

a) t/T = 0.25 b) t/T = 0.50

c) t/T = 0.75 d) t/T = 1.0

Figure A.6. Instantaneous vorticity fields obtained at different time steps (*t* is the local time-step and *T* is the total simulation time).

Analysis of the Interaction between Transient Flow and Blade Vibration using a 2D Model

To explore the forced response and flutter instability in a modern LPT due to the interaction of unsteady flow and the blade structure, the blade is prescribed a vibration with a frequency and amplitude in the flow simulation. The first vibration mode is approximated by imposing a periodic displacement in the pitch-wise direction on the blade as shown in Fig. A.7 and is used in this analysis. This means that each node of the blade has the same displacement and the blade periodically moves up and down, in the Y-direction, with a prescribed frequency and amplitude throughout the run. The first natural frequency, 250 Hz, obtained from the modal analysis, is adopted to be the

vibration frequency in this case. In the aeromechanical analysis of turbomachines, the vibration amplitudes of 1-3%C_{ax} are typically used in both experimental and numerical studies [44, 58]. As this study only simulates the flow at the mid-span section of the blade, a relatively small amplitude of 1%C_{ax} is considered and set to be the vibration amplitude.

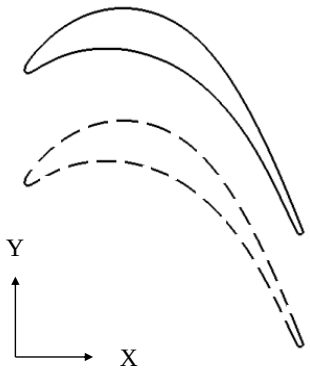

Figure A.7. Schematic diagram of the blade vibration showing the blade moving in the Y-direction.

The time-averaged pressure coefficient distribution computed from this analysis is first compared to the stationary blade case, and they are shown in Fig. A.8. In terms of pressure coefficient distributions on the blade surfaces, only a slight difference is seen between the two cases. This is understandable as the blade displacement is periodic in time and the time-averaged pressure distribution due to the vibration can be similar to that of the stationary case. However, it should be noted that this effect is also related to the frequency and amplitude of the vibration. A little pressure fluctuation due to the flow separation on the suction surface is also observed near the trailing edge.

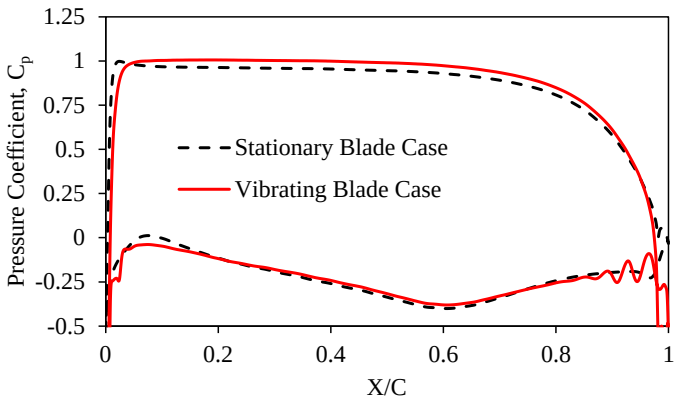

Figure A.8. The comparison of time-averaged pressure coefficient distributions between the stationary blade case and the vibrating blade case.

The effect of vibration on the unsteady flow can be clearly observed in the wake profiles (See Figure A.9). They are computed at the same location as discussed in the stationary case. A significant difference can be seen between the two cases as the flow is disturbed by the blade vibration. The blade experiences acceleration and deceleration on both pressure and suction surfaces due to the vibration, which leads to an increase and decrease in total pressure in the downstream region. This results in negative and positive wake profiles, as seen in Fig. A.9, and the magnitude of the wake is also much larger in the vibrating blade case compared to the stationary blade case.

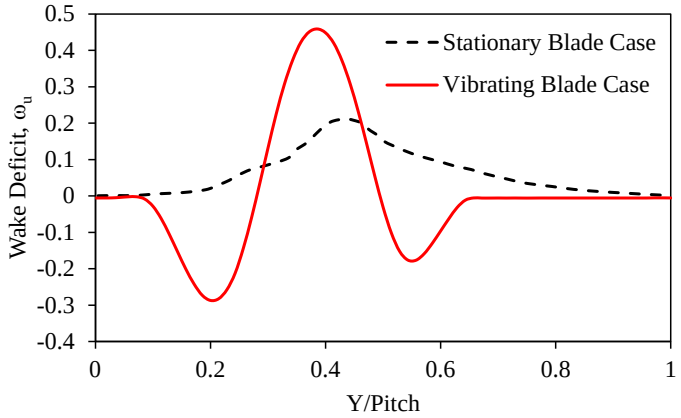

Figure A.9. The comparison of wake profiles between the stationary blade case and the vibrating blade case.

The evolution process of vorticity over vibration periods is demonstrated in Fig. A.10 which allows visualising the mechanism of the interaction between the flow unsteadiness and the blade structure vibration. As soon as the blade undergoes vibration, the blade structure motion triggers disturbances, and the vortex structures shed from the blade trailing edge. The blade produces similar vortex structures as vibration goes on and the initially produced vortex structures are pushed away by the latterly produced ones. After about 20 vibration periods, some of the vortex structures are mixed up with those from the neighbouring blades. The breaking down and mixing up of vortex structures are clearly observed beyond 30 vibration periods. As vibration periods go on, the highly unsteady vortex structures and completely turbulent flow fields are seen in the downstream region. Overall, it is seen that the flow is predominantly distorted by the blade movement and the periodically moving blade causes the recurring pattern of vortex

formation from the trailing edge of the blade. The frequency of vorticity is determined by the blade vibration frequency.

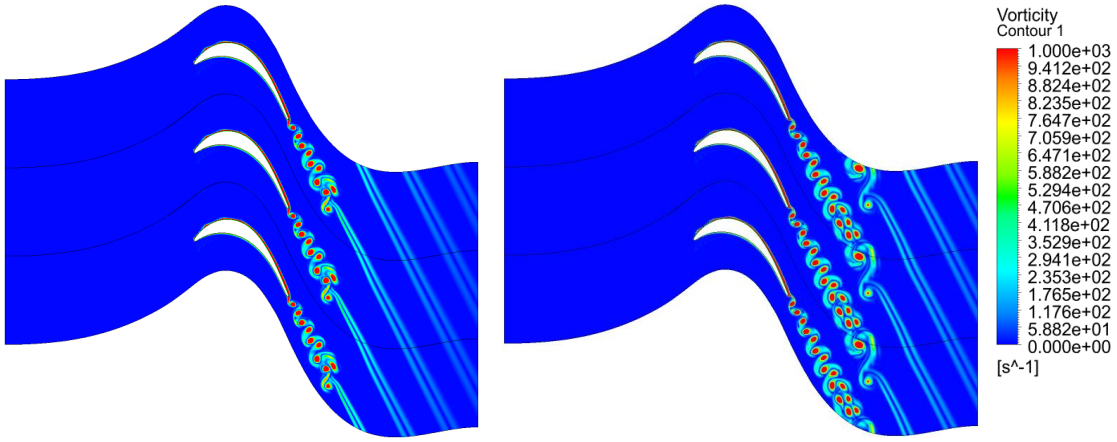

a) After 5 vibration periods b) After 10 vibration periods

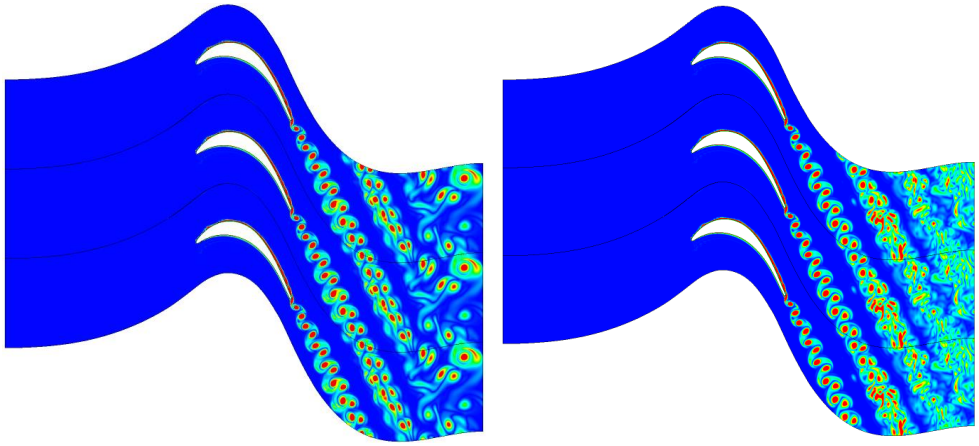

c) After 20 vibration periods d) After 30 vibration periods

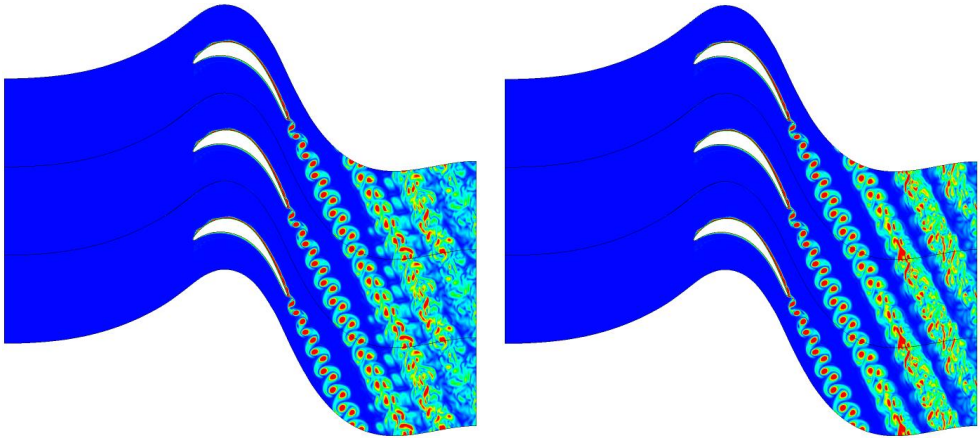

e) After 40 vibration periods f) After 50 vibration periods

Figure A.10. Instantaneous vorticity fields obtained after different vibration periods.

The close-up view of the vorticity around the trailing edge of the blade after 50 vibration periods is shown in Fig. A.11 to highlight the flow structures near the trailing edge. The

outer bound of the colourmap is increased to be able to clearly see the flow separation and vortex structures in this region. As seen, the rolling up of separated shear layer and flow recirculation, similar to KH rolls, are observed on the suction side near the trailing edge before shedding from the trailing edge. A little fluctuation in pressure distribution near the trailing edge, which was seen in Fig. A.8, is associated with this phenomenon.

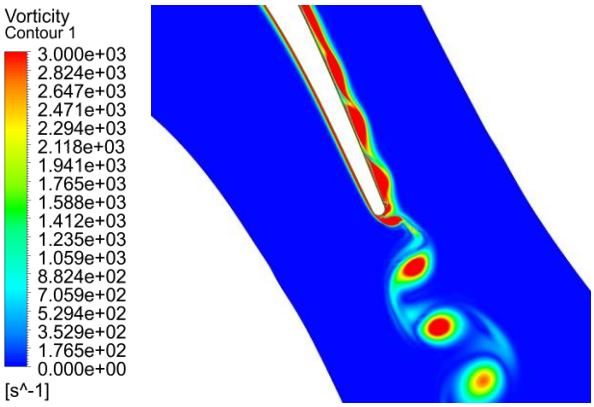

Figure A.11. Close-up view of the vorticity around the trailing edge of the blade after 50 vibration periods.

Figure A.12 compares well-developed flow fields from the stationary blade case and the vibrating blade case after 50 vibration periods in which the differences between the two cases can be observed. As seen, the flow field is dominated by the blade motion in the latter case. Furthermore, the flow structures are highly unsteady, more organised and stronger in the vibrating blade case, compared to the stationary blade case, due to the periodic movement of the blade. Therefore, the conclusion can be drawn from these observations that the blade vibration has a significant impact on the flow, and the unsteady flow structures are strongly influenced and controlled by the blade vibration frequency and amplitude.

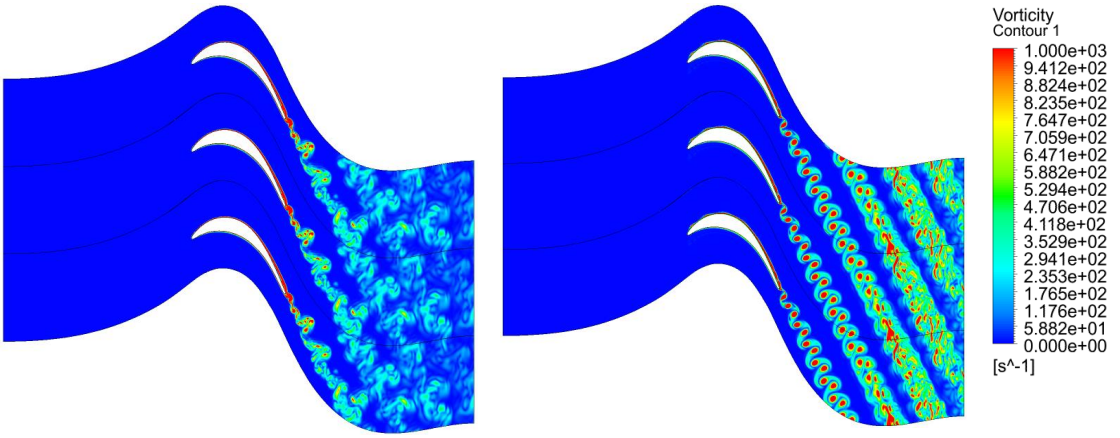

a) Stationary blade case b) Vibrating blade case

Figure A.12. The comparison of vorticity fields between the stationary blade case and the vibrating blade case after 50 vibration periods.

In addition to the time domain method, the frequency domain method is also used in this study using different harmonics to determine the capability of the frequency domain method on analysing the aeroelasticity and unsteady flow inside a modern LPT at a low Reynolds number involving the highly unsteady vorticity and wake. Figure A.13 presents the vorticity developed from the trailing edge of the blade within the initial vibration periods obtained from the time domain method and the harmonic balance method using different harmonics. As shown, the vorticity structures predicted by using 1 harmonic and 3 harmonics are not comparable to that of the time domain method which indicates that 3 harmonics are not even enough to resolve the flow structures. It is seen that using 5 harmonics produces similar vortex structures as the time domain method. However, none of them seems to have accurately captured flow structures leaving from the trailing edge. Although the flow resolution will be better with higher orders of harmonics, this will also increase the requirement of computational resources by a significant factor that could also be beyond the capabilities of supercomputers. Nevertheless, it can be said that the frequency domain solution method has the capability of capturing the complex and highly unsteady flow behaviour, and at least 5 harmonics are required to resolve the necessary flow structures inside this particular turbine.

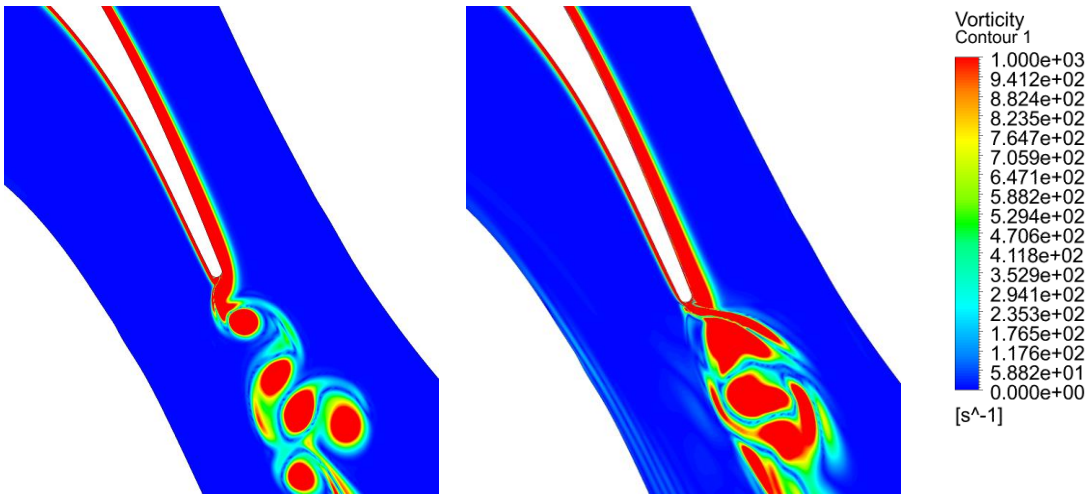

a) Time domain method b) Using 1 harmonic

c) Using 3 harmonics d) Using 5 harmonics

Figure A.13. The comparison of vorticity fields captured by the time domain method and the frequency domain method using different harmonics.

One of the important parameters in the aeromechanical analysis of turbomachines is the aerodynamic damping value, which is used to determine whether the blade vibration is stable. The URANS models are traditionally employed by the existing high-fidelity aeroelasticity solvers and they are still widely used in the industry to compute aerodynamic damping as they are computationally less expensive. In this study, the URANS simulation is also carried out in addition to the DNS simulation to examine the capability of the URANS model on not only computing the aerodynamic damping but also predicting the behaviour of the unsteady flow after interaction with the blade structure. The k-omega SST turbulence model is used for the URANS computation. For a direct comparison to the DNS computation, the same time-step and total run time are used. The aerodynamic damping values computed from both methods are presented in

Table A.1. It is seen that the aerodynamic damping predicted by the URANS model is comparable to that of the DNS model. Figures A.14 and A.15 show the comparison of the vorticity structures obtained from the URANS model and the DNS model. The results indicate that the URANS model can produce similar vortex structures as the DNS model in the near wake region after shedding from the trailing; however, a significant difference between the two models is seen in the far downstream region as the URANS model is unable to resolve the turbulent wake and flow structures in this region. Another distinguishing factor between the models is the flow separation. Although the size of the flow separation is similar in both models, the flow recirculation within the flow separation zone is not resolved by the URANS model. Therefore, it can be concluded that the use of the URANS model is theoretically problematic when the highly unsteady flow and the flow separation are the main concerns. However, it is encouraging to observe that the URANS model not only predicts the aeroelasticity parameters such as aerodynamic damping correctly but also somewhat captures highly unsteady flow structures leaving from the blade. This can be considered enough to be implemented in the frequency domain method to be applied to the aerodynamic and aeromechanical simulations of wind turbines. Figure A.16 describes the total wall work distribution on the blade which shows that the blade has a dominant stabilizing effect on the suction surface.

Table A.1. Aerodynamic damping of the blade.

Type of Model	Aerodynamic Damping
DNS	0.056
URANS	0.055

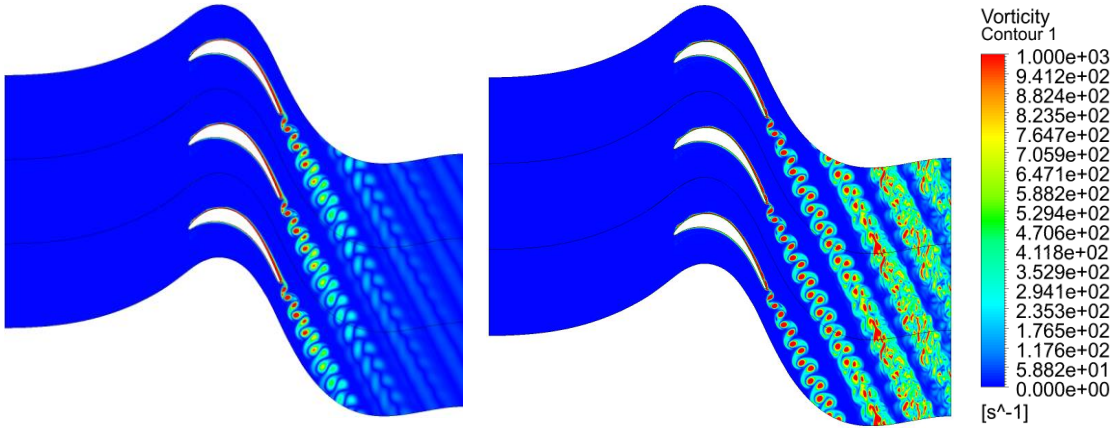

a) URANS model b) DNS model

Figure A.14. The comparison of vorticity fields between the URANS model and the DNS model.

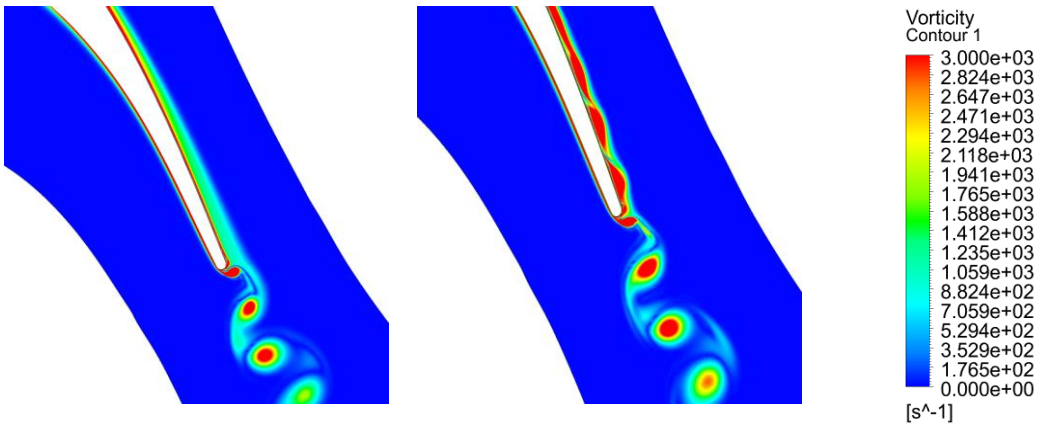

a) URANS model b) DNS model

Figure A.15. The comparison of close-up views of the vorticity around the trailing edge between the URANS model and the DNS model.

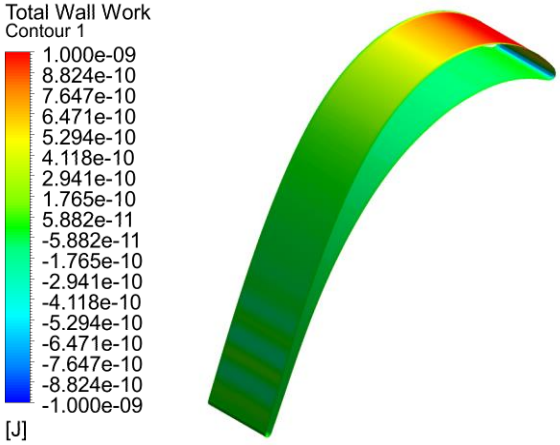

Figure A.16. Total wall work distribution on the blade surfaces (positive values represent stabilizing effect and negative values represent destabilizing effect).

Analysis of the Interaction between Transient Flow and Blade Vibration using a 3D Model

The modal analysis is initially performed using the 3D blade before the flow simulation to calculate the natural frequencies and the mode shapes of the blade structure. As the first vibration mode usually dominates in most blade vibrations, the first mode shape is prescribed to initiate the blade vibration and instabilities in the flow simulation. From the modal analysis, it is found that the first natural frequency of the T106A blade is 250 Hz. This frequency is set to be the vibration frequency of the blade vibration. Figure A.17 depicts the total mesh displacement of the first vibration mode shape of the T106A blade. The highest oscillation amplitude of the blade is defined to be 3% C_{ax} at the blade tip. Two different IBPAs of 0^o and 180^o are selected for the DNS study. Analysing the effect of the in-phase and out-of-phase vibration between two consecutive blade rows will

provide a detailed understanding of the complex physics behind the interaction between the transient flow and the blade vibration in different phases.

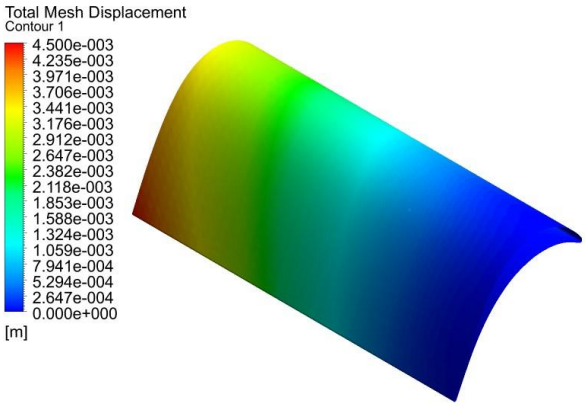

Figure A.17. Total mesh displacement of the first vibration mode of the T106A blade.

Figure A.18 shows the time-averaged pressure coefficient C_p variations over the suction and pressure sides of the LPT blade for both vibrating cases with IBPA=0^o and IBPA=180^o at different Reynolds numbers. The results are provided for different span sections. It can be observed that the pressure variations over the blade surfaces are primarily influenced by the blade oscillation with various IBPAs. At IBPA=180^o, there are substantial impacts on the blade because of the variation in the pitch length among the oscillating turbine blades. The influence is considerably higher in the blade tip region behind the shroud due to the stronger oscillations, especially when the flow over one blade is disrupted by those of the nearby blades. Similar flow behaviour is detected at IBPA=0^o. However, the flow fluctuations and perturbations are smaller in contrast to the IBPA=180^o case. The results show that small discrepancies are also detected within the inner areas of the blade in which the oscillation amplitude of the blade is small. In terms of the effect of the Reynold number on the pressure distributions, significant differences are seen between the two IBPA cases at Re = 2.5 × 10^4. They are mainly due to the flow unsteadiness and separation due to the low Reynolds number. Raising the Reynolds number to 5.1 × 10^4 reduces these differences in the blade inner region; however, the differences are still significant at 70% and 90% span sections. When the Reynolds number is further increased to 7.5 × 10^4, the pressure distributions at both IBPAs are similar at 30% and 50% span sections; but the differences between the two cases are slightly higher at 70% and 90% span sections due to the high oscillation and variation of pitch length between two consecutive blades at the IBPA of 180^o. Nevertheless, it can be said that

increasing the Reynolds number can reduce the differences in pressure distribution at IBPA=0^{o} and 180^{o}.

The effect of IBPA and Reynolds number on the spanwise vorticity production is presented in Fig. A.19. The results are extracted at the mid-span section of the blade. The flow separation and rolling up of the separated shear layers are seen on the suction surface of the blade when the Reynolds number is 2.5 × 10^{4}. At Re = 5.1 × 10^{4}, the flow unsteadiness and turbulence in the wake region is much higher in the case of IBPA=180^{o} compared to that of 0o. When Re = 7.5 × 10^{4}, the flow structures and vortex shedding from the trailing edge of the blade are similar in both IBPA cases; however, the mixing of flow structures is observed in the far downstream region at IBPA=180^{o}. From the results obtained, it can be deduced that increasing the Reynolds number can reduce the flow separation on the suction surface. It is also observed that the size of flow structures and recirculation become larger when raising the Reynolds number. Moreover, the structure of the vorticity in the downstream region is significantly dependent on the IBPA. The results illustrate that the flow disturbance and fluctuations in the vortex shedding process become noticeable by increasing IBPA from 0^{o} to 180^{o}.

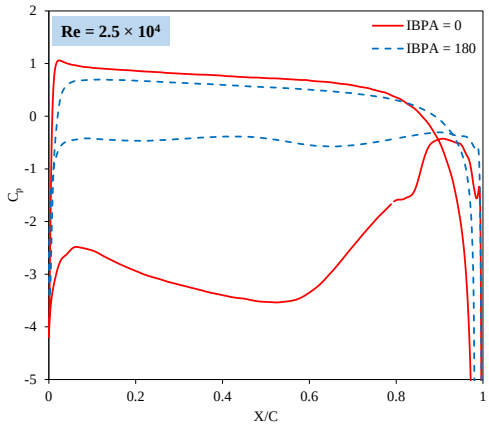

a) Re=2.5×10^{4}, 30% span

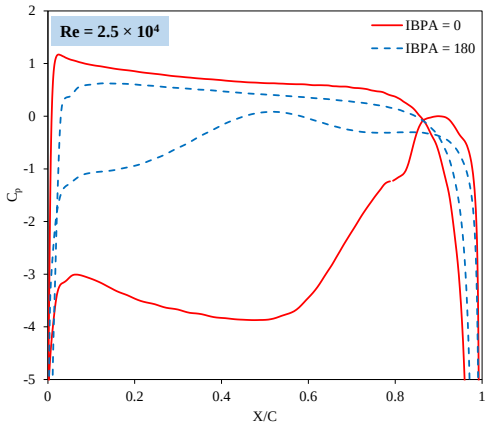

b) Re=2.5×10^{4}, 50% span

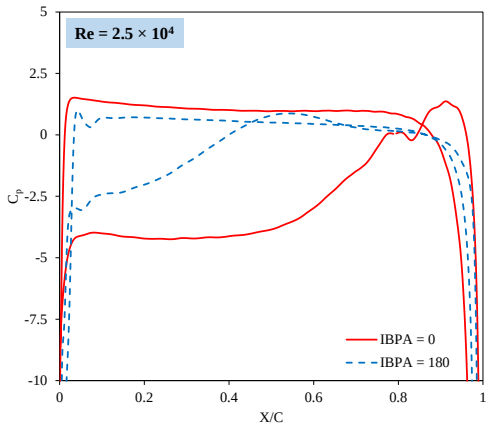

c) Re=2.5×10^4, 70% span

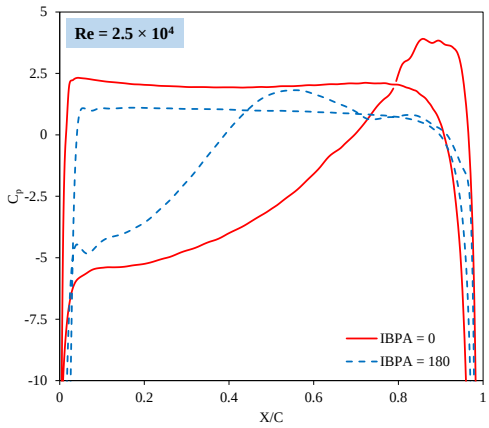

d) Re=2.5×10^4, 90% span

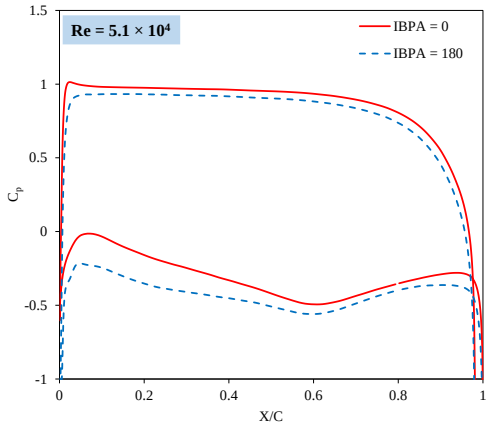

e) Re=5.1×10^4, 30% span

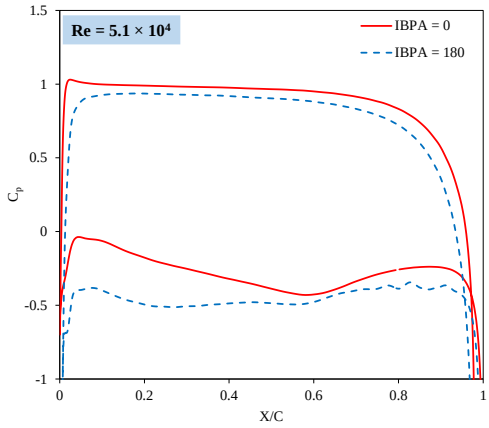

f) Re=5.1×10^4, 50% span

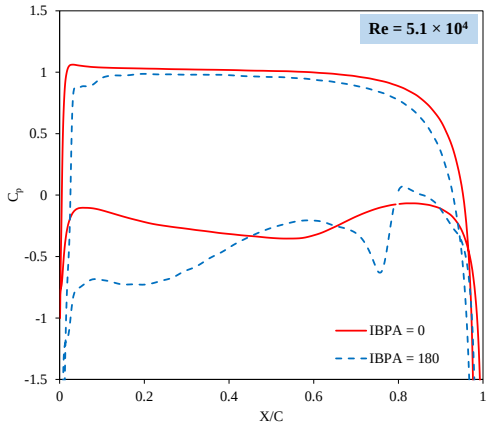

g) Re=5.1×10^4, 70% span

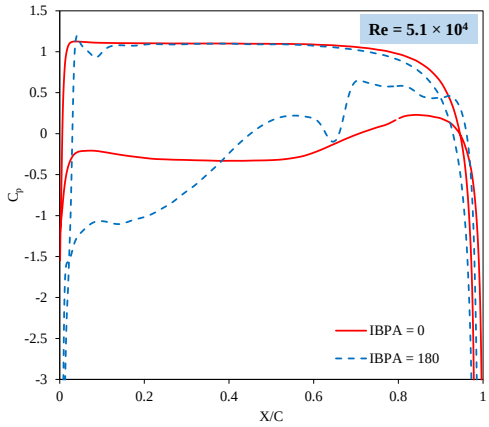

h) Re=5.1×10^4, 90% span

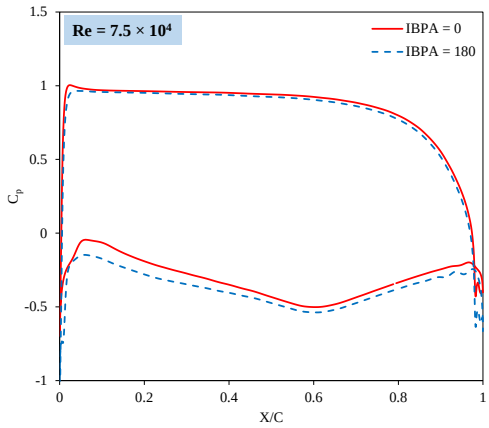

i) Re=7.5×10^4, 30% span

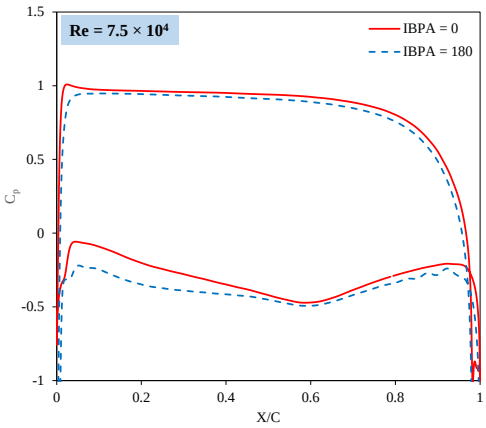

j) Re=7.5×10^4, 50% span

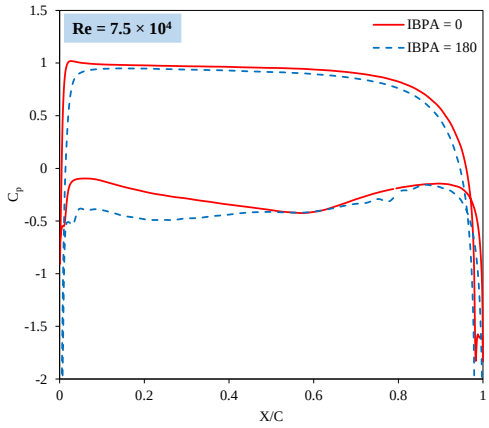

k) Re=7.5×10^4, 70% span

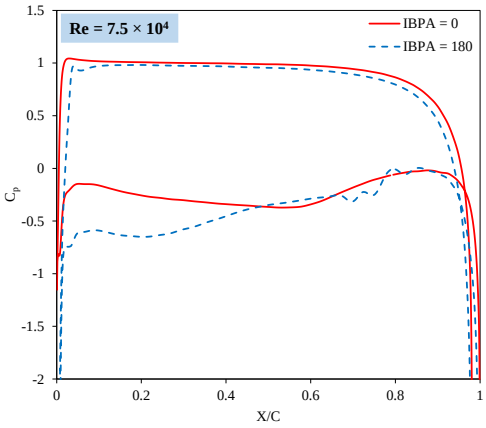

l) Re=7.5×10^4, 90% span

Figure A.18. C_p comparison between IBPA=0^o and 180^o at different blade sections at different Re numbers.

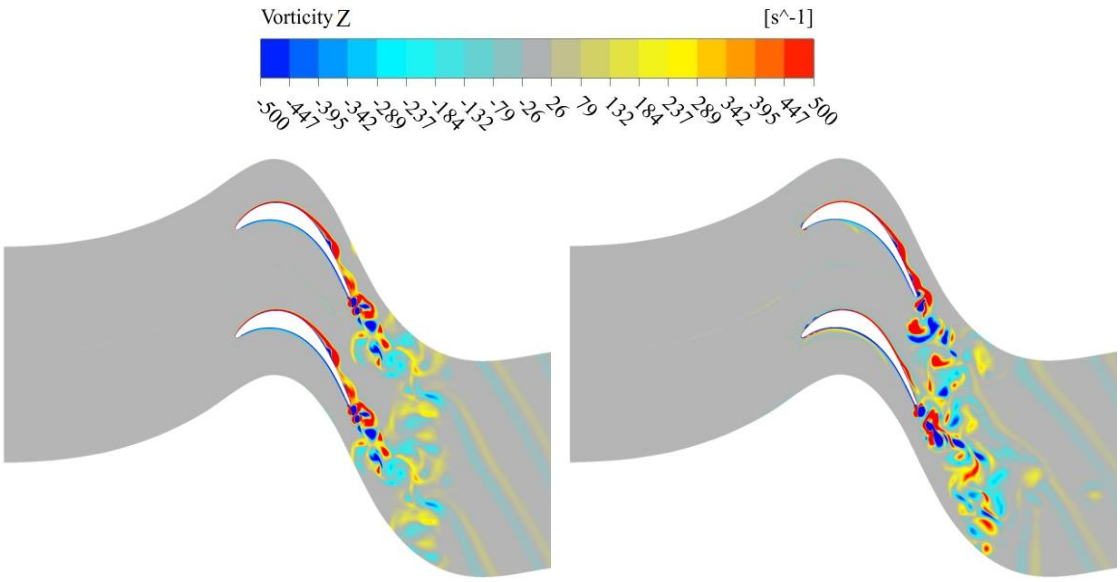

a) Re = 2.5 × 10^4, IBPA = 0^o

b) Re = 2.5 × 10^4, IBPA = 180^o

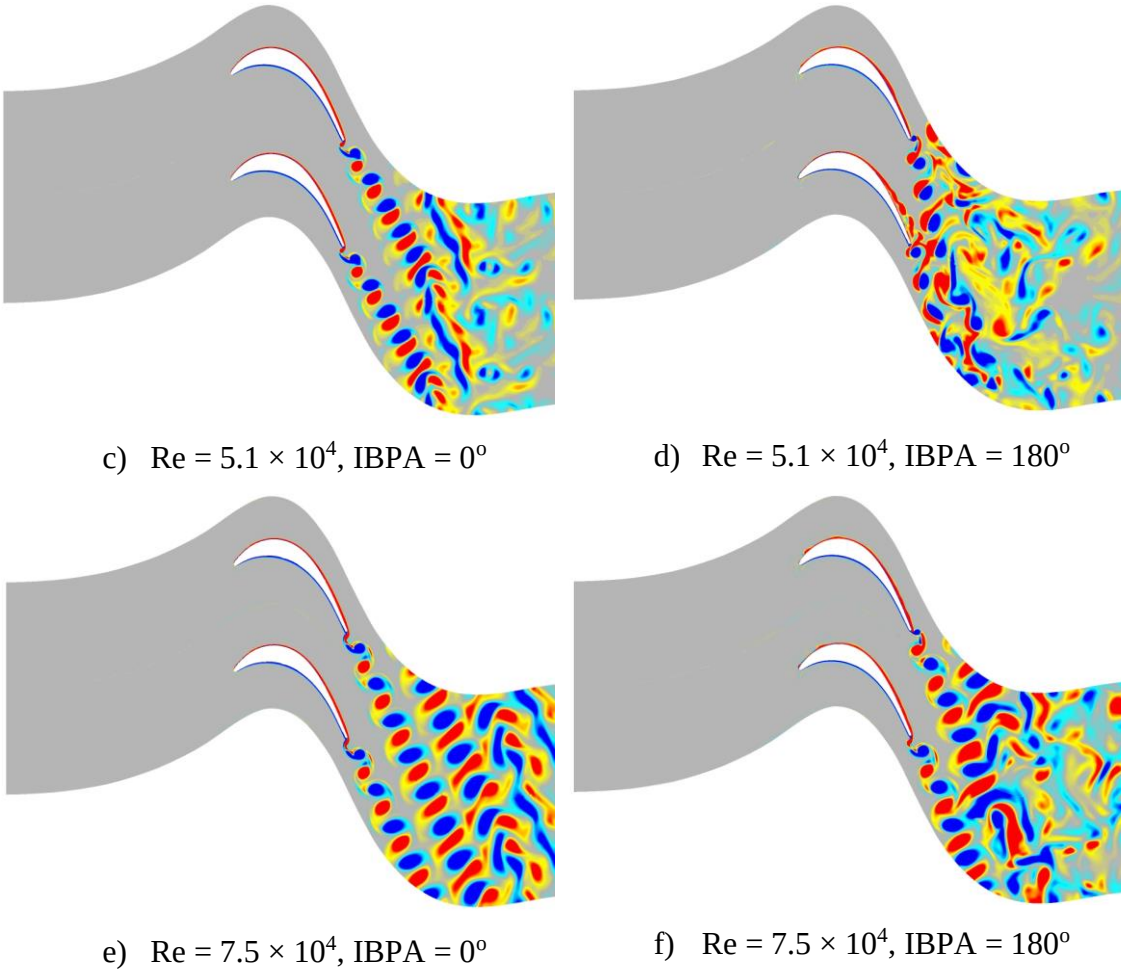

c) Re = 5.1×10^4, IBPA = 0^o d) Re = 5.1×10^4, IBPA = 180^o

e) Re = 7.5×10^4, IBPA = 0^o f) Re = 7.5×10^4, IBPA = 180^o

Figure A.19. Vorticity contours at different Reynolds numbers and IBPAs.

Figure A.20 shows the iso-surfaces of the vorticity generated from the vibrating blade with different IBPAs at different Reynolds numbers. The vortex structures are coloured by a function of the flow velocity. This figure highlights the effect of vibration and vibration phase angle on the flow and the development of flow structures. The flow is highly distorted by the blade vibration and it has a significant impact on the development of vortex structures. The vortex generation is dramatically amplified by the oscillating motion of the blade. The pattern of vortex generation and the size of vortex structures strongly depend on the vibration amplitude and phase angle. As the first vibration mode is considered for the blade vibration in this study, the blade is fixed at the hub and the blade displacement linearly increases along the span, and the maximum amplitude is observed at the tip near the trailing edge. Due to the nature of the first vibration mode, the vortex structures are small with some rolling up of the separated shear layer in the blade inner region where the vibration amplitude is low, and they become larger as it moves towards the tip along the span. The vortex generation is noticeably high starting from approximately the mid-span section of the blade, and it becomes much more

significant in the outer region near the shroud where the vibration amplitude is high. The vortex structures are also much larger in this region. In the case of 0^o IBPA, each blade row within the cascade triggers a similar pattern of vortex generation, and the flow structures are mixed up in the downstream region and the wake becomes turbulent. The effect of vibration phase angle on the unsteady flow and flow structures can be clearly seen in the 180^o IBPA case. In this case, the blades in a cascade are vibrating out of phase to each other with an angle of 180^o. Therefore, the pitch length between two consecutive blades changes in time within a vibration cycle, and it has a great impact on the vortex generation process. Due to this nature, the vortex structures generated from each blade row are highly disturbed by those of the neighbouring blades. This physical behaviour leads to higher turbulence in the wake region. The effect of blades vibrating out of phase is not just seen in the wake region, but also it is noticeable on the blade surfaces. The vortex structures start to develop near the leading edge before it becomes stronger near the trailing edge. In terms of Reynolds number, the flow separation and separation bubbles are observed on the suction surface in both IBPA cases at $Re = 2.5 \times 10^4$. When $Re = 5.1 \times 10^4$, a strong flow recirculation can be seen in the flow separation zone at $IBPA=180^o$ whereas the flow structures are mostly uniform on the suction surface with some detachment in the blade aft region near the trailing edge at $IBPA=0^o$. Similar flow behaviour is detected at $Re = 7.5 \times 10^4$; however, the flow structures and recirculation are much larger and stronger at this Reynolds number. Overall, it can be concluded that the flow is primarily influenced by the blade vibration, and the vibration amplitude and phase angle have significant consequences on the development of vortex structures at all Reynolds numbers. The vortex generation is much stronger in the blade outer region near the shroud where the vibration amplitude is large. The downstream wake and turbulence are higher in the 180^o IBPA case compared to the 0^o IBPA case. As the fluid velocity becomes higher with increasing Reynolds number, it can minimise the separation bubbles and reduce the flow separation.

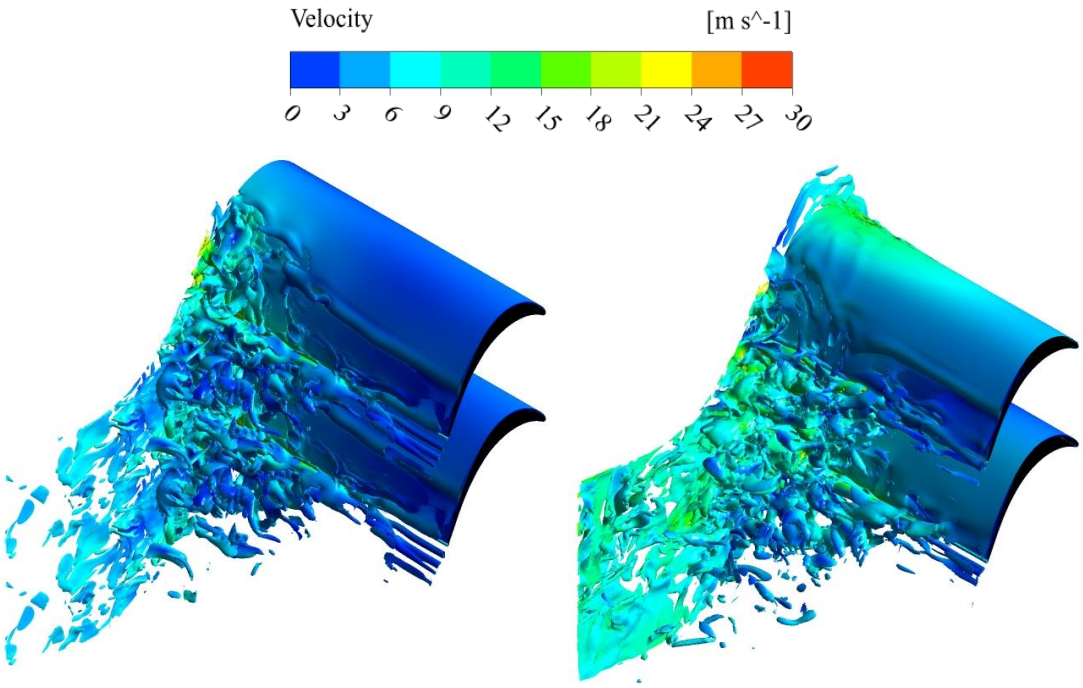

a) Re = 2.5×10^4, IBPA = 0^o

b) Re = 2.5×10^4, IBPA = 180^o

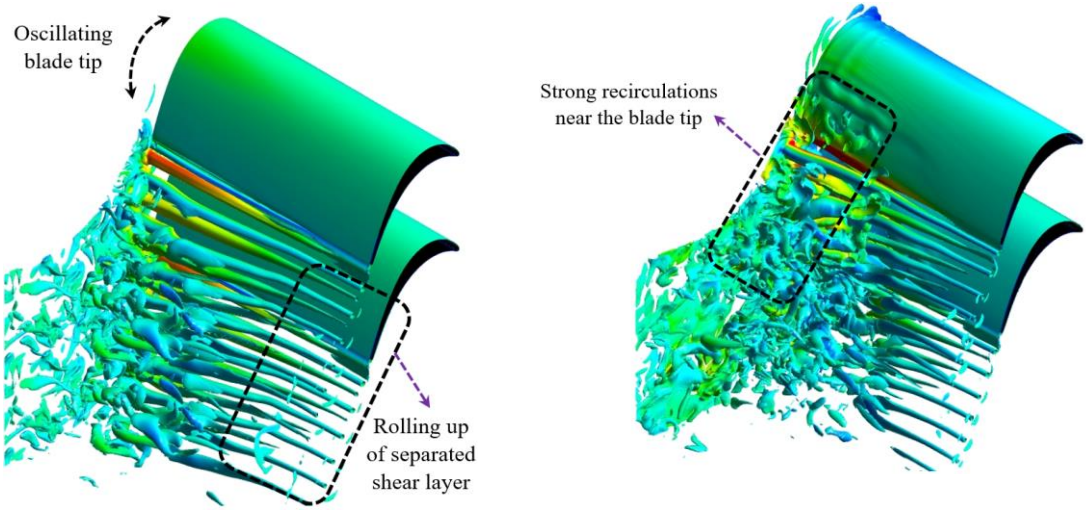

c) Re = 5.1×10^4, IBPA = 0^o

d) Re = 5.1×10^4, IBPA = 180^o

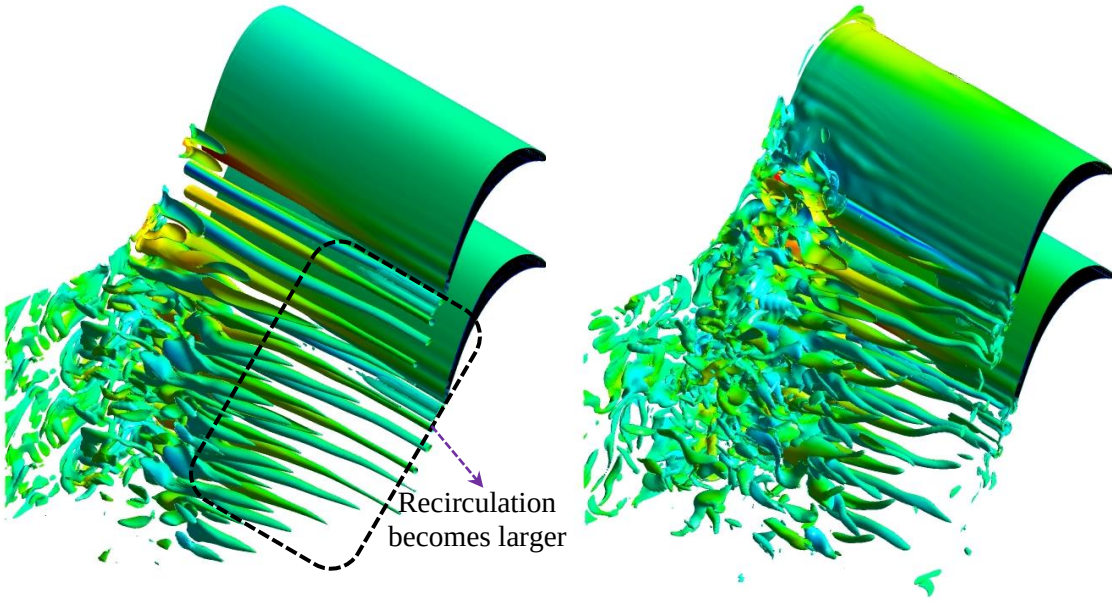

e) Re = 7.5 × 10^4, IBPA = 0^o f) Re = 7.5 × 10^4, IBPA = 180^o

Figure A.20. Iso-surfaces of vorticity at different Reynolds numbers and IBPAs.

A detailed analysis of the consequences of the blade vibration on the vortex generation process and the downstream wake will now be discussed based on the case at Re = 5.1 × 10^4. Figures A.21 and A.22 illustrate the instantaneous vorticity generation contours after different cycles of vibration at IBPA=0^o and 180^o. The recirculating flows are generated once the blade starts to oscillate, and the primarily generated vortex flows are pushed back by the newly generated recirculation at both IBPA values. It can be seen in Fig. A.21 that for IBPA=0^o, the periodic flow pattern of the recirculation is generated after different cycles of vibration. These vortex generations become noticeable after 10 oscillations, and the separated shear layer on the upper blade interacts with the lower one. The formation of the separation bubble near the trailing edge of the LPT blades become more non-uniform after 15 vibration periods at IBPA=0^o. In contrast, this non-uniform vortex generation at IBPA=180^o is more significant even after just five oscillations (See Fig. A.22). The rolling up of the recirculation and the separation of the flow are detected on the surface of the LPT blades after 10 vibration periods and it becomes stronger after 15 vibration periods. It can be seen that the size of the rolling up is larger and the flow disturbance is more noticeable after 20 oscillations. At IBPA=180^o, the downstream flow and wake are more unsteady and turbulent than that of the IBPA of 0^o case as the flow structures in the downstream region are highly distorted by those of the neighbouring blades, especially by the ones in the upper passage.

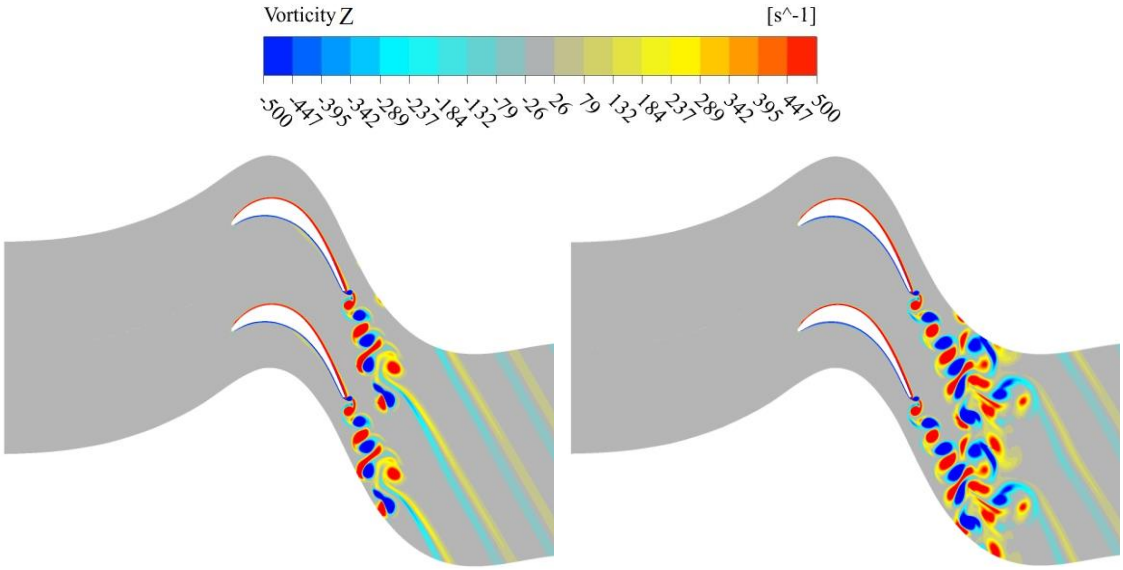

a) After 5 vibration periods

b) After 10 vibration periods

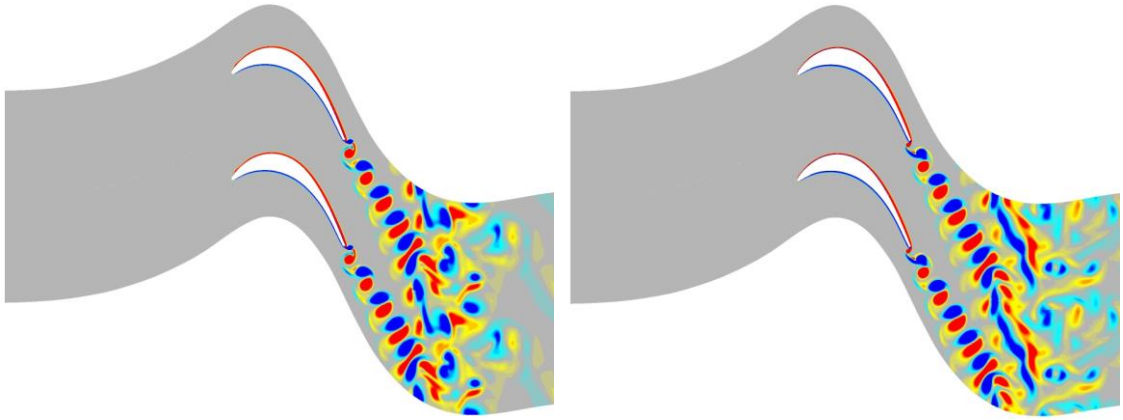

c) After 15 vibration periods

d) After 20 vibration periods

Figure A.21. Vortex generation process over different vibration periods at IBPA=0º.

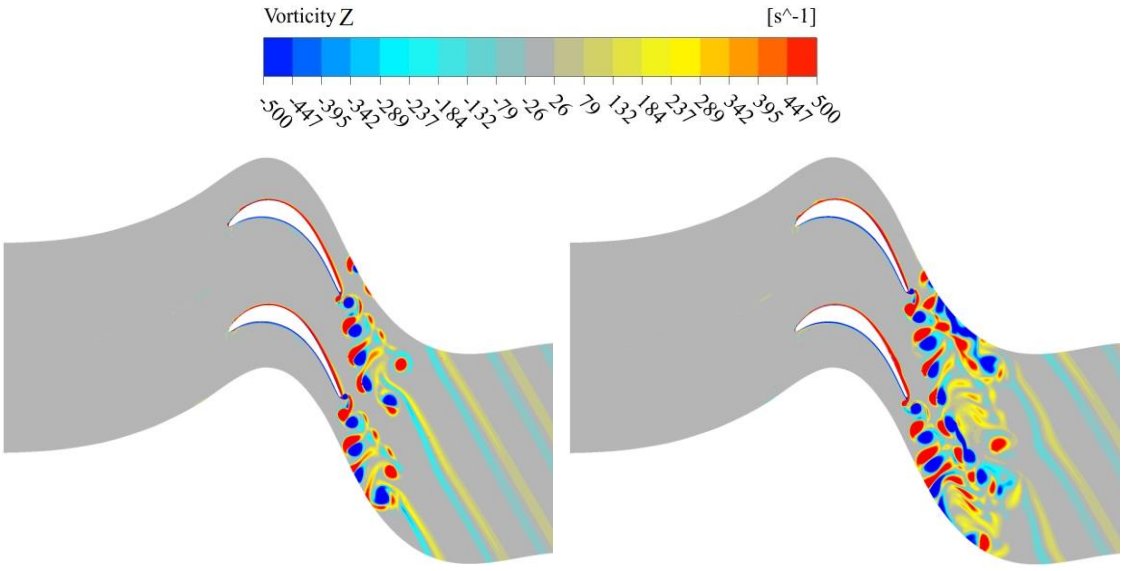

a) After 5 vibration periods

b) After 10 vibration periods

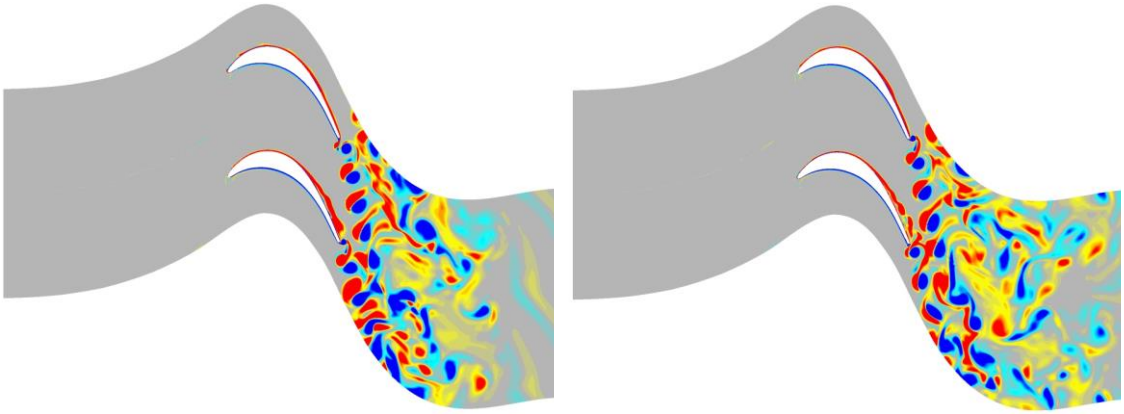

c) After 15 vibration periods d) After 20 vibration periods

Figure A.22. Vortex generation process over different vibration periods at IBPA=180^o.

The variations of the vorticity contours at various blade sections are presented in Figs. A.23 and A.24. The results are provided after 20 oscillation periods to envisage the effects of various oscillation phase-angles on the flow structures over the vibrating blades. It is observed that small and similar flow structures and recirculation are generated at 30% of the span in both IBPA cases. This is because of the small oscillation amplitude at 30% of span and therefore, the inter blade phase angle has a negligible impact. But obvious deviations among the cases are observed at 50% span, and these deviations become noticeable, by moving in the span-wise direction, at the 70% and 90% span sections. The flow structures from the vortex generation of the upper blade go down and mix with the recirculation generated from the lower blade just after shedding from the trailing edge at IBPA=180^o. On the other hand, similar flow structures and vortex generation processes are identified in each passage of the cascade at IBPA=0^o resulting in the turbulence in the wake region due to the flow mixing. At the external sections of the blade (50% or higher) for both IBPA=0^o and 180^o, the fluid combination happens as soon as it sheds from the trailing edge. Besides, the transitional flow structure and turbulent fluctuations of the flow become noticeable at IBPA=180^o. Consequently, the blade oscillation has a huge impact on the transitional flow structures and vortex generation process, and the shape of the recirculating flow is highly dependent on the amplitude of the blade oscillation and the value of IBPA between the two consecutive blades.

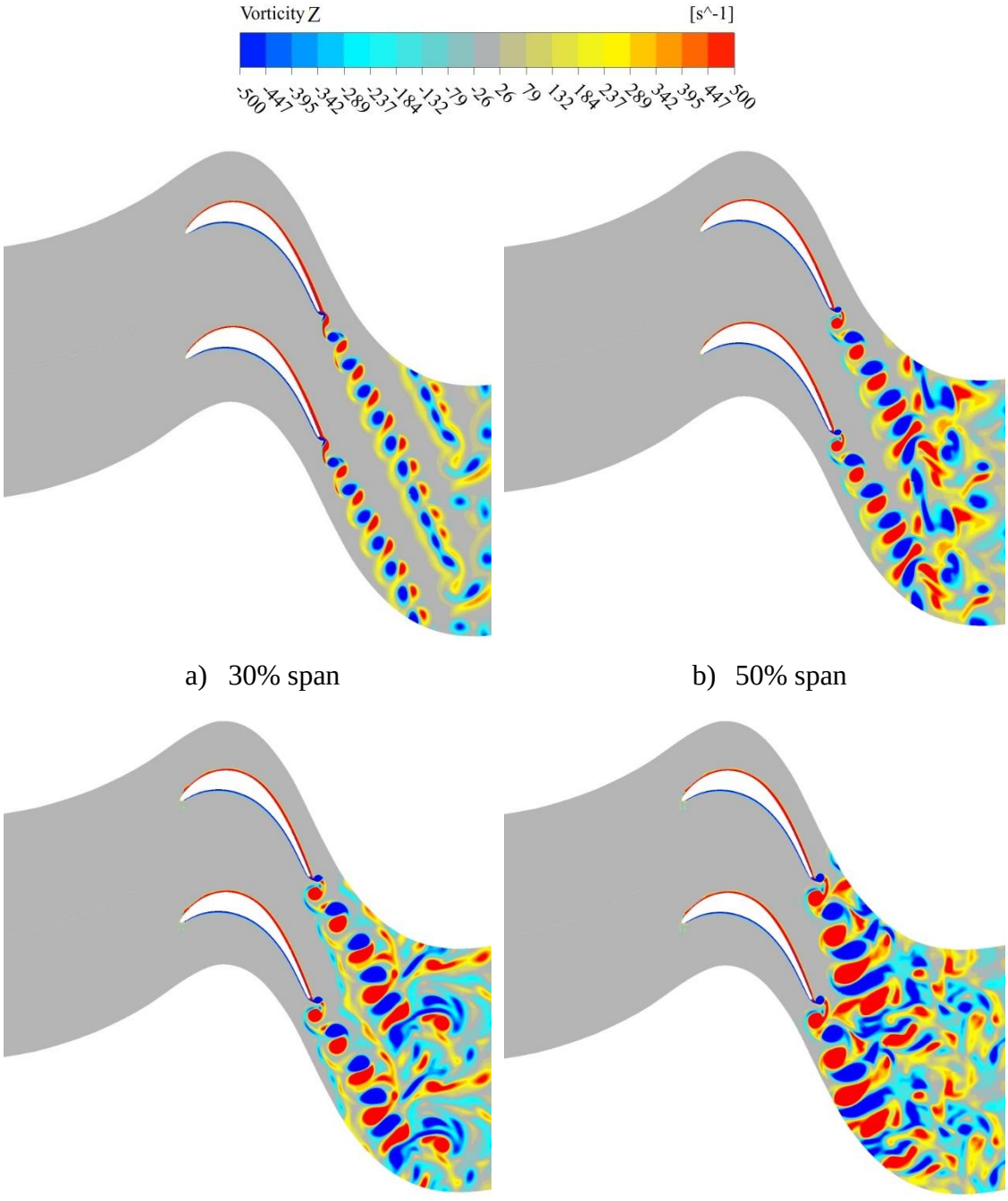

a) 30% span

b) 50% span

c) 70% span

d) 90% span

Figure A.23. Vorticity contours at different blade span sections at IBPA=0º.

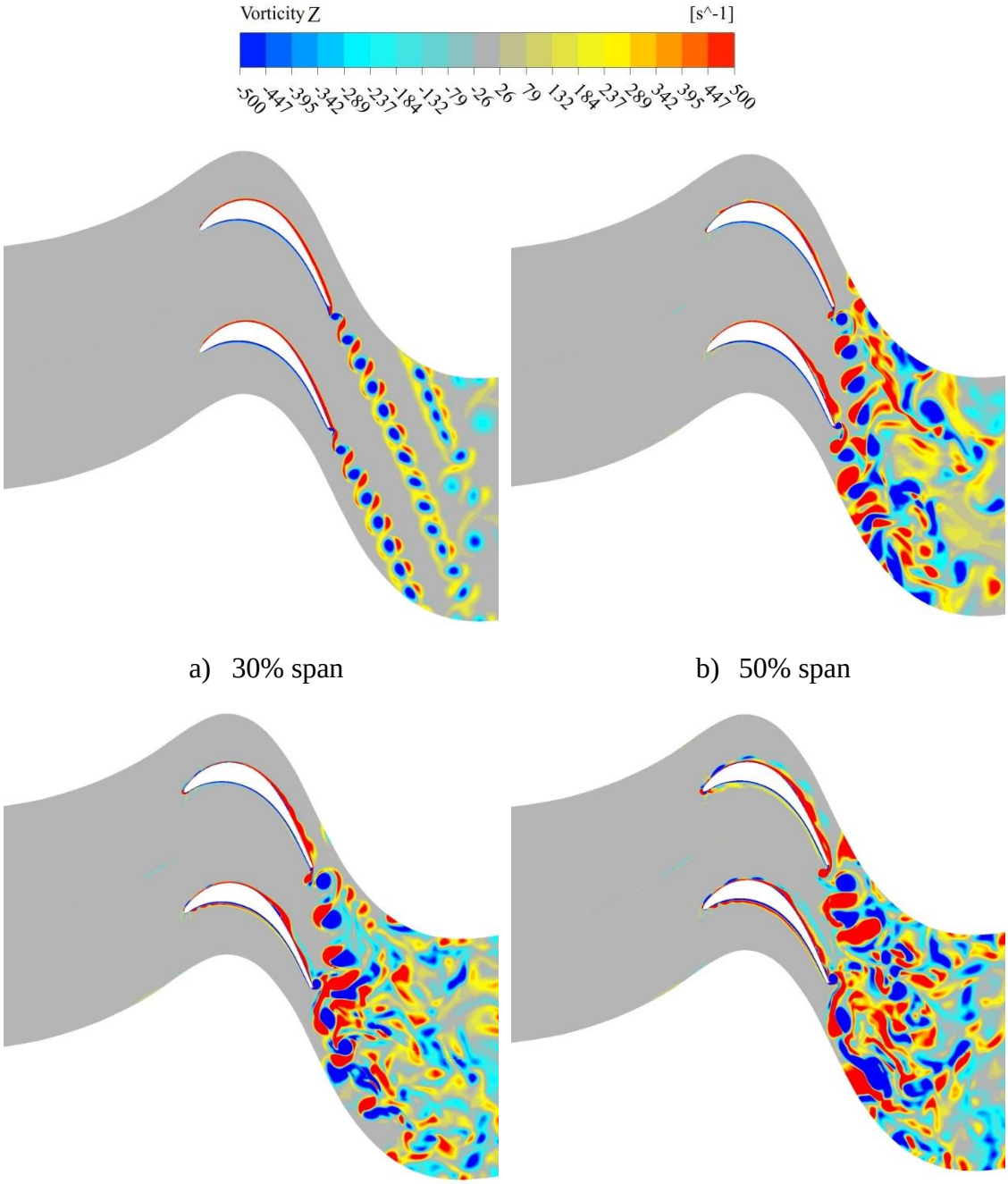

a) 30% span

b) 50% span

c) 70% span

d) 90% span

Figure A.24. Vorticity contours at different blade span sections at IBPA=180^{o}.

Figure A.25 depicts the wake profile variations for the stationary blade and oscillating blades with IBPA=0^{o} and 180^{o} at Re = 5.1 × 10^{4}. The results are provided for 40% chord downstream of the trailing edge at the blade mid-span of the lower passage. A significant difference is observed for the wake profiles between the stationary and oscillating blades, which indicates that the blades oscillations have a significant influence on the transient flow structures around the blades. It can be seen that the vibration raises the peak value of the wake profile compared to the stationary blade case. The results show that the wake

has a transverse profile at IBPA=0^o compared to 180^o, which has a wavy structure along the pitch direction. Figure A.26 shows the instantaneous pressure contours over the blades at different sections and IBPAs. It is seen that the pressure becomes higher as it moves towards the shroud from the hub. The blade vibration generates pressure bubbles from the trailing edge of the blade. The pressure fluctuation and pressure bubbles are stronger and larger in the section close to the shroud where the oscillation amplitude is higher than any other sections. The effect of IBPA on the pressure distribution can also be clearly observed in this figure. A similar pattern of pressure distribution and pressure bubbles are seen in each passage at IBPA=0^o as the blades move together in the same phase. However, the pressure deviations over the blade surfaces are much higher when the IBPA is 180^o. Due to the out-of-phase vibration mode, the pressure distribution around the blade in a passage is influenced by that of the neighbouring passages. The pressure bubbles left from the trailing edge of the blade are swayed by the blade oscillation with an IBPA of 180^o, and they are larger than those of the IBPA of 0^o case. It is also observed that the turbulence due to pressure fluctuation in the wake region is higher in the case of IBPA=180^o.

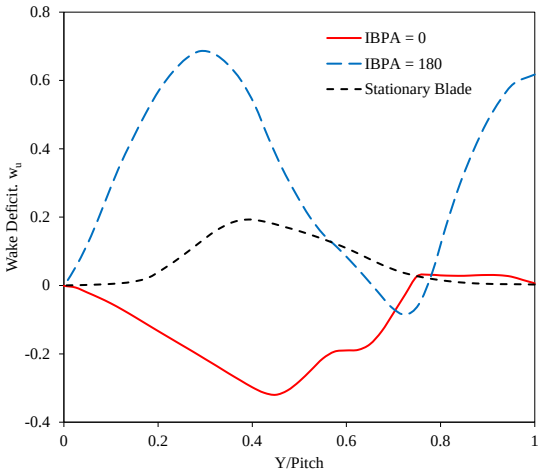

Figure A.25. Wake profiles from the stationary blade case and the vibrating blade cases at different IBPAs at Re=5.1 × 10^4.

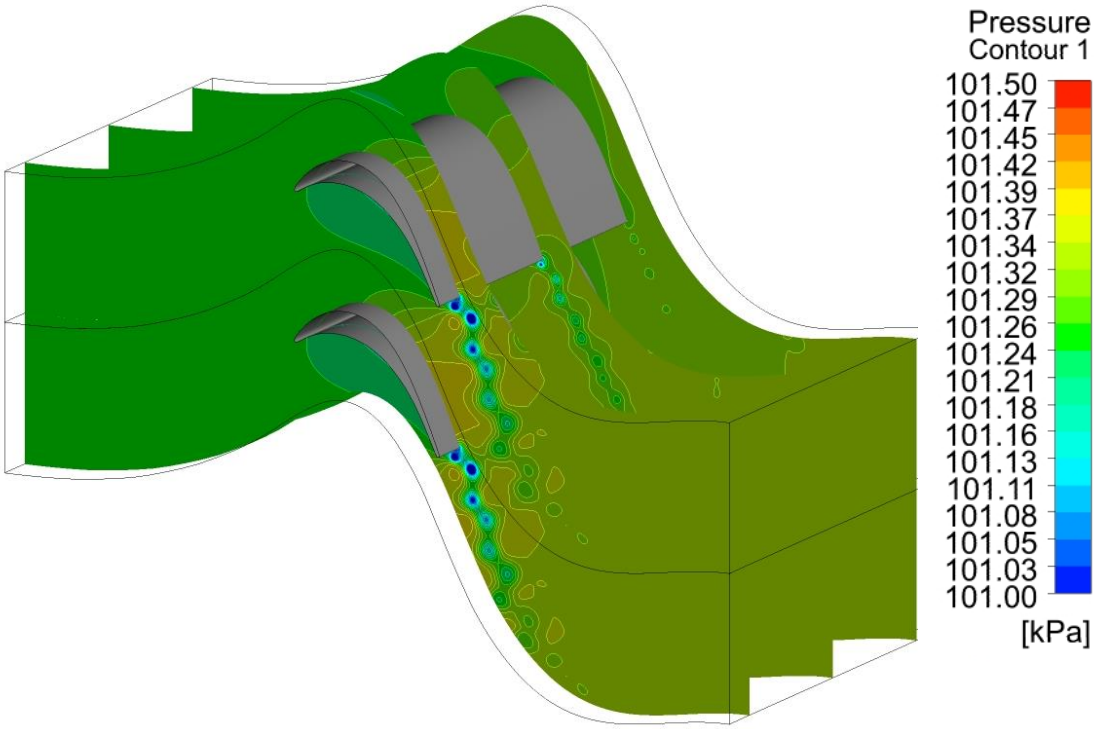

a) IBPA=0º

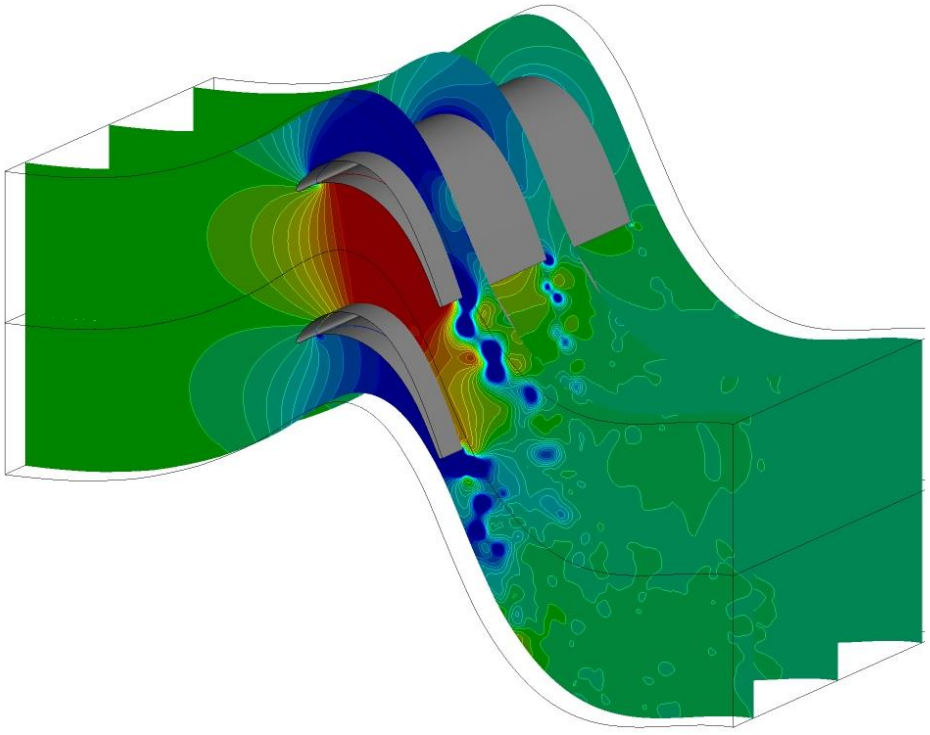

b) IBPA=180º

Figure A.26. Pressure contours from the vibrating blade cases at different IBPAs at Re=5.1 × 10^4.

Apart from the time accurate solution, typically known as the time-domain method, a frequency domain method is also employed in this study to investigate the capability of

this method on capturing and resolving unsteady flow structures due to the effect of the blade flutter. To this end, the flow simulations are conducted at Re = 5.1×10^4 using the frequency domain method using different harmonics, and the flow structures are compared to those of the time-domain method. Figures A.27 and A.28 compare the vorticity structures developed from the trailing edge of the blade within the initial periods of vibration at both IBPAs, resolved by the time-domain method and the frequency domain method using different harmonics. It is observed that the flow structures obtained from the frequency domain solution method using 5 harmonics are similar to that of the time-domain solution. Similar to the 2D model, it is also noticed that the flow structures leaving from the trailing edge of the blade are not accurately resolved even when using 5 harmonics. Although increasing the order of harmonic will enhance the flow resolution, this will escalate the computational resource requirement by a significant factor, which could even exceed the capability of most powerful computers. Therefore, it can be concluded that at least 5 harmonics are required to predict the vortex structures due to the effect of the blade flutter with different IBPAs in an LPT.

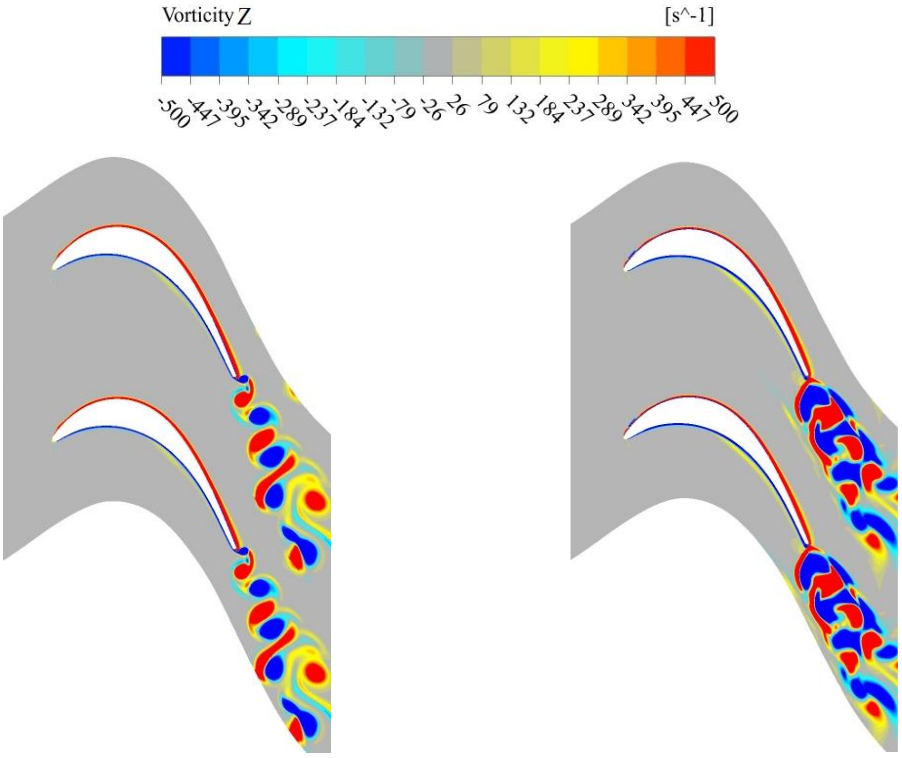

a) Time domain method b) 1 harmonic

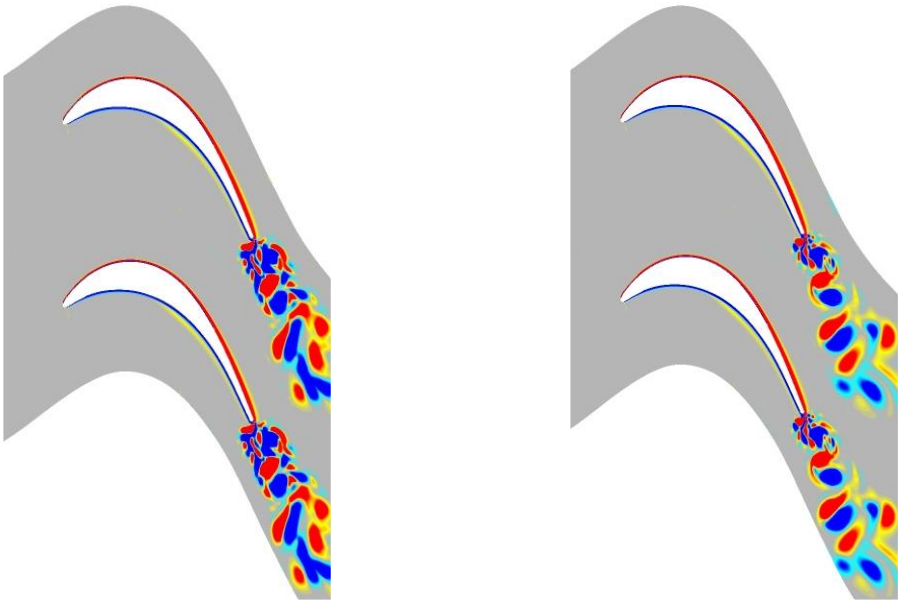

c) 3 harmonics d) 5 harmonics

Figure A.27. Comparison of vorticity structures between the time domain method and the frequency domain method using different harmonics at IBPA=0°.

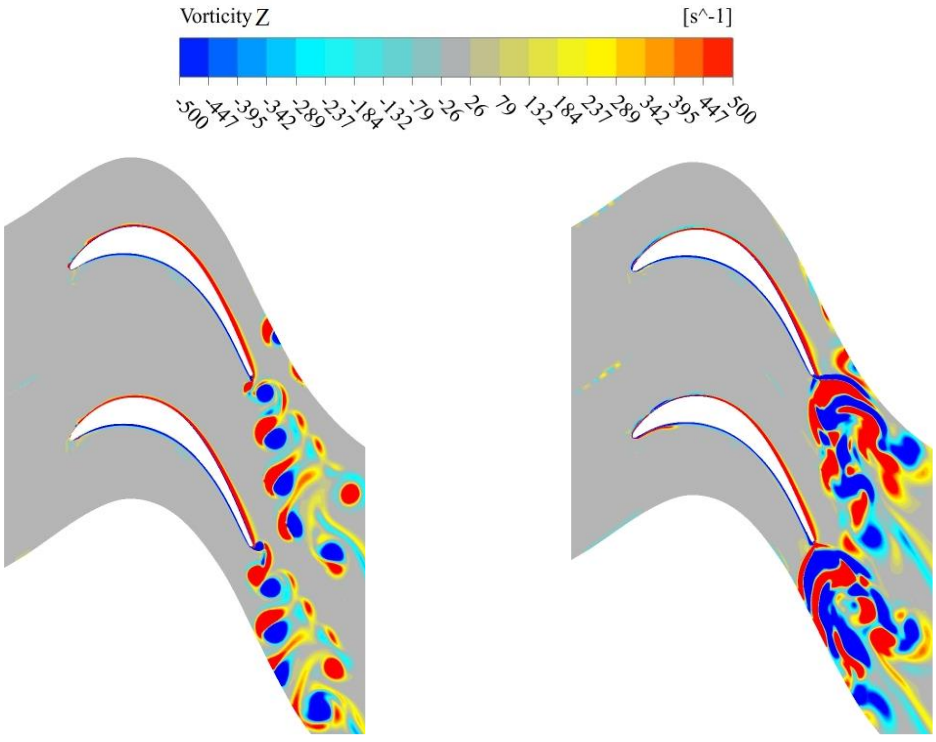

a) Time domain method b) 1 harmonic

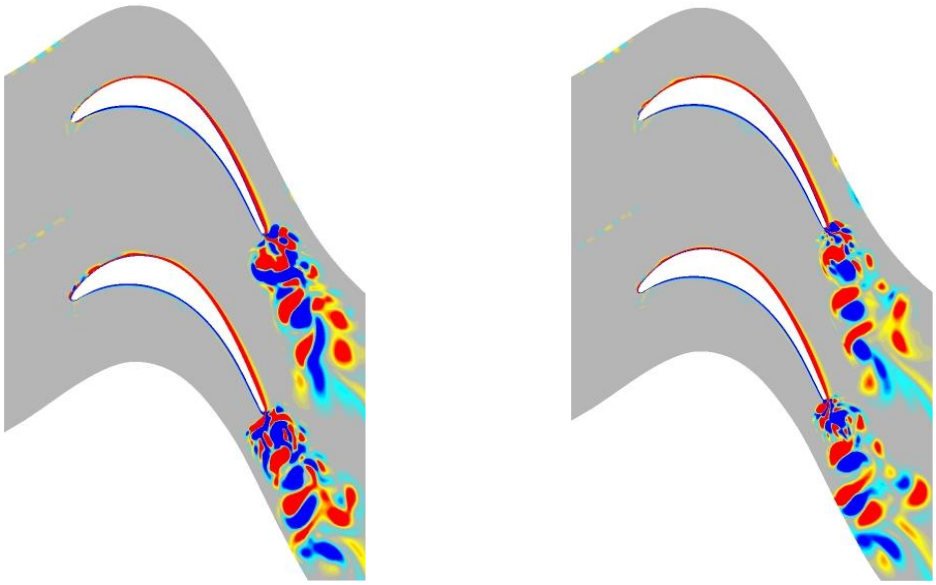

c) 3 harmonics d) 5 harmonics

Figure A.28. Comparison of vorticity structures between the time domain method and the frequency domain method using different harmonics at IBPA=180^o.

Further comparisons in terms of the unsteady pressure distribution, as well as the computation of the aerodynamic damping value between the time domain method and the frequency domain method, are also provided to ensure the accuracy of the latter method. The unsteady pressure coefficient and phase angle at different span sections are presented in Figs A.29 and A.30. The results are provided for both the time domain method and the frequency domain method (using five harmonics) at 30% and 90% of span. The results illustrate that both models agree well with each other. However, the required computation time for the frequency domain method is one to two orders of magnitude lower than the conventional time domain method. For high-resolution DNS simulations, selecting an efficient method with appropriate accuracy is essential. The aerodynamic damping parameter is one of the critical parameters in the design of turbomachines. Table A.2 shows the aerodynamic damping values for the blade with an IBPA=0^o and 180^o. The results are calculated from the time domain method and the frequency domain method. Excellent agreement is obtained between the two methods. The results show that the aerodynamic damping is positive for both cases indicating that the blade vibrations are stable at both IBPAs.

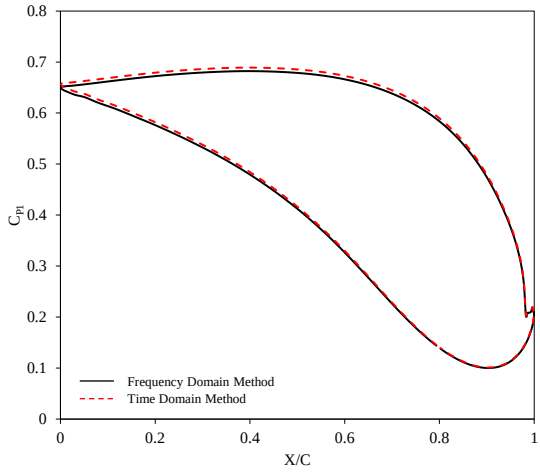

a) C_{p1} at 30% span

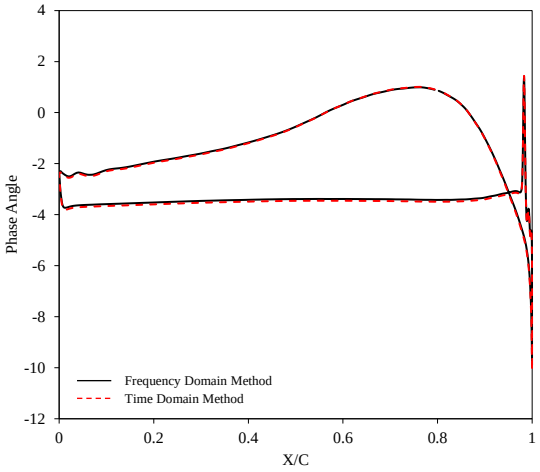

b) Phase angle at 30% span

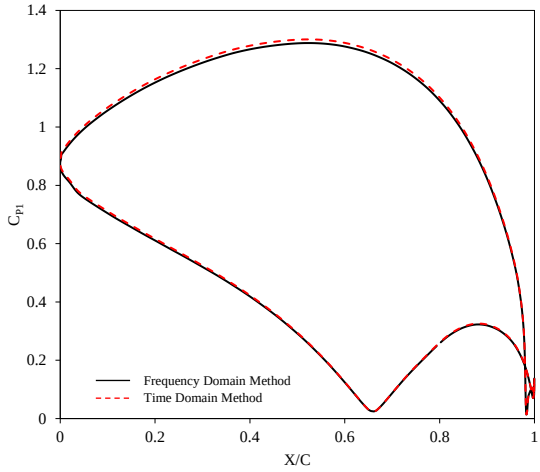

c) C_{p1} at 90% span

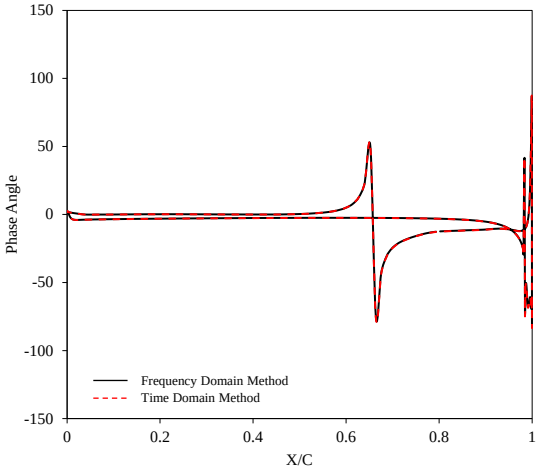

d) Phase angle at 90% span

Figure A.29. Unsteady pressure amplitude coefficient and phase angle at IBPA=0º obtained from the time domain method and the frequency domain method.

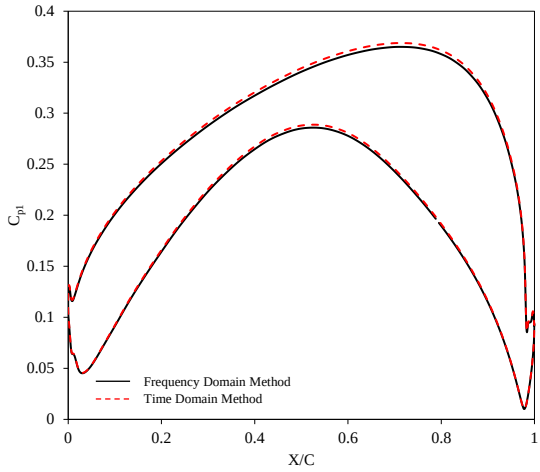

a) C_{p1} at 30% span

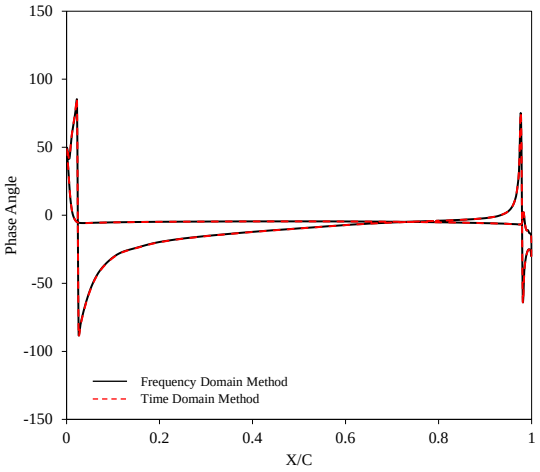

b) Phase angle at 30% span

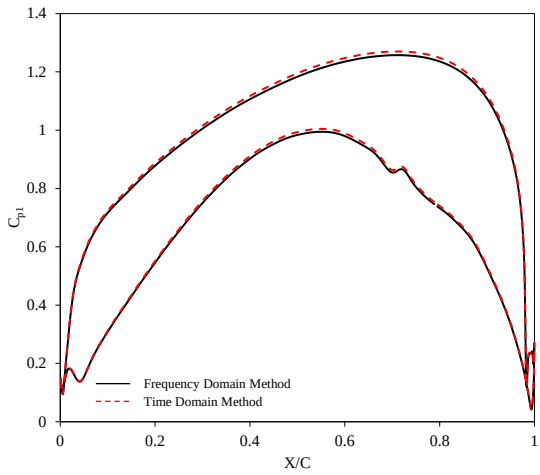

c) C_{p1} at 90% span

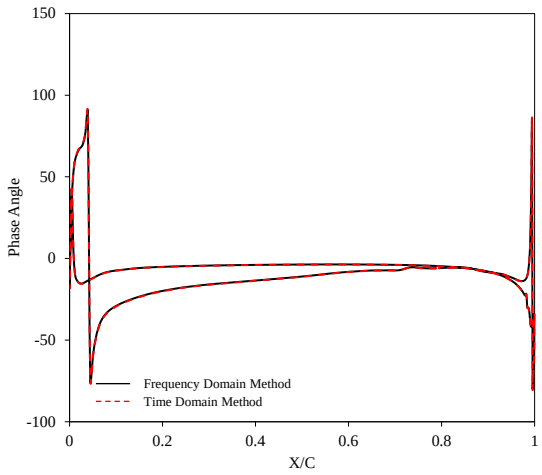

d) Phase angle at 90% span

Figure A.30. Unsteady pressure amplitude coefficient and phase angle at IBPA=180º obtained from the time domain method and the frequency domain method.

Table A.2. Aerodynamic damping of the blade at different IBPAs.

Case	Time Domain Method	Frequency Domain Method
IBPA=0º	0.027	0.025
IBPA=180º	0.053	0.050

The DNS simulations of the present study were performed on the Oswald HPC cluster at Northumbria University. 336 processors were used for the computations. It should be pointed out that the required memory for the frequency domain method is much higher compared to the time domain method. However, the computation time is reduced by 78% by using the frequency domain method. Besides, the accuracy of this method to predict the aeroelasticity parameters and the effect of the blade vibration on the vortex generation process is very high.

Summary of the Appendix

In this appendix, the numerical investigations of the transient flow and the blade structure inside the T106A low-pressure turbine using both 2D and 3D models are presented. A high-fidelity DNS method is used for the flow simulations. First of all, the CFD model employed in this study is validated against the experiment as well as the previous DNS simulations in terms of time-averaged pressure coefficient distribution, wake profile and wall shear stress.

Using the validated CFD model, the forced response and flutter instability in this turbine are investigated using both 2D and 3D models. Results from the 2D analysis show that a slight difference is seen between the vibrating blade case and the stationary blade case in terms of time-averaged pressure distribution whereas a significant difference is observed between them in terms of wake profiles. Visualisations of the flow structures indicate that the flow is highly distorted by the blade structure motion and the evolution of vortex structures are directly associated with the blade vibration.

The 3D analysis further proves that the unsteady flow is primarily affected by the blade vibration. The shape and the size of the vortex structures strongly depend on the vibration amplitude and phase angle, and they are considerably larger and stronger in the blade outer region where the amplitude of oscillation is high. This shows that the 3D vibration of the blade structure has a direct and significant impact on the unsteady flow. Although the 2D analysis can briefly provide the effect of vibration, it lacks in providing the effects associated with the 3D blade structure. Nevertheless, both 2D and 3D analyses indicate that the unsteady flow inside an LPT is highly influenced by the blade structure vibration, and the shape and the size of the vorticity are determined by the blade vibration. Therefore, it can be concluded that the wake in the downstream region of an LPT can be controlled by the blade vibration with a specified frequency and amplitude.

The 3D analysis also provides the effect of Reynolds number and the IBPA on the transitional flow structures and vortex generation. At IBPA=0^o, a recurring pattern of vortex generation was detected in each passage, and they are mixed up in the downstream region. However, at IBPA=180^o, the flow structures generated from the upper passage strongly influence those from the lower one and the mixing of the flow recirculation and vortex generation leads to the highly turbulent flow in the wake region. It is concluded that the flow instabilities and perturbations are stronger at IBPA=180^o than IBPA=0^o due to the effect of out-of-phase vibration which is associated with the pitch length between two consecutive blades changes within a vibration cycle. Moreover, the aerodynamic damping parameters are positive in all of the test cases, but it is higher at the IBPA of 180^o. The flow separation and instabilities are much higher at lower Reynolds numbers. Raising the Reynolds number can minimise the separation bubbles in the separation zone and can reduce the size of flow separation. The flow structures and recirculation become larger and stronger with increasing Reynolds number. The differences in pressure distribution on the aerofoil surfaces between both IBPA cases can be reduced by raising

the Reynolds number. However, the differences are still considerable in the blade outer region due to the high amplitude of oscillation near the blade tip.

The URANS computation is also conducted in this study and the results are compared to that of the DNS computation. It is found that the aerodynamic damping value predicted from the URANS model is well comparable to that of the DNS model. Although the vortex structures generated from the blade trailing edge are captured by the URANS model, the wake structures in the far downstream area, where the flows from each passage are mixed up, are not resolved by the URANS model. Furthermore, the flow separation and recirculation are also not accurately predicted by the URANS model. This is within expectation due to the averaging of flow paraments by URANS models.

In addition to the time domain method, the frequency domain method using different harmonics is also used in this study to determine the capability of this method in analysing aeroelasticity and the transient flow behaviour inside a modern LPT. Results show that at least 5 harmonics are required in both 2D and 3D models to resolve the necessary flow structures. In terms of computation time, the frequency domain method solves significantly faster than the traditional time domain method.

Overall, this study provides a comprehensive understanding of the physics behind the fluid-structure interaction process, and these understandings are relevant to and useful for other turbomachines including wind turbines. Furthermore, it is evident that the frequency domain method has the capability of analysing the highly unsteady flow, depending on the order of harmonics, at a reasonable computational cost. Although the URANS models are unable to accurately capture the highly unsteady flow field and complex vortex structures in an LPT, they can still be considered adequate for the study of aerodynamics and aeroelasticity of wind turbines with a good prediction on the aerodynamic damping and reasonable flow behaviour. Therefore, it is concluded that the URANS model using the frequency domain method is considered a suitable and reasonable approach for the aerodynamic and aeromechanical analysis of wind turbines if the computational resources are limited. However, if these resources permit, high fidelity numerical methods such as the DNS method should be approached for the accurate prediction of the flow structures.

References

[1] Pramod, J., 2016, "Kinetic Energy of Wind," Wind Energy Engineering, McGraw-Hill Education, New York, pp. 9-11.

[2] RenewableUK, 2020, "RenewableUK's Vision of the Transition Summary Report," https://www.renewableuk.com/news/508794/Powering-the-Future-RenewableUKs-Vision-of-the-Transition-Summary-Report.htm.

[3] UK Government, 2020, "The Ten Point Plan for a Green Industrial Revolution," https://www.gov.uk/government/publications/the-ten-point-plan-for-a-green-industrial-revolution/title.

[4] Feng, J., and Shen, W. Z., 2017, "Design optimization of offshore wind farms with multiple types of wind turbines," Applied Energy, 205, pp. 1283-1297.

[5] Action Renewables, 2019, "The evolution of wind turbines," https://actionrenewables.co.uk/news-events/post.php?s=the-evolution-of-wind-turbines.

[6] Zhang, P., and Huang, S., 2011, "Review of aeroelasticity for wind turbine: Current status, research focus and future perspectives," Frontiers in Energy, 5(4), pp. 419-434.

[7] Hansen, M. O. L., Sørensen, J. N., Voutsinas, S., Sørensen, N., and Madsen, H. A., 2006, "State of the art in wind turbine aerodynamics and aeroelasticity," Progress in Aerospace Sciences, 42(4), pp. 285-330.

[8] Chowdhury, S., Zhang, J., Messac, A., and Castillo, L., 2013, "Optimizing the arrangement and the selection of turbines for wind farms subject to varying wind conditions," Renewable Energy, 52, pp. 273-282.

[9] DuPont, B., Cagan, J., and Moriarty, P., 2016, "An advanced modeling system for optimization of wind farm layout and wind turbine sizing using a multi-level extended pattern search algorithm," Energy, 106, pp. 802-814.

[10] Shakoor, R., Hassan, M. Y., Raheem, A., and Wu, Y.-K., 2016, "Wake effect modeling: A review of wind farm layout optimization using Jensen′s model," Renewable and Sustainable Energy Reviews, 58, pp. 1048-1059.

[11] Sun, H., Yang, H., and Gao, X., 2019, "Investigation into spacing restriction and layout optimization of wind farm with multiple types of wind turbines," Energy, 168, pp. 637-650.

[12] Renewable Energy World, 2014, "History of Wind Turbines," https://www.renewableenergyworld.com/storage/history-of-wind-turbines/#gref.

[13] Manwell, J. F., McGowan, J.G. and Rogers, A.L., 2009, "Introduction: Modern Wind Energy and its Origins," Wind Energy Explained, John Wiley & Sons, Ltd, Chichester, pp. 1-22.
[14] Spera, D. A., 2009, Wind Turbine Technology: Fundamental Concepts in Wind Turbine Engineering, Second Edition, ASME Press.
[15] Hau, E., 2013, "Electrical Power from the Wind - The First Attempts," Wind Turbines: Fundamentals, Technologies, Application, Economics, E. Hau, ed., Springer Berlin Heidelberg, Berlin, Heidelberg, pp. 23-64.
[16] Betz, A., 1919, "Schraubenpropeller mit geringstem Energieverlust," Gottinger Nachrichten, pp. 193-213.
[17] Glauert, H., 1930, "Aerodynamic Theory," The Journal of the Royal Aeronautical Society, 34(233), pp. 409-414.
[18] Okulov, V. L., and Sørensen, J. N., 2008, "Refined Betz limit for rotors with a finite number of blades," Wind Energy, 11(4), pp. 415-426.
[19] Global Wind Energy Council (GWEC), 2019, "Global Wind Report 2019."
[20] Veers, P. S., Ashwill, T. D., Sutherland, H. J., Laird, D. L., Lobitz, D. W., Griffin, D. A., Mandell, J. F., Musial, W. D., Jackson, K., Zuteck, M., Miravete, A., Tsai, S. W., and Richmond, J. L., 2003, "Trends in the Design, Manufacture and Evaluation of Wind Turbine Blades," Wind Energy, 6(3), pp. 245-259.
[21] Manwell, J. F., McGowan, J.G. and Rogers, A.L., 2009, "Aerodynamics of Wind Turbines," Wind Energy Explained, John Wiley & Sons, Ltd, Chichester, pp. 91-155.
[22] Hau, E., 2013, "Physical Principles of Wind Energy Conversion," Wind Turbines: Fundamentals, Technologies, Application, Economics, E. Hau, ed., Springer Berlin Heidelberg, Berlin, Heidelberg, pp. 79-87.
[23] Hau, E., 2013, "Rotor Aerodynamics," Wind Turbines: Fundamentals, Technologies, Application, Economics, E. Hau, ed., Springer Berlin Heidelberg, Berlin, Heidelberg, pp. 89-166.
[24] Zhang, W., Cheng, W., Gao, W., Qamar, A., and Samtaney, R., 2015, "Geometrical effects on the airfoil flow separation and transition," Computers & Fluids, 116, pp. 60-73.
[25] Koca, K., Genç, M. S., Açıkel, H. H., Çağdaş, M., and Bodur, T. M., 2018, "Identification of flow phenomena over NACA 4412 wind turbine airfoil at low Reynolds numbers and role of laminar separation bubble on flow evolution," Energy, 144, pp. 750-764.

[26] Pramod, J., 2016, "Aerodynamics of Wind Turbine Blades," Wind Energy Engineering, McGraw-Hill Education, New York, pp. 41-62.
[27] Manwell, J. F., McGowan, J.G. and Rogers, A.L., 2009, "Mechanics and Dynamics," Wind Energy Explained, John Wiley & Sons, Ltd, Chichester, pp. 157-203.
[28] Hau, E., 2013, "Mechanical Drive Train and Nacelle," Wind Turbines: Fundamentals, Technologies, Application, Economics, Springer Berlin Heidelberg, Berlin, Heidelberg, pp. 305-383.
[29] Peeters, J., 2006, "Simulation of dynamic drive train loads in a wind turbine,"PhD Thesis, Katholieke Universiteit Leuven.
[30] Win Naung, S., 2016, "Optimum Design of Wind Turbine Gearbox,"Master's Thesis, Waseda University, Tokyo.
[31] Manwell, J. F., McGowan, J.G. and Rogers, A.L., 2009, "Electrical Aspects of Wind Turbines," Wind Energy Explained, John Wiley & Sons, Ltd, Chichester, pp. 205-256.
[32] Hau, E., 2013, "Electrical System," Wind Turbines: Fundamentals, Technologies, Application, Economics, Springer Berlin Heidelberg, Berlin, Heidelberg, pp. 385-428.
[33] Win Naung, S., and Miyashita, T., 2015, "Optimum Design of Wind Turbine Drivetrain," The Abstracts of the international conference on advanced mechatronics : toward evolutionary fusion of IT and mechatronics : ICAM, 2015.6, pp. 152-153.
[34] Kadhim, H. T., Rona, A., Gostelow, J. P., and Leschke, K., 2018, "Optimization of the non-axisymmetric stator casing of a 1.5 stage axial turbine," International Journal of Mechanical Sciences, 136, pp. 503-514.
[35] Jung, S. Y., Kim, J. J., Park, H. W., and Lee, S. J., 2018, "Comparison of flow structures behind rigid and flexible finite cylinders," International Journal of Mechanical Sciences, 142-143, pp. 480-490.
[36] Hodson, H. P., and Howell, R. J., 2005, "The role of transition in high-lift low-pressure turbines for aeroengines," Progress in Aerospace Sciences, 41(6), pp. 419-454.
[37] Himmel, C. G., 2010, "Ultra-high lift blades for low pressure turbines," University of Cambridge.
[38] Wentong, S., Weilin, Y., and Lucheng, J., 2018, "Effect of inlet total pressure non-uniform distribution on aerodynamic performance and flow field of turbine," International Journal of Mechanical Sciences, 148, pp. 714-729.
[39] Hodson, H. P., and Howell, R. J., 2005, "Bladerow interactions, transition, and high-lift aerofoils in low-pressure turbines," Annual Review of Fluid Mechanics, 37(1), pp. 71-98.

[40] Coull, J. D., and Hodson, H. P., 2011, "Unsteady boundary-layer transition in low-pressure turbines," Journal of Fluid Mechanics, 681, pp. 370-410.
[41] Panovsky, J., and Kielb, R. E., 1999, "A Design Method to Prevent Low Pressure Turbine Blade Flutter," Journal of Engineering for Gas Turbines and Power, 122(1), pp. 89-98.
[42] Waite, J. J., and Kielb, R. E., 2014, "Physical Understanding and Sensitivities of Low Pressure Turbine Flutter," Journal of Engineering for Gas Turbines and Power, 137(1).
[43] Waite, J. J., and Kielb, R. E., 2015, "The Impact of Blade Loading and Unsteady Pressure Bifurcations on Low-Pressure Turbine Flutter Boundaries," Journal of Turbomachinery, 138(4).
[44] Buchwald, P., Farahmand, A., and Vogt, D. M., 2019, "On the Influence of Blade Aspect Ratio on Aerodynamic Damping," Journal of Turbomachinery, 141(10).
[45] Corral, R., and Vega, A., 2015, "The Low Reduced Frequency Limit of Vibrating Airfoils—Part I: Theoretical Analysis," Journal of Turbomachinery, 138(2).
[46] Vega, A., and Corral, R., 2015, "The Low Reduced Frequency Limit of Vibrating Airfoils—Part II: Numerical Experiments," Journal of Turbomachinery, 138(2).
[47] Stadtmüller, P., 2001, "Investigation of wake-induced transition on the LP turbine cascade T106A-EIZ," DFG-Verbundprojekt Fo, 136(11).
[48] Garai, A., Diosady, L. T., Murman, S. M., and Madavan, N. K., "DNS of Low-Pressure Turbine Cascade Flows With Elevated Inflow Turbulence Using a Discontinuous-Galerkin Spectral-Element Method," Proc. ASME Turbo Expo 2016: Turbomachinery Technical Conference and ExpositionV02CT39A025.
[49] Wang, Y., Chen, F., Liu, H., and Chen, H., 2014, "Large eddy simulation of unsteady transitional flow on the low-pressure turbine blade," Science China Technological Sciences, 57(9), pp. 1761-1768.
[50] Wissink, J. G., 2003, "DNS of separating, low Reynolds number flow in a turbine cascade with incoming wakes," International Journal of Heat and Fluid Flow, 24(4), pp. 626-635.
[51] Ranjan, R., Deshpande, S., and Narasimha, R., 2016, "A high-resolution DNS study of compressible flow past an LPT blade in a cascade," arXiv preprint arXiv:1611.09746.
[52] Ranjan, R., Deshpande, S. M., and Narasimha, R., 2017, "New insights from high-resolution compressible DNS studies on an LPT blade boundary layer," Computers & Fluids, 153, pp. 49-60.

[53] Michelassi, V., Wissink, J., and Rodi, W., 2002, "Analysis of DNS and LES of Flow in a Low Pressure Turbine Cascade with Incoming Wakes and Comparison with Experiments," Flow, Turbulence and Combustion, 69(3), pp. 295-329.
[54] Wissink, J. G., and Rodi, W., 2006, "Direct Numerical Simulations of Transitional Flow in Turbomachinery," Journal of Turbomachinery, 128(4), pp. 668-678.
[55] Sandberg, R. D., Michelassi, V., Pichler, R., Chen, L., and Johnstone, R., 2015, "Compressible Direct Numerical Simulation of Low-Pressure Turbines—Part I: Methodology," Journal of Turbomachinery, 137(5).
[56] Michelassi, V., Chen, L.-W., Pichler, R., and Sandberg, R. D., 2015, "Compressible Direct Numerical Simulation of Low-Pressure Turbines—Part II: Effect of Inflow Disturbances," Journal of Turbomachinery, 137(7).
[57] Nakhchi, M. E., Win Naung, S., and Rahmati, M., 2020, "DNS of secondary flows over oscillating low-pressure turbine using spectral/hp element method," International Journal of Heat and Fluid Flow, 86, p. 108684.
[58] Huang, X. Q., He, L., and Bell, D. L., 2009, "Experimental and Computational Study of Oscillating Turbine Cascade and Influence of Part-Span Shrouds," Journal of Fluids Engineering, 131(5).
[59] Dowell, E. H., 2015, A Modern Course in Aeroelasticity, Springer International Publishing, Cham.
[60] Hansen, M. H., 2007, "Aeroelastic instability problems for wind turbines," Wind Energy, 10(6), pp. 551-577.
[61] Hau, E., 2013, "Vibration Characteristics," Wind Turbines: Fundamentals, Technologies, Application, Economics, Springer Berlin Heidelberg, Berlin, Heidelberg, pp. 233-268.
[62] Rezaei, M. M., Behzad, M., Haddadpour, H., and Moradi, H., 2017, "Aeroelastic analysis of a rotating wind turbine blade using a geometrically exact formulation," Nonlinear Dynamics, 89(4), pp. 2367-2392.
[63] Chaviaropoulos, P. K., Politis, E. S., Lekou, D. J., Sørensen, N. N., Hansen, M. H., Bulder, B. H., Winkelaar, D., Lindenburg, C., Saravanos, D. A., Philippidis, T. P., Galiotis, C., Hansen, M. O. L., and Kossivas, T., 2006, "Enhancing the damping of wind turbine rotor blades, the DAMPBLADE project," Wind Energy, 9(1-2), pp. 163-177.
[64] Ramdenee, D., Ilinca, A., and Minea, I. S., 2012, "Aeroelasticity of Wind Turbines Blades Using Numerical Simulation," Advances in Wind Power, pp. 87-120.

[65] Lee, K., Huque, Z., Kommalapati, R., and Han, S.-E., 2017, "Fluid-structure interaction analysis of NREL phase VI wind turbine: Aerodynamic force evaluation and structural analysis using FSI analysis," Renewable Energy, 113, pp. 512-531.

[66] Dose, B., Rahimi, H., Herráez, I., Stoevesandt, B., and Peinke, J., 2016, "Fluid-structure coupled computations of the NREL 5MW wind turbine blade during standstill," Journal of Physics: Conference Series, 753, p. 022034.

[67] Larsen, T. J., Hansen, A. M., and Buhl, T., 2004, "Aeroelastic effects of large blade deflections for wind turbines," Proceedings of The Science of Making Torque from Wind, pp. 238-246.

[68] Riziotis, V. A., Voutsinas, S. G., Politis, E. S., and Chaviaropoulos, P. K., 2004, "Aeroelastic stability of wind turbines: the problem, the methods and the issues," Wind Energy, 7(4), pp. 373-392.

[69] Hansen, M. H., 2003, "Improved Modal Dynamics of Wind Turbines to Avoid Stall-induced Vibrations," Wind Energy, 6(2), pp. 179-195.

[70] Hansen, M. H., 2004, "Aeroelastic stability analysis of wind turbines using an eigenvalue approach," Wind Energy, 7(2), pp. 133-143.

[71] Hansen, M. H., "Aeroelastic eigenvalue analysis of three-bladed wind turbines," Proc. 29. European rotorcraft forum, Deutsche Gesellschaft für Luft-und Raumfahrt.

[72] Thomsen, K., Petersen, J. T., Nim, E., Øye, S., and Petersen, B., 2000, "A Method for Determination of Damping for Edgewise Blade Vibrations," Wind Energy, 3(4), pp. 233-246.

[73] Bhat, R. B., 2016, Principles of Aeroelasticity, CRC Press, Boca Raton.

[74] Duncan, W. J., 1956, "An Introduction to the Theory of Aeroelasticity. Y. C. Fung. Galcit Aeronautical Series. John Wiley and Sons, New York, 1955. 490 pp. Illustrated. 84s," The Journal of the Royal Aeronautical Society, 60(544), pp. 284-284.

[75] Patil, S., Zori, L., Galpin, P., Morales, J., and Godin, P., "Investigation of Time/Frequency Domain CFD Methods to Predict Turbomachinery Blade Aerodynamic Damping," Proc. ASME Turbo Expo 2016: Turbomachinery Technical Conference and ExpositionV07BT34A028.

[76] Lobitz, D. W., 2004, "Aeroelastic stability predictions for a MW-sized blade," Wind Energy, 7(3), pp. 211-224.

[77] Lobitz, D. W., 2005, "Parameter Sensitivities Affecting the Flutter Speed of a MW-Sized Blade," Journal of Solar Energy Engineering, 127(4), pp. 538-543.

[78] Hansen, M., "Stability Analysis of Three-Bladed Turbines Using an Eigenvalue Approach," 42nd AIAA Aerospace Sciences Meeting and Exhibit.

[79] Bir, G., and Jonkman, J., 2007, "Aeroelastic Instabilities of Large Offshore and Onshore Wind Turbines," Journal of Physics: Conference Series, 75, p. 012069.

[80] Schepers, J., and Snel, H., 2007, "Model experiments in controlled conditions, final report," ECN, ECN-E-07-042, Petten, the Netherlands.

[81] Schepers, J., Boorsma, K., Cho, T., Gomez-Iradi, S., Schaffarczyk, P., Jeromin, A., Shen, W., Lutz, T., Meister, K., and Stoevesandt, B., 2012, "Final report of IEA Task 29, Mexnext (Phase 1): Analysis of Mexico wind tunnel measurements Tech. rep," ECN-E–12-004 ECN URL http://www.ecn.nl/publications/ECN-E--12-004.

[82] Snel, H., Schepers, J., and Pascal, L., "First results from Mexnext: Analysis of detailed aerodynamic measurements on a 4.5 diameter rotor placed in the large German Dutch Wind Tunnel DNW," Proc. European Wind Energy Conference and Exhibition (EWEC), Warsaw, Poland, 20-23 april 2010., ECN.

[83] Schepers, J. G., Boorsma, K., and Munduate, X., 2014, "Final Results from Mexnext-I: Analysis of detailed aerodynamic measurements on a 4.5 m diameter rotor placed in the large German Dutch Wind Tunnel DNW," Journal of Physics: Conference Series, 555, p. 012089.

[84] Krogstad, P.-Å., and Eriksen, P. E., 2013, "“Blind test” calculations of the performance and wake development for a model wind turbine," Renewable Energy, 50, pp. 325-333.

[85] Pierella, F., Krogstad, P.-Å., and Sætran, L., 2014, "Blind Test 2 calculations for two in-line model wind turbines where the downstream turbine operates at various rotational speeds," Renewable Energy, 70, pp. 62-77.

[86] Krogstad, P.-Å., Sætran, L., and Adaramola, M. S., 2015, "“Blind Test 3” calculations of the performance and wake development behind two in-line and offset model wind turbines," Journal of Fluids and Structures, 52, pp. 65-80.

[87] Hand, M. M., Simms, D.A., Fingersh, L.J., Jager, D.W., Cotrell, J.R., Schreck, S., and Larwood S.M, 2001, "Unsteady Aerodynamics Experiment Phase VI: Wind Tunnel Test Configurations and Available Data Campaigns," No. NREL/TP-500-29955, National Renewable Energy Laboratory.

[88] Simms, D., Schreck, S., Hand M., and Fingersh, L.J, 2001, "NREL Unsteady Aerodynamics Experiment in the NASA-Ames Wind Tunnel: A Comparison of Predictions to Measurements," No. NREL/TP-500-29494, National Renewable Energy Laboratory, Golden, Colorado.

[89] Jonkman, J., Butterfield, S., Musial, W., and Scott G., 2009, "Definition of a 5-MW Reference Wind Turbine for Offshore System Development," No. NREL/TP-500-38060, National Renewable Energy Laboratory, Golden, Colorado.

[90] Hsu, M.-C., Akkerman, I., and Bazilevs, Y., 2012, "Wind turbine aerodynamics using ALE–VMS: validation and the role of weakly enforced boundary conditions," Computational Mechanics, 50(4), pp. 499-511.

[91] Nejad, A. R., Guo, Y., Gao, Z., and Moan, T., 2016, "Development of a 5 MW reference gearbox for offshore wind turbines," Wind Energy, 19(6), pp. 1089-1106.

[92] O'Brien, J. M., Young, T. M., O'Mahoney, D. C., and Griffin, P. C., 2017, "Horizontal axis wind turbine research: A review of commercial CFD, FE codes and experimental practices," Progress in Aerospace Sciences, 92, pp. 1-24.

[93] Wang, Q., Wang, J., Chen, J., Luo, S., and Sun, J., 2015, "Aerodynamic shape optimized design for wind turbine blade using new airfoil series," Journal of Mechanical Science and Technology, 29(7), pp. 2871-2882.

[94] Wang, L., Liu, X., Renevier, N., Stables, M., and Hall, G. M., 2014, "Nonlinear aeroelastic modelling for wind turbine blades based on blade element momentum theory and geometrically exact beam theory," Energy, 76, pp. 487-501.

[95] Fernandez, G., Usabiaga, H., and Vandepitte, D., 2018, "An efficient procedure for the calculation of the stress distribution in a wind turbine blade under aerodynamic loads," Journal of Wind Engineering and Industrial Aerodynamics, 172, pp. 42-54.

[96] Rafiee, R., Tahani, M., and Moradi, M., 2016, "Simulation of aeroelastic behavior in a composite wind turbine blade," Journal of Wind Engineering and Industrial Aerodynamics, 151, pp. 60-69.

[97] Vries, O. d., 1979, "Fluid dynamic aspects of wind energy conversion," No. AG ARD-AG-243, Advisory Group for Aerospace Research and Development Paris, France.

[98] Xu, G., and Sankar, L. N., "Application of a Viscous Flow Methodology to the NREL Phase VI Rotor," Proc. ASME 2002 Wind Energy Symposium, pp. 83-93.

[99] Sørensen, J. N., 2011, "Aerodynamic Aspects of Wind Energy Conversion," Annual Review of Fluid Mechanics, 43(1), pp. 427-448.

[100] Buhl, M. L., 2005, "A New Empirical Relationship between Thrust Coefficient and Induction Factor for the Turbulent Windmill State " No. NREL/TP-500-36834, National Renewable Energy Laboratory, Golden, Colorado.

[101] Burton, T., Jenkins, N., Sharpe, D. and Bossanyi, E., 2011, "Aerodynamics of Horizontal Axis Wind Turbines," Wind Energy Handbook, pp. 39-136.

[102] Schepers, J. G., Snel, H., 1995, "Dynamic inflow. Yawed conditions and partial span pitch control," No. ECN-C-95-056, Netherlands Energy Research Foundation (ECN), Petten, Netherlands.
[103] Snel, H., and Schepers, J. G., 1995, "Joint investigation of dynamic inflow effects and implementation of an engineering method," No. ECN-C-94-107, Netherlands Energy Research Foundation (ECN), Petten, Netherlands.
[104] Burton, T., Jenkins, N., Sharpe, D. and Bossanyi, E., 2011, "Further Aerodynamic Topics for Wind Turbines," Wind Energy Handbook, pp. 137-192.
[105] Larsen, J. W., Nielsen, S. R. K., and Krenk, S., 2007, "Dynamic stall model for wind turbine airfoils," Journal of Fluids and Structures, 23(7), pp. 959-982.
[106] Liu, X., Lu, C., Liang, S., Godbole, A., and Chen, Y., 2019, "Improved dynamic stall prediction of wind turbine airfoils," Energy Procedia, 158, pp. 1021-1026.
[107] Chaney , K., Eggers, Alfred J. , Jr., Moriarty , P. J., and Holley, W. E., 2001, "Skewed Wake Induction Effects on Thrust Distribution on Small Wind Turbine Rotors," Journal of Solar Energy Engineering, 123(4), pp. 290-295.
[108] Dowler, J. L., and Schmitz, S., 2015, "A solution-based stall delay model for horizontal-axis wind turbines," Wind Energy, 18(10), pp. 1793-1813.
[109] Lanzafame, R., and Messina, M., 2012, "BEM theory: How to take into account the radial flow inside of a 1-D numerical code," Renewable Energy, 39(1), pp. 440-446.
[110] Murua, J., Palacios, R., and Graham, J. M. R., 2012, "Applications of the unsteady vortex-lattice method in aircraft aeroelasticity and flight dynamics," Progress in Aerospace Sciences, 55, pp. 46-72.
[111] Lee, H., and Lee, D.-J., 2019, "Numerical investigation of the aerodynamics and wake structures of horizontal axis wind turbines by using nonlinear vortex lattice method," Renewable Energy, 132, pp. 1121-1133.
[112] Chattot, J.-J., 2007, "Helicoidal vortex model for wind turbine aeroelastic simulation," Computers & Structures, 85(11), pp. 1072-1079.
[113] Breton, S.-P., Coton, F. N., and Moe, G., 2008, "A study on rotational effects and different stall delay models using a prescribed wake vortex scheme and NREL phase VI experiment data," Wind Energy, 11(5), pp. 459-482.
[114] Gaunaa, M., Sorensen, N., and Dossing, M., "Prediction of steady aerodynamic performance of rotors with winglets using simple prescribed wake methods," 49th AIAA Aerospace Sciences Meeting including the New Horizons Forum and Aerospace Exposition.

[115] Riziotis, V., Manolas, D., and Voutsinas, S., 2011, "Free-wake aeroelastic modelling of swept rotor blades," EWEA ConferenceBrussels, Belgium.
[116] JEONG, M.-S., YOO, S.-J., and LEE, I., 2012, "WIND TURBINE AERODYNAMICS PREDICTION USING FREE-WAKE METHOD IN AXIAL FLOW," International Journal of Modern Physics: Conference Series, 19, pp. 166-172.
[117] Jeong, M.-S., Kim, S.-W., Lee, I., Yoo, S.-J., and Park, K. C., 2013, "The impact of yaw error on aeroelastic characteristics of a horizontal axis wind turbine blade," Renewable Energy, 60, pp. 256-268.
[118] Rodriguez, S. N., and Jaworski, J. W., 2019, "Strongly-coupled aeroelastic free-vortex wake framework for floating offshore wind turbine rotors. Part 1: Numerical framework," Renewable Energy, 141, pp. 1127-1145.
[119] Rodriguez, S. N., and Jaworski, J. W., 2020, "Strongly-coupled aeroelastic free-vortex wake framework for floating offshore wind turbine rotors. Part 2: Application," Renewable Energy, 149, pp. 1018-1031.
[120] Rankine, W. J. M., 1865, "On the Mechanical Principles of the Action of Propellers," Transactions of the Institution of Naval Architects, 6.
[121] Froude, R. E., 1889, "On the Part Played in Propulsion by Differences of Fluid Pressure," Trans. Inst. Naval Architects, 30, p. 390.
[122] Fejtek, I., and Roberts, L., 1992, "Navier-Stokes computation of wing/rotor interaction for a tilt rotor in hover," AIAA Journal, 30(11), pp. 2595-2603.
[123] Rajagopalan, R. G., and Mathur, S. R., 1993, "Three dimensional analysis of a rotor in forward flight," Journal of the American Helicopter Society, 38(3), pp. 14-25.
[124] Sørensen, J. N., and Kock, C. W., 1995, "A model for unsteady rotor aerodynamics," Journal of Wind Engineering and Industrial Aerodynamics, 58(3), pp. 259-275.
[125] Aagaard Madsen, H., 1997, A CFD analysis of the actuator disc flow compared with momentum theory results, ; No corporate text available (Country unknown/Code not available).
[126] Mikkelsen, R., Sørensen, J. N., and Shen, W. Z., 2001, "Modelling and analysis of the flow field around a coned rotor," Wind Energy, 4(3), pp. 121-135.
[127] Sørensen, J. N., Shen, W. Z., and Munduate, X., 1998, "Analysis of wake states by a full-field actuator disc model," Wind Energy, 1(2), pp. 73-88.
[128] Troldborg, N., Sørensen, J. N., and Mikkelsen, R., 2007, "Actuator Line Simulation of Wake of Wind Turbine Operating in Turbulent Inflow," Journal of Physics: Conference Series, 75, p. 012063.

[129] Sørensen, J. N. r., and Shen, W. Z., 2002, "Numerical Modeling of Wind Turbine Wakes," Journal of Fluids Engineering, 124(2), pp. 393-399.
[130] Shen, W. Z., Zhu, W. J., and Sørensen, J. N., 2012, "Actuator line/Navier–Stokes computations for the MEXICO rotor: comparison with detailed measurements," Wind Energy, 15(5), pp. 811-825.
[131] Wang, L., Liu, X., and Kolios, A., 2016, "State of the art in the aeroelasticity of wind turbine blades: Aeroelastic modelling," Renewable and Sustainable Energy Reviews, 64, pp. 195-210.
[132] Kaya, M. N., Kose, F., Ingham, D., Ma, L., and Pourkashanian, M., 2018, "Aerodynamic performance of a horizontal axis wind turbine with forward and backward swept blades," Journal of Wind Engineering and Industrial Aerodynamics, 176, pp. 166-173.
[133] Lee, H. M., and Kwon, O. J., 2020, "Performance improvement of horizontal axis wind turbines by aerodynamic shape optimization including aeroealstic deformation," Renewable Energy, 147, pp. 2128-2140.
[134] Liu, Y., Xiao, Q., Incecik, A., Peyrard, C., and Wan, D., 2017, "Establishing a fully coupled CFD analysis tool for floating offshore wind turbines," Renewable Energy, 112, pp. 280-301.
[135] Wang, L., Quant, R., and Kolios, A., 2016, "Fluid structure interaction modelling of horizontal-axis wind turbine blades based on CFD and FEA," Journal of Wind Engineering and Industrial Aerodynamics, 158, pp. 11-25.
[136] Dai, L., Zhou, Q., Zhang, Y., Yao, S., Kang, S., and Wang, X., 2017, "Analysis of wind turbine blades aeroelastic performance under yaw conditions," Journal of Wind Engineering and Industrial Aerodynamics, 171, pp. 273-287.
[137] Yu, D. O., and Kwon, O. J., 2014, "Predicting wind turbine blade loads and aeroelastic response using a coupled CFD–CSD method," Renewable Energy, 70, pp. 184-196.
[138] Dose, B., Rahimi, H., Herráez, I., Stoevesandt, B., and Peinke, J., 2018, "Fluid-structure coupled computations of the NREL 5 MW wind turbine by means of CFD," Renewable Energy, 129, pp. 591-605.
[139] Dose, B., Rahimi, H., Stoevesandt, B., and Peinke, J., 2020, "Fluid-structure coupled investigations of the NREL 5 MW wind turbine for two downwind configurations," Renewable Energy, 146, pp. 1113-1123.
[140] Amin Allah, V., and Shafiei Mayam, M. H., 2017, "Large Eddy Simulation of flow around a single and two in-line horizontal-axis wind turbines," Energy, 121, pp. 533-544.

[141] Ciri, U., Petrolo, G., Salvetti, M. V., and Leonardi, S., 2017, "Large-eddy simulations of two in-line turbines in a wind tunnel with different inflow conditions," Energies, 10(6), p. 821.
[142] Choi, N. J., Hyun Nam, S., Hyun Jeong, J., and Chun Kim, K., 2013, "Numerical study on the horizontal axis turbines arrangement in a wind farm: Effect of separation distance on the turbine aerodynamic power output," Journal of Wind Engineering and Industrial Aerodynamics, 117, pp. 11-17.
[143] Korobenko, A., Yan, J., Gohari, S. M. I., Sarkar, S., and Bazilevs, Y., 2017, "FSI Simulation of two back-to-back wind turbines in atmospheric boundary layer flow," Computers & Fluids, 158, pp. 167-175.
[144] El Chazly, N. M., 1993, "Static and dynamic analysis of wind turbine blades using the finite element method," Renewable Energy, 3(6), pp. 705-724.
[145] Tarfaoui, M., Nachtane, M., and Boudounit, H., 2019, "Finite Element Analysis of Composite Offshore Wind Turbine Blades Under Operating Conditions," Journal of Thermal Science and Engineering Applications, 12(1).
[146] Bechly, M. E., and Clausen, P. D., 1997, "Structural design of a composite wind turbine blade using finite element analysis," Computers & Structures, 63(3), pp. 639-646.
[147] Song, F., Ni, Y., and Tan, Z., 2011, "Optimization Design, Modeling and Dynamic Analysis for Composite Wind Turbine Blade," Procedia Engineering, 16, pp. 369-375.
[148] He, J., Jin, X., Xie, S. Y., Cao, L., Lin, Y., and Wang, N., 2019, "Multi-body dynamics modeling and TMD optimization based on the improved AFSA for floating wind turbines," Renewable Energy, 141, pp. 305-321.
[149] Wang, L., and Sweetman, B., 2013, "Multibody dynamics of floating wind turbines with large-amplitude motion," Applied Ocean Research, 43, pp. 1-10.
[150] Jin, X., Li, L., Ju, W., Zhang, Z., and Yang, X., 2016, "Multibody modeling of varying complexity for dynamic analysis of large-scale wind turbines," Renewable Energy, 90, pp. 336-351.
[151] Bauchau, O. A., and Craig, J. I., 2009, "Euler-Bernoulli beam theory," Structural Analysis, O. A. Bauchau, and J. I. Craig, eds., Springer Netherlands, Dordrecht, pp. 173-221.
[152] Oñate, E., 2013, "Thick/Slender Plane Beams. Timoshenko Theory," Structural Analysis with the Finite Element Method Linear Statics: Volume 2. Beams, Plates and Shells, Springer Netherlands, Dordrecht, pp. 37-97.
[153] Arany, L., Bhattacharya, S., Adhikari, S., Hogan, S. J., and Macdonald, J. H. G., 2015, "An analytical model to predict the natural frequency of offshore wind turbines on

three-spring flexible foundations using two different beam models," Soil Dynamics and Earthquake Engineering, 74, pp. 40-45.
[154] Bazilevs, Y., Hsu, M.-C., Kiendl, J., and Benson, D. J., 2012, "A computational procedure for prebending of wind turbine blades," International Journal for Numerical Methods in Engineering, 89(3), pp. 323-336.
[155] Hsu, M.-C., and Bazilevs, Y., 2012, "Fluid–structure interaction modeling of wind turbines: simulating the full machine," Computational Mechanics, 50(6), pp. 821-833.
[156] Benra, F.-K., Dohmen, H. J., Pei, J., Schuster, S., and Wan, B., 2011, "A Comparison of One-Way and Two-Way Coupling Methods for Numerical Analysis of Fluid-Structure Interactions," Journal of Applied Mathematics, 2011, p. 853560.
[157] Vahdati, M., Sayma, A. I., Imregun, M., and Simpson, G., 2005, "Multibladerow Forced Response Modeling in Axial-Flow Core Compressors," Journal of Turbomachinery, 129(2), pp. 412-420.
[158] He, L., and Ning, W., 1998, "Efficient Approach for Analysis of Unsteady Viscous Flows in Turbomachines," AIAA Journal, 36(11), pp. 2005-2012.
[159] Hall, K. C., and Lorence, C. B., 1993, "Calculation of Three-Dimensional Unsteady Flows in Turbomachinery Using the Linearized Harmonic Euler Equations," Journal of Turbomachinery, 115(4), pp. 800-809.
[160] Hall, K. C., Thomas, J. P., and Clark, W. S., 2002, "Computation of Unsteady Nonlinear Flows in Cascades Using a Harmonic Balance Technique," AIAA Journal, 40(5), pp. 879-886.
[161] He, L., 2008, "Harmonic Solution of Unsteady Flow Around Blades with Separation," AIAA Journal, 46(6), pp. 1299-1307.
[162] Rahmati, M. T., He, L., and Wells, R. G., "Interface Treatment for Harmonic Solution in Multi-Row Aeromechanic Analysis," Proc. ASME Turbo Expo 2010: Power for Land, Sea, and Air, pp. 1253-1261.
[163] Rahmati, M., He, L., and Li, Y., "Multi-row interference effects on blade aeromechanics in compressor and turbine stages," Proc. Proceedings of the 13th International Symposium on Unsteady Aerodynamics, Aeroacoustics and Aeroelasticity of Turbomachines (ISUAAAT), paper S9-5.
[164] Rahmati, M. T., He, L., and Li, Y. S., 2015, "The Blade Profile Orientations Effects on the Aeromechanics of Multirow Turbomachines," Journal of Engineering for Gas Turbines and Power, 138(6), p. 062606.

[165] Rahmati, M. T., He, L., Wang, D. X., Li, Y. S., Wells, R. G., and Krishnababu, S. K., 2013, "Nonlinear Time and Frequency Domain Methods for Multirow Aeromechanical Analysis," Journal of Turbomachinery, 136(4), p. 041010.

[166] Liu, L., and Dowell, E. H., 2004, "The Secondary Bifurcation of an Aeroelastic Airfoil Motion: Effect of High Harmonics," Nonlinear Dynamics, 37(1), pp. 31-49.

[167] Liu, L., Dowell, E. H., and Thomas, J. P., 2007, "A high dimensional harmonic balance approach for an aeroelastic airfoil with cubic restoring forces," Journal of Fluids and Structures, 23(3), pp. 351-363.

[168] Vilmin, S., Lorrain, E., Hirsch, C., and Swoboda, M., "Unsteady Flow Modeling Across the Rotor/Stator Interface Using the Nonlinear Harmonic Method," Proc. ASME Turbo Expo 2006: Power for Land, Sea, and Air, pp. 1227-1237.

[169] Amato, G., Giovannini, M., Marconcini, M., and Arnone, A., 2018, "Unsteady Methods Applied to a Transonic Aeronautical Gas Turbine Stage," Energy Procedia, 148, pp. 74-81.

[170] Horcas, S. G., Debrabandere, F., Tartinville, B., Hirsch, C., and Coussement, G., 2017, "Rotor-tower interactions of DTU 10MW reference wind turbine with a non-linear harmonic method," Wind Energy, 20(4), pp. 619-636.

[171] Horcas, S. G., Debrabandere, F., Tartinville, B., Hirsch, C., and Coussement, G., 2017, "Extension of the Non-Linear Harmonic method for the study of the dynamic aeroelasticity of horizontal axis wind turbines," Journal of Fluids and Structures, 73, pp. 100-124.

[172] Howison, J., Thomas, J., and Ekici, K., 2018, "Aeroelastic analysis of a wind turbine blade using the harmonic balance method," Wind Energy, 21(4), pp. 226-241.

[173] Drofelnik, J., Da Ronch, A., and Campobasso, M. S., 2018, "Harmonic balance Navier-Stokes aerodynamic analysis of horizontal axis wind turbines in yawed wind," Wind Energy, 21(7), pp. 515-530.

[174] JAMESON, A., SCHMIDT, W., and TURKEL, E., "Numerical solution of the Euler equations by finite volume methods using Runge Kutta time stepping schemes," 14th Fluid and Plasma Dynamics Conference.

[175] Rao, S. S., 2011, Mechanical vibrations, Pearson.

[176] Fu, Z.-F., and He, J., 2001, Modal analysis, Butterworth-Heinemann.

[177] de Boer, A., van der Schoot, M. S., and Bijl, H., 2007, "Mesh deformation based on radial basis function interpolation," Computers & Structures, 85(11), pp. 784-795.

[178] Saxer, A. P., and Giles, M. B., 1993, "Quasi-three-dimensional nonreflecting boundary conditions for Euler equations calculations," Journal of Propulsion and Power, 9(2), pp. 263-271.
[179] Bechmann, A., Sørensen, N. N., and Zahle, F., 2011, "CFD simulations of the MEXICO rotor," Wind Energy, 14(5), pp. 677-689.
[180] Carrión, M., Woodgate, M., Steijl, R., Barakos, G., Gómez-Iradi, S., and Munduate, X., 2014, "CFD and Aeroelastic Analysis of the MEXICO Wind Turbine," Journal of Physics: Conference Series, 555, p. 012006.
[181] Herraez, I., Medjroubi, W., Stoevesandt, B., and Peinke, J., 2014, "Aerodynamic Simulation of the MEXICO Rotor," Journal of Physics: Conference Series, 555, p. 012051.
[182] Plaza, B., Bardera, R., and Visiedo, S., 2015, "Comparison of BEM and CFD results for MEXICO rotor aerodynamics," Journal of Wind Engineering and Industrial Aerodynamics, 145, pp. 115-122.
[183] Sørensen, N. N., Zahle, F., Boorsma, K., and Schepers, G., 2016, "CFD computations of the second round of MEXICO rotor measurements," Journal of Physics: Conference Series, 753, p. 022054.
[184] Martinez, J., Doerffer, P., Szulc, O., and Tejero, F., 2015, "Aerodynamic analysis of wind turbine rotor blades," Task Q, 19(2), pp. 129-140.
[185] Ghasemi, E., Bararnia, H., Soleimanikutanaei, S., and Lin, C. X., 2018, "Direct numerical simulation and analytical modeling of electrically induced multiphase flow," International Journal of Mechanical Sciences, 142-143, pp. 397-406.
[186] Ogino, K., Mamori, H., Fukushima, N., Fukudome, K., and Yamamoto, M., 2019, "Direct numerical simulation of Taylor–Couette turbulent flow controlled by a traveling wave-like blowing and suction," International Journal of Heat and Fluid Flow, 80, p. 108463.
[187] Watanabe, T., Zhang, X., and Nagata, K., 2019, "Direct numerical simulation of incompressible turbulent boundary layers and planar jets at high Reynolds numbers initialized with implicit large eddy simulation," Computers & Fluids, 194, p. 104314.
[188] Yang, L., Dong, M., Benshuai, F., Qiang, L., and Chenxi, Z., 2019, "Direct numerical simulation of fine flow structures of subsonic-supersonic mixing layer," Aerospace Science and Technology, 95, p. 105431.
[189] Zhu, H., Liu, W., and Zhou, T., 2020, "Direct numerical simulation of the wake adjustment and hydrodynamic characteristics of a circular cylinder symmetrically attached with fin-shaped strips," Ocean Engineering, 195, p. 106756.

[190] Kajishima, T., and Taira, K., 2017, Computational Fluid Dynamics, Springer International Publishing.